Low-temperature thermochronology: methodological studies and application in collisional orogens

Der Fakultät für Geowissenschaften, Geotechnik und Bergbau

der Technischen Universität Bergakademie Freiberg

eingereichte

DISSERTATION

zur Erlangung des akademischen Grades

doctor rerum naturalium

(Dr.rer.nat.),

vorgelegt
von Dipl.-Geol. Konstanze Stübner
geboren am 03.03.1979 in Leipzig

Freiberg, den

Acknowledgements

I am grateful for the help of many people who made this dissertation possible. Most of all I thank Lothar Ratschbacher for the splendid opportunity to work in the Pamirs, and for patience and guidance in the field and during data analysis and interpretation. Raymond Jonckheere is acknowledged for his advice on the methodological part of my thesis and on fission-track analysis for the applied projects. The most interesting ideas were born in vigorous discussions of the fission-track group at Freiberg.

Thank you to Uwe Martens who involved me into the Guatemala project by inviting me to participate in his field work. I would also like to thank Mike McWilliams and Jim Metcalf who supported me during my visit at Stanford University; together with many more colleagues there they made it a very memorable and successful stay for me. Pieter Vermeesch facilitated apatite (U-Th)/He measurements at ETH Zürich.

Field work in Tajikistan would not have been the same without Klaus Stanek, Richard Gloaguen and our Tajik collaborators Vladisav Minaev, Negmat Rajabov, Mustafo and Ilhomjon, and the most outstanding driver, Ibrahim. István Dunkl conducted the majority of (U-Th)/He analyses at Univ. Göttingen and provided a large batch of last-minute results; the study of Cenozoic exhumation in the Southwest Pamirs greatly benefited from his commitment.

Thanks also to all the colleagues and friends who supported me throughout my PhD, and my family who encouraged me in all my endeavours. This thesis was funded by a fellowship of the Studienstiftung des Deutschen Volkes and a one-year travel grant by the German Academic Exchange Council.

Abstract

Apatite (U-Th)/He and fission-track dating are low-temperature geothermochronometers of increasing importance in geological research, in particular for resolving the timing, rate and magnitude of vertical displacements of the upper crust resulting from climatic or tectonic factors. The calculation of radiometric ages and thermal histories from the fission-track record in a mineral relies on counts and measurements of etched fission tracks under an optical microscope. In recent work, it has been recognized that the sources of error are due to observational factors related to the manner in which the tracks are etched. The *first part* of this thesis therefore aims at a better understanding of the etching of nuclear tracks in minerals. A model is proposed based on detailed observations of track etch pits in minerals and numerical simulations that explains the characteristic features of track etch pits and their evolution with etching time.

In Chapter 2 the etch-pit geometries are interpreted in terms of periodic bond chains following the atomistic theory of crystal growth and dissolution. Periodic bond chains are identified, which relate triangular etch pits to tri-octahedral micas and diamond-shaped etch pits to di-octahedral lattices. A first-order estimate of the bond strengths between neighboring atoms along the periodic bond chains is in agreement with the relative track etch rates in the different investigated minerals. Hexagonal and star-shaped etch pits in tri-octahedral mica violate the lattice symmetries; they are explained by simultaneous etching of the front and back of mica subunits as a result of the fact that these have become detached during track formation by high-energy particles (swift-ion tracks, fission tracks). This work emphasized the influence of the lattice structure on the track formation process that is at odds with existing theories.

Periodic bond chains account for the outlines of etched nuclear tracks in different minerals but fall short of explaining a number of other observations, most prominently the curvature of etch pits, their complex diameter distribution, and variable growth rates according to the defect (alpha-recoil track, fission track, dislocation, etc.) and as a function of etching time. In Chapter 3, an atomistic etching model is proposed and implemented in a Monte Carlo computer simulation. Apparent horizontal and vertical growth rates during four stages of etch pit evolution are related to bond strength between neighbouring lattice units; the onset and duration of these stages are determined by the bond strength and the extent of the defect. Results show that high bond-strength minerals are better able to sustain angular features than low bond-strength minerals. Implications for particle track dating include: (1) the increase of the number of etched alpa-recoil tracks with etching time due to bulk etching is non-linear because the bulk etch rate is not constant; (2) the evolution of the etch-pit shape with continued etching can cause loss of tracks due to observation effects related to loss of contrast.

The *second part* focuses on two case studies integrating thermochronologic, structural, petrologic, and geochronologic data. Chapter 4 is a comprehensive study of the tectonic evolution of Central America. Previously unpublished petrologic, structural, and geochronologic data constrain Paleozoic amalgamation of Pangea, development of Mesozoic proto-Pacific arcs, and Jurassic intra-arc rifting. In the Early Cretaceous intra-arc rifting reverted to subduction and collision. A subduction zone developed along the south margin of southern Mexico; oblique subduction led to ophiolite emplacement and sinistral collision of the Caribbean arc (future Cuba, Hispaniola, Jamaica) along the Motagua suture zone in the Late Cretaceous. At ~40 Ma the Chortís block separated from southern Mexico under sinistral transtension; subsequently it was displaced ≤1100 km eastward to its present location in central Guatemala, south of the Motagua suture zone. Apatite fission track ages and structural data along the fault zones constrain individual faults strands through the Neogene and indicate that the Polochic fault zone, north of the Motagua suture zone, constitutes the active plate boundary. Chapter 4 demonstrates how geochronology, thermochronology, structural geology and petrology work together to unravel >400 Ma of a complex interplay of arc formation, rifting, and collision.

The second case study focuses on the Pamir Mountains in Tajikistan, which have received little attention to date due to their remote location in a politically unstable area. The Shaxdara gneiss dome of southwestern Pamirs has previously been interpreted as Archean−Proterozoic basement accreted to the Asia continental margin during amalgamation of Eurasia. It is reinterpreted in Chapter 5 as a Paleozoic−Mesozoic marine sediment sequence, metamorphosed in a Cretaceous Andean-type magmatic arc and overprinted subsequently by the India-Asia collision. The major achievement of this study is the recognition of large-scale extension in the Pamirs. Continued convergence between India and Asia in the Tertiary caused sinistral transpression along the western Pamirs and the formation of *en echelon* antiforms. Thickening is compensated by upper crustal extension confined to the thermally weakened gneiss domes. Apatite fission-track ages reveal late Miocene exhumation of the Shaxdara dome by tectonic denudation along the South Pamir normal fault. Apatite (U-Th)/He ages from high elevation samples reflect this cooling event; low-elevation samples indicate later exhumation by rapid incision of the Pjansch River, likely commencing in the Pleistocene. The Shaxdara dome study highlights the possibilities that low-temperature thermochronology opens up in the fields of geomorphology and neotectonics.

Zusammenfassung

Apatit (U-Th)/He- und Spaltspurendatierung sind Niedrigtemperatur-Geothermochronometer, die in den Geowissenschaften zunehmend an Bedeutung gewinnen, insbesondere bei der zeitlichen Einordnung von vertikalen Bewegungen in der oberen Kruste, von Hebungsraten und Hebungsbeträgen. Solche Hebungen resultieren aus tektonischen oder klimatischen Veränderungen. Die Berechnung von radiometrischen Altern und Temperaturgeschichten aus Spaltspuren im Mineral beruht auf Zählungen und Messungen geätzter Spuren unter dem Mikroskop. Neuere Studien zeigen, daß die Hauptfehlerquelle dabei Beobachtungsfaktoren im Zusammenhang mit der Ätzung der Spuren sind. Darum befaßt sich der *erste Teil* der Arbeit mit der Ätzung von Partikelspuren in Mineralien. Basierend auf Beobachtungen von Ätzgruben und einer numerischen Simulation wird ein Modell vorgeschlagen, das charakteristische Eigenschaften von Ätzgruben und deren Entwicklung mit zunehmender Ätzzeit erklärt.

In Kapitel 2 werden geometrische Eigenschaften von Ätzgruben mit Hilfe der atomistischen Theorie von Kristallwachstum und –lösung interpretiert. „Periodic bond chains“ (Bindungsketten) werden identifiziert, welche die dreieckigen Ätzgruben in tri-oktaedrischen und rautenförmigen Ätzgruben in di-oktaedrischen Glimmern erklären. Eine grobe Abschätzung der Bindungsstärken zwischen benachbarten Atomen entlang der Bindungsketten stimmt mit den relativen Ätzgeschwindigkeiten in verschiedenen Mineralien überein. Hexagonale und sternförmige Ätzgruben in tri-oktaedrishen Glimmern stehen im Widerspruch zur Kristallsymmetrie; sie werden durch gleichzeitiges beidseitiges Ätzen der einzelnen Glimmer-Schichten erklärt. Diese wurden bei der Spurenentstehung durch hochenergetische Teilchen (Ionenspuren, Spaltspuren) voneinander getrennt. Die Arbeit betont den Einfluß der Kristallstruktur auf die Spurenentstehung; dies steht im Widerspruch mit bestehenden Theorien.

Bindungsketten erklären zwar die Form geätzter Partikelspuren in verschiedenen Mineralien, nicht aber eine Reihe von weiteren Beobachtungen, wie zum Beispiel die Krümmung von Ätzgruben, ihre komplexe Durchmesser-Verteilung und die Wachstumsraten, die für verschiedene Arten von Defekten (Alpha-Rückstoß Spuren, Spaltspuren, Dislokationen, etc.) und mit der Ätzzeit variieren. In Kapitel 3 wird daher ein atomistisches Ätzmodell vorgeschlagen und als Monte Carlo Computersimulation realisiert. Die Entwicklung der Ätzgruben wird in vier Stadien unterteilt. Scheinbare vertikale und horizontale Wachstumsraten hängen von den Bindungsstärken ab, Beginn und Dauer der Stadien von der Bindungsstärke und der Größe des Defekts. Starke Bindungen resultieren in eckigeren Ätzformen als schwache Bindungen. Für Partikel-Datierungen bedeutet das, daß die Anzahl geätzer Alpha-Rückstoß Spuren nicht linear mit der Ätzzeit steigt, da (1) die vertikale Ätzrate nicht konstant ist und (2) die Entwicklung der

Ätzgrubenform mit zunehmender Ätzzeit zum Verlust von Ätzgruben aufgrund von verringertem Kontrast führen kann.

Der *zweite Teil* besteht aus zwei Fallstudien, die thermochronologische, strukturelle, petrologische und geochronologische Daten umfassen. Kapitel 4 ist eine umfassende Studie über die tektonische Entwicklung Zentralamerikas. Bisher unveröffentlichte Daten belegen die paläozoische Amalgamierung von Pangäa, Entstehung von mesozoischen Proto-Pazifischen magmatischen Bögen und jurassische Grabenbildung (Rifting) entlang der magmatischen Bögen. In der frühen Kreide ging Rifting wieder zu Subduktion und Kollision über. Entlang des Südrands von Süd-Mexiko entstand eine Subduktionszone; schräge Subduktion führte in der späten Kreide zur Entstehung von Ophiolit-Decken und sinistraler Kollision des karibischen Bogens (Kuba, Hispaniola, Jamaica) entlang der Motagua Suturzone. Um 40 Ma trennte sich der Chortís Block unter sinistraler Transtension von Süd-Mexiko. Seitdem hat er sich ≤1100 km nach Osten zu seiner heutigen Position in Zentral-Guatemala südlich der Motagua Sutur verlagert. Spaltspuren- und Struktur-Daten zeigen, welche Störungen im Neogen aktiv waren; sie belegen, daß die aktive Plattengrenze die Polochic Störung nördlich der Motagua Sutur ist. Kapitel 4 zeigt, wie Geochronologie, Thermochronologie, Strukturgeologie und Petrologie zusammenarbeiten können, um >400 Ma einer komplexen Geschichte aus magmatischer Bogen-Entwicklung, Rifting und Kollision zu enträtseln.

In der zweiten Fallstudie geht es um den Pamir in Tadschikistan; dieser wurde aufgrund der Abgelegenheit und der instabilen politischen Lage bisher wenig untersucht. Der Shaxdara Gneisdom im südwestlichen Pamir wurde bisher als archaisch-proterozoisches Grundgebirge aufgefaßt, das während der Amalgamierung von Eurasien an den Südrand Asiens angeschweißt wurde. In Kapitel 5 wird der Dom als paläozoisch-mesozoische Sedimentsequenz reinterpretiert, die in einem kretazischen kontinentalen magmatischen Bogen metamorphisiert und während der Indien-Asien Kollision überprägt wurde. Als bedeutendstes Ergebnis dieser Arbeit wurde großräumige Extension im Pamir festgestellt. Indien-Asien Konvergenz im Tertiär führte zu sinistraler Transpression im westlichen Pamir und zur Ausbildung von *en echelon* Gneisdomen. Die Krustenverdickung wird durch Extension in der oberen Kruste kompensiert. Extension ist an die thermisch geschwächten Gneisdome gebunden. Apatit Spaltspurenalter zeigen spätmiozäne Exhumierung des Shaxdara-Doms durch tektonische Denudation entlang der Süd-Pamir Abschiebung an. Apatit (U-Th)/He-Alter aus größeren topographischen Höhen sind durch dieses miozäne Ereignis geprägt; Proben aus niedrigeren Höhen kennzeichnen spätere Exhumierung durch schnelle Einschneidung des Pjansch-Flusses, welche wahrscheinlich im Pleistozän begann. Diese Studie betont vor allem die Möglichkeiten, die sich aus der Anwendung der Thermochronologie auf dem Gebiet der Geomorphologie und Neotektonik eröffnen.

Contents

List of Tables and Figures

Geometries of etched fission and alpha-recoil tracks

Revelation of nuclear tracks and dislocations

The North American−Caribbean plate boundary

Appendix

Late Miocene exhumation of the Shaxdara gneiss dome

Appendix

Chapter 1

1. Summary

Apatite (U-Th)/He and fission-track dating are low-temperature geothermochronometers of increasing importance in geological research, in particular for resolving the timing, rate and magnitude of vertical displacements of the upper crust resulting from climatic or tectonic factors. The calculation of radiometric ages and thermal histories from the fission-track record in a mineral relies on counts and measurements of etched fission tracks under an optical microscope. In recent work, it has been recognized that the sources of error are due to observational factors related to the manner in which the tracks are etched. The *first part* of this thesis therefore aims at a better understanding of the etching of nuclear tracks in minerals. A model is proposed based on detailed observations of track etch pits in minerals (**Chapter 2**) and numerical simulations (**Chapter 3**) that explains the characteristic features of track etch pits and their evolution with - etching time.

The *second part* focuses on two case studies integrating thermochronologic, structural, petrologic, and geochronologic data. **Chapter 4** is a comprehensive study of the tectonic evolution of Central America. Previously unpublished petrologic, structural, and geochronologic data constrain Paleozoic amalgamation of Pangea, development of Mesozoic proto-Pacific arcs, Jurassic intra-arc rifting, Early and Late Cretaceous subduction and emplacement of oceanic lithosphere and subduction-accretion complexes, and Tertiary to Recent strike-slip faulting, forming the Caribbean and North America plate boundary. Apatite and (U-Th)/He data provide important information for the Tertiary to Recent deformation and exhumation history.

In contrast to Central America, little is known about the tectonic evolution of the Southern Pamir Mountains of Tajikistan. New geochronologic and structural data (**Chapter 5**) demonstrate that the Shaxdara gneiss complex, previously considered as Archean-Proterozoic basement, is instead of Phanerozoic origin. Apatite fission-track and (U-Th)/He age data allow the identification of the largest extensional gneiss dome in the entire India−Asia collision zone and constrain Miocene exhumation of the gneiss dome under top-to-south, syn-collisional extension. (U-Th)/He ages point to a late episode of rapid river incision, possibly related to deep-to-intermediate seismic activity beneath the Southern Pamirs.

2. Chapter 2: Geometries of etched fission and alpha-recoil tracks

Despite its practical importance for fission-track and recoil-track dating, nuclear-track etching in minerals has, in general, received little attention compared to track revelation in glasses and plastics. Current estimates of the efficiencies with which fission tracks are etched and counted in different minerals and crystallographic planes are based on old models involving two

traditional etching velocities: v_t (track etching velocity along the nuclear defect) and v_v (bulk etching velocity of the mineral surface).

Observations of etched fission tracks in apatite reveal that their complex geometries result from the superposition of a track channel and a surface etch pit. Thus (1) etch pit evolution cannot be described by traditional models based on v_t and v_v; (2) the surface etch pit holds no information on the defect properties along the nuclear track or the nature of the defect and thus should be disregarded in studies aimed at particle identification based on etched-track profiles in minerals.

Etched recoil tracks in micas present a different case because the nuclear track is too short to produce a separate channel and etch pit. In addition, the sheet structure of the detector reduces the problem of correlating etch figures in different crystallographic planes to two dimensions. The etch-pit geometries are interpreted in terms of periodic bond chains following the atomistic theory of crystal growth and dissolution. It follows from detailed observations that the periodic bond chains in phlogopite are O-Mg-O chains within the octahedron layer; the periodic bond chains in biotite have the same orientation and composition except for partial substitution of Mg^{2+} with Fe^{2+}. Following this interpretation, the periodic bond chains in muscovite are O-Al-O chains at the back and front of the octahedral subunit. According to this model triangular etch pits are characteristic of tri-octahedral micas and diamond-shaped etch pits for di-octahedral lattices. A first-order estimate of the bond strengths between neighboring atoms along the periodic bond chains is in agreement with the relative track etch rates in the different investigated minerals.

Hexagonal and star-shaped etch pits that violate the lattice symmetries occur in tri-octahedral but not in di-octahedral micas when the linear energy transfer from the particle to the lattice exceeds a critical limit. Their anomalous shapes are due to simultaneous etching of the front and back of individual tetrahedral-octahedral-tetrahedral (TOT) subunits as a result of the fact that these have become detached. The loss of cohesion between TOT units over a much larger radius (~1 μm) than the track diameter (5-10 nm) is an indication of discontinuous track formation and of the influence of the lattice structure on the track formation process that is at odds with existing theories.

3. Chapter 3: Revelation of nuclear tracks and dislocations

Periodic bond chains account for the outlines of etched nuclear tracks in different minerals (Chapter 2) but fall short of explaining a number of other observations made in the course of these studies. Most prominent is the fact that the etch-pit sides and faces are curved to a variable extent. Detailed measurements also reveal that etched recoil tracks have a complex diameter dis-

tribution. The lateral and vertical etch pit growth rate varies according to the defect (alpha-recoil track, fission track, dislocation, etc.) and as a function of etching time. In Chapter 3, an atomistic etching model for minerals is proposed and implemented in a Monte Carlo computer simulation.

The simulations show that there are four stages in the evolution of an etch pit. During the first stage, the etch pit is an inverted pyramid; its horizontal and vertical dimensions increase at a constant rate; the apparent horizontal (v_h) and vertical (v_d) growth rates are faster than during all subsequent stages but nevertheless less than the step retreat rate (v_s) on account of surface etching (v_v). The pyramid apex is truncated in the second stage; it is thereafter bounded by an expanding bottom plane and shrinking lateral walls; this is accompanied by a gradual decrease of v_h; v_d drops to zero and then shows a gradual further decrease; negative v_d indicate a slow decrease of the etch-pit depth; the bottom plane acquires a concave-up curvature; the outward curvature of the walls, initiated during the first stage, increases. During the third stage the etch pit consists of a single concave-up bottom plane; v_h and v_d decrease at declining rates; consecutive etch pit profiles are scalable in the horizontal direction. A fourth stage is inferred but not documented by the simulations; it sets in when v_h is reduced to zero; unless this corresponds to an as yet unidentified steady-state condition, the etch pit from here on forth shrinks until it eventually disappears.

The onset and duration of these stages are determined by the extent of the defect or nuclear track below the etched mineral surface and the bond strength ϕ between neighbouring lattice atoms. High-ϕ minerals are better able to sustain angular features than low-ϕ minerals. The sole cause for this succession is the process of stochastic rounding of confined steps and faces due to a statistical bias. The size distribution of etched recoil tracks is due to (1) the size distribution of the latent tracks, (2) the random truncation of the surface tracks, (3) the variable rate of etch-pit enlargement and (4) the fact that new tracks are exposed at the surface due to surface etching. The greater size of dislocation, fission-track and ion-track etch pits is due to their greater extent below the surface. The increase of the number of etched tracks with etching time due to bulk etching is non-linear because the bulk etch rate v_v is not constant. The evolution of the etch-pit shape with continued etching can cause loss of tracks due to observation effects related to loss of contrast.

4. Chapter 4: The North American–Caribbean plate boundary

The northern margin of the Caribbean plate in Guatemala and Honduras is one of the worldwide few continental transform plate boundaries. These are characterized by high seismic activity (San Andreas fault zone, South Alpine fault). In Guatemala and Honduras, this plate boundary comprises (from north to south) the Polochic fault zone, cutting the Maya block of the

North American plate, the Chuacús complex, the Motagua suture zone that is currently active as a strike-slip fault zone (the Motagua fault zone), and the Chortís block, currently part of the Caribbean plate. Large ophiolites occur both north and south of the Motagua fault zone.

Structural, geochronologic, and petrologic data permit correlations between the Maya and Chortís blocks and tectonostratigraphic complexes of southern Mexico and the northern Caribbean. A common high-pressure metamorphic event in the Chuacús complex of Guatemala and the Acatlán complex of southern Mexico identifies them as parts of the Early Paleozoic Alleghanian–Appalachian orogeny along the southern margin of North America. Permotriassic U/Pb zircon ages document development of a proto-Pacific magmatic arc, which initiated after final amalgamation of Pangea along its western margin. Jurassic rifting, related to the opening of the Gulf of Mexico, is reflected in high-temperature/low-pressure metamorphism, anatexis, and rift-related sedimentation. Intra-arc rifting separated the Chortís block from southern Mexico and generated the oceanic crust preserved in the ophiolites south of the Motagua fault zone (on the Chortís block).

In the Early Cretaceous rifting reverted to subduction and ultimate collision of the Chortís block with southern Mexico. Continued proto-Pacific subduction is reflected in Cretaceous arc-related magmatism that is widespread on the Chortís block and in southern Mexico.

In the Late Cretaceous, the southern margin of the Chortís block and the Maya block with its leading Chuacús complex was involved into highly oblique subduction; it led to the emplacement of the oceanic crust preserved north of the Motagua fault zone, and sinistral collision of these North American units with the Caribbean arc (future Cuba, Hispaniola, Jamaica). Spectacular sinistral transpression is preserved in the structural record of the Chuacús complex north of the Motagua fault zone. Imbrication is dated at 75-60 Ma by $^{40}Ar/^{39}Ar$ and apatite fission-track cooling ages.

The separation of the Chortís block from southern Mexico under sinistral transtension is reflected in the apatite fission-track and (U-Th)/He ages of ~40 Ma in southern Mexico and syn-kinematic minerals in mylonite zones in the Chortís block, dated by U/Pb, Rb/Sr, and in particular Ar/Ar geochronology. Its eastward displacement along the active plate boundary amounts to ≤1100 km to date. Apatite fission-track ages and structural data along the fault zones constrain individual faults strands through the Neogene and indicate that the Polochic fault zone, north of the Motagua suture zone, constitutes the active plate boundary.

Chapter 4 demonstrates how geochronology, thermochronology, structural geology and petrology work together to unravel >400 Ma of a complex interplay of arc formation, rifting, and collision.

5. Chapter 5: Late Miocene exhumation of the Shaxdara gneiss dome

The Pamir Mountains in Tajikistan have received little attention to date due to their remote location in a politically unstable area. The major achievement of this study is the recognition of a large extensional dome (Shaxdara gneiss dome) in the southwestern Pamirs.

The Shaxdara gneiss dome has previously been interpreted as Archaen−Proterozoic basement accreted to the Asia continental margin during Paleozoic−Mesozoic amalgamation of Eurasia. It is re-interpreted in Chapter 5 as a Paleozoic−Mesozoic marine sediment sequence, metamorphosed in a Cretaceous Andean-type magmatic arc and overprinted subsequently by the India-Asia collision.

Structural and thermochronologic results constrain the evolution of the Shaxdara gneiss dome since the Oligocene. Continued convergence between India and Asia caused transpression along the western Pamirs. The *en echelon* arrangement of three gneiss complexes in the western Pamirs suggest a common origin as antiforms resulting from buckling and crustal thickening with a sinistral wrenching component. Thickening is compensated by upper crustal extension confined to the thermally weakened gneiss domes.

A detailed apatite fission-track study constrains tectonic denudation and exhumation of the footwall beneath a major south dipping shear/fault zone during the late Miocene. Apatite (U-Th)/He ages from high elevation samples reflect this cooling event; in contrast, low-elevation samples indicate later exhumation by rapid incision of the Pjansch river, likely commencing in the Pleistocene. Slightly older ages from low-elevation samples along the Shaxdara river may suggest an older age of the latter. Post-Miocene rapid exhumation is tentatively suggested to be linked to deep seismicity recorded beneath the Shaxdara dome, but further interpretation is premature.

The Shaxdara dome study highlights the possibilities that low-temperature thermochronology opens up in the fields of geomorphology and neotectonics.

Chapter 2

Observations on the geometries of etched fission and alpha-recoil tracks with reference to models of track revelation in minerals

(published in *Radiation Measurements*, vol. 39, 2005)

Abstract

The kinetic and atomistic theories of crystal growth and dissolution are used to interpret the shapes and orientations of fission-track, recoil track and dislocation etch pits in tri-octahedral phlogopite and di-octahedral muscovite. An atomistic approach combined with symmetry considerations lead to the identification of the periodic bond chains that determine the etch pit morphologies and relative etch rates at a chemical level: O-Mg-O in phlogopite, O-Mg-O-Fe in biotite and O-Al-O in muscovite. Using first-order estimates of the bond strengths, it is possible to account for the relative track etch rates in these minerals. The reported, sometimes simultaneous, occurrence of triangular, polygonal and hexagonal etch pit contours in phlogopite, some of which violate the crystal symmetry, suggests that the cohesion of the phlogopite lattice is lost over a much larger radius than that of the track core around the trajectories of particles for which the energy loss exceeds a threshold value. This is interpreted as an indication of pronounced sublattice and anisotropic effects during track registration.

1. Introduction

Despite its practical importance for fission-track dating, nuclear track etching in minerals has, in general, received little attention compared to track revelation in glasses and plastics. Outdated etching models still form the basis of current estimates of the efficiencies with which fission tracks are etched and counted in different minerals and crystallographic planes (Fleischer et al., 1975; Gleadow, 1978; 1981). It has been argued that the existing estimates of the combined etching and counting efficiencies (ηq) are in error (Jonckheere and Van den haute, 1996; 1998; 1999) and that ηq depends on the track length distribution in the sample (Jonckheere and Van den haute, 2002). If this is so, then the calculated fission-track ages could be inaccurate irrespective of the fact whether they are determined using the absolute approach (ϕ-method; Price and Walker, 1963; Jonckheere, 2003) or a standard-based approach (Z and ζ dating methods; Hurford and Green, 1983; Hurford, 1990; 1998).

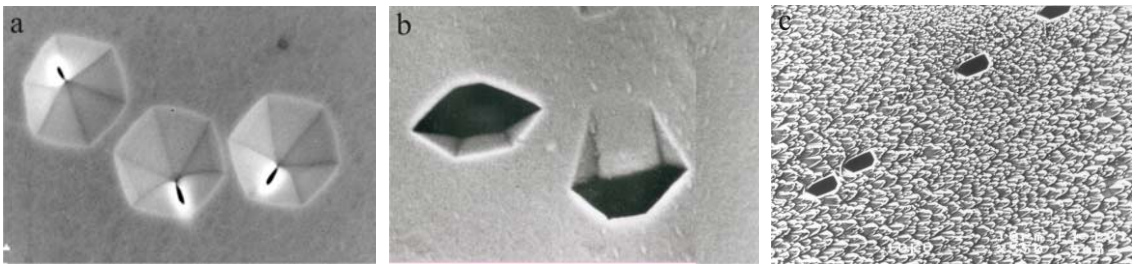

Figure 1. Etched fission tracks (a, b) and dislocations (c) in pitted (a; basal), scratched (b; prism) and textured (c) surfaces of apatite.

Etched fission tracks in apatite possess complex, composite geometries, consisting of a track channel and additional facets at its intersection with the surface. The channel is parallel to the latent track and not affected by the orientation of the etched surface. In contrast, the structures at the surface depend on its crystallographic orientation. Surface etch pits in apatite are prominent in basal planes (Figure 1a), less so in prismatic (Figure 1b) and absent in most higher index planes (Figure 1c). Identical etch pits develop where dislocations, small-angle grain boundaries and cracks intersect the surface. These etch pits are well developed at low etchant concentrations and reflect the crystal symmetry with little influence of the track orientation. They are less well-developed and their shape is to some extent influenced by the orientation of the track at higher concentrations (Jonckheere and Van den haute, 1996). According to the law of mass action, the chemical reaction between the etchant and the crystal surface is, at all stages, further from equilibrium for a more concentrated than for a less concentrated etchant, and the etch rate is consequently greater. This suggests that the different development and geometries of surface etch pits is determined by the reaction rate. The preceding leads us to conclude that the complex track geometries result from the *superposition* of two entirely independent etch pits:

(1) a *track etch pit* (channel) and (2) a *surface etch pit*, which has *nothing* whatsoever to do with the defect properties along the nuclear track.

This has a number of significant consequences: (1) the composite geometries of etched nuclear tracks in minerals *cannot* be described by an etch model based on the two traditional etching velocities, v_t (track etching velocity) and v_b (bulk etching velocity); this accounts for the limited success of attempts to predict track geometries in minerals based on extensions of the (v_b, v_t)-model appropriate for isotropic detectors (Wagner, 1968; Gleadow, 1978; Thiel and Külzer, 1978; Somogyi, 1981); (2) the geometry of the surface etch pit is not only independent of the defect properties along a nuclear track, but also of the nature of the defect, and therefore holds no information on v_t; this implies that studies aimed at particle identification based on etched-track profiles in minerals should disregard the surface etch pit; based on an alternative model for track revelation in minerals (Jonckheere and Van den haute, 1996), it is doubtful whether even the track-channel profile allows one to make inferences about v_t, and therefore about the track forming particle; this leaves the etch-anneal-etch method (Green et al., 1978) as the only method for the identification of the track forming particle based on track etching in minerals.

Progress in our understanding of track revelation in minerals has been hindered by confusion about the meaning of "etching velocity". It is clear that, in models derived from those for isotropic detectors, an etching velocity is understood to be the rate of displacement of a *point on a surface* in a given direction. It follows from this definition that the track (channel) *cross-section* is a direct reflection of the variation of the etching velocity with orientation (Yamada et al. 1994). Although such a definition works for isotropic detectors, it is important to note that it is in conflict with the kinetic theories of crystal growth and dissolution (Frank, 1958; Irving, 1962; Jaccodine; 1962), wherein an etching velocity (radial shift velocity; v_r) is a property of a *crystallographic plane*. The radial shift velocity v_r is a *vector* normal to a crystallographic plane equal in magnitude to its rate of translation parallel to itself. Even before Frank (1958) published his kinetic theory, Hartman and Perdok (1955a, b, c) had published an atomistic theory of crystal growth and dissolution based on the concept of *periodic bond chains*. Here, we attempt to interpret the geometries of etched recoil tracks in phlogopite and muscovite in terms of these theories.

2. Regular etch pits

The fact that phlogopite ($KMg_3[(OH)_2AlSi_3O_{10}]$) and muscovite ($KAl_2[(OH)_2AlSi_3O_{10}]$) are sheet silicates reduces the problem of correlating the etch figures in different crystallographic planes to one in two dimensions. The phlogopite lattice is made up of a stack of tetrahedron and octahedron layers (Klockmann, 1978; Putnis, 1992; Figure 2). The tetrahedron layer is a two-dimensional network of corner-sharing SiO_4-tetrahedra with partial substitution of Si by Al. In

end-member phlogopite, the octahedron layer is a two-dimensional network of edge-sharing MgO_6-octahedra. An octahedron layer sandwiched between two tetrahedron layers forms the TOT-unit, which is repeated along the ***c***-axis. The TOT-units are only weakly held together by electrostatic forces, mediated by shared K^+-ions. The TOT-unit of muscovite is made up of the same two tetrahedron subunits as in phlogopite but the octahedron subunit consists of AlO_6-octahedra. All (three out of three) possible octahedron cation sites are occupied by Mg^{2+} in phlogopite (tri-octahedral mica), whereas only two out of three possible octahedron cation sites are occupied by Al^{3+} in muscovite (di-octahedral mica). Biotite is a tri-octahedral mica similar to phlogopite in which part of the Mg^{2+} has been substituted by Fe^{2+}. The Fe end-member is annite.

Figure 3 is a photomicrograph of etched alpha-recoil tracks and dislocations in the cleavage plane (001) of phlogopite. This discussion centres on two observations: (1) the etch-pit contours are triangular; (2) the triangles at the front and back of a phlogopite sheet are oriented in opposite directions (Figure 4). Triangular contours have been reported before by Patel and Ramanathan (1962a,b), Brauer (1971) and Hashemi-Nezhad (1997). Measurements by Hashemi-Nezhad (1998) showed that the etch pits are not equilateral but isosceles triangles. Hashemi-Nezhad (1998) also pointed out the 180°-rotation of etch pits at the front and the back of a mica sheet. It is clear from Figure 3 that this is a simplification, and that the sides and bottom of the etch pits are curved. This is no concern here; it is shown elsewhere that the etch pit curvature as well as the fact that recoil-track and dislocation etch pits are different sizes is also explained by the kinetic and atomistic etching theories (Jonckheere et al., in prep.).

It is interesting to note that although the recoil-track etch pits in Figure 3 possess a range of diameters, all have identical profiles. This points to an equilibrium form. The etched recoil-track diameters are at least an order of magnitude larger than the size of latent tracks ($\sim 10^2$ nm; Jonckheere and Gögen, 2001). The simple geometries compared to those of fission tracks (e.g. Figure 6 of Gögen and Wagner, 2000) imply that there is no superposition of a track etch pit and a surface etch pit, but only a surface etch pit. In contradiction with the conclusion of Fleischer (2003), this means that no information about the physical properties (dE/dx) of the latent track can be gleaned from the etch-pit profile. The absence of steps in the track profiles (Figure 3) also speaks against the assertion that unetchable gaps exert a significant influence on the revelation of recoil tracks and co-determine the effective track etch rate v_t.

The kinematic approach implies the principle of reciprocity (Batterman, 1957; Frank, 1958; Frank and Ives, 1962; Jonckheere and Van den haute, 1996), which states that upon dissolution (etching) a convex form becomes bounded by the planes with the highest radial shift velocities (fast etching) and a concave form becomes bounded by the planes with the lowest radial shift

velocities (slow etching). Reciprocity is better known in connection with the reverse process: upon growth a convex form becomes bounded by the slowest growing planes and a concave form becomes bounded by the fastest growing planes. The co-existence of a *distinct* track etch-pit and surface etch-pit in the case of fission tracks (Figure 1) is thus a consequence of the fact that the former is a concave form, whereas the latter is a convex-concave form (convex intersections with the etched surface).

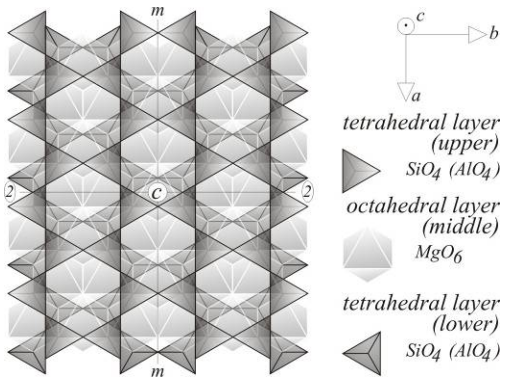

Figure 2. The TOT-unit of phlogopite viewed perpendicular to the a,b-plane. K-atoms between the units are not shown. The crystallographic axes and the components of the tetrahedron and octahedron layers are indicated on the right.

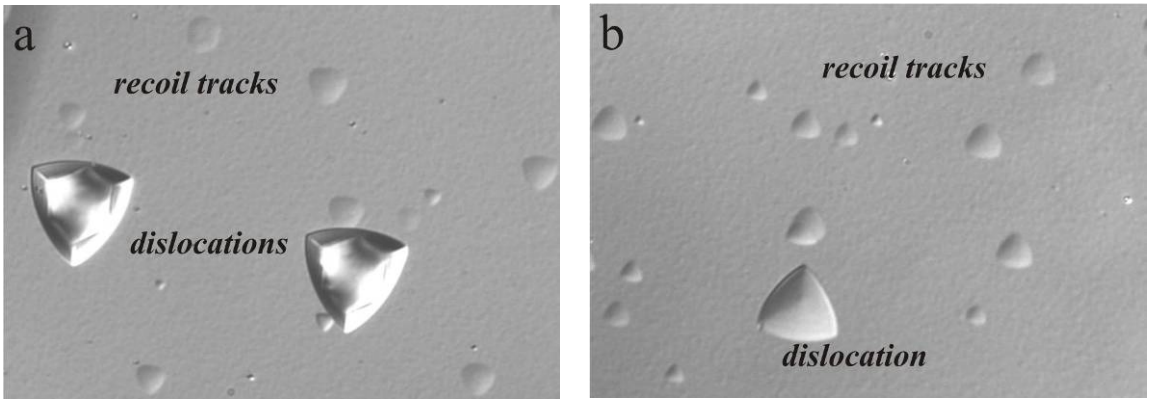

Figure 3. Etched alpha-recoil tracks and dislocations in the cleavage plane of a phlogopite sample. Note the triangular etch pit contours. The hexagonal shapes inside the dislocations are not the bases of the etch pits but due to the fact that the dislocations extend throughout the thickness of the sample and have been etched from both sides.

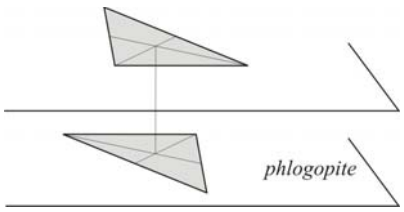

Figure 4. Orientation of the etched alpha-recoil tracks at the front and back of a phlogopite sample.

In the case of phlogopite and muscovite it is possible to treat the mineral as a stack of independent sheets and to assign radial shift velocities to different *directions* in the (001)-plane, reducing the problem to two dimensions. Although the recoil-track etch pits in Figure 3 have been identified as surface etch pits, they are *concave* forms within the two dimensions of a sheet, and bounded by the *slowest etching* directions. According to an atomistic approach, these directions correspond to those of the periodic bond chains. These are, per definition, straight, continuous, periodic chains of strong chemical bonds between the lattice atoms. Because it requires more energy to break these bonds than those in other directions, etching proceeds by nucleation and removal of the atoms at the extremities of the half-chains on either side of the nucleus, parallel to the chain direction.

Assuming that they are equilateral triangles, the etch pits are bounded by three periodic bond chains at 60° to each other. The simplest assumption is that the sides of the etch pits also have identical radial shift velocities. This suggests that the three periodic bond chains have the same chemical composition, i.e. are made up of the same sequence of atoms. Because neighbouring TOT-units are held together by weak electrostatic forces, the periodic bond chains cannot cross from one unit to the next and are thus situated *within* the TOT-unit, i.e. parallel to the (0,0,1)-plane. The symmetry of phlogopite is 2/m with a twofold axis parallel to the ***b***-axis and a mirror plane perpendicular to the ***b***-axis (Figure 2). It follows from the fact that the etch pits at the front and back of a phlogopite sheet are oriented in *opposite* directions that one periodic bond chain is perpendicular to the ***a***-axis, i.e. oriented along [1,0,0]. Given the orientation (60°) of the remaining periodic bond chains to the first, it follows that they must correspond to the directions [1,1,0] and [1,-1,0]. These three directions correspond to the sides of the etch pit on *one side* of a phlogopite sheet; the directions of the sides of the etch pit on the *reverse side* are obtained by applying the twofold rotational symmetry around ***b***: [-1,0,0], [-1,1,0] and [-1,-1,0].

The periodic bond chains cannot be made up of atoms from *all three* subunits of the TOT-unit, i.e. from *both* tetrahedron layers *and* the octahedron layer, because there can then be only *one set* of periodic bond chains for the entire TOT-unit, in which case it would be impossible for etch pits on either side of a phlogopite sheet to point in opposite directions. In addition, if such a set of periodic bond chains were rotated 180° about the ***b***-axis, it would give rise to a set of six intersecting chains, in which case the etch pit would be hexagonal. Furthermore, the front and back periodic bond chains cannot be situated *within* the upper and lower tetrahedron subunits, since each of these has a sixfold axis. This means that there are six equivalent orientations with which it is impossible to construct anything other than a hexagonal etch pit. It is possible that a periodic bond chain is made up of atoms from *one* tetrahedron layer *and* from the octahedron layer but an examination of the phlogopite lattice shows that there is no obvious chain of Mg-O-

Si bonds along [1,0,0], [1,1,0] and [1,-1,0] (Figure 2; Jonckheere et al., in prep.) or, for reasons of symmetry, along [-1,0,0], [-1,1,0] and [-1,-1,0]. The remaining possibility is that the periodic bond chains are made up of linked atoms from the octahedron subunit *alone*. As before, they cannot be constituted of atoms from the entire subunit, since this implies that there cannot be separate and differently oriented sets of three periodic bond chains for the front and the back of the phlogopite sheet. This leads to the conclusion that one set of periodic bond chains is situated in within the top half of the octahedron unit, whereas the second set must then be situated within the bottom half. Having established the crystallographic orientations of the periodic bond chains as well as the subunit of the TOT-structure in which they must be situated, it is a matter of inspection of the phlogopite lattice to establish that the periodic bond chains along all these directions are chemically identical and made up of simple O-Mg-O chains (Figure 5a).

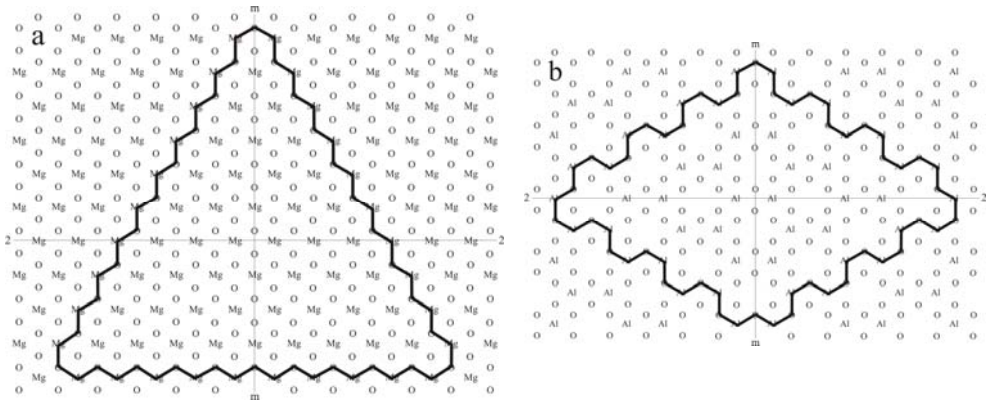

Figure 5. The octahedron subunits of (a) phlogopite (tri-octahedral) and (b) muscovite (di-octahedral) mica. In (a) three periodic bond chains (O-Mg-O) form an equilateral triangle; in (b) four periodic bond chains (O-Al-O) form a diamond.

Biotite has the same tri-octahedral structure as phlogopite; it is thus not surprising the etch pits have the same triangular shape. The periodic bond chain is Mg-O-Fe-O because part of the Mg^{2+} in the octahedron subunit is substituted by Fe^{2+}; the Fe/Mg-ratio depends of the extent of the substitution. Muscovite is di-octahedral with Al^{3+} instead of Mg^{2+} as the octahedral cation;the periodic bond chains are thus O-Al-O. However, because one out of three octahedron cation sites is unoccupied, the O-Al-O chains are not oriented as in phlogopite or biotite; the etch pits are diamond-shaped and bounded by [1,1,0], [1,-1,0], [-1,1,0] and [-1,-1,0] (Figure 5b, 6). There is no difference in the orientation of macroscopic etch pits at the front and the back of a muscovite sheet.

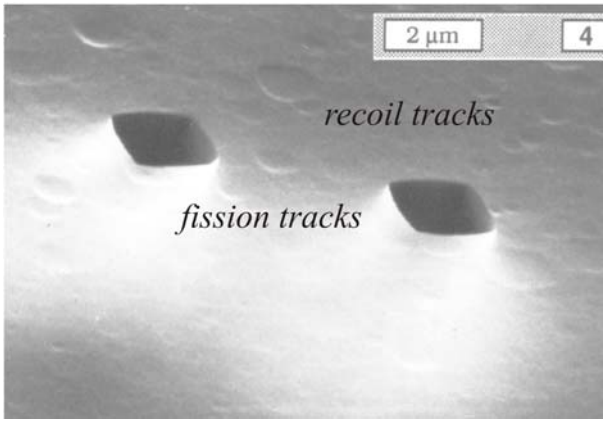

Figure 6. Diamond shaped contours of etched fission and alpha-recoil tracks in muscovite (oblique angle SEM photomicrograph).

A first-order estimate of the relative strengths of the periodic bond chains can be obtained from the bond-strengths of the di-atomic molecules: Mg-O: 363 kJ/mol; Fe-O: 390 kJ/mol; Al-O: 511 kJ/mol (Kerr, 1995). The greater strength of the Al-O bond could explain the lower track etch rate in muscovite compared to that of phlogopite or biotite for the same etchant (40% HF). It typically takes 20 min. to etch fission tracks in muscovite to a diameter of a few microns whereas it takes only 40 seconds in the dark micas. Although the Fe-O and Mg-O bond strengths are similar, biotite is more susceptible to chemical attack because Fe^{2+} can oxidize to Fe^{3+} in the presence of an electron acceptor (F^-), thus disturbing the charge balance (Faure, 1998). This accounts for the fact that alpha-recoil-tracks in biotite etch faster than in phlogopite (Lang et al., 2002a,b).

3. Irregular etch pits

The etched-track contours in phlogopite and biotite are not always triangular. Hashemi-Nezhad (1997; 1998) reported that etched fission-tracks in phlogopite can have triangular, polygonal or hexagonal contours. Lang et al. (2002a,b) observed that the etched tracks produced by ion irradiation of phlogopite at normal incidence can have triangular or hexagonal contours. These studies established that hexagonal tracks are associated with high energy-loss particles.

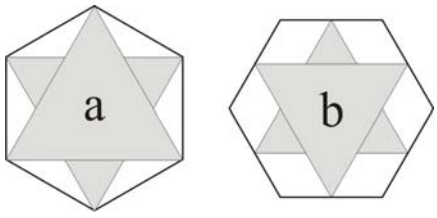

Figure 7. Relative orientation of hexagonal and triangular track contours in phlogopite; (a) as observed (Hashemi-Nezhad; 1998); (b) not observed.

Hashemi-Nezhad (1998) calculated that hexagonal tracks predominate at [dE/dx]-values in excess of ~10 MeV/µm, whereas there are only triangular tracks below ~8 MeV/µm, in reasonable agreement with the results of Lang et al. (2002a,b): triangular tracks below ~5 MeV/µm and hexagonal tracks above ~8 MeV/µm. This dependence on the properties of the track-forming particle appears to contradict the fact that etched-track contours in minerals are determined by the properties of the detector. Figure 3 of Hashemi-Nezhad (1998) also shows that the hexagonal etch pits are not bounded by directions parallel to those bounding the triangular etch pits (Figure 7) and thus not by the directions with the lowest radial shift velocities.

We propose that the passage of an ion for which [dE/dx] exceeds a threshold value alters the phlogopite structure, and, in particular, that the TOT-units become disconnected over a large radius around the actual track, so that the etchant has access to the front and back of each TOT-unit when the sample is etched (Figure 8). Much like the hexagonal dislocation cores in Figure 3, this leads to a *superposition* of the triangular etch pits with opposite orientation at the front and the back of each unit, consistent with the orientation of the hexagonal-etch pit contours as in (a) rather than (b) in Figure 7. In contrast, the TOT-units remain connected at [dE/dx]-values below the threshold value, and the etchant has access *from the top* (surface) only, giving rise to triangular etch pits. Between 8 and 10 MeV/µm (Hashemi-Nezhad, 1998) or 5 and 8 MeV/µm (Lang et al., 2002a,b), the units are partially disconnected, giving rise to an alternation of triangular and hexagonal contours along one and the same track (Hashemi-Nezhad, 1998). Interference between triangular and hexagonal etch pits could also produce polygonal etch pits, although the fact that these are observed associated with fission tracks with random orientations but not with ion tracks at normal incidence to the detector surface suggests that the track orientation has an effect.

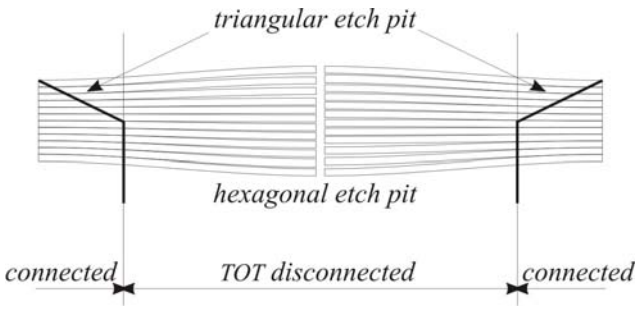

Figure 8. The loss of cohesion between the TOT-units along a nuclear track in phlogopite leads to them being etched from the front and back, producing hexagonal track contours. A triangular contour develops at the surface.

Two observations support this interpretation. First, Lang et al. (2002a,b) reported an abrupt increase of the track etch rate v_t at the precise [dE/dx]-value where the etched-track contours switch from triangular to hexagonal, although v_t does not depend on [dE/dx] on either side of

this critical value. As far as we could ascertain, there are no theoretical or experimental indications that there is a fundamental change in the track formation process or in the resulting track structure at a specific [dE/dx]-value in the electronic stopping regime, either in mica or in other detectors. Such an abrupt transition is more in accord with a change in the lattice properties of the detector. Second, the lateral extent over which the TOT-units are disconnected must be finite (Figure 8), so that the hexagonal track channels cannot increase their diameter indefinitely and etching must revert to the normal mechanism for intact phlogopite, i.e. in the form of triangular etch pits growing from the surface down (Figure 8). This explains the shallow triangular depression surrounding the hexagonal track channels reported by Lang et al. (2002b).

The phlogopite structure gives an indication of the processes that can lead to the disconnection of the TOT-units. The diameter of the hexagonal track channels indicates that the TOT-units are disconnected over a distance from the core of ~10^3 latent track diameters. This could come about by the neutralisation of the K^+-ions between the units or by their radial evacuation, possibly involving a collision cascade channelled parallel to the (001)-plane. This mechanism is hypothetical and must be supported by further experiments involving a range of ions and energies as well as a range of natural and synthetic sheet silicates. It seems probable that they will confirm that pronounced sublattice and pronounced anisotropic effects are involved in nuclear track formation in sheet silicates.

4. Conclusions

The complex geometries of etched fission-tracks, recoil-tracks and dislocations in apatite, phlogopite and muscovite demonstrate that etch models based on those for isotropic detectors are not suitable for mineral track detectors. We must reintroduce the concept of a radial shift velocity, v_r, which is characteristic of a crystallographic plane as a whole, and represented by vector normal to the plane equal in magnitude to its rate of translation parallel to itself.

The kinetic and atomistic theories of crystal growth and dissolution explain the different shapes and orientations of etch pits in the di-octahedral and tri-octahedral micas. An atomistic approach and symmetry considerations allow identification of the periodic bond chains that determine the etch pit morphologies and etch rates at a chemical level: O-Mg-O in phlogopite, O-Mg-O-Fe in biotite and O-Al-O in muscovite. Using first-order estimates of the relative bond strengths, it is possible to account for the relative etch rates of these minerals in HF.

The reported, sometimes simultaneous, occurrence of different etch pit contours in phlogopite, some of which violate the crystal symmetry, suggests that the cohesion of the phlogopite lattice is lost over a much larger radius than that of the track core around the trajectories of particles for which the energy loss exceeds a certain threshold value.

Acknowledgement

The authors are indebted to Prof. Dr. J.-C. Hadler-Neto (Instituto de Física Gleb Wataghin, Universidade Estadual de Campinas, Brazil) and the organisers of the Second Latin American Symposium on Nuclear Tracks (3-7 November, 2003, São Pedro, São Paulo, Brazil) for their invitation to present these results before a forum of experts. Reviews from Dr. R. Ketcham (University of Texas at Austin) and an unknown referee were helpful in improving the manuscript.

References

Batterman, B.W, 1957. Hillocks, pits and etch rate in Germanium crystals. J. Appl. Phys. 28, 1236-1241.

Brauer, K.H., 1971. Results of the etching method on crystals of the mica group (in German). Akademie Verlag GmbH, Berlin, 115 p.

Faure, G., 1998. Principles and applications of geochemistry (2nd ed.). Prentice Hall Inc., Upper Saddle River, New Jersey, 600 p.

Fleischer, R.L., 2003. Etching of recoil tracks in solids. Geochim. Cosmochim. Acta 67, 4769-4774.

Fleischer, R.L., Price, P.B., Walker, R.M., 1975. Nuclear tracks in solids. Principles and applications. Univ. of Calif. Press, Berkeley, 604 p.

Frank, F.C., 1958. On the kinematic theory of crystal growth and dissolution processes. In : Growth and perfection of crystals (T.H. Doremus, B.W. Roberts, D. Turnbull eds.). John Wiley, London, 411-419.

Frank, F.C., Ives, M.B., 1962. Orientation-dependent dissolution of Germanium. J. Appl. Phys. 31, 1996-1999.

Gleadow, A.J.W., 1978. Anisotropic and variable track etching characteristics in natural sphenes. Nucl. Track Detection 2, 105-117.

Gleadow, A.J.W., 1981. Fission track dating methods: what are the real alternatives? Nucl. Tracks 5, 3-14.

Gögen, K., Wagner, G.A., 2000. Alpha-recoil track dating of quaternary volcanics. Chem Geol. (Isot. Geosci. Sect.) 166, 127-137.

Green, P.F., Bull, R.K., Durrani, S.A., 1978. Particle identification from track etch-rates in minerals. Nucl. Instr. Meth. 157, 185-193.

Hartman, P., Perdok, W.G., 1955a. On the relations between structure and morphology of crystals I. Acta Cryst. 8, 49-52.

Hartman, P., Perdok, W.G., 1955b. On the relations between structure and morphology of crystals II. Acta Cryst. 8, 521-524.

Hartman, P., Perdok, W.G., 1955c. On the relations between structure and morphology of crystals III. Acta Cryst. 8, 525-529.

Hashemi-Nezhad, S.R., 1997. Geometry of charged particle tracks in crystalline detectors. Rad. Meas. 28, 167-170.

Hashemi-Nezhad, S.R., 1998. The triangular track contours in phlogopite mica detectors and discontinuity of the etchable damage. Nucl. Instr. Meth. B142, 98-110.

Hurford, A.J., 1990. Standardization of fission-track dating calibration: Recommendation by the Fission-track Working Group of the I.U.G.S. Subcomission on Geochronology. Chem. Geol. (Isot. Geosci. Sect.) 80, 171-178.

Hurford, A.J., 1998. Zeta: the ultimate solution to fission-track analysis calibration or just an interim measure? In: Advances in fission-track geochronology (P. Van den haute, F. De Corte, eds.). Kluwer Academic Publishers, Dordrecht, 19-32.

Hurford, A.J., Green, P.F., 1983. The zeta age calibration of fission-track dating. Isot. Geosci. 1, 285-317.

Irving, B.A., 1962. Chemical etching of semiconductors. In: The electrochemistry of semiconductors (P.J. Homes ed.). Academic Press, London, New York, 256-289.

Jaccodine, R.J., 1962. Use of modified free energy theorems to predict equilibrium growing and etch shapes. J. Appl. Phys. 33, 2643-2647.

Jonckheere, R., Gögen, K., 2001. A Monte-Carlo calculation of the size distribution of latent alpha-recoil tracks. Nucl. Instr. Meth. B183, 347-357.

Jonckheere, R., Stübner, K., Enkelmann, E., in prep. On the imperfect geometries of etched nuclear tracks in minerals. Geochim. et Cosmochim. Acta.

Jonckheere, R., Van den haute, P., 1996. Observations on the geometry of etched fission tracks in apatite: implications for models of track revelation. Amer. Mineral. 81, 1476-1493.

Jonckheere, R., Van den haute, P., 1998. On the frequency distributions per unit area of the dimensions of fission tracks revealed in an internal and external mineral surface and in the surface of an external detector. Rad. Meas. 29, 135-143.

Jonckheere, R., Van den haute, P., 1999. On the frequency distributions per unit area of the projected and etchable lengths of surface-intersecting fission tracks: Influences of track revelation, observation and measurement. Rad. Meas. 30, 155-179.

Jonckheere, R., Van den haute, P., 2002. On the efficiency of fission-track counts in an internal and external apatite surface and in a muscovite external detector. Rad. Meas., 35, 29-40.

Kerr, J.A., 1995. Strengths of chemical bonds. In: CRC Handbook of chemistry and physics (76th ed.) (D.R. Lide, H.P.R. Frederikse, eds.), CRC Press, Boca Raton, Florida, 9/51-9/73.

Klockmann, F., 1978. Textbook of mineralogy (16th ed., revised and extended by P. Ramdohr and H. Strunz). Ferdinand Enke Verlag, Stuttgart, pp. 876 (in German).

Lang, M., Glassmacher, U., Moine, B., Müller, C., Neumann, R. and Wagner, G.A., 2002a. Heavy-ion induced defects in phlogopite imaged by scanning force microscopy. Surf. Coat. Technol. 158/159, 439-443.

Lang, M., Glassmacher, U., Moine, B., Müller, C., Neumann, R. and Wagner, G.A., 2002b. Artificial ion tracks in volcanic dark mica simulating natural radiation damage: a scanning force microscopy study. Nucl. Instr. Meth. B191, 346-351.

Patel, A.R., Ramanathan, R., 1962a. Etching of mica cleavages. Acta Cryst. 15, 860-862.

Patel, A.R., Ramanathan, R., 1962b. Etching of synthetic fluorphlogopite. Amer. Mineral. 47, 1195-1201.

Price, P.B., Walker, R.M., 1963. Fossil tracks of charged particles in mica and the age of minerals. J. Geophys. Res. 68, 4847-4862.

Putnis, A., 1992. Introduction to mineral sciences. Cambridge University Press, Cambridge, pp. 457.

Somogyi G., 1980. Development of etched nuclear tracks. Nucl. Instr. Meth. 173, 21-42.

Thiel, K., Külzer, H., 1978. Anisotropy of track registration in natural feldspar crystals. Rad. Eff. 35, 50-56.

Wagner, G.A., 1968. Tracks from spontaneous nuclear fission of ^{238}U as a means of dating apatite and a contribution to the geochronology of the Odenwald (in German). N. Jb. Min. Abh. 110, 252-286.

Yamada R., Tagami T., Nishimura S., 1994. Assessment of overetching factor for fission track length measurement in zircon. Chem. Geol. (Isot. Geosci. Sect.) 104, 251-259.

Chapter 3

Revelation of nuclear tracks and dislocations: A Monte Carlo simulation of mineral etching

(accepted for publication in *Geochimica Cosmochimica Acta*, 2008)

Abstract

A simple atomistic Monte Carlo simulation suggests that there are up to four stages in the evolution of an etch pit in the (001)-surface of an idealised regular lattice. During the first stage, the etch pit is an inverted pyramid; its horizontal and vertical dimensions increase at a constant rate; the apparent horizontal (v_h) and vertical (v_d) growth rates are faster than during all subsequent stages but nevertheless less than the step retreat rate (v_s) on account of surface etching (v_v). The pyramid apex is truncated in the second stage; it is thereafter bounded by an expanding bottom plane and shrinking lateral walls; this is accompanied by a gradual decrease of v_h; v_d drops to a negative value indicating a slow decrease of the etch-pit depth; the bottom plane acquires a concave-up curvature; the outward curvature of the walls, initiated during the first stage, increases. During the third stage the etch pit consists of a single concave-up bottom plane; v_h and v_d decrease at declining rates; consecutive etch pit profiles are scalable in the horizontal direction. The hypothetical fourth stage is inferred but not documented by the simulations; it sets in when v_h is reduced to zero; unless this corresponds to an as yet unidentified steady-state condition, the etch pit from here on forth shrinks until it eventually disappears altogether. The sole cause for this succession is the process of stochastic rounding of confined steps and faces.

The triangular footprint of recoil-track, fission-track, ion-track and dislocation etch pits in trioctahedral mica and its compliance with the monoclinic symmetries implies that the relevant periodic bond chains are O-Mg/Fe-O chains in the octahedral layer. The size distribution of etched recoil tracks is due to (1) depth variations resulting from the size distribution of the latent tracks, (2) the random truncation of the surface tracks, (3) the variable rate of etch-pit enlargement and (4) the fact that new tracks are exposed at the surface due to surface etching. The greater size of dislocation, fission-track and ion-track etch pits is due to their greater extent below the surface. The increase of the number of etched tracks with etching time due to bulk etching is non-linear because the bulk etch rate v_v is not constant. The evolution of etch-pit shape with continued etching can also cause loss of tracks due to observation effects related to loss of contrast.

1. Introduction

Some etch pits in mica (Figure 1a) have been identified as the sites of lattice damage produced by the recoiling daughter nuclei of alpha-disintegrating isotopes. Huang and Walker (1967) and Huang et al. (1967) proposed that counting of etched recoil tracks could be the basis of a radiometric dating method founded on the same principles as the fission-track method (Price and Walker, 1962; 1963; Fleischer et al., 1975). The mean size of unetched recoil tracks (~100 nm; Jonckheere and Gögen, 2001; Stübner and Jonckheere, 2006) is ~10^3 times smaller than the length of unetched fission tracks (~10-20 μm; Jonckheere, 2003). Their accumulation rate, on the other hand, is ~10^6 times faster than that of spontaneous fission tracks. Thus, the number of recoil tracks intersecting a unit mineral surface is ~10^3 times greater than that of fossil fission tracks accumulated over the same period of time (Huang and Walker, 1967; Huang et al., 1967). This makes it possible, in principle, to date geological events (Gögen and Wagner, 2000; Glasmacher et al., 2003) and archaeological artefacts (Garrison et al., 1978). The principles and potential applications of alpha-recoil-track dating are summarized in Faure (1998), Wagner (1998) and Geyh (2005).

The fission-track method has become an important tool for geological investigations (Gleadow et al., 2002). The recoil-track method, in contrast, is not an accepted radiometric dating method for two main reasons. Recoil-track dating requires measurements of the uranium and thorium contents of the sample. This presents practical problems due to their ppb-concentrations in mica but no problems of principle because these can now be measured with different methods. The core problem, however, is relating the number of recoil-track etch pits per unit area of an etched mica surface (ρ_{RT}) to the volumetric recoil-track density (N_{RT}). A better understanding of recoil-track etching is therefore required. This contribution attempts to relate the shapes and sizes of recoil-track etch pits in phlogopite to the relevant properties of the latent tracks and the etching properties of the mineral. Section 2 lists the characteristics of etched recoil tracks. Section 3 outlines the principles of a numerical etching simulation based on an atomistic approach. The reasons for agreements and disagreements between the observations and simulations are discussed in section 4. Conclusions relating to the recoil-track dating method are formulated in section 5.

2. Observations

The present observations relate to etched recoil tracks in natural phlogopite ($KMg_3(OH)_2AlSi_3O_{10}$). Figure 1 is a photomicrograph of etched dislocations, recoil tracks and ion tracks in the cleavage plane of phlogopite. The observations below can be subdivided into those relating to their shape, size and number. The accompanying comments list earlier related observations and summarize their current interpretation.

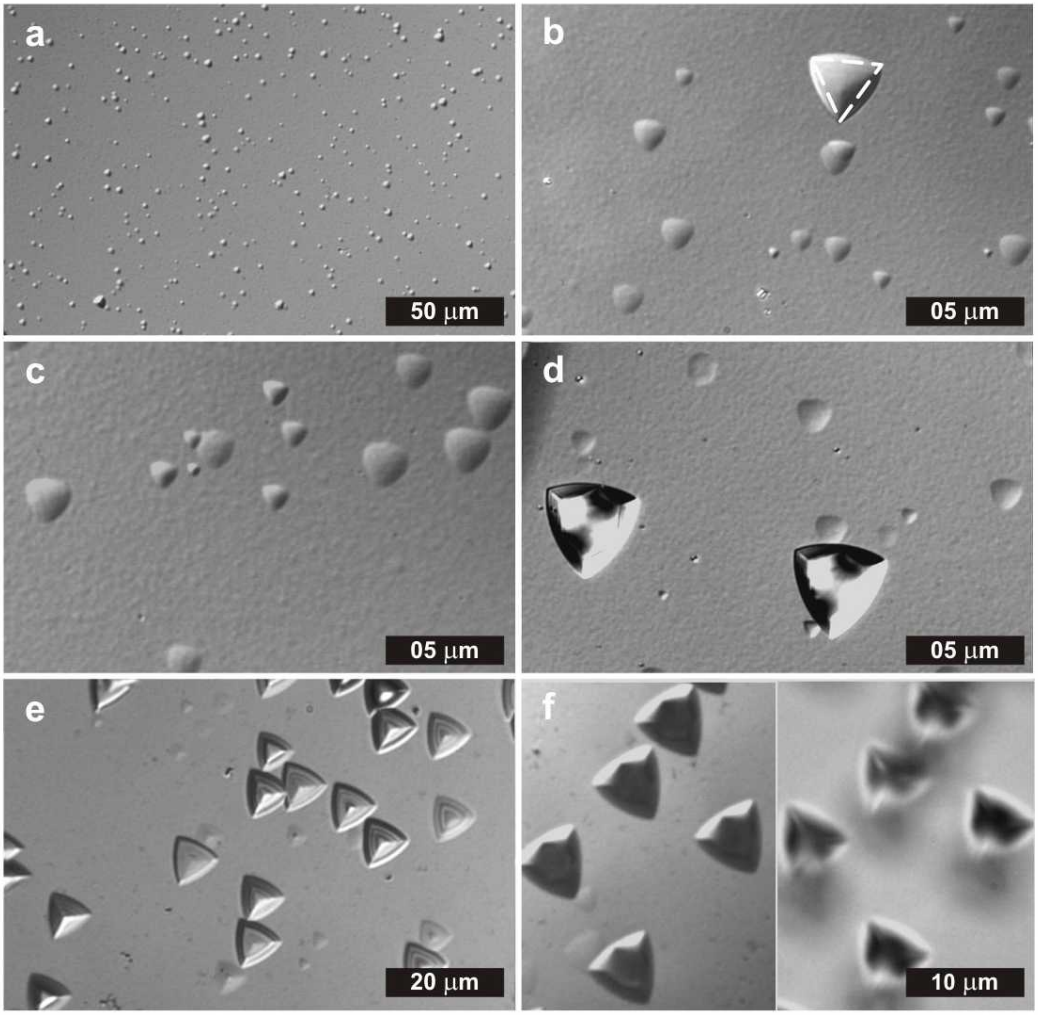

Figure 1. Photomicrographs of recoil-track, ion-track and dislocation etch pits in phlogopite etched in 48% HF at 23°C; (a) low-magnification incident-light differential interference contrast image of a carbon-coated surface etched for 150 s; (b)-(d) high-magnification images of identical samples showing triangular contours, curving, size range and much larger dislocation etch pits in (b) and (d); (e) incident-light image of an uncoated phlogopite surface irradiated through a wedge-shaped macrofol degrader with a perpendicular Xe-beam, illustrating a range of etch-pit evolution stages; the stepped appearance of some etch pits due to intermittent track structure is not observed at recoil-track etch pits; (f) incident (left) and transmitted-light (right) images of mirror etch-pits at the back and front of the same sample at a position where the Xe-beam pierced the phlogopite thickness (~30 μm).

2.1. Track outline

Although none of the etch pits in Figure 1 has straight sides, their basic shape is triangular. Triangular etch-pit contours at dislocations in phlogopite have been reported by Patel and Ramanathan (1962a; b) and Brauer (1971) and observed at fission tracks by Hashemi-Nezhad (1985; 1997). Hashemi-Nezhad (1998) showed that the triangles are not strictly equilateral, and called attention to the 180° rotation of etch pits at the front and the back of a mica sheet. Observations of recoil tracks in minerals, including the use of electron and atomic force microscopes and plasma etching, have been published by Katcoff (1969), Turkowsky (1969), Snowden-Ifft et

al. (1993) and Brown and Liu (1996). More recent observations of similar etch pits at other defects are provided by Rufe and Hochella (1999) and Aldushin et al. (2006).

Jonckheere et al. (2005) related the triangular etch-pit shapes and their relative orientations at the front and back of a phlogopite sheet to non-stoechiometric periodic bond chains (Hartmann and Perdok, 1955a-c) within the octahedral unit (O-Mg-O). Bickmore et al. (2001) had earlier identified the stoechiometric periodic bond chains of tri-octahedral 2:1 sheet silicates as [110], [1-10] and [010] on a theoretical basis. Because of the stoechiometric condition, these are made up of elements from the octahedral and both tetrahedral layers. This presents two problems: (1) these periodic bond chain orientations cannot account for the distinct etch-pit orientations at the front and back of a phlogopite sheet (Figure 1f); (2) these orientations are not consistent with the monoclinic symmetry of the phlogopite lattice (2/m). It is therefore hereafter assumed that the phlogopite TOT-unit contains two sets of periodic bond chains: [100], [-110] and [-1-10] and [-100], [110] and [1-10] (Figure 2). Each set is symmetric about the mirror plane perpendicular to the b-axis and one is converted into the other by the twofold axis parallel to b. These orientations correspond to those of the O-Mg-O-chains in the upper and lower half of the octahedral layer (Jonckheere et al., 2005). This conclusion supports that of Grim and Güven (1978) that it is more realistic to subdivide the 2:1 sheet silicate lattice into tetrahedral and octahedral units for periodic bond chain analysis. The fact remains that [100] and [-100] are composite chains consisting of [-110] and [-1-10] and [110] and [1-10] links (Figure 2). The theoretical question whether or not this disqualifies them as periodic bond chains or potential orientations of the edges of closed concave etch pits is not addressed in this work.

2.2. Curved shape

It is clear from Figure 1 that the triangular shape is an approximation and that the edges of the etch pits are arched. Gögen (1999) observed a correlation between etch-pit curvature and the rate of etch-pit growth in a set of biotite samples etched in identical conditions. The edge curvature also varies within a sample; the edges of large or shallow recoil-track etch pits are more arched than those of small (Figure 1b-c) or deep ones (Figure 1d). Rounding not only affects the etch-pit contour but also the internal face(s). Some recoil-track etch pits are saucer shaped with a rounded bottom and no other discernable internal structure (Figures 1b-d); this is also the case at short dislocations (Figure 1b) while long dislocations possess clear internal structure consisting of distinct curved faces intersecting along straight edges (Figure 1d). The rounding of edges and face(s) of recoil-track etch pits is considered a significant feature and an important criterion for evaluating the present simulations. The phenomenon is known from etching experiments but it is not the automatic outcome of theories aimed at predicting the dissolution shapes of crystals.

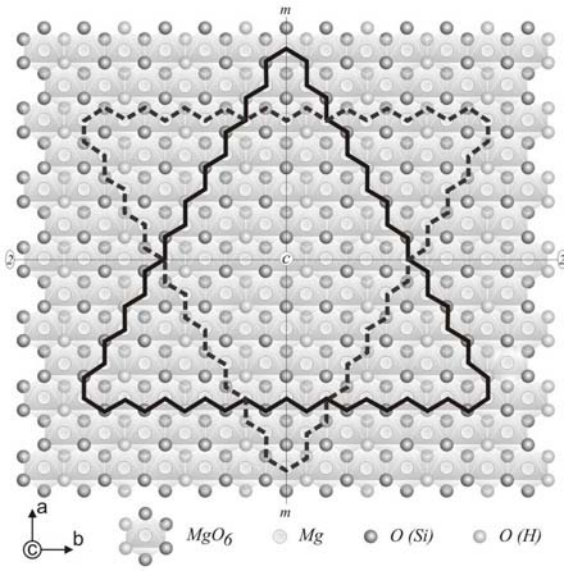

Figure 2. View perpendicular to (001) of the octahedral layer of the phlogopite lattice, m: mirror plane and (2) two-fold axis of the complete structure; thick lines: periodic bond chains at front (solid) and back (dashed).

Kinetic calculations are based on the radial shift velocities v_r of different faces; v_r is a vector normal to a face equal in magnitude to its rate of displacement parallel to itself. A dissolution plot (Jaccodine, 1962), i.e. a polar plot of v_r, or a reluctance plot (Frank, 1958; Frank and Ives, 1960; Irving, 1960; 1962), i.e. a polar plot of $1/v_r$, is the basis of kinetic calculations. Kinetic calculations can produce curved faces depending on the variation of the radial shift velocities around the maxima in the reluctance plot or minima in the dissolution plot. These plots are, however, the result of experimental measurements of the radial shift velocities. Thus, although kinetic calculations can produce curved faces, they do not actually explain them.

The atomistic theory of growth and dissolution (Hartmann and Perdok, 1955a; b; c; Hartmann, 1958; Grimbergen et al., 1998) does not explain curvature. According to this approach, growth and dissolution are governed by straight unbroken chains of strong bonds (periodic bond chains). Three sorts of faces are distinguished: (1) F (flat), parallel to two or more periodic bond chains; (2) S (stepped), parallel to just one, and (3) K (kinked), parallel to none. F-faces are the slowest etching because it requires the formation of a nucleus and subsequent retreat of the surrounding steps from the nucleation site. A concave etch pit is thus bounded by F-faces (Jonckheere and Van den haute, 1996), which are, per definition, flat. If, as in the case of mica, all the periodic bond chains lie in one plane (the (001) plane of phlogopite) then an etch pit extending from (001) into the interior cannot be bounded by F-faces but must be bounded, instead, by S (or K) faces, that need not be flat. The rounded bottoms of recoil-track etch pits are consistent with the atomistic model but not so the arched etch-pit contours at their intersection with (001). The atomistic approach explains neither the curved faces nor edges of fission-track, recoil-track or dislocation etch pits.

The molecular kinetics approach (Lacmann et al., 1974a; b) is a hybrid of the kinetic and atomistic approaches insofar as the shift velocities of crystal faces are calculated from those of the faces of an equilibrium form (E-form), related to the periodic bond chains of Hartmann and Perdok (1955a; b; c), but in fact based on earlier thermodynamic considerations of Kossel (1927), Stranski (1928) and Burton et al. (1951). The molecular kinetics approach does address the aspect of curvature but it is important to note that wherever curvature exists, it is residual curvature inherited from the original shape of the dissolving crystal. Much of the work of Lacmann et al. (1974a; b) is indeed concerned with the dissolution forms of single crystal spheres. In all these cases, the radius of curvature remains constant or decreases. The molecular kinetics method thus does not explain the increase or creation of curvature observed at recoil-track etch pits and dislocations. The matter is more clear-cut: curved faces have a more or less transient existence in two specific cases: (1) dissolution of single crystal spheres and (2) growth on the surface of hemispherical hollows. In the complementary cases of (3) growth of single crystal spheres or (4) dissolution of the surface of hemispherical cavities, the growth (G-form) and dissolution forms (D-form) are made up of flat faces (Figure 4 in Lacmann et al., 1974a; b ; Franke et al., 1975; Heimann et al., 1975; Siesmayer et al., 1975).

2.3. Track size

The recoil-track etch pits visible under an optical microscope are an order of magnitude larger than the latent tracks (Jonckheere and Gögen, 2001; Stübner and Jonckheere, 2006). It is therefore reasonable to assume that their size does not reflect the extent of lattice damage but is a consequence of etching. "Size" here and in the following refers to the etch-pit dimensions parallel to (001), measured from corner to corner. Recoil-track etch pits are always smaller than those at dislocations, fission tracks and ion tracks. The latter have a uniform size in a given sample except for occasional smaller etch pits at short dislocations and shallow tracks (Figure 1). Recoil-track etch pits, in contrast, exhibit a range of sizes from almost zero to a maximum; the track-size distribution is unimodal and negatively skewed (Figure 3a).

Dislocation etch pits grow at a constant rate with etching time (te). The intercept of a regression line to the dislocation data in Figure 3b is indistinguishable from 0; a regression line through the origin also fits quite well (correlation coefficient r = 0.96). This confirms that the size of the unetched defectis negligible and that there is no appreciable lag time before the onset of etch-pit growth. In contrast, the increase of the mean recoil-track etch-pit size with t_e is sub-linear. The data in Figure 3b fit a two-parameter exponential function ($s = a\,[1 - e^{-bt_e}]$; r = 0.98) although there are no theoretical grounds for this equation. In addition, recoil track etch pits do not grow at the same rate; this is illustrated in Figure 4: track 2 starts out much smaller than track 1 but has attained about twice its size at the end of the sequence.

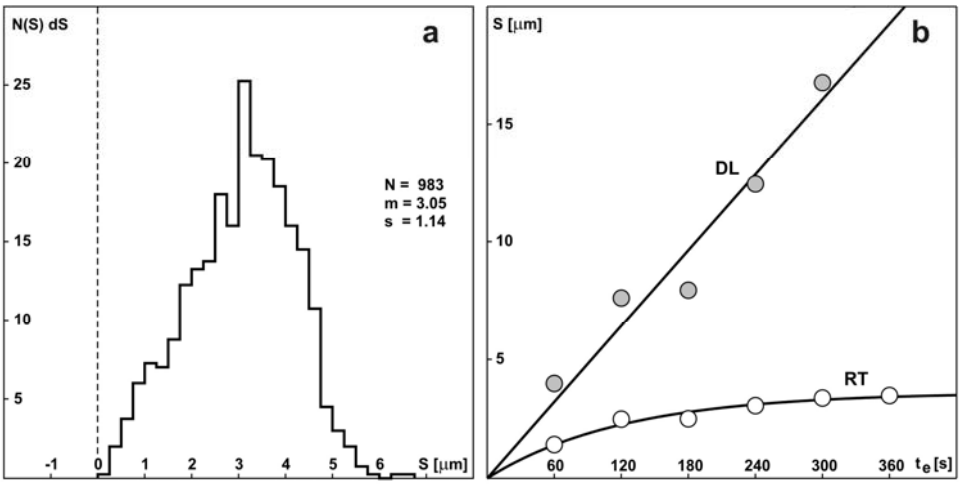

Figure 3. Dimensions of recoil-track and dislocation etch pits; (a) size distribution of recoil-track etch pits; etching conditions: 420 s in 48% HF at 23°C; N = number of measurements; m = mean (μm); s = standard deviation (μm); (b) graph of the mean size S (μm) of recoil-track (RT) and dislocation (DL) etch pits as a function of etching time t_e (s); etching conditions: 48% HF at 23°C; S is measured from corner to corner.

The recoil-track etching model of Gögen and Wagner (2000) is derived from earlier models of fission-track etching and based on three velocities: v_t (track) and v_v (vertical), both perpendicular to (001), and v_h (horizontal) parallel to (001). The latent recoil track provides an uninterrupted chain of preferential nucleation sites extending into the crystal; v_t is thus perpendicular to (001) and effectively infinite compared to v_v and v_h. Horizontal step retreat around the nucleation site in the uppermost (001) plane at a rate v_s uncovers the underlying plane and allows step retreat to set in there, and so on. The slopes of the etch-pit walls are thus determined by the unit cell dimensions in a nearest-neighbour model. Preferential nucleation ceases when the etchant reaches the lower end of the latent recoil track and v_t reverts to v_v. This creates a flat-bottomed etch pit; it is permanent because the same v_v acts at the etch-pit bottom as at the surface; its depth remains constant but its horizontal size increases indefinitely at the rate v_h.

Because $v_v \times t_e$ is large compared to the size of latent recoil tracks, new tracks are exposed at the surface and the number of recoil-track etch pits increases as a linear function of t_e, much like fission tracks in glass (Green and Durrani, 1978; Somogyi, 1980) except that the critical angle $\theta_c = 0$. This model predicts a linear increase of the number of recoil-track etch pits (section 2.4) up to a limit where the individual tracks become indistinguishable due to overlap (Gögen, 1999; Gögen and Wagner, 2000). The model implies that the track-size distribution is homogeneous between 0 and $\sim v_h \times t_e$ (tracks added due to bulk etching at the rate v_v) with a superimposed peak at $v_h \times t_e$ (tracks intersecting the original surface), again much like the diameter distribution of fission tracks in glass for $\theta_c = 0$ (Van den haute, 1985). This kinetic model does not address the basic shapes and orientations or the curvature of etch pits. The fact that it fails to ac-

count for the different sizes of recoil-track etch pits and of those at dislocations, fission and ion tracks in the phlogopite (001)-plane nevertheless constitutes a weak point.

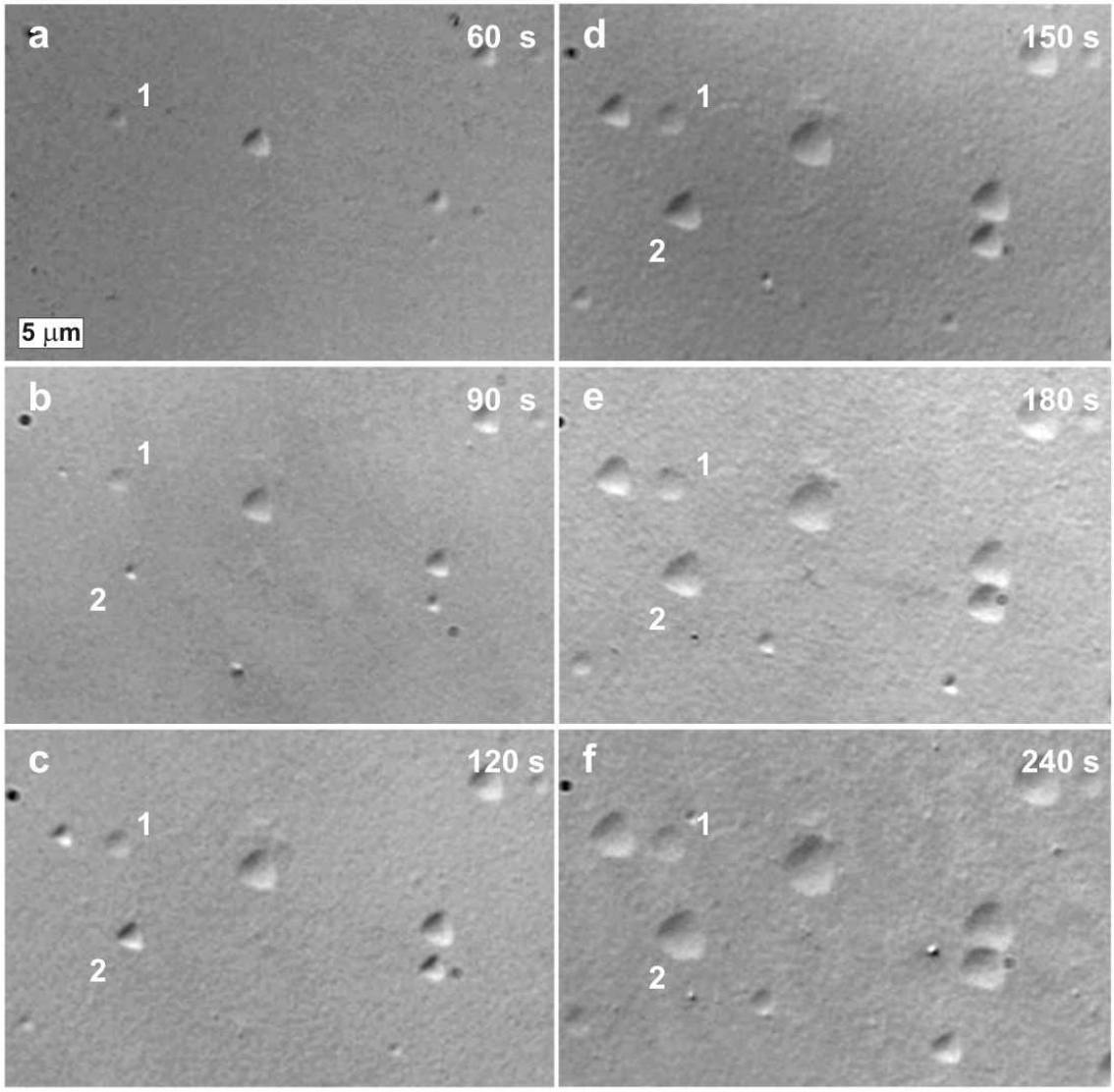

Figure 4. High-magnification incident-light differential-interference-contrast photomicrograph sequence of recoil-track etch pits in phlogopite etched for 60 to 240 s (48% HF at 23°C), illustrating the different growth rate of the individual tracks and its decrease with increasing etching time; the addition of tracks due to bulk etching, the change of the etch-pit shape and the roughening of the surface are also apparent.

2.4. Number

The earliest investigations brought to light that the number of recoil-track etch pits per unit area (ρ_{RT}) increases with etching time t_e. Huang and Walker (1967) and Huang et al. (1967) observed a sharp increase of ρ_{RT} in muscovite mica during the first 2h of etching followed by a plateau between t_e = 2 and 20h (48% HF). They associated the initial increase of ρ_{RT} with a spectrum of nucleation times for different tracks. Hashemi-Nezhad and Durrani (1981) reported

an initial increase of ρ_{RT} in biotite etched in 36% HF for 3 min followed by a levelling-off or decrease between t_e = 3 and 6 min. The authors ascribed the first phase to bulk etching (section 2.3) and the second to loss of contrast in the electron microscope images as the track size increased. Gögen and Wagner (2000) found a linear increase of ρ_{RT} with t_e for phlogopite up to t_e = 20 min and then a levelling-off due to track overlap (40% HF). These investigators counted the tracks with a phase contrast microscope, as had Huang and Walker (1967) and Huang et al. (1967). The earlier observations should not be considered as superseded by the more recent in view of the great difference in the bulk etch rates v_v of muscovite on the one hand and phlogopite and biotite on the other.

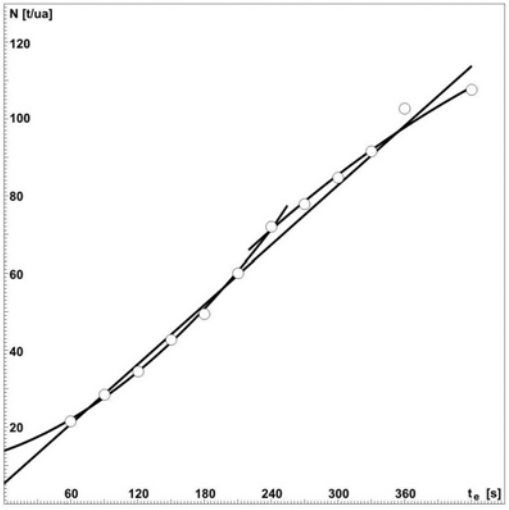

Figure 5. The number (N) of recoil-track etch pits per unit area as a function of etching time te (s); the linear and a two-segment quadratic least-squares fits illustrate the problems of estimating the intercept and slope of the function in the absence of an a priori model of the dependence of N on te; etching conditions: 48% HF at 23°C.

Glasmacher et al. (2003) confirmed the trend and interpretation of Gögen and Wagner (2000) based on tracks counts in dark micas etched for 5 to 107 min in 4% HF with the aid of a differential interference contrast microscope and a scanning force microscope. Stübner et al. (2006) discuss the results of step-etch experiments on phlogopites from the ~12 ka Laacher See tuff in the German Eifel region. The tracks were etched for 1 to 6 min. in 48% HF; after etching, the samples were carbon coated to create a reflecting surface and the etch pits counted with an optical microscope equipped with incident-light differential interference contrast. The graph of ρ_{RT} *versus* t_e suggests small deviations from the linear trend (Figure 5). The investigators point out that the model of Gögen and Wagner (2000) that predicts a linear trend is itself in question insofar as it fails to explain the shapes and sizes of the recoil-track etch pits. In particular, the assumption that v_v is constant is difficult to reconcile with the increased surface roughness with increasing t_e (Figure 4). Without the assumption of a constant v_v, it cannot be assumed that $\rho_{RT} \sim t_e$.

3. Simulation

There is renewed interest in the science of crystal dissolution for its environmental and technological significance (Lasaga and Lüttge, 2003). More and more studies make use of computer simulations based on kinetic or atomistic principles. Kinetic Monte Carlo or Molecular Dynamics calculations, parameterised using thermodynamic or *ab initio* principles have been successful at quantitative simulation of measured dissolution rates (McCoy and LaFemina, 1997; Lüttge 2005) and incorporating the effects of pH, temperature, saturation, ionic strength, inhibition, etc. (Lasaga and Lüttge 2004). Most programs are tailored to specific applications but some are more general (Cuppen et al., 2000; 2002; 2006; Hines, 2001; van Veenendaal et al., 2002, Lasaga and Lüttge, 2003). Our aim is to simulate the evolution of nuclear track etch pits in minerals. The aspects relevant to nuclear track applications are different from the priorities of mineral dissolution studies. We therefore adopt a non-specific (Kossel) crystal, solvent (etchant) and defect (nuclear track). The Kossel lattice has 3 orthogonal bond chains of equal strength ϕ along [100], [010] and [001] (Figure 6); only interactions between nearest neighbours are considered. Probabilities are assigned to the removal of a unit depending on the number i of occupied nearest-neighbour positions (Cuppen et al., 2000):

$$p_i = kT/h\ e^{-i(\phi/½kT)} \qquad (1)$$

Equation (1) implies that the ratio p_3 (kink elimination; p_k):p_4 (step nucleation; p_s):p_5 (surface nucleation; p_n) increases with increasing ϕ; angular features would thus be expected to persist for longer in a high-ϕ mineral. Re-attachment of building units is not allowed; the bond strength is set so that: $\phi/kT = 2$ at ambient temperature (Cuppen et al., 2000); in order to investigate the effects of ϕ-variation due to chemical substitutions, e.g. Fe/Mg substitution in biotite (Gögen, 1999), simulations are also performed for ϕ/kT-values from 1.90 to 2.10. The simulations do not use a physical unit of time so that the rate constant kT/h is immaterial. It is clear that the regular Kossel lattice is not suited for reproducing the triangular etch pits in the (001) plane of monoclinic phlogopite. It is however more convenient for simulations. The fact that the etch pits in (001) are bounded by identical steps is also in agreement with the assumption that the periodic bond chains of phlogopite consist of identical chains of O-Mg-O bonds in (001) (section 2.1; Figure 2). The "solid on solid" condition is imposed that prevents overhanging or undercutting structures; this implies that each building block is connected to its underlying nearest neighbour along the [001] direction.

A matrix S_{ij} represents the surface; i and j ($1 \leq i,j \leq 2500$) are the co-ordinates of a surface element in a- and b-axis units; S_{ij} is the distance from the unetched surface at (i,j) in c-axis units. At the start of the simulation, $S_{ij} = 0$ at all $(i,j) \neq (1,1)$; S_{ij} increases by 1 when a surface element

is removed. The track is represented by $S_{11} > 0$, so that one quadrant of an etch pit, containing one corner and half the adjoining sides, is modelled. Periodic boundary conditions are imposed to prevent edge effects. Separate simulations were performed for $S_{11} = 0$, 50, 75 and 100. In view of the c-axis unit (10.2 Å; Hazen and Burnham, 1973) and the recoil-track size distribution in phlogopite, which has maxima at ~30 and ~100 nm (Stübner and Jonckheere, 2006), $S_{11} = 100$ corresponds to the maximum extent of a recoil track below (001); $S_{11} = 50$ and 75 represent smaller tracks or tracks truncated by the unetched surface and $S_{11} = 0$ the absence of a track.

Etching is simulated using a basic Monte Carlo process. During a first sweep, the neighbourhood of each surface element is examined and the appropriate elimination probability assigned to that element. During a second sweep, the surface elements are removed according to their assigned probabilities. The two operations are separated to avoid cascades. This approach is perhaps less efficient in terms of processor time and memory usage than the more common n-fold way algorithm (Bortz et al., 1975; Cuppen et al., 2000; 2002; 2006) but it has the advantage that several surface elements can be eliminated during each cycle and that there is no need for time-scaling: each cycle corresponds to an equal unit of real time. The code is written in Sun Microsystems Java™; MathWorks Matlab™ was used for evaluating and plotting the results.

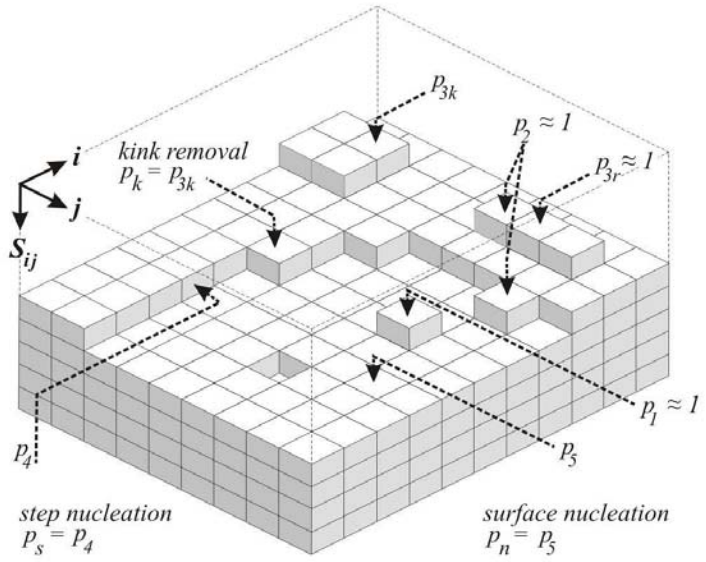

Figure 6. Model representation of the (001)-surface of a Kossel crystal showing building units with different nearest neighbour configurations and their associated removal probabilities (p_1,... p_5); also shown are the basic steps of surface nucleation, step nucleation and kink removal with their probabilities (p_n, p_s, p_k); i,j: matrix coordinates along the x and y-axis; S_{ij}: depth below the initial surface.

In line with the Kossel model as the simplest representation of the crystal, the nuclear track is simulated by a chain of empty sites perpendicular to the surface. Nuclear tracks have properties such as orientation, intermittency, up to unknown damage density distributions. On the other hand, a recoil track results from up to eight successive nuclear recoils in random directions so that it is difficult to assign an orientation to such a track. Etched recoil tracks with diameters of several microns are moreover tens of times larger than the damaged regions (Jonckheere and Gögen, 2001; Stübner and Jonckheere, 2006). Thus insofar as the latent track provides a chain of preferential nucleation sites stretching down through a stack of lattice planes, whether exactly below each other or with a limited random offset, the actual damage distribution within the latent track is immaterial to the shape of the etch pit. This is validated by the fact that etched recoil tracks never show signs of relict orientations (skewed etch pits) or of intermittent etching (stepped etch pits).

This is not the case for extended linear nuclear tracks and defects such as fission tracks, ion tracks, line dislocations, etc. It is indeed a question of considerable interest inhowfar their etched-track geometries reflect the properties of the latent track and can be used to infer the nature of the track-forming particle. Some of the tightest constraints on the occurrence of exotic particles (magnetic monopoles, cold dark matter, etc.) predicted by unified physical theories are derived from investigations of etch pits in ancient micas. Ongoing simulations must enable us to determine which latent-track properties are preserved through the successive etching stages identified in this work; we intend to report the results at a later stage.

4. Discussion

The basic variables for the simulations are the vertical extent or depth of the nuclear track or defect (d), the bond strength (ϕ) and etching time (t_e; number of iterations); the dependent variables are the bulk etch rate (v_v), etch-pit shape, size, depth and aspect ratio; the effective rates of horizontal growth (v_h) and depth increase (v_d) are derived from their variation with t_e. The simulation results are shown in Figures 7, 8 and 9: colour-coded topographies (Figure 7), bulk etch rates (Figure 8a), etch-pit sizes (Figure 8b), horizontal etch rate (Figure 8c), etch-pit depths (Figure 8d), rate of depth increase (Figure 8e) and aspect ratio (Figure 8f) as functions of t_e and ϕ; etch-pit contours are shown for different d, ϕ and t_e in Figures 8g and 8h; the evolution of the etch-pit cross-section as a function of t_e is discussed on the basis of Figure 9.

4.1. Bulk etch rate

The bulk etch rate v_v is low at first because the unetched surface is free of steps and kinks so that etching proceeds at a rate limited by surface nucleation ($p_n = p_5$; eq. 1). An initial roughness is created that increases the rate at which material is removed up to a maximum corresponding to a constant surface step density (Liang et al., 1996). The onset of this plateau after a

few 10^4 iterations is independent of ϕ within the investigated parameter range (Figure 8a). The constant limiting value of v_v increases with decreasing ϕ. The time dependence of v_v is similar to that reported by Lasaga and Lüttge (2003). Our observations on phlogopite agree with the simulation results insofar that the surface acquires a courser texture with increasing etching time (Figure 4), without, however, reaching a steady-state condition after 600 s etching (40% HF at 23ºC). It is assumed that etching of clusters of point defects contributes to a continued roughening of the surface.

4.2. Etch pit contour

The footprint of the simulated track etch pits is square, curved-sided angular or circular (Figure 7). Their contours are sometimes indistinct due to a low signal (track depth) to noise (surface roughness) ratio; this is the case when the track is short or the bond strength is low. Rounding of the etch pits is reflected in their aspect ratio α, i.e. the ratio of their maximum to minimum horizontal dimension. For the simulated etch pits, α ranges from ~1.4 (square) to ~1.0 (circular). In all cases, α decreases with increasing number of iterations (Figure 8f). This evolution towards a rounded shape is punctuated by two longer-lived transient states with a clear transition phase between them. The first, at $\alpha \approx 1.33$, persists longer at deeper defects and in high-ϕ crystals and corresponds to still quite straight-sided angular etch pits. It occurs during stage 2 in the evolution of the etch-pit profile (section 4.3), when the rounding of the etch-pit sides is not yet influenced by the curvature of the etch-pit bottom; α then decreases again at the onset of stage 3 (section 4.3) until a second longer-lived transient state is attained. In general, shallower defects (depth 50) attain more circular contours earlier than deep defects (depth 100; Figure 8h); the shape of the deepest etch pits at that point is co-determined by ϕ (Figure 8f); the positive correlation between α and ϕ is in line with the expectation that high-ϕ crystals can sustain angular features for longer than low-ϕ minerals (Figure 8g).

The curvature of the etch-pit sides in these simulations is neither the result of extraneous factors, such as etchant or etch-product diffusion, nor of specific assumptions about the energies associated with nearest-neighbour, even less with next-nearest-neighbour, etc., interactions. There is no tailoring of the model or parameter tuning to produce any systematic effect at all. It is therefore proposed that step curvature is instead the result of a statistical bias due to the lateral confinement of steps enclosing an etch pit (Figure 10). Step retreat proceeds by step nucleation at a rate p_s, followed by kink removal on both sides of the nucleated site at a rate p_k. The finite step length due to its confinement introduces bias because a lesser number of suitable kink sites is available near the ends of the step than at its centre. This entails that the effective rate of step retreat is lower towards its extremities than at its centre (Figure 10). This is enough to produce and augment the curvature of a step in the first etching stages, during which long stretches of

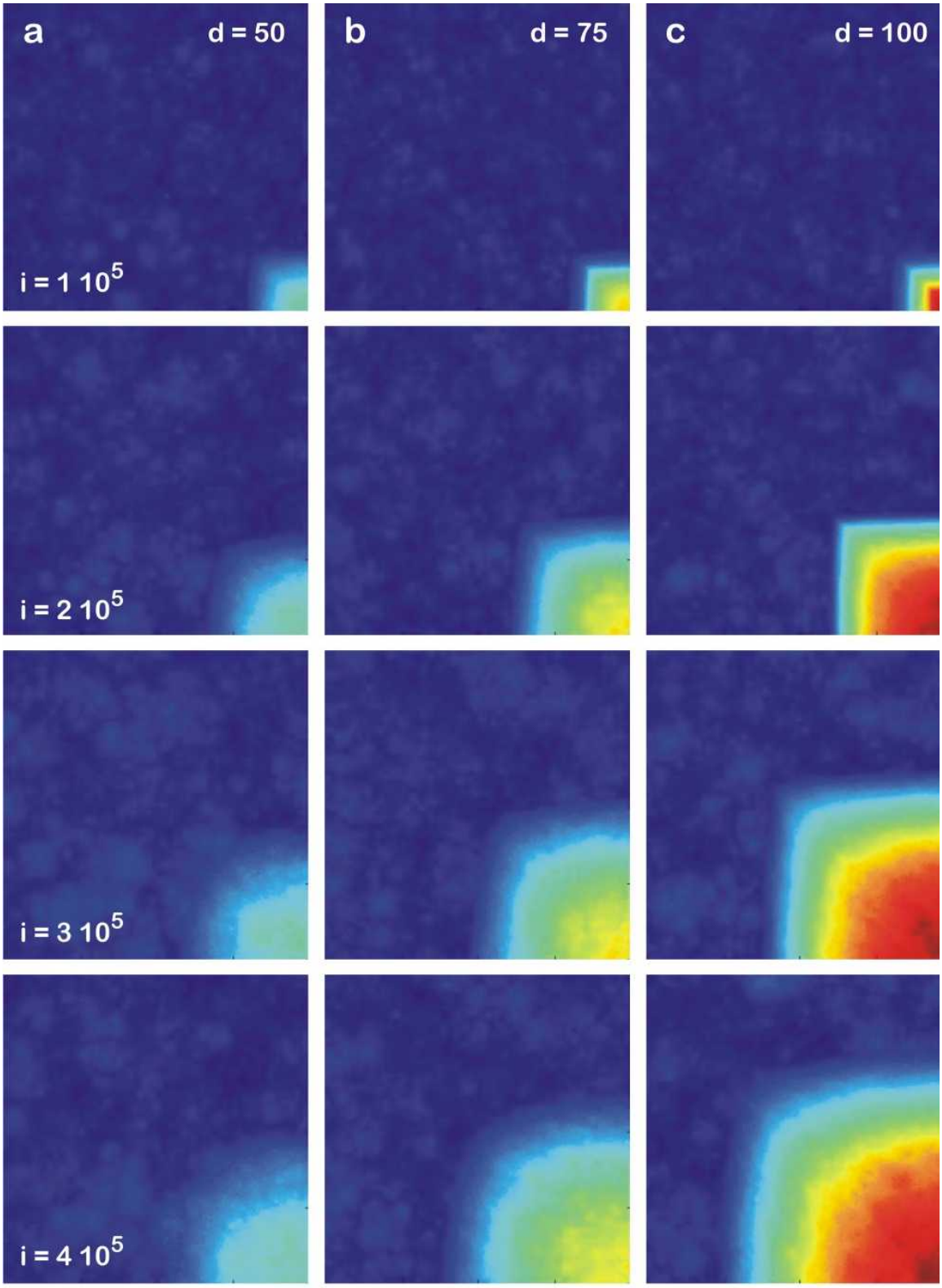

Figure 7. Three series of simulated etch pits illustrating the variation of shape and evolution depending on the model parameters. Bond strength $\phi/kT = 2.05$; initial track depth: (a) d = 50; (b) d = 75; (c) d = 100. The number of iterations i increases down each column from 1 to 4 10^5. The etch-pit contours become more rounded with increasing i (prolonged etching); etch pits at deeper defects hold on longer to their angular shape; shallower defects lead to shallower etch pits with less distinct contours and stronger curvature.

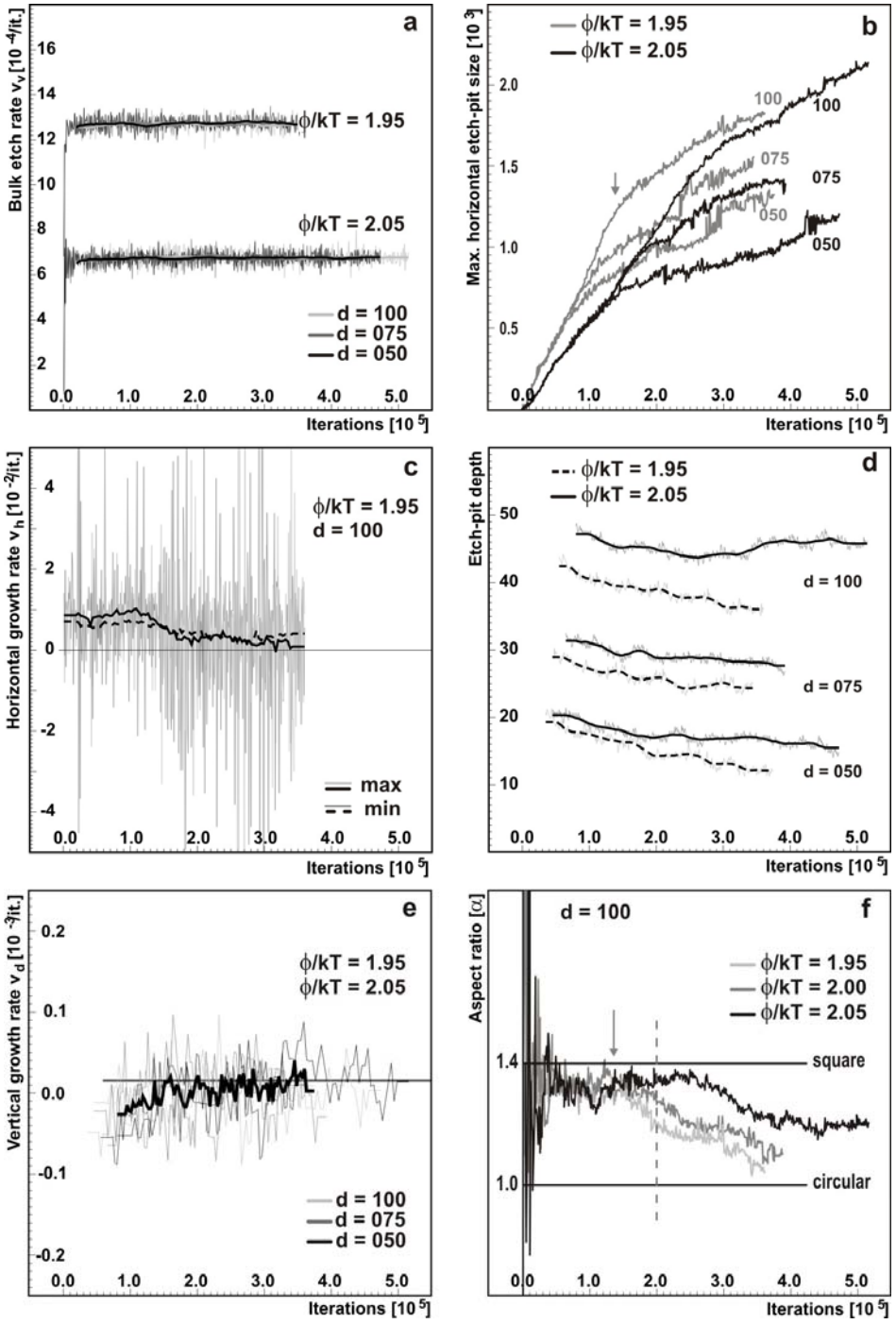

Figure 8. Simulation results: (a) surface (bulk) etching velocities (v_v) against the number of iterations; (b) maximum etch-pit radii against iterations; the plot for ϕ/kT = 1.95 and d = 100 corresponds to Figure 9; the arrow marks the onset of stage three at ~1.4 10^5 iterations; (c) apparent maximum (lighter) and minimum (darker) horizontal growth rate (v_h) against the number of iterations; the thick black lines are the running means (solid: maximum v_h; dashed: minimum v_h); (d) etch-pit depth d against the number of iterations; the data start at the onset of stage two; the thick lines are running means; (e) apparent rate of increase (v_d) of the etch-pit depth against the number of iterations; thin lines: running averages for ϕ/kT = 1.95 and 2.05 and d = 50, 75 and 100; thick black line: mean running average; the data start at the onset of stage two; (f) aspect ratio (α) against the number of iterations for ϕ/kT = 1.95, 2.00 and 2.05 and d = 100; the arrow indicates the onset of stage three for ϕ/kT = 1.95 (Figure 9); the dashed line at 2 10^5 iterations refers to Figure 8g.

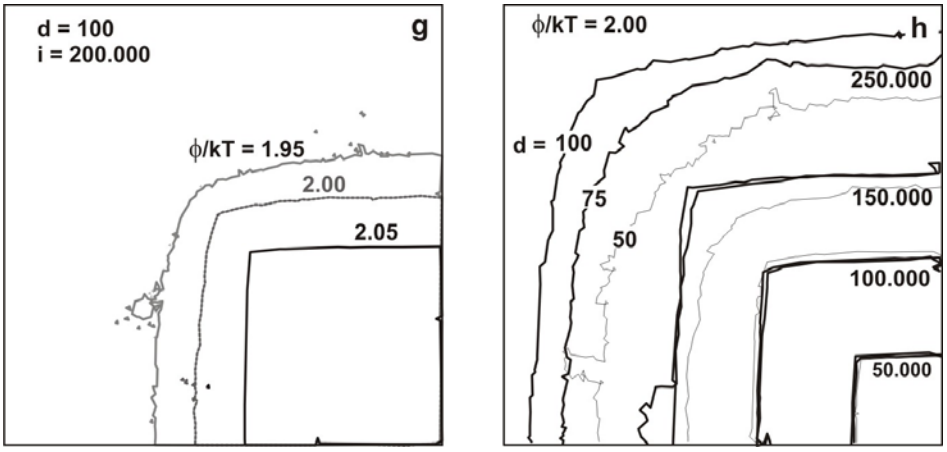

Figure 8 (continued). (g) comparison of etch-pit contours for ϕ/kT = 1.95, 2.00 and 2.05 (d = 100; 2 10^5 iterations); note that weaker bonds give rise to more curved and less well-defined etch-pit contours than stronger ones; the corresponding aspect ratios are indicated by the dashed line in Figure 8f; (h) etch-pit contours for ϕ/kT = 2.00 and d = 50 (thin line), 75 (intermediate) and 100 (thick line) after 5, 10, 15 and 25 10^4 iterations; note that, at the same number of iterations, shallower defects cause smaller and more curved etch pits than deeper defects.

the step front remain straight. The fact that the length of the step bordering an etch pit increases as etching proceeds tends to enhance this effect. In practice, it makes no difference if kink sites are created by step nucleation, as assumed in the simulation, or are produced as a result of thermal distortions of the lattice. The same stochastic mechanism also explains the increasing curvature of the etch-pit bottom (Figure 10).

The preceding views step curvature as a result of drag at its extremities. It is also possible to look at it from a different perspective. Given a single step nucleation, the midsection of the step has the highest likelihood of being exposed after a given time, assuming that probabilities are balanced such that the next step nucleation event happens before the current step is fully cleared away. Because of this, it is more likely that the next step will be nucleated near the middle, in turn exposing the next lattice row, and so forth.

4.3. Etch pit profile

Three stages can be distinguished in the evolution of a nuclear-track etch pit (Figure 9). During the first stage, the etch pit is an inverted pyramid bounded by four flat walls meeting in a point along the track. The pyramid faces are stepped at the lattice scale; the inter-step spacing (n; tread) increases with increasing ϕ. In the simulations, n increases from ~4.5 to ~6 for the investigated range of ϕ-values (ϕ/kT = 1.90- 2.10). The apparent rate of etch-pit growth perpendicular to the step direction (v_h) is less than that of step retreat (v_s) owing to the simultaneous lowering of the surface due to bulk etching (v_v). Within the model $v_h = v_s - n\, v_v$. Similarly, the apparent rate at which the depth of the etch pit increases (v_d) is given by: $v_d = v_s - 1/n\, v_v$. Thus v_d is independent of the etch rate v_t of the damaged lattice along the track (track etch rate).

When the tip of the etch pyramid arrives at the end of the track or defect, it is truncated by the slowest etching plane (Jonckheere and Van den haute, 1996), in this case (001). Thus, during the second stage, the etch pit is bounded by both lateral walls and a distinct bottom plane. In first approximation, the etch pit acquires a pan shape with a constant depth ($v_d = 0$) because its bottom plane has the same orientation and etch rate as the surface; the etch-pit size continues to grow at the same rate as before (v_h). The etch-pit evolution up to this point is consistent with the

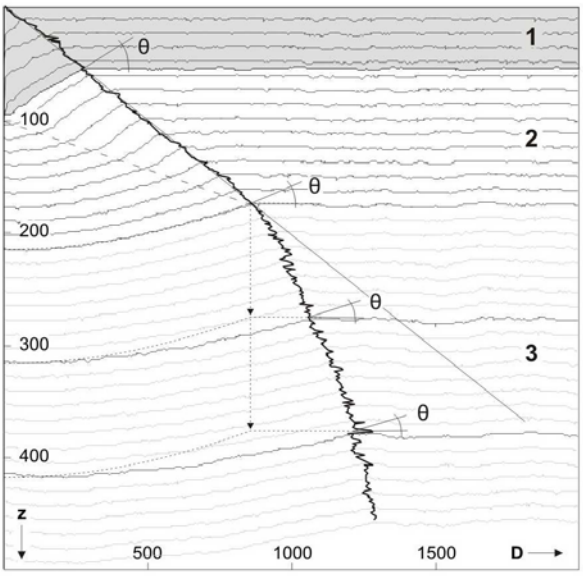

Figure 9. Sequence of calculated etch-pit profiles (bond strength $\phi/kT = 1.95$; initial depth d = 100; interval:1 10^4 iterations) illustrating stages 1, 2 and 3; the postulated fourth stage is outside the range of these calculations; z is depth and D is diameter in cell (matrix) units. Note the gradual elimination of the etch-pit walls and the arching of the bottom plane during the second stage and the horizontal stretching (dashed line) of the etch-pit profile during the third, along with the decreasing lateral growth rate and intersection angle θ.

etching model of Gögen and Wagner (2000). Huang et al. (1967) showed great foresight in criticising this (implicit) model for failing to account for the different rates of enlargement of shallow recoil-track etch pits and fission-track etch pits. The model indeed implies etch-pit geometries that are independent of the nature of the defect. Besides a constant depth and a constant rate of diameter increase, kinetic considerations also predict that the stepped etch-pit walls are translated parallel to themselves, because the angle of their convex intersection with the surface is the same as that of their concave intersection with the etch-pit bottom (cosine rule; Jonckheere and Van den haute, 1996).

The simulations agree with this model in just one respect: the quasi-constant rate of etch-pit enlargement (v_h; Figures 8b and 8c). In contrast, the etch-pit depth decreases at a rate that is greatest at the onset of the second stage ($v_d < 0$; Figure 8e). The pyramidal faces shrink while

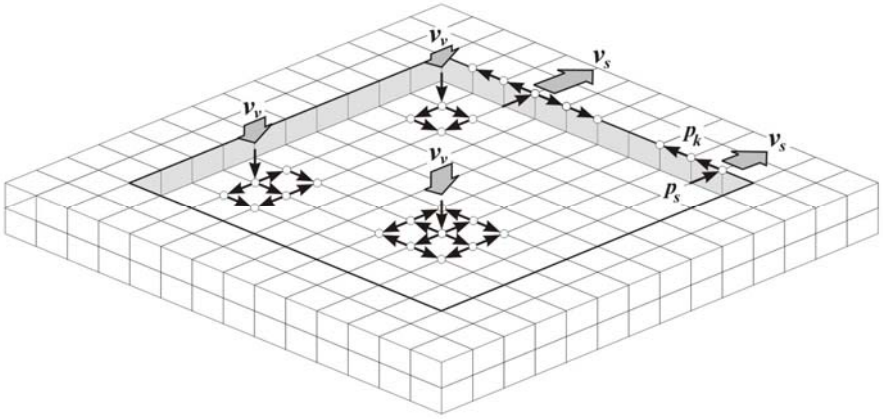

Figure 10. Principle of stochastic curving of confined steps and faces. The bulk etch rate v_v and step retreat rate v_s are the net result of a range of possible sequences of surface nucleation (p_n), step nucleation (p_s) and kink removal (p_k). Lateral confinement of a step or face excludes part of the sequences and reduces v_v and v_s towards the edges and corners of an etch pit, which cause its outward and downward curvature.

remaining macroscopically flat. The etch-pit profile does not remain self-similar as during the first stage but evolves from angular to rounded (Figure 9). The proposed interpretation attributes these phenomena to a single cause: the lateral confinement of the (001)-face at the bottom of the etch pit. The rounding of the etch-pit profile is a result of the fact that less effective nucleation sites are situated along the edges and in particular in the corners of the (001)-face at the bottom of the etch-pit (Figure 10). As before, this effect is augmented by the gradual retreat of the steps as etching proceeds. As a result, the etch rate of the (001)-face at the bottom of the etch pit is less than that of an unconfined (001)-surface (v_v), leading to a decrease of the etch-pit depth. This effect is compounded by the increased etch rate of the surface due to its acquired roughness. The rate of depth decrease declines ($v_d \rightarrow 0$) as the ratio of the circumference to the area of the (001)-face at the etch-pit bottom is reduced and its roughness increases. The shrinkage of the pyramidal faces and $v_d < 0$ is due to drag resulting from curvature of the bottom plane (Figures 9 and 11).

The third stage starts with the elimination of the pyramidal faces; the etch pit thereafter consists of a single concave-up bottom face made up of concentric steps (Figure 9). Both v_h and α decrease (Figures 8b, c and f), i.e. the etch pit becomes more rounded and its size increases at a slowing rate while its depth remains almost the same ($v_d \rightarrow 0$; Figure 8e). This means that the etch-pit profile does not remain self-similar. Instead, the simulations suggest that the etch-pit cross-section scales in the horizontal direction (Figure 9); this implies that the inter-step spacing increases. Earlier considerations related to step curving provide a plausible mechanism for this increasing inter-step spacing. Step curve results from a local lowering of the step retreat rate v_s at its extremities due to statistical bias (section 4.2). For a step of fixed length, the curved extremities act as boundaries confining the central linear segment of the step. It is thus expected that the curved outer sections extend inwards towards the centre, causing an overall reduction of

v_s; this mechanism suggests an inverse correlation between the drag effect and the length of the step. Thus the longer outer steps of a stage-three etch pit move faster than the shorter inner steps. This first-order hypothesis is testable because it predicts that longer steps move faster than shorter ones of equal curvature.

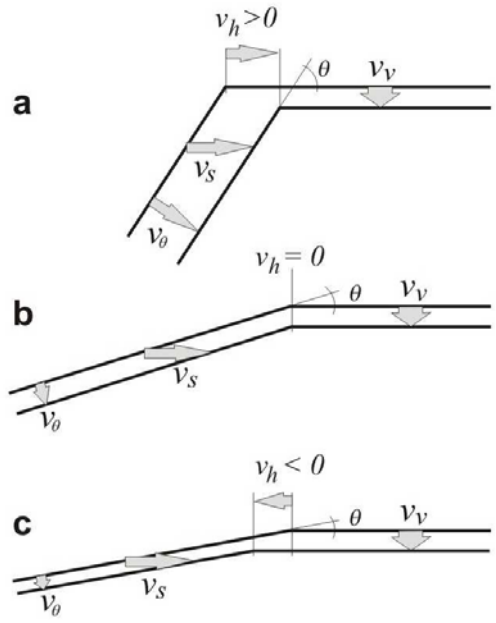

Figure 11. Relationship between the apparent horizontal growth rate (v_h) of an etch pit, the bulk etch rate (v_v), the step retreat rate (v_s) and the radial shift velocity ($v_\theta = v_s \sin \theta$) of a face tangent to the etch-pit rim at an angle θ to the surface; (a) $\tan \theta > v_v/v_s \rightarrow v_h > 0$; (b) $\tan \theta = v_v/v_s \rightarrow v_h = 0$; (c) $\tan \theta < v_v/v_0 \rightarrow v_h < 0$.

The third stage with decreasing positive v_h and increasing negative v_d is not final because the signs of both v_h and v_d are reversed on unlimited linear extrapolation. There thus exists a fourth stage, characterized by a reversal and/or convergence of v_h and/or v_d to asymptotic values. The simulations do not reach this stage due to the limited grid size. This cannot be circumvented by simulating shorter tracks because they are drowned by noise. It is nevertheless legitimate to attempt to constrain stage four by extrapolating the mechanisms operating during stage three. The simulations show that $v_d \rightarrow 0$ during stage three, in line with the conclusion that $v_d = 0$, based on the first-order approximation that the bottom of the etch pit and the surrounding surface are parallel (001) lattice planes with identical radial shift velocities. The matter is complicated by second-order effects such as the relative expanse and relative roughness of the bottom of the etch pit compared to that of the surrounding surface and their effects on the etch rates of these surfaces.

Assuming $v_d = 0$, then the horizontal growth of the etch pit reduces the acute angle θ between its rim and the surface (Figure 9); the decrease of θ in turn reduces v_h (Jonckheere and Van den haute, 1996; Figure 11). When $\theta = \arctan(v_v/v_s)$ then $v_h = 0$ and the etch pit has attained its maximum size. This is counteracted to a finite extent by an increase of v_s due to increased

step length. Thus first-order effects result in an etch pit of constant horizontal size and depth. The sum of second-order effects could, however, cause the etch pit to shrink and vanish after a finite etching time. E.g., if the trend towards increased inter-step spacing persists, then it could cause both a backlash that leads to a reduction of the etch-pit depth ($v_d < 0$) and reduce θ still further so that $v_h < 0$. The matter is too close to call; new simulations could bring the answer but require extensions of the grid size and number of iterations that are outside the scope of the present program.

5. Conclusion

Huang and Walker (1967) and Huang et al. (1967) identified numerous shallow etch pits in muscovite as sites of localised lattice damage produced by the recoil nuclei resulting from the alpha-disintegration of uranium and thorium impurities and proposed that these could constitute the basis of a recoil-track dating method, based on similar principles as the fission-track method. Right from the beginning, these same investigators commented that: "*preliminary data … indicate that the rate of enlargement of the shallow pits may be different from the rate of enlargement of fission-track pits. If this surprising result is confirmed it would indicate that the track etching phenomenon in mica is a more complicated process than was hitherto believed*" (Huang et al., 1967). This unexpected problem has been addressed in the present work.

5.1. Etch-pit evolution

A simple atomistic Monte Carlo simulation suggests that there are up to four stages in the evolution of an etch pit in the (001)-surface of an idealised regular lattice. During the first stage, the etch pit is an inverted pyramid; its horizontal and vertical dimensions increase at a constant rate; the apparent horizontal (v_h) and vertical growth rates (v_d) are faster than during all subsequent stages but nevertheless lower than the step retreat rate v_s on account of surface etching (v_v). The pyramid apex is truncated in the second stage; it is thereafter bounded by an expanding bottom plane and shrinking lateral walls; v_d drops to negative values causing a slow decrease of the etch-pit depth; the bottom plane acquires a concave-up curvature; the outward curvature of the walls, initiated during the first stage, increases. During the third stage the etch pit is made up of a single concave-up bottom plane; the rate of decrease of v_h slows; consecutive etch-pit cross-sections are scalable in the horizontal directions. The fourth stage is inferred but not documented by the simulations; in first approximation, it is characterized by $v_h = v_d = 0$ but the sum of second-order effects and random fluctuations could cause the etch pit to shrink in all directions and disappear.

5.2. Essential premises

It is not unimportant that this complex evolution emerges despite the simplest modelling assumptions. The assumed Kossel lattice is a regular and isotropic representation of the periodic

arrangement of units added in growth and removed in dissolution or etching. Each etch step consists of one of just three possible events: surface nucleation, step nucleation or kink removal; the associated probabilities (p_n, p_s, p_k) depend on the number of nearest neighbours. Long-range interactions, re-addition, surface diffusion and thermal deformation of the lattice are not considered. The sole cause for the succession of etching stages is the process of stochastic rounding of confined steps and faces. The etch-pit depth, diameter, and contour depend on defect size and the binding energy ϕ, which in turn determines the ratio of p_n, p_s and p_k. No aspect of the etch-pit shape or growth rate is influenced by the etch rate along the defect (track; v_t) on condition that $v_t > v_d$.

This loss of information is a particular feature of the proposed model. In contrast to Gögen and Wagner (2000), the track diameter is not directly related to the effective duration that the track has been etched. In contrast to Fleischer (2003) the etch pit retains no memory at all of the track formation process. Besides recoil tracks, the results should also be valid for fission tracks, ion tracks and dislocations, although these tracks are not often etched beyond stage 1 or 2 in practical applications, as a consequence of their greater length.

5.3. Trioctahedral mica

The triangular footprint of recoil-track, fission-track, ion-track and dislocation etch pits in trioctahedral mica and its compliance with the monoclinic symmetries (2/m) leads us to reaffirm that the relevant periodic bond chains (Hartman and Perdok, 1955a-c) are O-Mg/Fe-O chains in the upper and lower halves of the octahedral layer (Jonckheere et al., 2005). This calls into question whether it is right to impose the conditions that each periodic bond chain must consist of stoechiometric units that are not part of another chain (Grim and Güven, 1978; Bickmore et al., 2001). The upper and lower sets of periodic bond chains form mirrored equilateral triangles in an idealised lattice (Figure 2). The fact that the etch pits are not quite equilateral (Hashemi-Nezhad, 1998) is ascribed to lattice distortion to accommodate the misfit between the tetrahedral and octahedral layers, perhaps amplified by the presence of unbound surface atoms (Putnis, 1992; Dahl, 1996). The rounding of the triangular form is ascribed to the process of stochastic curving.

The complex size distribution of recoil-track etch pits (Figure 3a) is attributed to : (1) the size distribution of the latent tracks (Jonckheere and Gögen, 2001; Stübner and Jonckheere, 2006); (2) variable truncation of surface-intersecting tracks; (3) the variable rate of growth depending on the etch-pit stage; (4) exposure of new tracks at the surface due to bulk etching. The greater size of dislocation, fission-track and ion-track etch pits and their more angular contour is due to their greater extent below the surface and the consequent longer duration of stage 1. The quasi-linear increase of the number of etched tracks per unit surface (ρ_{RT}) with etching time (t_e)

is due to bulk etching at a quasi-constant rate. It is not excluded that there is an upper limit to ρ_{RT} if the stage 4 is such that etch pits disappear, although this phenomenon may be obscured by etch-pit overlap.

5.4. Recoil-track dating

According to Gögen and Wagner (2000), the number of recoil tracks per unit volume (N_{RT}), and from it, the recoil-track age (t_{RT}) of a sample can be computed from the slope or intercept of a plot of ρ_{RT} against t_e**:**

$$\rho_{RT}(t_e) = N_{RT} [R_e + v_v t_e] - \rho_0(v_v, v_h, R_e) \quad (2)$$

in which R_e represents the dimension of the etchable section of a latent alpha-recoil track. The correction term ρ_0 and its dependence on v_v, v_h and R_e are the result of an assumed observation threshold described by a critical etched-track diameter. It has since been established that the size of recoil tracks, and thus R_e, is not constant but possesses an age-dependent bimodal distribution (Jonckheere and Gögen, 2001; Stübner and Jonckheere, 2006). It is clear from the present simulations that v_h is also not constant but decreases with increasing t_e; the onset of stage 2 depends on the vertical extent of the truncated track below the surface, and thus in part on R_e: $v_h = v_h (t_e, R_e)$. The intercept of $\rho_{RT} (t_e)$ is therefore quite difficult to relate to the sample age; its slope, in contrast, depends on v_v alone. However, our simulations and observations indicate that v_v increases from a minimum at $t_e = 0$ to a maximum when a certain limiting surface roughness is attained. The increased surface roughness, together with the evolution of etch-pit shape with continued etching can also cause loss of tracks due to observation effects related to loss of contrast rather than size.

Stübner et al. (2006) suggested an alternative recoil-track age determination based on the ratio r of small-sized tracks (≤50 μm) to that of larger-sized tracks (>50 μm) and the Th/U-ratio. The present results confirm that the size distribution of etched recoil tracks reflects the size distribution of the latent tracks but with distortions: (1) tracks added to the population due to bulk etching are etched for an unknown length of time; (2) truncated tracks etch to a lesser size than identical full tracks; (3) it is not clear if tracks etch to a maximum size or shrink again thereafter (fourth stage); the latter implies that the same size could occur twice in the evolution of a track etch pit. The deconvolution of the etch-pit size distribution is thus problematic.

Acknowledgement

K. Stübner is indebted to the Studienstiftung des Deutschen Volkes and the Deutsche Akademische Austauschdienst (DAAD); R. Jonckheere is beholden to the Deutsche Forschungsgemeinschaft (DFG) for financial support under grants RA 442-20 and RA 442-26. The authors are grateful to K. Gögen for critical discussion and to R. Ketcham and two anonymous reviewers for their detailed and professional comments.

References

Aldushin K., Jordan G. and Schmahl W. W. (2006) Basal plane reactivity of phyllosilicates studied in situ by hydrothermal atomic force microscopy (HAFM). Geochim. Cosmochim. Acta 70, 4380-4391.

Bickmore B. R., Bosbach D., Hochella M. F. Jr., Charlet L. and Rufe E. (2001) In situ atomic force microscopy study of hectorite and nontronite dissolution: Implications for phyllosilicate edge surface structures and dissolution mechanisms. Am. Mineral. 86, 411-423.

Bortz A. B., Kalos M. H. and Lebowitz J. L. (1975) A new algorithm for Monte Carlo simulation of Ising spin systems. J. Comput. Phys. 17, 10-18.

Brauer K. H. (1971) Results of the etching method applied to crystals of the mica group. Akademie Verlag GmbH, Berlin, pp. 115 (in German).

Brown N. M. D. and Liu Z. H. (1996) The etching of natural alpha recoil tracks in mica with an argon RF-plasma discharge and their imaging via atomic force microscopy. Appl. Surf. Sci. 93, 89-100.

Burton W. K., Cabrera N. and Frank F. C. (1951) The growth of crystals and the equilibrium structures of their faces. Philos. Trans. Royal Soc. London A243, 299-358.

Cuppen H. M., Meekes H., van Enckevort W. J. P. and Vlieg E. (2006) Birth-and-spread growth on the Kossel and non-Kossel surface. J. Cryst. Growth 286, 188-196.

Cuppen H. M., Meekes H., van Veenendaal E., van Enckevort W. J. P., Bennemann, P., Reedijk M. F., Arsic J. and Vlieg E. (2002) Kink density and propagation velocity of the [010] step on the Kossel (001) surface. Surf. Sci. 506, 183-195.

Cuppen H. M., van Veenendaal E., van Suchtelen J., van Enckevort W. J. P. and Vlieg E. (2000) A Monte Carlo study of dislocation growth and etching of crystals. J. Cryst. Growth 219, 165-175.

Dahl P. S. (1996) The crystal-chemical basis for Ar retention in micas: inferences from interlayer partitioning and implications for geochronology. Contrib. Mineral. Petrol. 123, 22-39.

Faure G. (1998) Principles and applications of geochemistry. Prentice Hall Inc., Upper Saddle River, New Jersey, pp. 600.

Fleischer R. L. (2003) Etching of recoil tracks in solids. Geochim. Cosmochim. Acta 67, 4769-4774.

Fleischer R. L., Price P. B. and Walker R. M. (1975) Nuclear tracks in solids. Principles and applications. Univ. of Calif. Press, Berkeley, pp. 604.

Frank F. C. (1958) On the kinematic theory of crystal growth and dissolution processes. In Growth and Perfection of Crystals (eds. T.H. Doremus, B.W Roberts and D. Turnbull). Wiley, London, U.K. pp. 411-419.

Frank F. C. and Ives M. B. (1960) Orientation dependent dissolution of Germanium. J. Appl. Phys. 31, 1996-1999.

Franke W., Lacmann R. and Heimann R. (1975) The dissolution form of single crystal spheres III. Dissolution forms of Ge and Si. J. Cryst. Growth 28, 145-150.

Garrison E. G., McGimsey C. R. and Zinke O. (1978) Alpha-recoil tracks in archeological ceramic dating. Archaeometry 20, 39–46

Geyh M. A. (2005) Handbuch der Physikalischen und Chemischen Altersbestimmung. Wissenschaftliches Buchgeschäft, Darmstadt, pp. 211 (in German).

Glasmacher U. A., Lang M., Klemme S., Moine B., Barbero L., Neumann R. and Wagner G. A. (2003) Alpha-recoil tracks in natural dark mica: dating geological samples by optical and scanning force microscopy. Nucl. Instrum. Meth. Phys. Res. B209, 351–356.

Gleadow A. J. W., Belton D. X., Kohn B. P. and Brown R. W. (2002) Fission track dating of phosphate minerals and the thermochronology of apatite. In Phosphates, Geochemical, Geobiological, and Materials Importance (eds. M.J. Kohn et al.). Rev. Mineral. Geochem. 48, 579-630.

Gögen K. (1999) The alpha-recoil-track dating method: theoretical and experimental development and dating of mica. Doctoral Thesis, Rupertus Carola Univ., Heidelberg.

Gögen K. and Wagner G. A. (2000) Alpha-recoil track dating of Quaternary volcanics. Chem. Geol. 166, 127-137.

Green P. F. and Durrani S. A. (1978) A quantitative assessment of geometry factors for use in fission-track studies. Nucl. Track Detection 2, 207-213.

Grim R. E. and Güven N. (1978) Bentonites. Geology, mineralogy, properties and uses. Developm. Sedimentol. 24. Elsevier, Amsterdam.

Grimbergen R. F. P., Meekes H., Bennema P., Strom C. S. and Vogels L. J. P. (1998) On the prediction of crystal morphology. I. The Hartman-Perdok Theory Revisited. Acta Cryst. A54, 491-500.

Hartman P. (1958) The equilibrium form of crystals. Acta Cryst. 11, 459-464.

Hartman P. and Perdok W. G. (1955a) On the relation between structure and morphology of crystals I. Acta Cryst. 8, 49–52.

Hartman P. and Perdok W. G. (1955b) On the relation between structure and morphology of crystals II. Acta Cryst. 8, 521–524.

Hartman P. and Perdok W. G. (1955c) On the relation between structure and morphology of crystals III. Acta Cryst. 8, 525–529.

Hashemi-Nezhad S. R. (1985) On the parameters affecting the track opening geometry in biotite mica. Nucl. Instrum. Meth. A234, 172-176.

Hashemi-Nezhad S. R. (1997) Geometry of etched charged particle tracks in crystalline detectors. Rad. Meas. 28, 167-170.

Hashemi-Nezhad S. R. (1998) The triangular track contours in phlogopite mica detectors and discontinuity of the etchable damage. Nucl. Instrum. Meth. Phys. Res. B142, 98-110.

Hashemi-Nezhad S. R. and Durrani S. A. (1981) Registration of alpha-recoil tracks in mica: The prospects for alpha-recoil dating method. Nucl. Tracks Solids 5, 189-205.

Hazen R. M. and Burnham C. W. (1973) The crystal structures of one-layer phlogopite and annite. Am. Mineral. 58, 889-900.

Heimann R., Franke W. and Lacmann R. (1975) The dissolution form of single crystal spheres IV. Dissolution of MgO. J. Cryst. Growth 28, 151-156.

Hines M. A. (2001) The picture tells the story: using surface morphology to probe chemical etching reactions. Intern. Rev. Phys. Chem. 20, 645-672.

Huang W. H. and Walker R. M. (1967) Fossil alpha-recoil tracks: A new method of age determination. Science 3766, 1103-1106.

Huang W. H., Maurette M. and Walker R. M. (1967) Observations of fossil a-particle recoil tracks and their implications for dating measurements. In Radioactive Dating and Methods of Low-level Counting (IAEA, Vienna) 415- 429.

Irving B. A. (1960) Shapes of etch hillocks and pits and their correlation with measured etch rates. J. Appl. Phys. 31, 109-111.

Irving B. A. (1962) Chemical etching of semiconductors. In The Electrochemistry of Semiconductors (ed. P.J. Holmes). Academic, London. pp. 256-289.

Jaccodine R.J. (1962) Use of modified free energy theorems to predict equilibrium growing and etching shapes. J. Appl. Phys. 33, 2643-2647.

Jonckheere R. (2003) On the ratio of induced fission-track densities in a mineral and a co-irradiated muscovite external detector with reference to fission-track dating of minerals. Chem. Geol. 200, 41-58.

Jonckheere R., Enkelmann E. and Stübner K. (2005) Observations on the geometries of etched fission and alpha-recoil tracks with reference to models of track revelation in minerals. Rad. Meas. 39, 577-583.

Jonckheere R. and Gögen K. (2001) A Monte-Carlo calculation of the size distribution of latent alpha-recoil tracks. Nucl. Instrum. Meth. Phys. Res. B183, 347-357.

Jonckheere R. and Van den haute P. (1996) Observations on the geometry of etched fission tracks in apatite: implications for models of track revelation. Am. Mineral. 81, 1476-1493.

Katcoff S. (1969) Alpha-recoil tracks in mica: registration efficiency. Science 166, 382-384.

Kossel W. (1927) On the theory of crystal growth. Nachrichten von der Gesellschaft der Wissenschaften zu Göttingen 2, 135–143 (in German).

Lacmann R., Franke W. and Heimann R. (1974a) The dissolution form of single crystal spheres I. Theory for the molecular kinetics interpretation. J. Cryst. Growth 26, 107-116.

Lacmann R., Franke W. and Heimann R. (1974b) The dissolution form of single crystal spheres II. Theory for the molecular kinetics interpretation. J. Cryst. Growth 26, 117-121.

Lasaga A. C. and Lüttge A. (2003) A model for crystal dissolution. Europ. J. Mineral. 15, 603-615.

Lasaga A.C. and Lüttge A. (2004) Mineralogical approaches to fundamental crystal dissolution kinetics. Am. Mineral. 89, 527-540.

Liang Y., Baer D. R., McCoy J. M. and LaFemina J. P. (1996) Interplay between step velocity and morphology during the dissolution of $CaCO_3$ surface. J. Vac. Sci. Technol. A14, 1368-1375.

Lüttge A. (2005) A kinetic model of etch pit coalencence and dissolution. Am. Mineral. 90, 1776-1783.

McCoy J. M. and LaFemina, J. P. (1997) Kinetic Monte Carlo investigation of pit formation at the CaCO3 (10-14) surface–water interface. Surf. Sci. 373, 288-299.

Patel A. R. and Ramanathan R. (1962a) Etching of mica cleavages. Acta Cryst. 15, 860-862.

Patel A. R. and Ramanathan R. (1962b) Etching of synthetic fluorphlogopite. Am. Mineral. 487, 1195-1201.

Price P. B. and Walker R. M. (1962) Observation of fossil particle tracks in natural micas. Nature 196, 732-734.

Price P. B. and Walker R. M. (1963) Fossil tracks of charged particles in mica and the age of minerals. J. Geophys. Res. 68, 4847-4862.

Putnis A. (1992) Introduction to mineral sciences. Cambridge Univ. Press, Cambridge, pp. 457.

Rufe E. and Hochella M. F. Jr. (1999) Quantitative assessment of reactive surface area of phlogopite during acid dissolution. Science 285, 874-876.

Siesmayer B., Heimann R., Franke W. and Lacmann R. (1975) The dissolution form of single crystal spheres V. Dissolution of α-Al_2O_3. J. Cryst. Growth 28, 157-161.

Snowden-Ifft D., Price P. B., Nagahara L. A. and Fujishima A. (1993) Atomic-force-microscopic observations of dissolution of mica at sites penetrated by keV/nucleon ions. Phys. Rev. Lett. 70, 2348-2351.

Somogyi G. (1980) Development of etched nuclear tracks. Nucl. Instrum. Meth. Phys. Res. 173, 21-42.

Stranski I.N. (1928) The theory of crystal growth. Zeitschr. Phys. Chem. 136, 259–278.

Stübner K. and Jonckheere R. C. (2006) A Monte-Carlo calculation of the size distribution of latent alpha-recoil tracks in phlogopite: implications for the recoil-track dating method. Rad. Meas. 41, 55-64.

Stübner K., Jonckheere R. C. and Ratschbacher L. (2006) Alpha-recoil track densities in mica and radiometric age determination. Rad. Meas. 40, 503-508.

Turkowsky C. (1969) Electron-microscopic observation of artificially produced alpha-recoil tracks in albite. Earth Planet. Sci. Lett. 5, 492-496.

Van den haute P. (1985) The density and the diameter of fission tracks in glass with repect to age interpretation. Nucl. Tracks 10, 335-348.

van Veenendaal E., Nijdam A. J. and van Suchtelen J. (2002) Simulation of crystal shape evolution in two dimensions. J. Cryst. Growth 235, 603-618.

Wagner G. A. (1998) Age determination of young rocks and artefacts. Physical and Chemical Clocks in Quaternary Geology and Archaeology. Springer, Berlin, pp. 466.

Chapter 4

The North American–Caribbean plate boundary in Mexico–Guatemala–Honduras

(submitted for publication in *Tectonics*, 2008)

Abstract

The boundary between the Caribbean and North American plates records extensive offsets and deformation related to relative motion among the North American, South American, and Caribbean plates. We use new structural, geochronologic, and petrologic data to investigate which crustal sections of the Motagua suture zone in Guatemala and Honduras accommodated the large-scale sinistral offset along the northern Caribbean plate boundary. We also develop the chronologic and kinematic framework for these interactions, and test for Paleozoic to Recent geologic correlations among the Maya block, the Chortís block, and the terranes of southern Mexico and the northern Caribbean. Our principal findings relate to how the Motagua suture zone partitions deformation: whereas the southern Maya block and the southern Chortís block record the Late Cretaceous- early Tertiary collision and eastward sinistral translation of the Greater Antilles arc, the northern Chortís block preserves evidence for northward stepping of the plate boundary with the translation of this block to its present position since the Late Eocene. During the Late Miocene the translation boundary again stepped northward, once again affecting the Maya block and imprinting and reactivating the Tonala (southeastern Mexico) and Polochic (Guatemala) shear and fault zones. Collision and translation are recorded in the ophiolite and subduction-accretion complex (North El Tambor Group), the continental margin (Chuacús complex) and the Laramide foreland fold–thrust belt of the Maya block as well as the overriding Greater Antilles arc complex. The Las Ovejas complex of the northern Chortís block contains a significant part of the history of the eastward migration of the Chortís block; it constitutes the southern part of the arc that facilitated the breakaway of the Chortís block from the Xolapa complex of southern Mexico. While the Late Cretaceous collision is spectacularly sinistral transpressional, the Eocene–Recent translation of the Chortís block is by sinistral wrenching with transtensional and transpressional episodes.

Our reconstruction of the Late Mesozoic–Cenozoic evolution of the Motagua suture zone identifies Proterozoic to Mesozoic connections among the southern Maya block, the Chortís block, and the terranes of southern Mexico: (i) in the Early Paleozoic, the Acatlán complex of the southern Mexican Mixteca terrane, the Chuacús complex of the southern Maya block, and likely also the Chortís block were part of the Alleghanian–Appalachian orogen along the southern margin of North America; (ii) after the final amalgamation of Pangea, an arc developed

along its western margin, causing magmatism and regional amphibolite-facies metamorphism in southern Mexico, the Chuacús complex, and the Chortís block. The separation of North and South America also rifted the Chortís block from southern Mexico. Rifting ultimately resulted in the formation of the Late Jurassic–Early Cretaceous oceanic crust of the South El Tambor Group; rifting and spreading terminated before the Hauterivian. Remnants of part of the southwestern Mexican Guerrero complex, which also rifted from southern Mexico, remain in the Chortís block; these complexes share Jurassic metamorphism. In the late Early Cretaceous the South El Tambor Group ophiolite and subduction–accretion complex was emplaced onto the Chortís block and the Chortís block collided with southern Mexico. Related arc magmatism and high-T/low-P metamorphism (Taxco–Viejo–Xolapa arc) of the Mixteca terrane spans all of southern Mexico. The Chortis block shows continuous Early Cretaceous–Recent arc magmatism.

1. Significance of the study

We present new structural, geochronologic and petrologic data to document the Paleozoic–Tertiary pressure–temperature–deformation–time (P-T-d-t) history of the southern part of the Maya and northern part of the Chortís blocks, and the Polochic, Motagua, and Jocotán-Chamelecón fault zones along the northern Caribbean plate boundary in southern Mexico, central Guatemala, and northwestern Honduras. The principal questions we address are: which crustal sections of the Motagua suture zone accommodated the large-scale sinistral offset along the plate boundary, what was the timing of offset and deformation, and in what kinematic framework did it occur? We also investigate Paleozoic to Tertiary geologic correlations between the Maya block, the Chortís block, the tectonostratigraphic complexes ("terranes") of southern Mexico, and the arc/subduction complexes of the northern Caribbean.

2. The northern Caribbean plate boundary

The Caribbean plate represents a lithospheric unit between the North and South American plates. Its western and eastern margins consist of subduction zones with volcanic arcs (Central America Isthmus, Lesser Antilles), whereas the northern and southern margins correspond to transpression, subsidiary strike-slip, or transtension zones (Polochic–Motagua, Cayman, Greater Antilles, North Andean and South Caribbean; e.g., Pindell et al., 2006). The Motagua suture zone (MSZ) of southeastern Mexico, Guatemala, and Honduras extends from the Pacific Ocean to the Caribbean Sea for ~400 km E–W and ~80 km N–S (e.g., Beccaluva et al., 1995). It represents the northwestern Caribbean plate boundary and links the Cayman trough pull-apart basin in the east with the subduction zone of the Pacific plate in the west (Fig. 1A). The exposure of the MSZ within continental crust of southern North America and northern Central America facilitates multi-method studies of its late-stage, intra-continental evolution.

The MSZ represents a broad Mesozoic–Tertiary transpressional system, dominated by the Polochic and the Motagua fault systems (Fig. 1B and 1C). Donnelly et al. (1990) defined the suture between the North American and Caribbean plates as the Motagua fault *sensu stricto*, separating the Maya block from the Chortís block. These blocks showcase a geologic history that encompasses Middle Proterozoic to Quaternary and have long been recognized as important elements in understanding the interaction of Laurentia, Gondwana, and the (Proto-)Pacific domains (e.g., Keppie, 2004; Dickinson and Lawton, 2001). Most tectonic models suggest that collision of the Maya and Chortís blocks occurred along S- or N-dipping subduction zones during the Cretaceous, and caused emplacement of Jurassic–Cretaceous proto-Caribbean oceanic crust onto the blocks; thrusting of metamorphic and sedimentary strata was bivergent N and S of the MSZ (e.g., Meschede and Frisch, 1998; Beccaluva et al., 1995 and literature therein). Since Late Cretaceous–early Tertiary, the MSZ developed into a sinistral wrench zone due to the dif-

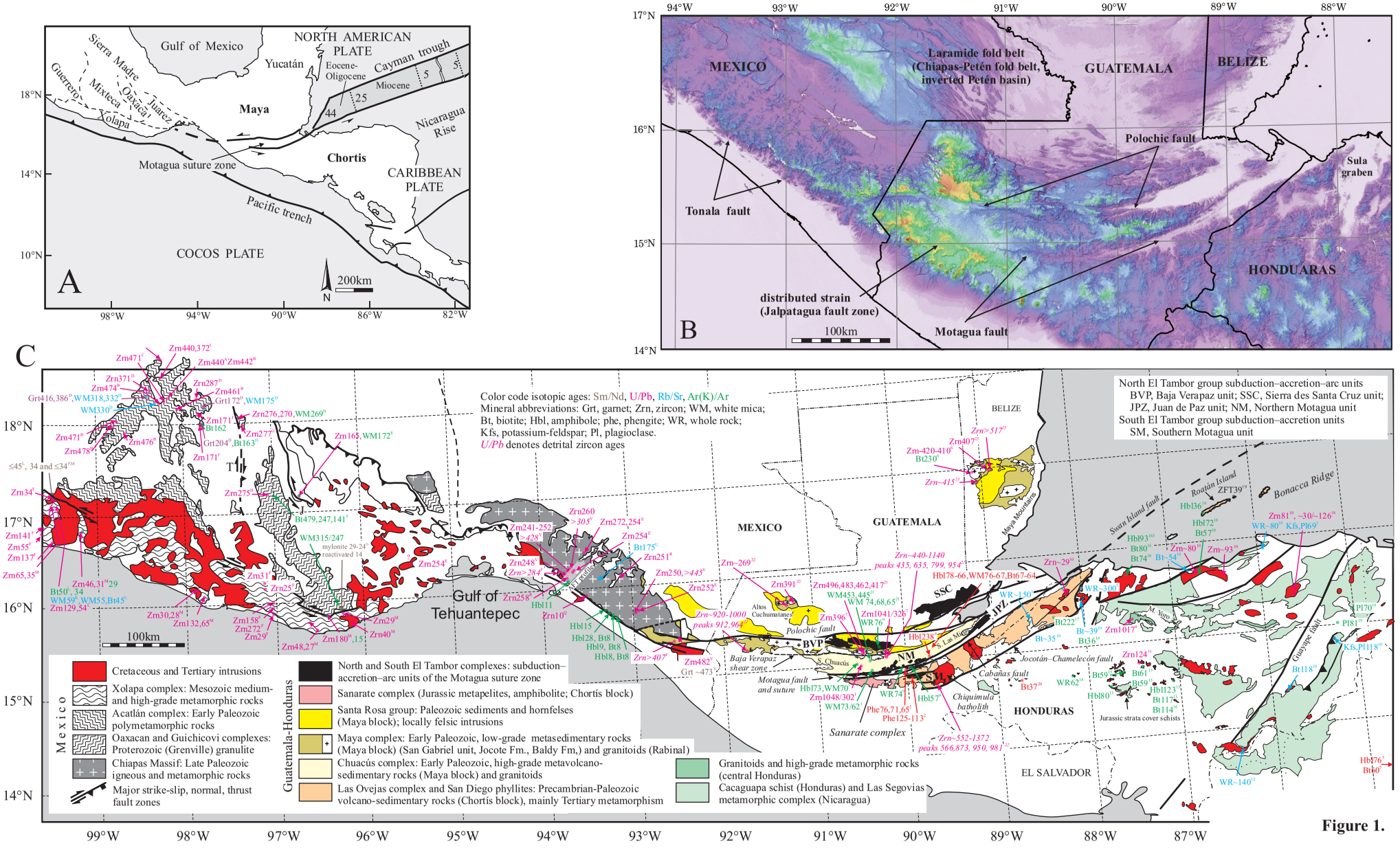
A
Gulf of Mexico
NORTH AMERICAN PLATE
Yucatán
Sierra Madre
Guerrero
Mixteca
Oaxaca
Juarez
Xolapa
Maya
Eocene-Oligocene
Miocene
Cayman trough
5
5
25
44
Nicaragua Rise
Chortis
Motagua suture zone
CARIBBEAN PLATE
Pacific trench
COCOS PLATE
200km
N
18°N
14°N
10°N
98°W
94°W
90°W
86°W
82°W
B
17°N
16°N
15°N
14°N
94°W
93°W
92°W
91°W
90°W
89°W
88°W
MEXICO
Laramide fold belt
(Chiapas-Petén fold belt,
inverted Petén basin)
GUATEMALA
BELIZE
Polochic fault
Sula graben
Tonala fault
HONDURAS
distributed strain
(Jalpatagua fault zone)
Motagua fault
100km
C
Color code isotopic ages: Sm/Nd, U/Pb, Rb/Sr, Ar(K)/Ar
Mineral abbreviations: Grt, garnet; Zrn, zircon; WM, white mica;
Bt, biotite; Hbl, amphibole; phe, phengite; WR, whole rock;
Kfs, potassium-feldspar; Pl, plagioclase.
U/Pb denotes detrital zircon ages
North El Tambor group subduction–accretion–arc units
BVP, Baja Verapaz unit; SSC, Sierra des Santa Cruz unit;
JPZ, Juan de Paz unit; NM, Northern Motagua unit
South El Tambor group subduction–accretion units
SM, Southern Motagua unit
Gulf of Tehuantepec
MEXICO
GUATEMALA
BELIZE
HONDURAS
EL SALVADOR
Maya Mountains
Roatán Island
Bonacca Ridge
Swan Island fault
Polochic fault
Motagua fault and suture
Baja Verapaz shear zone
Chiquimula batholith
Sanarate complex
Cabañas fault
Jocotán–Chamelecón fault
Guayape fault
Jurassic strata cover schists
Los Cuchumatanes
Chuacús
Alos
SSC
JPZ
BVP
NM
SM
100km
Mexico
Guatemala-Honduras
Cretaceous and Tertiary intrusions
Xolapa complex: Mesozoic medium- and high-grade metamorphic rocks
Acatlán complex: Early Paleozoic polymetamorphic rocks
Oaxacan and Guichicovi complexes: Proterozoic (Grenville) granulite
Chiapas Massif: Late Paleozoic igneous and metamorphic rocks
Major strike-slip, normal, thrust fault zones
North and South El Tambor complexes: subduction–accretion–arc units of the Motagua suture zone
Sanarate complex (Jurassic metapelites, amphibolite; Chortís block)
Santa Rosa group: Paleozoic sediments and hornfelses (Maya block); locally felsic intrusions
Maya complex: Early Paleozoic, low-grade metasedimentary rocks (Maya block) (San Gabriel unit, Jocote Fm., Baldy Fm,) and granitoids (Rabinal)
Chuacús complex: Early Paleozoic, high-grade metavolcano-sedimentary rocks (Maya block) and granitoids
Las Ovejas complex and San Diego phyllites: Precambrian-Paleozoic volcano-sedimentary rocks (Chortís block), mainly Tertiary metamorphism
Granitoids and high-grade metamorphic rocks (central Honduras)
Cacaguapa schist (Honduras) and Las Segovias metamorphic complex (Nicaragua)
99°W
98°W
97°W
96°W
95°W
94°W
93°W
92°W
91°W
90°W
89°W
88°W
87°W
18°N
17°N
16°N
15°N
14°N

Figure 1.

ferent velocities of the North American and Caribbean plates (e.g., DeMets, 2001). In southern Mexico, Guatemala, and Honduras this still active fault system has dismembered the collisional blocks as well as the allochthonous remnants of the former oceanic crust; the latter comprises shaly mélange, containing blocks of serpentinized ophiolite fragments, and metamorphic rocks such as amphibolite, eclogite, albitite, and jadeitite (e.g., Tsujimori et al., 2005). Inferred displacement accommodated along the MSZ is controversial, but magnetic anomalies within the Cayman trough suggest a maximum of ~1100 km; spreading rates in the trough were ~3 cm/a from 44–30 Ma and ~1.5 cm/a thereafter (Rosencrantz et al., 1988). Active faulting and volcanism related to eastward subduction of the Pacific plate overprinted the ophiolite emplacement and intra-continental translation features within the crust of Mexico, Guatemala, and Honduras (e.g., Guzmán-Speziale, 2001).

3. Methods

U/Pb, Ar/Ar, Rb/Sr, and fission-track geochronology provided absolute age information on the geologic history. Table 1 (all Tables are given in Appendix A) gives locations and descriptions of analyzed samples. We conducted isotope-dilution analyses (ID-TIMS) of zircon fractions at UW Seattle; analytic and data processing details are similar to Herrmann et al. (1994). At Stanford and St. Petersburg, we used ion microprobe dating to investigate samples with multifaceted zircon internal structures; the Stanford SHRIMP-RG and St. Petersburg SHRIMP II methodologies are those of DeGraaff-Surpless et al. (2002) and Williams (1998), respectively.

Figure 1. (A) Plate tectonic framework of northern Central America and crustal complexes ("terranes") of southern Mexico. Numbers in the Cayman trough give age of transitional to oceanic lithosphere (from Rosencrantz et al., 1988). (B) SRTM digital elevation model of the Motagua suture zone in southern Mexico, Guatemala, and Honduras, highlighting neotectonic structures such as the Polochic, Motagua, and Tonala strike-slip faults and NNE-trending grabens (e.g., Sula). (C) Basement geology of southern Mexico and northern Central America and available reliable geochronologic data surrounding the Motagua suture zone. References for Belize, Guatemala, and Honduras: 1: Ortega-Gutiérrez et al. (2004); 2: Harlow et al. (2004); 3: Horne et al. (1976a); 4: Manton (1996); 5: Venable (1994); 6: Steiner and Walker (1996); 7: recalculated from Gomberg et al. (1968); 8: Sutter referenced in Donnelly et al. (1990); 9: Bertrand et al. (1978); 10: Manton and Manton (1984); 11: Drobe and Oliver (1998); 12: Donnelly et al. (1990); 13: Emmet (1983); 14: Italian Hydrothermal (1987; reported in Rogers, 2003); 15: Horne et al. (1976b); 16: Horne et al. (1974); 17: MMAJ (1980; reported in Rogers, 2003); 18: Manton and Manton (1999); 19: Weiland et al. (1992); 20: Bargar (1991); 21 (Ortega-Obregón et al. (2008); 22, Solari et al. (2008); 23, Martens et al. (2008). References for Mexico: A: Ortega-Gutiérrez et al. (1999); B: Talavera-Mendoza et al. (2005); C: Sánchez-Zavala et al. (2004); D: Yañez et al. (1991); E: Weber et al. (2006a); F: Ducea et al. (2004a); G: Elías-Herrera and Ortega-Gutiérrez (2002); H: Solari et al. (2001); I: Vega-Granillo et al. (2007); J: Keppie et al. (2004); K, Morán-Zenteno (1992); L, Solari et al. (2007); M, Herrmann et al. (1994); N, Elías-Herrera et al. (2005); O, Tolson (2005); P, Robinson et al. (1989); Q, Wawrzyniec et al. (2005); R, Weber et al. (2005); S, Alaniz-Alvarez et al. (1996); T, Solari et al. (2004); U, Schaaf et al. (2002); V, Weber et al. (2008). Ages without a label are our own data from southern Mexico.

U/Pb data presentation on Concordia, weighted mean and relative probability diagrams employed Isoplot 3.0 (Ludwig, 2003). We used cathodoluminescence (CL) to image the internal structure of the zircons prior to analysis. Ar/Ar analytical procedures are similar to Hacker et al. (1996), Grimmer et al. (2003), and Cerca et al. (2007). Argon was released by furnace step-heating or single-grain laser fusion. Ar/Ar isotope-correlation diagrams are presented only for those samples that appear to contain excess ^{40}Ar, as indicated by systematically discordant (e.g., saddle-shaped) age spectra and/or non-atmospheric $^{40}Ar/^{36}Ar$ intercepts. Rb/Sr mineral ages were measured by isotope dilution at Freiberg and GFZ Potsdam using whole rock and one to several mineral fractions. The methodological and technical aspects of apatite fission-track (AFT) thermochronology, including the calculation and comparison of ages obtained by the independent ϕ, and the standard-based Z and ζ methods, follow Grimmer et al. (2002); we use ϕ ages. Titanite fission-track (TFT) analytical techniques are those of Ratschbacher et al. (2006).

Structural field measurements comprise foliation, lineation, kinematic criteria, tension gashes, folds, faults, and their relative age relationships. Shear sense was deduced on the meso- and micro-scale using indicators like σ and δ clasts, s–c fabrics, asymmetric boudinage, and the interpretation of lattice preferred orientation (LPO) of quartz measured by U-stage or electron back-scatter diffraction (EBSD). Microstructures reflecting type of polygonization and recrystallization in quartz and feldspars yielded additional information about deformation temperatures. On outcrop scale, ductile deformation features were measured to estimate structural geometries and principle strain axes ($X \geq Y \geq Z$). We used faults and associated striae to analyze brittle deformation. 'Paleostress' methods, employing fault and striae orientations, slip-sense of the hanging wall, and confidence level for the slip-sense determination, enabled the calculation of the orientation of the stress axes ($\sigma_1 \geq \sigma_2 \geq \sigma_3$) and the stress ratio R [$R=(\sigma_2-\sigma_3)/(\sigma_1-\sigma_3)$]. The confidence level is expressed in the data plots by distinct slip-sense arrows and allows the judgment of the quality of our database. The basic requirements for paleostress analysis are data sets that originate from a homogeneous stress field. Thus, data from multiply deformed rocks were separated into subsets, each the result of one homogeneous stress field. Separation of data was guided by field evidence (polyphase slip along faults) and supplemented by graphical (incompatibility of data as seen from stereoplots) and mathematical analyses (large angle between measured striae and theoretical orientation of maximum shear stress on the fault). Curved fibers behind fault steps and crosscutting relationships provided relative movement chronologies. Paleostress was calculated using the program package of Sperner et al. (1993) and Sperner and Ratschbacher (1994), and principal stress axes are displayed together with the fault-striae data in lower hemisphere, equal area stereoplots.

To record petrography as well as PT conditions of rocks, we examined polished thin sections by polarization microscopy and microprobe analyses. Mineral analyses were performed using a JEOL JXA-8900R electron microprobe equipped with five spectrometers at Freiberg. Major and minor elements were determined at 15 kV acceleration voltage and a beam current of 20 nA with counting times of 20 s for Si, Al, Mg, Ca, Sr, Ba and K, and 30 s for Fe, Ni, Na, Cr, Mn and Ti. The standard sets of the Smithonian Institute (Jarosewich et al., 1980) and of MAC^{TM} were used for reference. Mineral abbreviations follow Kretz (1983) and Spear (1995). The microprobe dataset is compiled in Bachmann (2003) and available from the authors.

4. Basement and cover of the Maya and the Chortís blocks

Figure 2 presents lithostratigraphic columns of the southern Maya block, the MSZ, and the north-central Chortís block, based on the compilations given in Donnelly et al. (1990) and Rogers (2003). We modified the columns according to our new data and the recent literature (discussed below) and, where available, added stratigraphic range (converted into Ma), thickness, reliable radiometric ages, PT estimates, and first-order depositional environment interpretations. In addition, we show columns of units that we will use in the discussion for correlation and refinement of tectonic models, and present relative probability diagrams displaying our own and published geochronology of these units.

4.1. Cover sequences

In general, the Maya block (Fig. 2B) records shelf evolutions during Late Paleozoic and Cretaceous; these were followed by terrestrial–shallow marine rift (Late Jurassic) and submarine-fan (Late Cretaceous) developments. Along the MSZ, likely mostly Early Cretaceous ophiolites are imbricated with probably Upper Jurassic to Upper Cretaceous submarine-fan and ocean-basin deposits (North El Tambor Group and El Pilar Formation, Fig. 2A) and Maya-block basement (Chuacús complex); they are unconformably overlain by molasse (Subinal Formation). In the Sierra de Santa Cruz (Fig. 1C), massive ophiolitic rocks with rare basalts of island-arc affinity are imbricated with Maastrichtian to Eocene (~80-50 Ma) carbonate–arenaceous pre-flysch and flysch (Sepur Formation; Wilson, 1974; Beccaluva et al., 1995). Aptian and Cenomanian (~120–95 Ma) sedimentary rocks of the Petén basin of northern Guatemala (Maya block) record a pelagic facies, reflecting maximum transgression and an open marine connection to the Gulf of Mexico to the north, and the Proto-Caribbean seaway to the south (Fourcade et al., 1999). During the latest Maastrichtian and Danian (~70–60 Ma), the southern Petén basin (Fig. 1B) was a deep siliciclastic sink, the Sepur foredeep basin. The depocenter of this basin shifted from south during the late Campanian to north during the latest Maastrichtian and early Danian; this led to the demise of the pre-existing carbonate platform over more than 100 km from south to north.

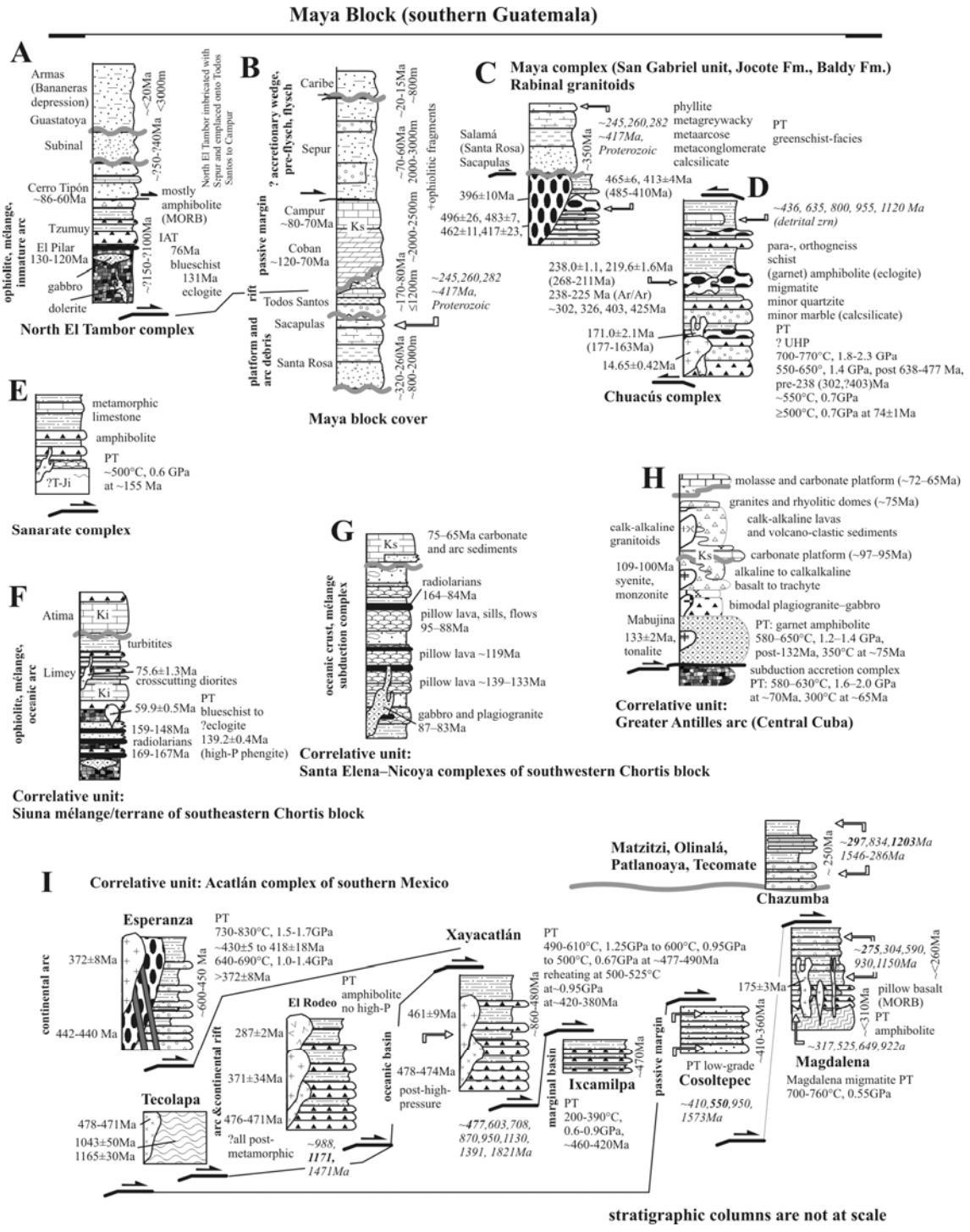

Figure 2. (Litho)stratigraphic and pressure–temperature–time–deformation evolution and depositional environment interpretation of the Maya block, the Motagua suture zone, and the northern Chortís block and correlative units in southern Mexico and the southern Chortís block (see text for discussion of correlations). Ages in italics are detrital zircon ages from Talavera-Mendoza et al. (2005) and located in the stratigraphic sequence by an arrow; other ages from magmatic rocks and are those reported in the captions of Fig. 1C and the text. Pressure–time conditions from this paper and literature are reviewed in the text.

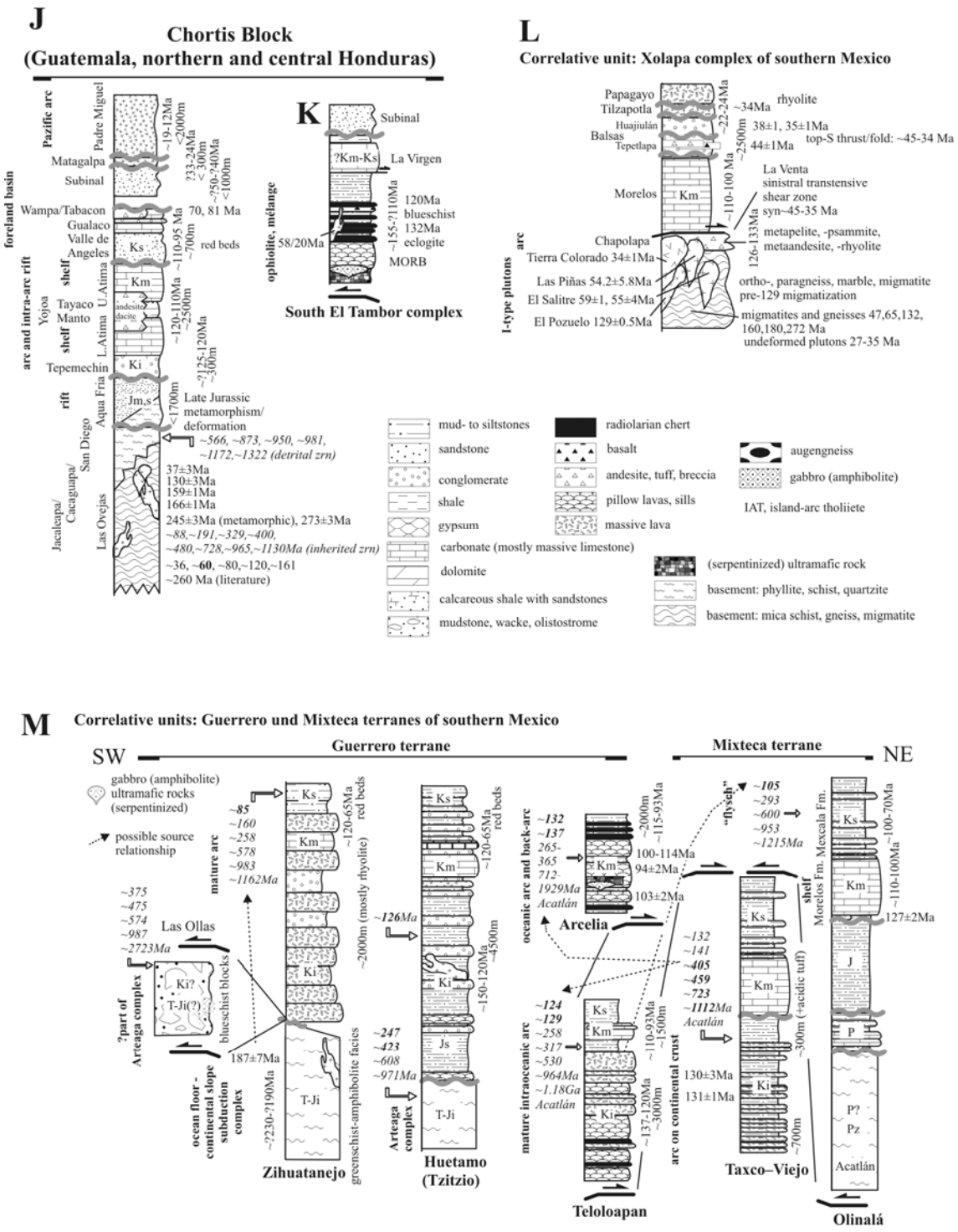

Figure 2. (continued)

The ophiolites south of the Motagua fault (South El Tambor Group, Fig. 2K) are limited to the north by the Cabañas fault (southern strand of the Motagua fault zone) and are overlain by Subinal molasse and in the south by the Tertiary–Recent magmatic arc; they are cut by felsic intrusives. Together with Late Jurassic–Cretaceous 'mélange', they cover basement of the Las Ovejas complex and the San Diego Group of the Chortís block. Rare basaltic sections of these 'southern' ophiolites show mid-ocean ridge basalt (MORB) affinity (Beccaluva et al., 1995). In

the north-central Chortís block (Fig. 2J), the clastic, partly turbiditic, rift-related Agua Fria Formation was deformed during Late Jurassic (Viland et al., 1996). It is overlain by the shallow-marine, shelf-type Yojoa Group that contains arc and intra-arc rift deposits (Roger et al., 2007a). Possibly two molasse sequences are present: the mainly red beds of the Albian–Cenomanian Valle de Angeles Group and the ?Eocene Subinal Formation. Thus, molasse-type deposits occur on the Chortís during late Early to Late Cretaceous times (Valle de Angeles Group), whereas marine platform carbonates developed on the Maya block (Coban and Campur Groups). Top-to-N thrust imbrication affected the Jurassic–Cretaceous sequence during Late Cretaceous (Donnelly et al., 1990; Colon fold belt of Rogers et al., 2007b).

4.2. Basement complexes

Clear definition and subdivision of the rock units that comprise the MSZ (Fig. 1C) remain elusive principally because Cenozoic faults delineate parts of these units. This section describes the major units of the MSZ from north (Maya block) to south (Chortís block).

Chuacús complex (Maya block)

In Guatemala, Ortega-Gutiérrez et al. (2004) described the Chuacús complex as schists and gneisses outcropping between the Motagua fault and the Baja Verapaz shear zone of the Salamá–Rabinal area (Fig. 1C). Chuacús schists and gneisses contain quartz + albite + white mica + epidote/zoisite ± garnet ± biotite ± amphibole (barroisite/taramite/pargasite) ± omphacite ± allanite ± chlorite ± calcite ± titanite ± rutile (Martens et al., 2005). Banded migmatites that contain (garnet) amphibolite (locally relict eclogite), calcsilicate, and marble are uncommon. Rare quantitative petrology suggests upper greenschist- to amphibolite-facies conditions up to 650°C at ~1.1 GPa; retrogression to greenschist facies is poorly documented (Machorro, 1993; van den Boom, 1972). Both foliation concordant and discordant quartz–albite–white mica pegmatites are associated with the gneisses. Eclogitic relicts contain possible ultra-high pressure metamorphism, and pyroxene with up to 45 vol. % omphacite and garnet together with phengite + rutile + kyanite + zoisite + epidote. Thermobarometric analyses yielded ~740°C at 2.3 GPa with retrogression at ~590°C and ~1.4 GPa. Decompression seems associated with local partial melting (Ortega-Gutiérrez et al., 2004). In eastern Guatemala (San Agustín Acasaguastlán), orthogneiss (quartz-monzonite, granodiorite) outcrops together with high-grade, typical Chuacús paragneiss; the latter locally shows sillimanite and abundant K-feldspar. The volcanosedimentary protolith is younger than ~440 Ma based on detrital zircons (Solari et al., 2008).

Salamá metasediments (San Gabriel unit) and the Rabinal granitoids (Maya block)

The metasediments were grouped into an older clastic and metavolcanic succession, the San Gabriel unit (Ortega-Obregón et al., 2008), which is intruded by the Rabinal granite, and a younger clastic and calcareous succession, likely part of the Santa Rosa Group; the basal con-

glomerate beds comprise the Sacapulas Formation of van den Boom (972). Ortega-Obregón et al. (2004, 2008) proposed an up to 5 km wide sinistral–reverse shear zone, the Baja Verapaz shear zone, juxtaposing Chuacús gneiss and San Gabriel metasediments intruded by the Rabinal granite; deformation is most pronounced within 300 m of the Chuacús–San Gabriel boundary. The lateral continuation of the shear zone is unknown. The San Gabriel unit has a continental depositional environment and is pre-Silurian, given by the age of the Rabinal granitoids (see below); it resembles low-grade metasediments in western Guatemala, where it is post-Middle Proterozoic based on detrital zircon geochronology (Solari et al., 2008). The Santa Rosa Group Salamá metasediments yielded Early Carboniferous crinoids (van den Boom, 1972) and Mississippian (Tournaisian) conodonts (Ortega-Obregón et al., 2008). The Rabinal granitoids are spatially poorly defined, as their sheared margins and the surrounding metasediments have similar appearance; they are predominately fault-bounded and widely tectonized.

Maya Mountains (Maya block)

Metamorphic rocks in the core of the Maya mountains of Belize are low-grade metasediments that locally yielded Carboniferous–Permian fossils and were correlated with the Santa Rosa Group (Bateson, 1972). Contact metamorphic andalusite and chloritoid appear in the vicinity of the Mountain Pine Ridge granitoids (Jackson et al., 1995).

Existing Geochronology: Maya block

Three zircon fractions of a Rabinal granite-gneiss yielded a concordant 396 ± 10 Ma age (recalculated from the data given by Gomberg et al., 1968). Four zircon fractions combining two Chuacús gneiss samples south of Salamá gave a lower intercept U/Pb age of 326 ± 85 Ma (again recalculated from Gomberg et al., 1968). All zircon analyses of three Rabinal granite and one pegmatite of Ortega-Obregón et al. (2008) are discordant; they yielded lower intercepts of 496 ± 26 and 417 ± 23 Ma (granite), and 462 ± 11 Ma (pegmatite), and an upper intercept of 483 ± 23 Ma (granite). Muscovite from two pegmatites cutting the San Gabriel unit yielded K/Ar cooling ages of 453 ± 4 and 445 ± 5 Ma. Ortega-Obregón et al. (2008) suggested intrusion of the Rabinal granitoids between ~462 and 453 Ma. Three single zircon and two small populations from leucosome interbedded with relict eclogite (El Chol area) yielded intercept U/Pb ages of 302 ± 6 Ma and 1048 ± 10 Ma (Ortega-Gutiérrez et al., 2004). The fossils in the Santa Rosa Group rocks imply a post-Early Carboniferous metamorphic age for these metasediments. K/Ar and Ar/Ar ages exist from Chuacús-complex rocks; they are mostly poorly located and documented. Hornblende, white mica, and biotite gave Ar/Ar ages of 78–66 Ma, 76–67 Ma, and 67–64 Ma, respectively (Sutter, 1979). Amphibole from garnet amphibolite and white mica from retrograde phengite-bearing gneiss yielded K/Ar ages of ~73 Ma and ~70 Ma, respectively. Coarse- and finer-grained white mica from foliated meta-pegmatite gave ~73 Ma and ~62 Ma,

respectively (weighted mean ages from several fractions given by Ortega-Gutiérrez et al., 2004). The oldest Ar/Ar age from the Chuacús complex is ~238 Ma (amphibole; Sutter cited in Donnelly et al., 1990). White mica from a Chuacús complex metasediment and a late-tectonic pegmatite ≥4 km south of the main trace of the Baja Verapaz shear zone gave ages between 74.1 ± 1.3 Ma and 65.3 ± 1 Ma; they were suggested to date shearing along the Baja Verapaz zone (Ortega-Obregón et al. (2008). The fossils in the Santa Rosa Group metasediments of the Maya mountains imply a post-Permian age for the low-grade overprint. U/Pb zircon and monazite ages obtained from two batholiths in the Maya mountains (Steiner and Walker, 1996) yielded 410–420 Ma, indicating that some of the metasediments are not Santa Rosa Group; K/Ar biotite ages of these igneous rocks are 230 ± 9 Ma (weighted mean of 7 dates compiled in Steiner and Walker, 1996).

El Tambor Group: metamorphic–metasomatic rocks of the Motagua suture zone

The El Tambor Group comprises dismembered ophiolitic sheets of serpentinized peridotite, eclogite and jadeitite blocks, mylonitized gabbro, (garnet) amphibolite, pillow lavas, radiolarian cherts, and low-grade metasediments (e.g., Tsujimori et al., 2005; Chiari et al., 2004; Beccaluva et al., 1995; Harlow, 1994; Bertrand and Vuagnat, 1975). Regional prehnite–pumpellyite-facies metamorphism affected the volcanic rocks, forming albite + chlorite, predominantly pumpellyite, and locally prehnite. Centimeter- to m-scale interlayering of mafic rocks, siliceous marble, and quartzite (probably metamorphosed chert), are reported in the La Pita complex of the eastern MSZ (Martens et al., 2005); assemblages with barroisite + garnet + epidote + albite + white mica are characteristic. Jadeitite formed sporadically within the serpentinite matrix of the El Tambor mélange; it consists of jadeitic pyroxene with minor paragonite, phengite, phlogopite, albite, titanite, zircon, apatite, and garnet and formed at 100–400°C and 0.5–1.1 GPa (Harlow, 1994). Two contrasting high-P belts contain lawsonite eclogite and zoisite eclogite south and north of the Motagua valley, respectively. The lawsonite eclogites (South El Tambor Group, Fig. 2K) record unusually low-T–high-P with prograde eclogite facies at ~450°C and ~1.8–2.4 GPa, followed by retrogression with infiltration of fluids at <300°C and ~0.7 GPa (Tsujimori et al., 2004, 2005, 2006). Amphibolitized, paragonite-bearing zoisite eclogites (North El Tambor Group, Fig. 2A) in antigorite schist north of the Cabañas fault formed at significantly higher T, 600–650°C at 2.0–2.3 GPa (Tsujimori et al., 2004).

Existing Geochronology: El Tambor Group

Two Sm/Nd mineral isochrons from South El Tambor Group eclogites gave ages of 131.7 ± 1.7 and 132.0 ± 4.6 Ma, which are identical to the 130.7 ± 6.3 Ma age from eclogite sampled north of the fault (Brueckner et al., 2005). The southern eclogites show MORB major and trace element patterns and are isotopically depleted ($^{87}Sr/^{86}Sr$ ratios of 0.70374 and 0.70489, ε_{Nd} of

+8.6 and +9.2). One North El Tambor Group eclogite has a significantly more enriched signature ($^{87}Sr/^{86}Sr$ = 0.70536; ε_{Nd} = -2.1; Brueckner et al., 2005). Harlow et al. (2004) obtained Ar/Ar white mica ages from jadeitite, albitite, mica-bearing metamorphic rocks, and altered eclogite within the MSZ, ranging between 77–65 Ma for the northern high-P belt, and 125–113 Ma for the southern belt; however, the samples are not well located. In the northern belt, three phengite-only samples are indistinguishable within error at 76 Ma, whereas two phengite–phlogopite–paragonite mixtures are younger at 71 and 65 Ma. The 600–650°C peak T of the northern high-P rocks suggest that the phengite (closing T ~400°C, von Blanckenburg et al., 1989) date retrogression under blueschist-facies conditions when Na–Al–Si-rich fluids produced jadeitite and albitite in serpentinite (Harlow, 1994). All dated minerals from the southern belt are phengite; four ages are within error at 120 Ma, one is older, two younger. These ages likely date fluid infiltration during blueschist-facies retrograde metamorphism. Bertrand et al. (1978) reported K/Ar mineral and whole-rock ages from poorly located samples attributed to the North El Tambor Group. We divided their samples regionally and recalculated the ages: a metadolerite from the Baja Verapaz ophiolite sheet (Fig. 1C) north of Salamá yielded ~76 Ma, three metadiabase samples from pillow basalt overlying the Chuacús complex gave a weighted mean whole-rock age of ~74 Ma (their $^{40}Ar/^{36}Ar$ versus $^{40}K/^{36}Ar$ isochron gives atmospheric $^{40}Ar/^{36}Ar$), and six amphibole separates from garnet amphibolites of the same unit yielded a weighted mean age of 57.2 ± 5.4 Ma (again, atmospheric $^{40}Ar/^{36}Ar$ with an 'isochron age' of ~56 Ma). All ages probably date metamorphism.

The available petrology (lawsonite and zoisite eclogites south and north of the MSZ, respectively), geochronology (~120 and 76 Ma for blueschist-facies retrogression south and north of the MSZ, respectively), and isotope geochemistry (isotopically depleted versus enriched south and north of the MSZ, respectively) demonstrate the existence of two distinct subduction–accretion belts along the MSZ (herein named South and North El Tambor Groups), even though ages of crust formation and eclogite-facies metamorphism may appear similar.

Las Ovejas complex (Chortís block)

The Las Ovejas complex comprises biotite schist, gneiss, migmatite, (garnet) amphibolite, marble, and deformed metagranitoids. Specifically, amphibolite (≤15% of the Las Ovejas complex in Guatemala), garnetiferous gneiss, staurolite schist, garnet–two-mica schist, and marble with calcsilicate layers are exposed together with metaigneous rocks, diorite, tonalite, granodiorite, and minor gabbro. Mineral assemblages define amphibolite-facies conditions; metamorphic grade of rocks containing staurolite increases toward the northwest where a sillimanite-zone was identified (IGN, 1978). Both basement and cover of the northern Chortís block continue as the Bonacca Ridge, forming a series of islands south of the Swan Island Fault (Fig. 1C),

the southern boundary fault to the Cayman trough. Roatán Island, which is the best studied (Avé Lallemant and Gordon, 1999), exposes amphibolite-facies basement with (augen)gneiss, schist, amphibolite (partly metagabbro), marble, and rare pegmatite.

San Diego phyllite and Cacaguapa schist (Chortís block)

The undated San Diego metamorphic rocks consist of phyllite, and minor thin quartzite and slate layers (Schwartz, 1976). Their stratigraphic age is post-Early Cambrian as the youngest detrtial zircons are ~520 Ma (Solari et al., 2008). The Chiquimula batholith thermal overprint produced cordierite and andalusite (Clemons, 1966). Greenschist-facies and locally higher grade metamorphic rocks in Honduras include calcareous phyllite, white mica–chlorite and graphitic schists and slate ('younger sequence' of Horne et al., 1976a). The San Diego phyllites of southern Guatemala and northern Honduras are correlated with the Cacaguapa schists south and east of the Jocotán-Chamelecón fault system (Fig. 1C; Burkart, 1994). The greenschist-facies lithology at Roatán Island comprises (quartz) phyllite, chlorite schist, serpentinite, chert, and marble to limestone; locally granite porphyry is present (Avé Lallemant and Gordon, 1999).

Sanarate complex

The westernmost basement outcrop south of the MSZ comprises partly retrograde amphibolite, garnet- and quartz-bearing amphibolite, retrograde leucogabbro, chlorite–epidote–hornblende schist, micaschist, phyllite, and chlorite phyllite; massive amphibolite is characteristic. Ductile deformation geometry and kinematics, PT conditions, and Jurassic metamorphism are distinctly different from that in the Las Ovejas complex (see below). The basement is in fault contact with Tertiary andesite and red beds and is cut by andesite dikes. Due to its distinct lithology and P-T-dt parameters, we distinguish this complex from the other units of the Chortís block; however, its boundaries and lithostratigraphy are mostly unknown. Along its eastern boundary the Sanarate-complex rocks shows W-dipping foliation and apparently thrusted top-to-E over South El Tambor Group metaclastic rocks that show distinctly lower metamorphic grade.

Existing Geochronology: Las Ovejas complex, San Diego phyllite and Cacaguapa schist, igneous rocks

Most of the available geochronology is, in a modern sense, poorly documented and samples are only approximately located (Fig. 1C). U/Pb zircon ages on igneous rocks are: ~93 Ma (Rio Julian granite), ~80 Ma (sheared Rio Cangrejal orthogneiss), 81.0 ± 0.1 (El Carbon granodiorite), ~29 Ma (Banderos granodiorite; all Manton and Manton, 1984), 124 ± 2 Ma (dacite; Drobe and Oliver, 1998), and ~1 Ga (orthogneiss, ?equivalent to Las Ovejas complex; Manton, 1996). We recalculated the zircon data of the El Carbon granite of Manton and Manton (1999) and obtained lower and upper intercepts of 30 ± 19 Ma and 126 ± 42 Ma, respectively. De-

formed granitic plutons gave a 300 ± 6 Ma Rb/Sr whole-rock isochron for the Quebrada Seca complex (Horne et al., 1976a); the foliated plutons intrude amphibolite-facies metasedimentary and metavolcanic rocks indicating that the metamorphism of the high-grade rocks is post-Permian. Granitoids gave the following Rb/Sr ages: 150 ± 13 Ma (San Marcos granodiorite, whole rock; Horne et al., 1976a), ~69 Ma (K-feldspar and plagioclase, cooling age of sheared El Carbon granodiorite; Manton and Manton, 1984), ~80 Ma (whole-rock isochron, Trujillo granodiorite; Manton and Manton, 1984), 140 ± 15 Ma (Dipilto granite, whole rock; Donnelly et al., 1990), 118 ± 2 Ma (Carrizal diorite, K-feldspar and plagioclase; Manton and Manton, 1984), ~54 Ma (Rio Cangrejal granodiorite), 39 Ma (Sula Valley [Ulúa graben] granodiorite), and 35 Ma (Confadia granite; all biotite cooling ages; Manton and Manton, 1984). K/Ar cooling ages of igneous rocks comprise: 93.3 ± 1.9 Ma , 80.5 ± 1.5 Ma and 73.9 ± 1.5 Ma (Tela augite-tonalite, one amphibole and two biotite ages from different samples; Horne et al., 1974), 72.2 ± 1.5 Ma and 56.8 ± 1.1 Ma (Pedras Negras tonalite, amphibole and biotite; Horne et al., 1974), 35.9 ± 0.7 Ma (San Petro Sula granodiorite, biotite; Horne et al., 1974), 122.7 ± 2.5 Ma and 117.0 ± 1.9 Ma (San Ignacio granodiorite, hornblende and biotite; Emmet, 1983), 114.4 ± 1.7 Ma (San Ignacio adamellite, biotite; Horne et al., 1974), 79.6 ± 1.6 Ma (gabbro dike, amphibole; Emmet, 1983), 62.2 ± 2.6 Ma (diorite, whole rock; Italian Hydrothermal, 1987, reported in Rogers, 2003), 60.6 ± 1.3 Ma and 59.3 ± 0.9 Ma (Minas de Oro granodiorite, biotite; Horne et al., 1976b and Emmet, 1983), 58.6 ± 0.7 Ma (San Francisco dacite pluton, biotite; Horne et al., 1976b). Ar/Ar ages are from andesite and diorite of the eastern Chortís block (75.6 ± 1.3 Ma and 59.9 ± 0.5 Ma, amphibole and biotite; Venable, 1994). A K/Ar biotite age of 222 ± 8 Ma from micaschist probably reflects a Triassic thermal event (MMAJ, 1980). Hornblende from the amphibolite-facies basement of Roatán Island yielded 36.0 ± 1.2 Ma, and a granite porphyry from Barbareta Island, east of Roatán Island, yielded a 39.4 ± 2.8 Ma zircon fission-track age (closing T ~250°C; Avé Lallemant and Gordon, 1999).

5. New Geochronology

Tables 2 and 3 report ID-TIMS and ion-probe U/Pb geochronology and Figures 3 and 4 visualize the U/Pb data in Concordia diagrams and present representative zircon CL pictures, respectively. Our new Ar/Ar and Rb/Sr mineral ages are summarized in Tables 4 and 5, respectively, and are plotted in Figure 5. In this paper, we discuss Phanerozoic U/Pb ages; late Middle Proterozoic ages, which we find in both the Maya and Chortís blocks, will be reported elsewhere. Our AFT and TFT data are listed in Table 6; confined track-length data appear in Table 7. Figure 6 depicts AFT age–versus–elevation diagrams for the Chuacús and Las Ovejas complexes of Guatemala/Honduras and the Chiapas massif of southeastern Mexico (Fig. 1C), and modeled T-t paths for selected samples (Chuacús and Las Ovejas complexes, granitoids). We excluded the samples from western Guatemala from the age–versus–elevation data (too few

readings and widely spaced) and also emphasize that ~~also~~ the plotted data do not strictly fulfill the criteria for exhumation estimates from age–versus–elevation data; for example, the samples cover considerable horizontal distances. We assigned errors to the elevation data, as several samples were collected in the early-1990s when hand-held GPS-receiver precision was still inferior and large-scale topographic maps were locally unavailable. We emphasize that the regression data that we present are first-order estimates. Figure 7 shows the regional distribution of ages, highlights age groups, and depicts T-t fields for selected regions. We employed standard closing temperatures for the T-t diagrams: Ar hornblende, high-T steps, 525 ± 25°C, low-T steps, 400 and 300 ± 100°C, depending on grain size; Ar white mica, 350 ± 25°C; Ar biotite, 300 ± 25°C; Ar K-feldspar, 400 ± 100°C for high-T steps and 200 ± 25°C for low-T steps, depending on the likely presence of single or multiple domains; Rb white mica, 500 ± 25°C, except for cm-sized, pegmatitic white mica, 600 ± 100°C; Rb biotite, 275 ± 25°C; TFT, 275 ± 50°C; AFT, 100 ± 25°C; exceptionally, errors were set higher, imposed by variable grain size and strong deformation. Zircon crystallization was taken as 800 ± 50°C, except where zircon growth occurred during peak-T metamorphism and related migmatization, which is constrained by our new petrology (see below). We excluded a few samples from the T-t diagrams: ages from sample 5C-36 of the Chuacús complex immediately below North El Tambor Group serpentinite, as these rocks show extreme, late-stage metasomatism; ages from very coarse-grained, pegmatitic white mica. In the following section, we present the data; we relate the ages to the main temperature–deformation (Td) events in the petrology and structure sections.

5.1. U/Pb zircon geochronology

Sample G18s (stop G1; Fig. 3A) is a migmatitic gneiss from the Chuacús complex of western Guatemala overprinted by lower greenschist-facies deformation. Four fractions with identical 75–125 μm grains but different magnetic properties were utilized for ID-TIMS analysis. A discordia fit to 3 fractions yields intercepts of 220.0 ± 3.5 and 1292 ± 39 Ma (MSWD = 0.78); one of these fractions is concordant at 215.92 ± 0.18 Ma. The fourth fraction is concordant at 268.04 ± 0.55 Ma. CL images (Fig. 4) depict well-rounded cores with variable but mostly high U-content, and low U (on average 63 ppm), oscillatory zoned rims with Th/U ratios (on average 0.7) that imply magmatic origin. The weighted average of 6 grains analyzed with the SHRIMP gives a 207-corrected 217.7 ± 7.3 Ma age, within error of the concordant TIMS fraction. We interpret the weighted average age of 215.9 ± 0.78 Ma of the SHRIMP and TIMS data as the age of migmatization within the basement of the western Chuacús complex. Sample GM1 (stop GM15, Fig. 3A) is quartz phyllite north of the Chuacús complex west of Salamá that is likely part of the Santa Rosa Group. Zircons are rounded but a significant portion is sub-euhedral. Besides ages >1Ga, we obtained 4 concordant ages at 416.5 ± 1.6 Ma, 282.2 ± 1.7 Ma, 260.4 ± 2.9 Ma, and 245.1 ± 2.9 Ma. The Devonian spot has low Th/U (0.012), the other zircons (Th/U on

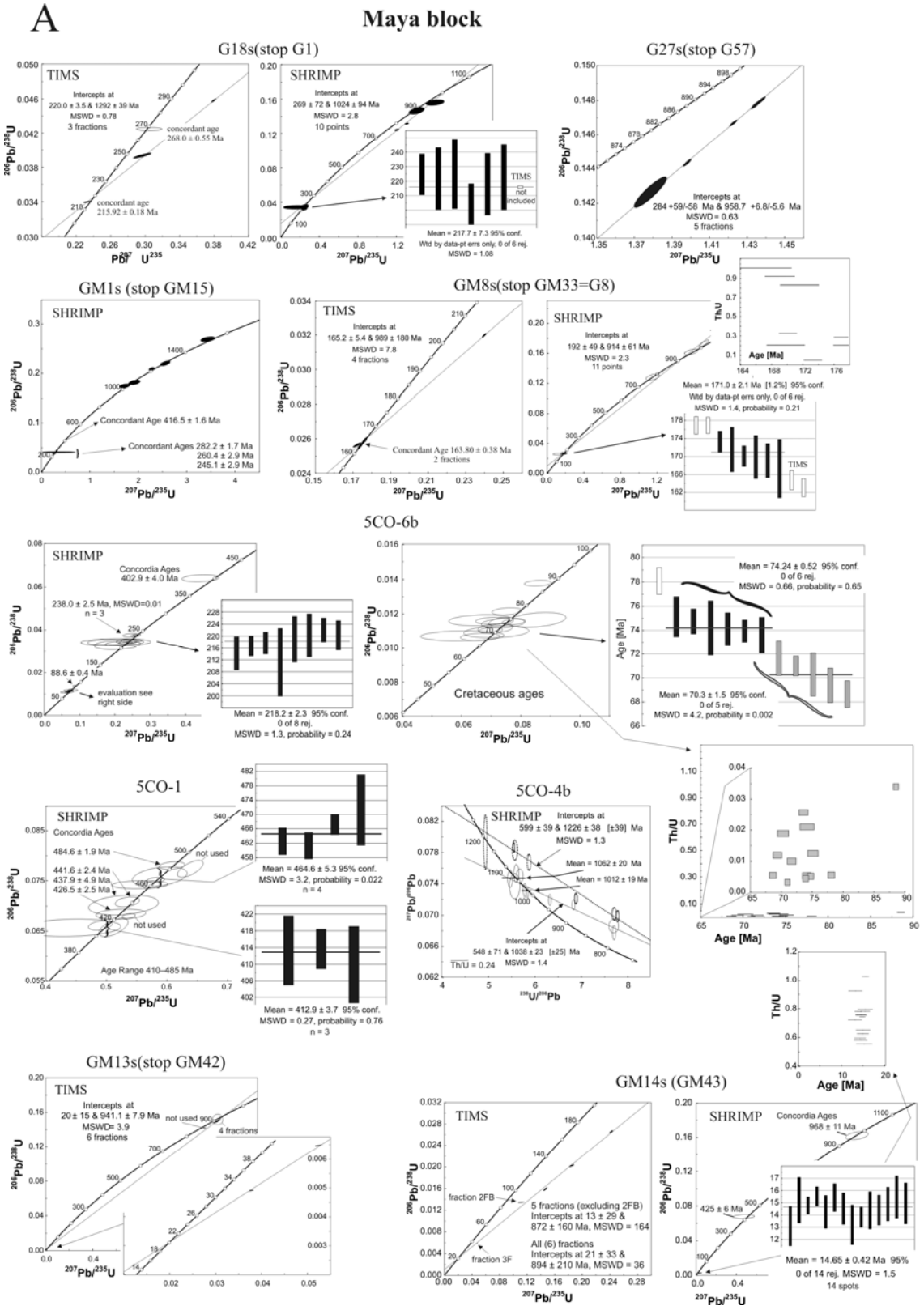

Figure 3. (figure caption see next page)

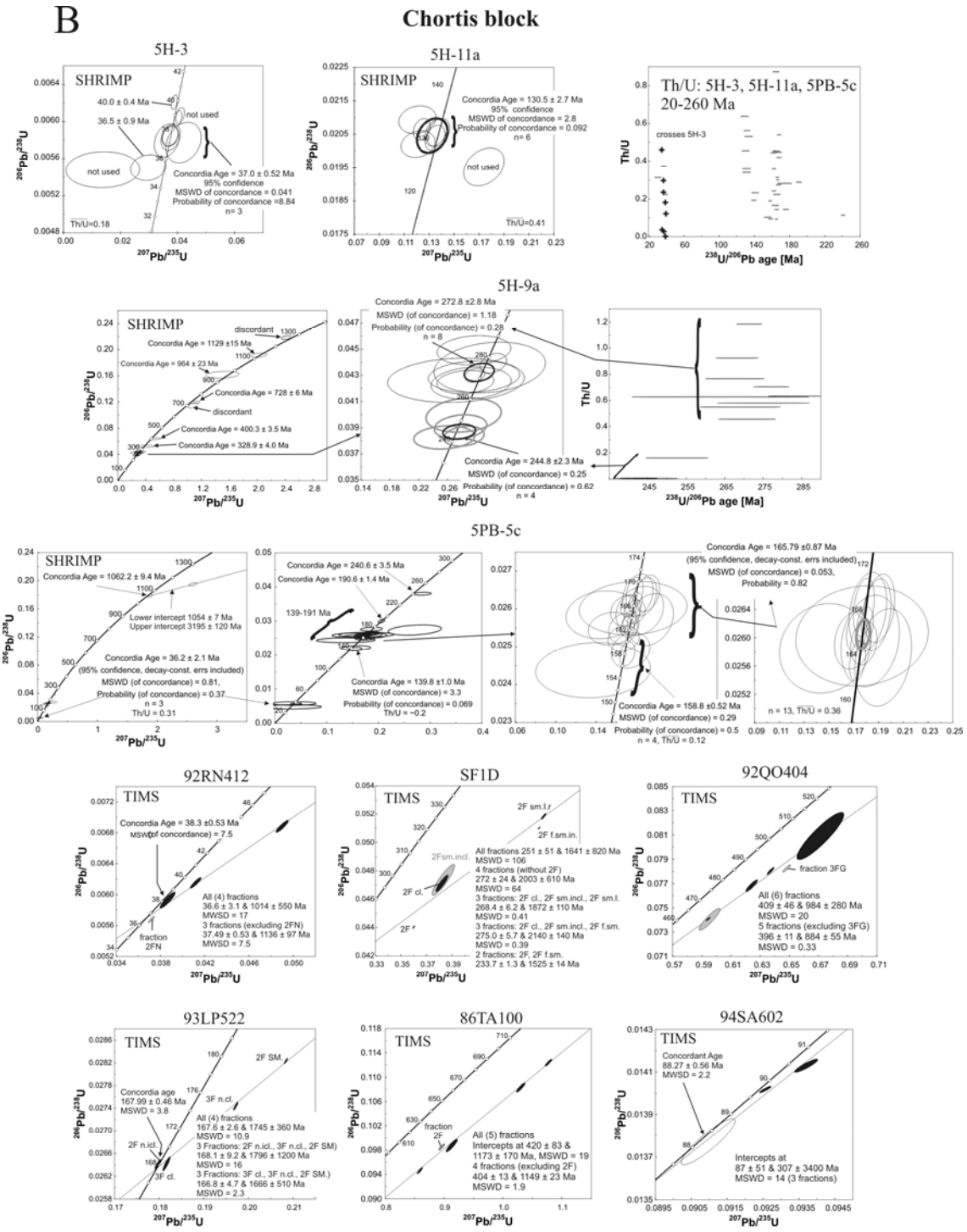

Figure 3. (continued) U/Pb zircon data and age interpretation. See Table 1 for sample location and Tables 2 and 3 for data listings. ID-TIMS results are shown with 2σ error ellipses and discordias are given as lines. SHRIMP results show 2σ error ellipses and are corrected for common Pb. Selected age groups are displayed as weighted average and relative probability diagrams (ages are 207-corrected). Data evaluation and plotting was supported by the program package of Ludwig (2003). MSWD, mean square weighted deviation. The upper intercept ages and ages older than early Paleozoic will be discussed elsewhere. (A) Data from the Chuacús complex of the Maya block. (B) Data from the Chortís block; all SHRIMP ages are from the northeastern edge of the Las Ovejas complex and granitoids intruding it. Th/U diagrams aid discrimination of metamorphic and magmatic zircon (rims).

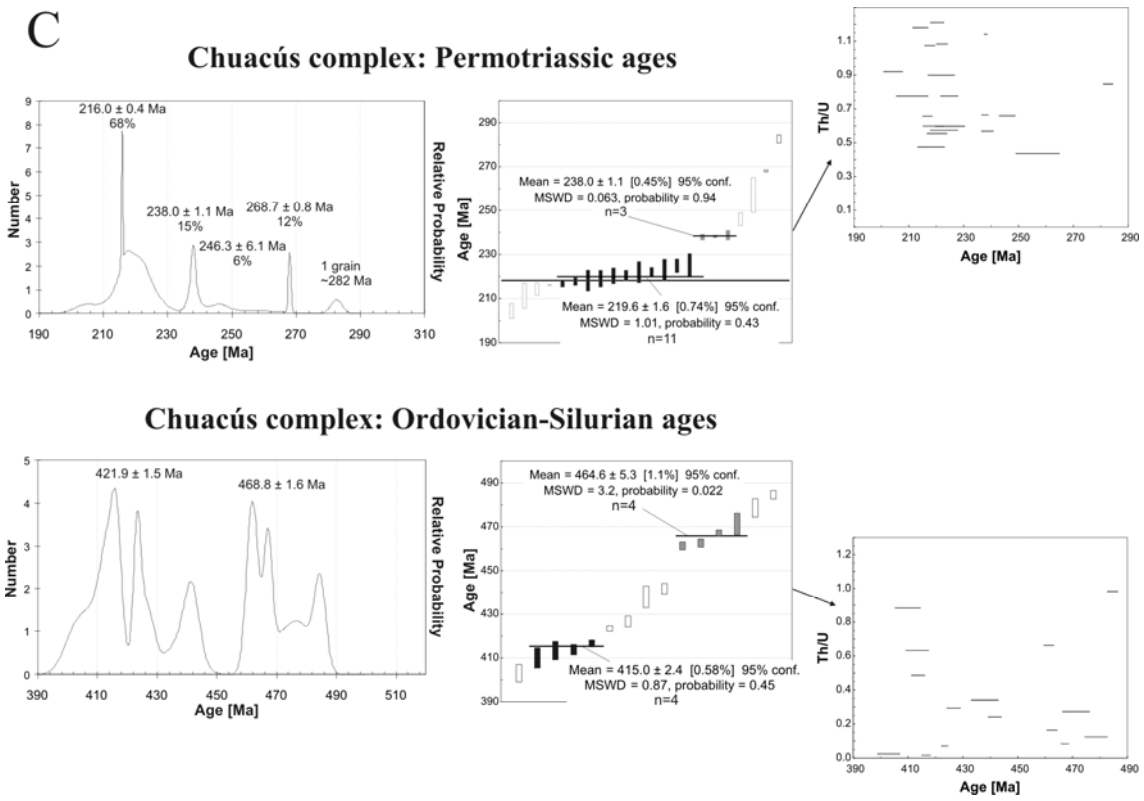

Figure 3. (continued) (C) Pooling of all SHRIMP ages from all samples for the Permotriassic and Ordovician-Silurian dates of the Chuacús complex (Maya block) and definition of ages groups. Left column: Relative probability and age groups defined by Isoplot's 'deconvolution of multiple age components' routine. Central column: Weighted average of 207-corrected ages; ages with filled error bars are included in the indicated mean, excluded data are interpreted as Pb loss, analysis of overlapping age domains, or a wide age range. Right column: Th/U diagrams.

average 0.64) likely crystallized from a magma (note difference in luminescence of 416 Ma and 257 Ma grains in Fig. 4). Our ages imply post-Early Triassic deposition for some parts of the Santa Rosa Group. Sample GM8s (stop G8; Fig. 3A) is Chuacús granite overprinted by greenschist-facies mylonitization from western Guatemala. Four zircon fractions with variable grain size and magnetic properties define lower and upper intercepts at 165.2 ± 5.4 Ma and ~990 Ma, respectively (ID-TIMS); one fraction is weakly reverse discordant and two fractions define a concordant age of 163.80 ± 0.38 Ma. CL images show oscillatory zoned rims around Proterozoic cores (Fig. 4) and oscillatory zoned coreless grains with marked changes in luminescence from center to rims; the ages of these grains are identical within error. Consequently, the Th/U ratios obtained from SHRIMP spots are variable and are with one exception >0.2, implying magmatic origin. The 207-corrected ages for a prominent group of 6 rims and coreless grains yield a weighted average of 171.0 ± 2.1 Ma. This likely dates granite emplacement. Sample 5CO-1 is two-mica, K-feldspar-porphyroblastic orthogneiss, mylonitized during low-T overprint, from the north-central Chuacús complex; it defines the 'Rabinal' granitoids in the area of San Miguel Chicaj. Rounded, often mottled, Proterozoic cores are surrounded by in general thin, structureless, often high-U rims that have

variable but magmatic Th/U ratios (mean 0.4) (Fig. 4). 207-corrected spot ages, mostly from rims but also from a few coreless grains with relatively flat CL response, range from 410 to 485 Ma (Fig. 3A). There may be two age groups with weighted average ages of 464.6 ± 5.3 Ma and 412.9 ± 3.7 Ma; Th/U ratios are similar. Sample 5CO-4b, high-P metamorphic (see below) garnet orthogneiss, comprises complex, mostly Proterozoic zircons. Grain shapes include both rounded and prismatic–idiomorphic. In general, low-U cores are surrounded by variable, higher-U rims that both have Proterozoic ages (1180–1017 Ma concordant spots; Fig. 3A). Spots that include the former grain portions and tiny, very luminescent low-U outer rims, irresolvable with the spot size

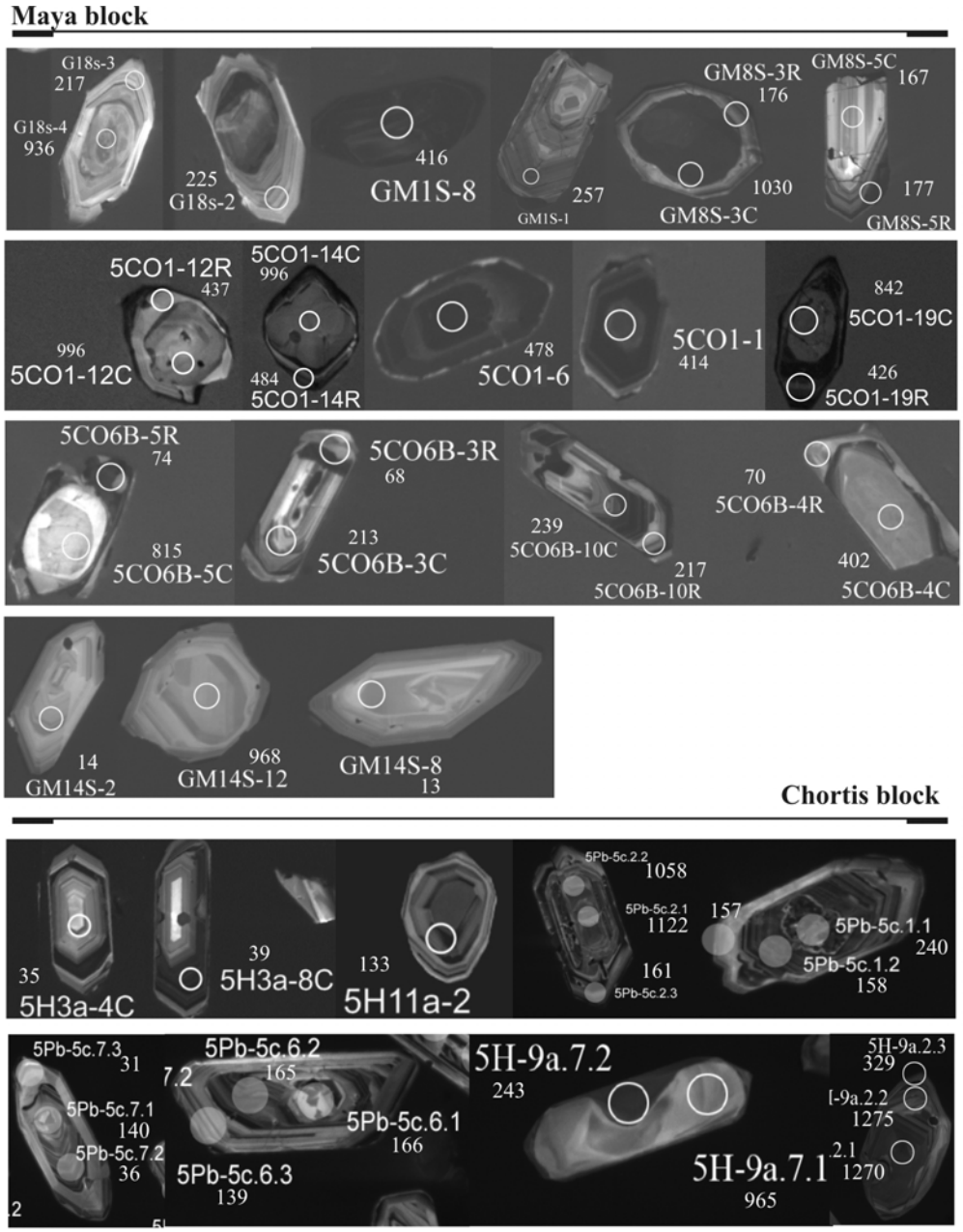

Figure 4. Cathodoluminescence images of typical zircons. Numbers give sample, spot, and spot age (in Ma, below or above the sample number).

we employed, yielded the youngest ages. The lower intercepts of discordia fitted to two groups of grains indicate crystallization at 638–477 Ma, predating the high-P metamorphic event. Sample 5CO-6b (south-central Chuacús complex, El Chol area), a two-mica orthogneiss, is intruded by very coarse-grained pegmatite and interlayered with paragneiss and garnet amphibolite; the latter contains relict eclogite (see petrology). All rock types are ductilely deformed. We analyzed the orthogneiss. The zircons are complex (Figs. 3A and 4): we detected a few well-rounded Proterozoic cores, one core that has flat CL response, low, likely metamorphic Th/U (0.020) and a 207-corrected age of 402.9 ± 4.0 Ma, and many oscillatory zoned grains with magmatic Th/U (on average 0.82); three of the latter spots give a concordia age of 238.0 ± 2.5 Ma, and 8 spots yield a well-defined group with a weighted average of 218.2 ± 2.3 Ma. Almost all grains have mostly thin (5-40 μm) overgrowths with flat CL response and low Th/U (on average 0.01) that span 89 to 69 Ma. The oldest grain has the highest Th/U and likely samples different age domains (core and rim). Selected omission of grains from the remaining group yields one statistically significant group of 6 grains with a weighted average age of 74.24 ± 0.52 Ma and 5 younger spots that may constitute a cluster at 70.3 ± 1.5 Ma; the latter group may be geologically meaningless, if it reflects progressive Pb loss of grains from the former group. Sample 5CO-6b is most straightforwardly interpreted as a Triassic magmatite that inherited Proterozoic and Early Paleozoic zircons and experienced high-T metamorphism during Late Cretaceous, likely contemporaneous with pegmatite injection; similar very coarse-grained pegmatites also yielded Late Cretaceous K/Ar (Ortega-Gutiérrez et al., 2004) and Rb/Sr white mica cooling ages (see below). The regional significance of magmatism is supported by Triassic hornblende and white-mica cooling ages from this region (238–225 Ma, Sutter referenced in Donnelly et al., 1990; see below). The high-P event is pre-Middle Triassic.

Samples GM13s (stop GM42) and GM14s (stop GM43) (Fig. 3A) are from western Guatemala. GM13s is Chuacús (?ortho)gneiss and GM14s ductilely undeformed granite intruding gneisses along the Polochic fault. Seven zircon fractions of GM13s with different magnetic properties and, in part, grain size yielded lower and upper intercepts at 20 ± 15 Ma and 941 ± 7.9 Ma, respectively. We analyzed 5 fractions of GM14s differing in grain size and magnetic properties; all are discordant and yield lower and upper intercepts at 21 ± 33 Ma and ~894 Ma. Phanerozoic spot ages of zircons from GM14s gave one concordia age at 425.5 ± 6.0 Ma and 14 spots with a 14.65 ± 0.42 Ma weighted average age. These ages demonstrate middle Miocene Central American arc magmatism.

Sample 5H-3 is syn-tectonic, syn-migmatitic, plagioclase-rich granite gneiss associated with migmatite, leucogranite, and gabbro–diorite; it is typical of the Las Ovejas complex and crops out at the western flank of the Ulúa graben in northwestern Honduras. 207-corrected spot ages on typically magmatic zircons (Fig. 3B, 4) range from 40.0 ± 0.4 Ma to 36.5 ± 0.9 Ma with

3 grains defining a concordia age at 37.0 ± 0.52 Ma. We interpret this age as the age of magmatism and deformation. Sample 5H-9a comprises orthogneiss and migmatite south of the Jocotán fault zone that are distinctly different in grain-size (coarse) and deformation (weak) from the gneisses and migmatites of the Las Ovejas complex along the MSZ. Besides Proterozoic ages there are concordant spot ages at 400.3 ± 3.5 Ma and 328.9 ± 4.0 Ma. There are two main age groups: 272.8 ± 2.8 Ma (8 spots) and 244.8 ± 2.3 Ma (4 spots). These groups have distinctly different Th/U ratios and CL-response (Figs. 3B and 4). The younger group, likely metamorphic, has mean Th/U at 0.04 and appear dark and unzoned in CL. The older group has mean Th/U of 0.7 and clear oscillatory zoning. We suggest Early Permian protolith crystallization and Early Triassic metamorphism. Sample 5H-11a is low-T, mylonitic orthogneiss (phyllonite), likely meta-rhyolite intercalated with paragneiss and marble; the sample is also from the Jocotán fault zone. Six out of seven 207-corrected spot ages yield a 130.5 ± 2.7 Ma concordia age (Fig. 3B); Th/U ratios are on average 0.41. We interpret this date as reflecting Early Cretaceous magmatism. Sample 5PB-5c is a small orthogneiss pod in massive migmatite that is enclosed in large granite in easternmost Guatemala; it is associated with garnet amphibolite (see petrology). Three spots define a 36.2 ± 2.1 Ma concordia age (Fig. 3B), likely the age of migmatization. One of the spots is from a relatively high-U, oscillatory zoned central grain portion that is surrounded by a rim poorer in U (Fig. 4); this rim is ~5 Ma (31.2 ± 1.2 Ma) younger. The major group of Phanerozoic ages spans 140–191 Ma with two, likely significant, age groups: 158.8 ± 0.52 Ma (n = 4) and 165.79 ± 0.87 Ma (n = 13); the consistently lower Th/U ratios (on average 0.12) of the former (the latter has on average 0.36) support the grouping. There are other Phanerozoic concordant spots at 139.8 ± 1.0 Ma (n = 2), 190.6 ± 1.4 Ma (n = 1), and 240.6 ± 3.5 Ma (n = 1). We suggest a Middle Jurassic granite protolith that inherited Proterozoic to Early Jurassic zircons. Sample 92RN412 is granitic gneiss surrounded by amphibolite-facies rocks from the Las Ovejas complex of northwestern Honduras; it is grossly the same rock as 5H-3. Rb/Sr and K/Ar biotite cooling ages are ~39 and ~36 Ma, respectively (Horne et al., 1976a, 1974). Three of four zircon fractions with different grain size and magnetic properties plot close to concordia, one fraction is concordant at 38.3 ± 0.53 Ma. All fractions define intercepts at 36.6 ± 3.1 Ma and ~1014 Ma (Fig. 3B), three are at 37.49 ± 0.53 Ma and ~1136 Ma. The ~38 Ma age is within error identical to sample 5H-3. The age constrains deformation within the eastern Las Ovejas complex to be younger than 39 Ma (see below). Sample 94SA602 is amphibolite within the metamorphic sequence that contains the granite gneiss of sample 92RN412; the protolith was probably gabbro. We obtained three zircon fractions that plot close to and on concordia, defining a lower intercept at 88 ± 51 Ma (Fig. 3B); the concordant fraction is at 88.27 ± 0.56 Ma, likely dating gabbro crystallization. Sample 93LP522 is granite south of the Jocotán–Chamelecón fault zone. Four zircon fractions define a lower intercept at 167.6 ± 2.6 Ma, on concordant fraction is at 167.99 ± 0.46 Ma (Fig. 3B); the ~168 Ma age is within error identical to sample 5PB-5c and

demonstrates Middle Jurassic magmatism in the Chortís block. Samples SF1D, 92QO404, and 86TA100 typify metamorphic rocks of the central Chortís block in central Honduras (Precambrian . SF1D is weakly deformed granite gneiss surrounded by Jurassic metasedimentary rocks of the Jurassic Agua Fria metamorphic rocks, but the contact relationships are unclear. All five fractions are discordant and lower intercept ages between 275 and 234 Ma can be defined (Fig. 3B). 92QO404 is porphyric granite surrounded by phyllite. Six fractions define intercepts at 405 ± 22 Ma and ~935 Ma (Fig. 3B). 86TA100 is augen schist with white mica, quartz, epidote, microcline, biotite, and garnet. 5 fractions define 481 ± 36 and 1315 ± 130 Ma (Fig. 3B). Besides Grenville inheritance, these samples support Ordovician–Silurian magmatism in the Chortís block.

Figure 3C pools all Permotriassic and Ordovician–Silurian ages of all samples from the Chuacús complex and illustrates our approach to identify age groups. Isoplot's 'deconvolution of multiple age components' routine defines groups displayed on relative probability diagrams; we consider only part of these groups significant and interpret them geologically in the discussion section. The age of the groups is interpretatively refined by calculating weighted averages using selected omission of grains from the total data. One rejection criteria assumes that the old ages are variably affected by overlap onto older regions of the same grain; another assumes that the youngest ages have had partial Pb loss. Our grouping is also guided by the Th/U values of the spots (Fig. 3C).

5.2. Ar/Ar and Rb/Sr geochronology

We analyzed the ages of deformation and metamorphic cooling of the Maya and Chortís block rocks by Ar/Ar and Rb/Sr analysis of syn- to post-tectonic minerals. We also dated cooling in pre- to post-tectonic plutons, again providing age limits for deformation. Sample G19s (stop G1, Fig. 5A) is weakly migmatitic western Chuacús gneiss retrogressed to hornblende–epidote schist during localized but high-strain, low-T (≥400°C) sinistral shear. Two sericite fractions of different grain size yielded nearly identical weighted mean ages (WMA). The pooled 67 ± 1 Ma age is interpreted to slightly post-date low-T plasticity in the shear zones. Sample G27s (stop G57, western Guatemala, Fig. 5A) is migmatitic Chuacús gneiss associated with amphibolite and shows low-T mylonitization along discrete sinistral shear zones; undeformed, likely Miocene (~15 Ma, see above) granite occurs in the vicinity. The age spectrum is complex and the ~37 Ma WMA may reflect partially reset Late Cretaceous–early Tertiary biotite.

Sample 5CO-4b is garnet gneiss associated with K-feldspar–porphyroblastic gneiss and schist from the north-central Chuacús complex; metamorphism evolved through a high-P stage and amphibolite– to epidote–amphibolite-facies retrogression (see below). Low-Si phengite and biotite are part of the recrystallized groundmass (≤510°C, ~0.7 GPa). The phengite spectrum is weakly

hump-shaped but the total-fusion (TFA), WMA, and isochron (IA) ages correspond within error at 67 ± 2 Ma; the biotite is ~3 Ma younger. A Rb/Sr phengite–plagioclase–whole rock isochron is within error of the Ar/Ar ages (Fig. 5B). Epidote–amphibolite-facies retrogression is thus Late Cretaceous. Sample G10s (stop G29) is from the southern Chuacús complex and comprises marble interlayered with garnet micaschist and gneiss just north of El Tambor Group serpentinites. The Ar/Ar age of coarse white mica in the marble overlaps a Rb/Sr biotite age (G11s) of nearby two-mica orthogneiss within error at ~67 Ma (Fig. 5B). Sample G12s (stop G31) is fine-grained, mylonitic orthogneiss (~1 Ga, unpublished U/Pb zircon) north of G10s. The grain size is due to dynamic recrystallization of quartz at the transition between subgrain rotation and grain-boundary migration (~425°C, e.g., Stipp et al., 2002). White mica is related to the recrystallization fabric, includes albite, and is cogenetic with a second generation of garnet and chlorite; the ubiquitous albite may be due to Na-rich fluid exchange between the Chuacús complex and the El Tambor Group rocks in the hanging wall. Mylonitization and fluid exchange occurred at or slightly after 70 ± 3 Ma (Ar/Ar white mica, Fig. 5B). Samples 5PB-13b and 5PB-14 typify rocks of the east-central Chuacús complex: 5PB-13b is coarse-grained garnet amphibolite associated with garnet micaschist metamorphosed at ~540°C and ~0.7 GPa (see below). 5PB-14 is hornblende–mica–chlorite schist with quartzitic layers formed at identical PT conditions. Quartz recrystallized dynamically by subgrain rotation and grain-boundary migration. The hornblende spectrum of 5PB-13b is complex with an age component older than 137 Ma; several steps are at 65 ± 6 Ma. The latter are within error of the Ar/Ar (5PB-14) and Rb/Sr (5PB-13b) white mica ages (Fig. 5B). As the closing temperatures for these systems are close to the peak-T conditions represented by the syn-kinematic minerals, deformation is dated at ≥65 Ma. Sample 5PB-9b is retrograde biotite–chlorite gneiss from ortho–paragneiss intercalations at the eastern end of the Chuacús-complex outcrop in the Sierra des Santa Cruz. Mylonitization is upper greenschist facies with basal <a> slip and grain-boundary migration recrystallization in quartz and coexisting fracturing and incipient recrystallization in feldspar. The Ar/Ar white mica spectrum is classic hump-shaped (52–62 Ma) indicating ^{40}Ar excess, the Rb/Sr white mica–whole rock isochron is at 76.5 ± 0.59 Ma (Fig. 5B). Samples 5CO-5a,b, 5CO-6b, 887C, and 885 are from the south-central Chuacús complex and typical for the garnet amphibolite–micaschist–biotite-(?ortho)gneiss–meta-pegmatite intercalations of this region. The pegmatites are variably deformed but massive stocks are weakly strained. All rocks share various stages of post-tectonic annealing. Garnet amphibolite 5CO-5a is retrogressed from ~600°C at ~1.4 GPa to ~560°C at 1.1 GPa. The phengite Ar-release spectrum is hump-shaped, indicating ^{40}Ar excess; a low low-T plateau is at 225 ± 5 Ma (Fig. 5B). Hornblende shows a classic loss-profile spectrum (~720 Ma to ~153 Ma). The 70.0 ± 1.5 Ma Ar/Ar white mica age from intercalated quartzofeldspatic paragneiss sample 887C expresses Late Cretaceous overprint, also highlighted by our U/Pb zircon geochronology (see above). Rb/Sr meta-pegmatite white mica ages are

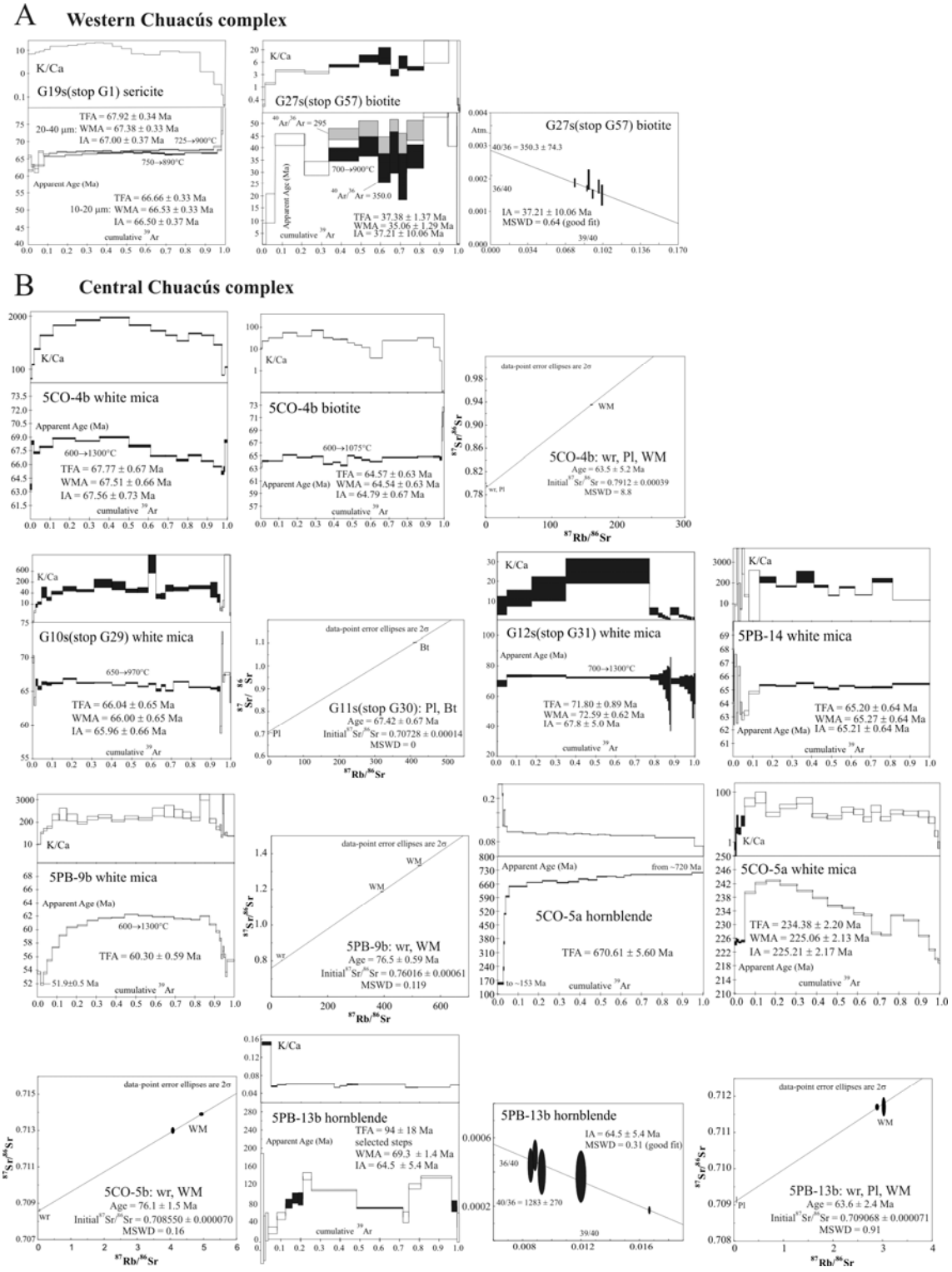

Figure 5. New $^{40}Ar/^{39}Ar$ spectra and Rb/Sr whole rock–feldspar–mica 'isochrons'. See Table 1 for sample locations and Tables 4 and 5 for age data and interpretations. Weighted mean ages (WMA) were calculated using black steps of the given temperature range; TFA, total fusion age; IA, isochron age. Uncertainties are ±1σ. 'Atm.' in the isochron diagrams is the $^{40}Ar/^{36}Ar$ ratio of the atmosphere (295.5). MSWD, mean square weighted deviation. Abbreviations: WR, whole rock; Pl, plagioclase; Kfs, K-feldspar; WM, white mica; Bt, biotite.

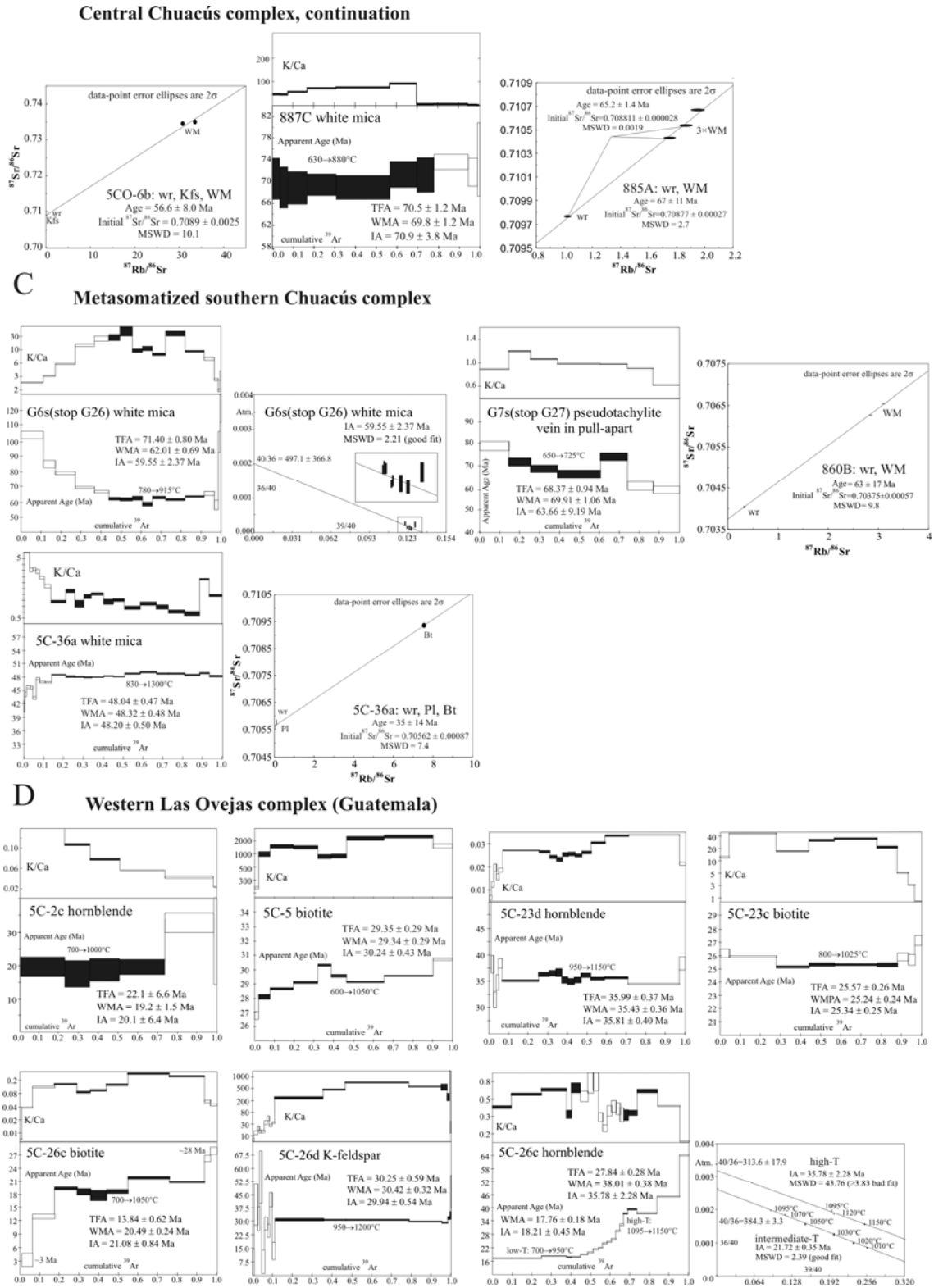

Figure 5. (continued)

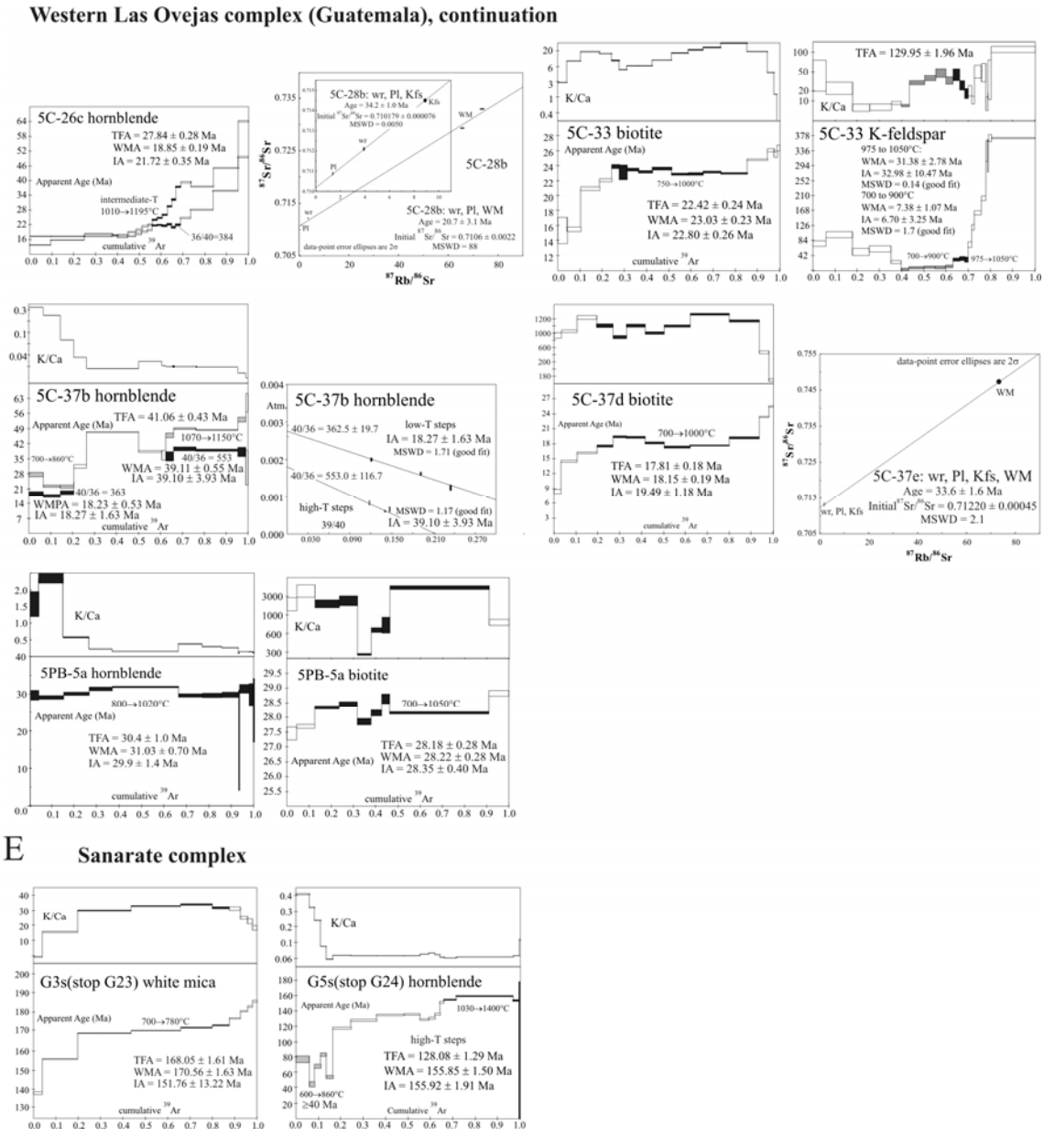

Figure 5. (continued)

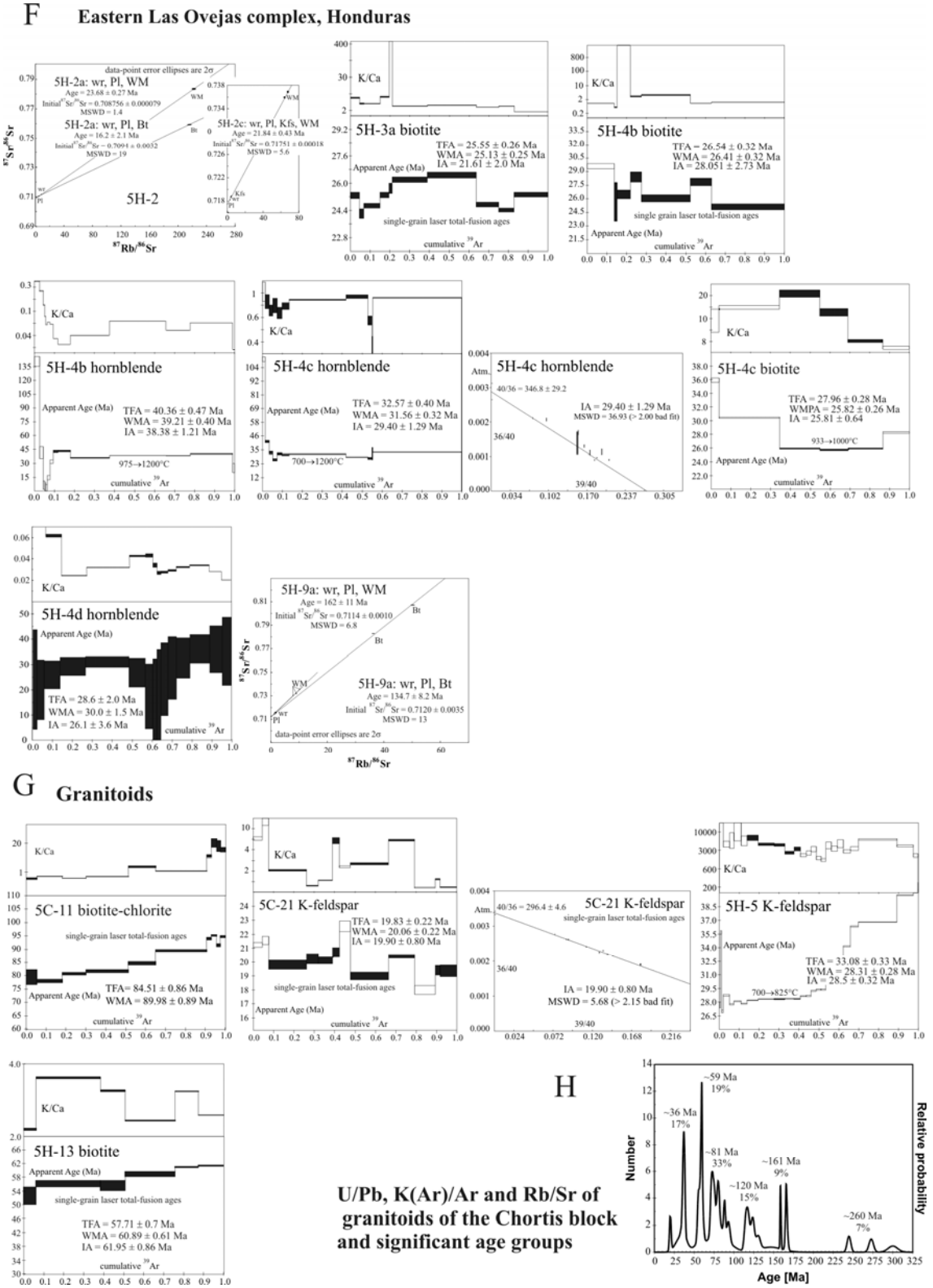

Figure 5. (continued)

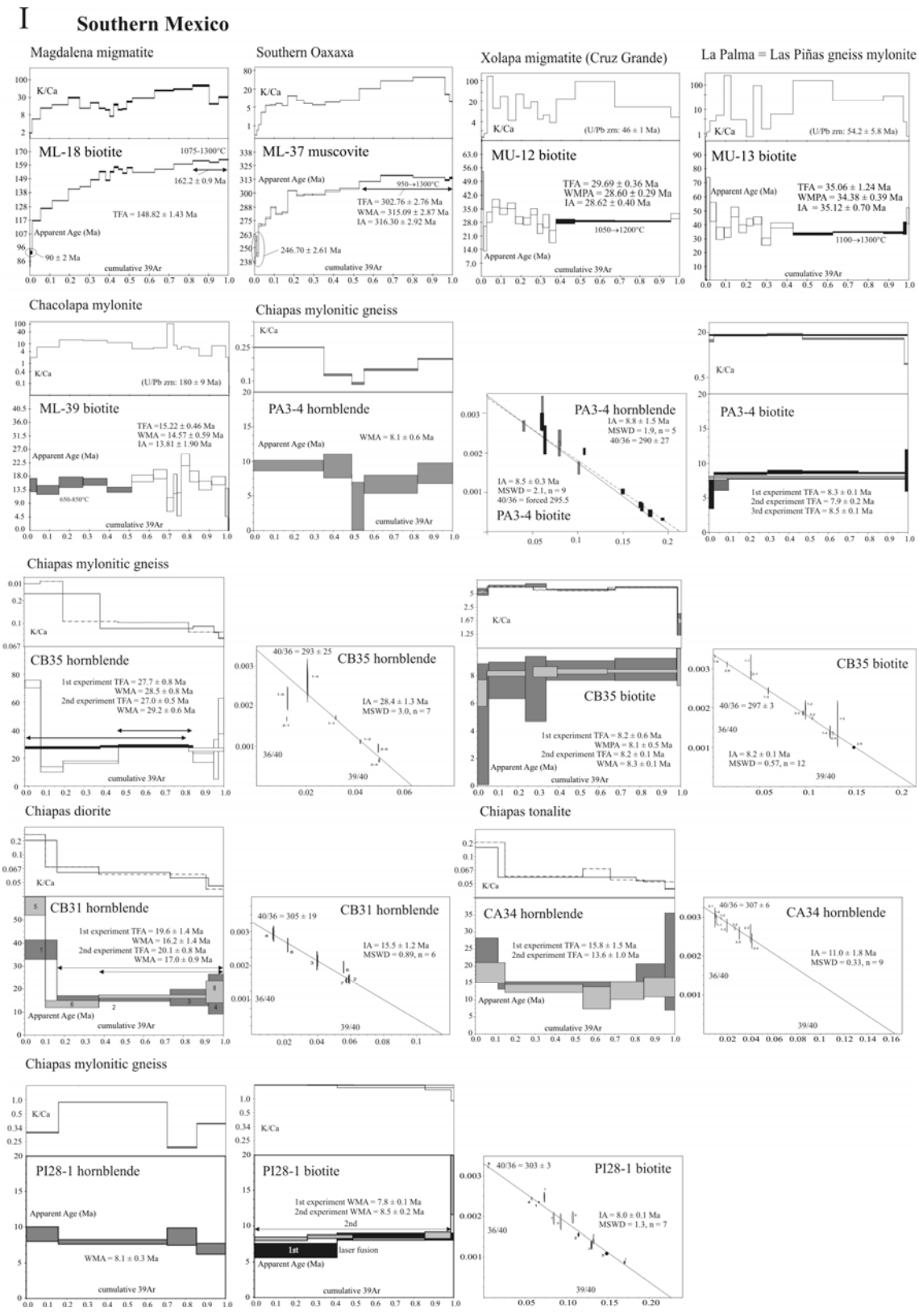

Figure 5. (continued)

at 76.1 ± 1.5 (5CO-5b), 57 ± 8 (5CO-6b), and 67 ± 11 Ma (885A, extremely coarse grained mica from the Guatemarmol mine west of Granados), demonstrating Late Cretaceous pegmatite emplacement; our ages confirm those from foliated meta-pegmatite (K/Ar 73–62 Ma) of Ortega-Gutiérrez et al. (2004). We interpret our ages as Triassic cooling during amphibolite-facies retrogression of relict eclogite and Cretaceous reheating associated with regional metamorphism and local magmatism.

Samples G6s, G7s, 860B, and 5C-36a (Fig. 5C) are Chuacús rocks immediately below the North El Tambor Group rocks. These localities show imbrication of basement (now retrograde phyllonite, chlorite phyllite, epidotized biotite gneiss, carbonate-bearing garnet–actinolite mica-schist), marble (San Lorenzo marble), serpentinite, and low-grade meta-siltstones (Jones Formation). They share a history of extreme fluid flow that resulted in strong retrogression, local carbonate and albite 'metasomatism' and post-tectonic garben formation, and locally intense quartz veining. White mica of G6s (station G26), retrogressed basement, has a U-shaped spectrum indicating ^{40}Ar excess with a flat-portion at 60 ± 5 Ma (Fig. 5C), comprising most of the released Ar. Retrograde biotite gneiss G7s (station G27) exhibits cm-sized pull-apart-type tension gashes locally filled with pseudotachylite that spectacularly dates brittle–ductile, sinistral transtension at ~70 Ma (Fig. 5C). 5C-36a shows coarse white mica from relict gneiss in overall fine-grained, locally biotite-rich phyllonite; its 48 ± 1 Ma Ar/Ar and the 35 ± 14 Ma Rb/Sr biotite ages are the youngest ages encountered in the Chuacús complex rocks and may reflect long-lasting fluid activity.

The following samples characterize metamorphism and deformation in the Las Ovejas unit und cooling of associated granitoids (Fig. 5D). Sample 5C-2c is partly mylonitic amphibolite intercalated with paragneiss and quartzite and crosscut by diabase dikes. Hornblende is clearly syn-kinematic to sinistral shear deformation and shows two high-T steps at >30 Ma and a low-T 'plateau' at 20 ± 2 Ma; we attribute little significance to these ages, as only few steps are available due to a furnace problem. Sample 5C-5 is phyllite faulted against Tertiary–Quaternary volcanic rocks along the Jocotán fault zone. Syn-kinematic biotite shows Ar-loss from ~31 Ma to ~26 Ma with a mid-T 'plateau' at 29 ± 2 Ma (Fig. 5D). This age indicates early Oligocene Jocotán fault activity, coeval with mylonitization in the Las Ovejas unit (see below). Samples 5C-23c,d comprise biotite gneiss and amphibolite in a unit of partly migmatitic gneiss, metagabbro, and granitic gneiss that is typical Las Ovejas complex lacking retrogression. Syn-kinematic, fibrous hornblende gives a WMA of 35.5 ± 1.0 Ma; biotite is at 23.3 ± 0.5 Ma and thus >10 Ma younger. Biotite of nearby 5C-33 gneiss depicts a loss profile from ~26 Ma to ~15 Ma with a mid-T 'plateau' at 23 ± 2 Ma, identical to biotite of 5C-23c. K-feldspar shows a loss profile from ~370 Ma to ~6 Ma; the low-T steps, forming a good-fit IA with atmospheric

$^{40}Ar/^{36}Ar$ at 7 ± 2 Ma, are difficult to interpret geologically. The high-T steps indicate cooling at 32 ± 4 Ma (Fig. 5D). Although from the vicinity of large post-tectonic granite, we interpret our 5C-23 and 5C-33 station ages to date amphibolite-facies metamorphism and associated migmatization; the minerals lack post-tectonic annealing and are in part syn-kinematic to sinistral strike-slip deformation. The amphibole ages closely approximate the age of deformation (~35 Ma); it remains unclear at these stations whether the late cooling through biotite closure (~23 Ma) may indicate long-lasting deformation, reactivation, or slow cooling. Samples 5C-26c,d comprise garnet amphibolite and garnet-bearing biotite gneiss of the lithologic unit described above; distinct rocks are migmatitic gneiss and garnet-bearing leucosome. 5C-26c hornblende is aligned in the foliation (low strain) and exhibits a loss profile from ~64 Ma to 17 Ma. Multiple-step degassing allowed deconvolution into sub-plateaus that were analyzed with isochrons (Fig. 5D). A low-T 'plateau' at 18 ± 2 Ma has approximately atmospheric $^{40}Ar/^{36}Ar$, an intermediate-T 'plateau' at 21 ± 2 Ma is non-atmospheric but exhibits a good-fit isochron, and a high-T 'plateau' at 36 ± 3 Ma is only weakly non-atmospheric. The intermediate and low-T 'plateaus' are within error of the 20 ± 2 Ma WMA for mid-T steps of a biotite–minor chlorite mixture; this biotite has a loss profile from ~28 Ma to ~3 Ma. The high-T steps of K-feldspar give 30 ± 1 Ma. Sample 5C-37b, again typical Las Ovejas complex of eastern Guatemala, is amphibolite associated with migmatitic biotite gneiss and meter-sized bodies of leucogranite. The hornblende spectrum is complex but contains a high-T 'plateau' with a WMA of 39 ± 3 Ma, calculated for a $^{40}Ar/^{36}Ar$ of 553, and a low-T 'plateau' with a WMA of 18 ± 3 Ma, calculated for a $^{40}Ar/^{36}Ar$ of 362; the K/Ca ratios of the latter suggests a contribution of gas released from biotite micro-inclusions. 5C-37d biotite reveals Ar loss ~26 to ~9 Ma and a mid-T 'plateau' at 19 ± 2 Ma. The leucogranite gives a white mica–K-feldspar–plagioclase–whole rock Rb/Sr isochron of 33.6 ± 1.6 Ma. Located in the far-field of the large granitoids that were mapped crosscutting the Las Ovejas complex, stations 5C-26 and 5C-37 typify cooling from amphibolite-facies metamorphism at ~37 Ma and, possibly, relatively slow cooling throughout the Oligocene–Miocene. The Rb/Sr leucogranite white mica age supports the field observation that these small melt bodies are cogenetic with late Eocene metamorphism and migmatization. Sample 5C-28b is pegmatite gneiss crosscutting typical Las Ovejas biotite gneiss; its Rb/Sr whole rock–plagioclase–K-feldspar isochron is at 34.2 ± 1.0 Ma and a whole-rock–plagioclase–white mica isochron at ~21 Ma. Sample 5PB-5a is weakly deformed garnet amphibolite associated with massive migmatite and small orthogneiss bodies and represents a huge xenolith in granite. Peak-PT estimates using core-sections of minerals such as garnet that lack deformation are ~630°C at 0.7 GPa (see petrology); the analyzed hornblende (WMA of 30 ± 2 Ma) and biotite (WMA at 28.2 ± 0.4 Ma) are syn-kinematic matrix minerals that date deformation and rapid cooling during weak, still amphibolite-facies retrograde overprint, also detected in the garnet rims; peak-T conditions are at ~36 Ma (U/Pb zircon, see above).

Samples G3s and G5s (stops G23 and G24; Fig. 5E) are phyllite and quartz-bearing amphibolite from the Sanarate complex, respectively. Quartz shows low-T plasticity with grain-growth inhibition and some post-tectonic annealing; together with hornblende and white mica it is syn-kinematic in discrete mylonite zones. The white mica spectrum of G3s shows Ar-loss from ~195 Ma to ~137 Ma with a mid-T 'plateau' at 155 ± 10 Ma, and G5s hornblende from ~157 Ma to ~40 Ma; a high-T 'plateau' is at 156 ± 5 Ma and low-T steps at ≥40 Ma. We interpret these data as indicating Middle–Late Jurassic deformation and Tertiary reactivation.

The next sample group comprises Las Ovejas complex of northern Honduras and structurally the footwall block of the Ulúa graben (Figs. 1B, 5F); our dating aimed establishing potential along-strike changes in deformation/metamorphism/magmatism and Ulúa-graben formation. Sample 5H-2a is post-tectonic, weakly deformed garnet–white mica-bearing pegmatite in migmatitic biotite gneiss and rare leucogranite sills, and 5H-2c is a more strongly deformed, finer-grained variety of the pegmatite (augen gneiss); these magmatites are outcrop-scale intrusives. The coarse white mica of 5H-2a is at 23.68 ± 0.27 Ma (Rb/Sr whole rock–plagioclase–white mica) and provides a younger bound for the intrusion of the pegmatite protolith. The white mica–K-feldspar–plagioclase–whole rock isochron of 5H-2c is ~2 Ma younger (Fig. 5F), likely reflecting the higher strain. Sample 5H-3a is small, weakly deformed but syn-tectonic granite in strongly migmatitic biotite gneiss; the 22 ± 4 Ma IA of 10 biotite crystals analyzed by single-grain laser fusion is >10 Ma younger than the intrusion age of the granite (~37 Ma, U/Pb zircon, see above). Nearby station 5H-4 typifies the heterogeneous lithology of the Las Ovejas complex in this area. Sample 5H-4b is biotite and hornblende-bearing pegmatite at the rim of a small, weakly deformed leucogranite body; all magmatites at this locality are deformed and in several cases the strain is concentrated in leucocratic dikes. The 38 ± 2 Ma hornblende is identical to the age of the concordant zircon fraction of nearby granite gneiss 92RN412 (see above), biotite is >10 Ma younger at 25 ± 3 Ma (laser single-grain ages). Sample 5H-4c shows syn-kinematic hornblende and biotite from a sinistral transtensive, greenschist-facies shear zone in amphibolite: hornblende is at 30 ± 2 Ma, biotite show a 25 ± 2 Ma mid-T 'plateau' (Fig. 5F); these ages best date formation of the Ulúa graben (see also below). Large hornblende crystals of sample 5H-4d, the weakly deformed host amphibolite to the above shear zone, contain small hornblende crystals and are within error (29 ± 3 Ma) of the syn-kinematic amphiboles. Sample 5H-9a, orthogneiss and migmatite that yielded Permotriassic U/Pb zircon ages (see above) and are distinctly different from the Las Ovejas complex rocks, gives Rb/Sr whole rock–plagioclase–white mica and biotite isochrons of ~162 and ~135 Ma, respectively. These dates have two possible interpretations: either they reflect very slow cooling from the Permotriassic metamorphic/magmatic event or Middle Jurassic reheating not reflected in the zircon geochronology in this sample but detected in the Las Ovejas complex of Guatemala and in the central

Chortís block of Honduras. We prefer the latter interpretation, as we consider extremely slow cooling unlikely in the active tectonic setting of early Mesozoic northern Central America.

We dated cooling in a few of the mostly undeformed granitoids of the northern Chortís block (Fig. 5G). Sample 5C-11, granodiorite of the Chiquimula batholith, shows biotite partly altered to chlorite; 10 grains dated by laser fusion give a 90 ± 10 Ma WMA. Eight out of 12 K-feldspar grains of sample 5C-21, sub-volcanic granite also from the Chiquimula batholith, have a 20 ± 1 Ma laser-fusion WMA; this demonstrates a composite nature of this batholith. K-feldspar of sample 5H-5, granite from the rift flank of the Ulúa graben, shows Ar loss from ~37 Ma to ~28 Ma; the low-T 'plateau' at 28.3 ± 0.5 Ma indicates rapid cooling (Fig. 5G). In line with the syn-kinematic hornblende and biotite ages reported from this area (see above), this age suggests initiation of formation of the Ulúa graben at 28 ± 3 Ma. Six biotite grains of sample 5H-13, granite from south of the Las Ovejas unit, gave a laser-fusion age of 59 ± 3 Ma. The lack of modern U/Pb geochronology still impedes clear age assignments of plutonic events in the Chortís block. Due to the often sub-volcanic nature of these granitoids, we assume that the available geochronologic data reflect, to first-order, these events. Figure 5H pools all granitoid data and gives first-order groupings: there is significant magmatism at ~36 Ma starting ≥40 Ma, at ~59 Ma, and less significant at ~81 Ma, ~120 Ma, ~161 Ma, and ~260 Ma.

For correlative purposes (see discussion), we analyzed a few samples from southern Mexico with the Ar/Ar method (Fig. 5I). Sample ML-18 is Magdalena migmatite of the eastern Acatlán complex (Figs. 1C and 2G). Biotite shows Ar loss from ~163 to ~88 Ma; a low-T 'plateau' is at 90 ± 2 Ma, a high-T 'plateau' at 162 ± 2 Ma; the latter traces cooling from migmatization and San Miguel dike intrusion (175–171 Ma U/Pb ages; e.g., Keppie et al., 2004; Talavera-Mendoza et al., 2005). White mica from sample ML-37, mylonitic gneiss of the southernmost Oaxaca complex (Fig. 1C), shows Ar loss from a high-T 'plateau' at 315 ± 3 Ma to a low-T 'plateau' at 247 ± 3 Ma; the latter corresponds to ages of Permotriassic arc magmatism/metamorphism, exemplified by the Chiapas massif of southeastern Mexico (e.g., Weber et al., 2006a). Biotite from sample MU-12, migmatitic gneiss at Cruz Grande (Xolapa complex, Fig. 1C) yielded 29 ± 1 Ma (WMA), in line with cooling from widespread ~35–30 Ma Xolapa plutonism (Herrmann et al., 1994; Ducea et al., 2004a). Sample MU-13 is Las Piñas mylonitic orthogneiss, sampled east of La Palma, which forms the structural top of the Xolapa complex. Solari et al. (2007) reported a 54.2 ± 5.8 Ma intrusion age (U/Pb zircon), and 50.5 ± 1.2 Ma and 45.3 ± 1.9 Ma cooling ages (K/Ar and Rb/Sr biotite, respectively) from a moderately deformed variety. Our sample was specifically taken to date low-T, high-strain mylonitic flow (~300°C) along the Tierra Colorada (Riller et al., 1992) or La Venta (Solari et al., 2007) top-to-NW, sinistral-transtensional shear zone; syn-kinematic biotite is at 35 ± 1 Ma. Sample ML-39, mylonitic gneiss at Pochutla, is from a narrow, late-stage shear zone in the regional Chacolapa shear zone

along the northern edge of the eastern Xolapa complex; its major sinistral strike-slip stage is constrained at 29–24 Ma (Tolson, 2005; Nieto-Samaniego et al., 2006). Our 15 ± 2 Ma biotite age suggests reactivation, also indicated by faulting in the 29 ± 1 Ma, post-mylonitic Pochutla granite (Herrmann et al., 1994; Meschede et al., 1996).

Samples PA3-4, PI28-1, CB31, CB35, and CA34 are from the Chiapas massif of southeastern Mexico (Figs. 1C and 5I). A belt of small plutons along the southwestern margin of the massif is associated with metamorphic rocks that are partly mylonitized and faulted along a NW-trending, >100 km long zone named Tonala shear zone by Wawrzyniec et al. (2005). The late ductile and brittle kinematics is sinistral strike-slip, overprinting an older, higher-T fabric; the zone likely connects to similar sinistral strike-slip fabrics and plutons along the Polochic fault (Fig. 1C; see below). Our goal was to obtain ages for the intrusions and sinistral shear. Hornblende of diorite CB31 and tonalite CA34 yielded 15.5 ± 1.5 Ma and 11 ± 2 Ma, respectively; the former and latter are similar to 14.65 ± 0.42 granite GM14c along the Polochic fault zone of westernmost Guatemala (see above) and a 10.3 ± 0.3 Ma, pervasively sheared pluton (U/Pb zircon, Wawrzyniec et al., 2005) of the Tonala shear zone, respectively. Hornblende and biotite from three mylonitic gneisses (PA3-4, CA35, PI28-1) gave within error identical ages at ~8.2 Ma, interpreted to date sinistral shear deformation. One hornblende age (PA3-4) at 28.5 ± 1.5 Ma may be interpreted as approximating the age of the higher-T flow/metamorphism, in line with Oligocene deformation ages along the northern margin of the Xolapa complex (see above).

5.3. Fission-track thermochronology

Our TFT and AFT thermochronology is only reconnaissance in nature. The two TFT ages support available Ar/Ar and Rb/Sr geochronology, being close to biotite cooling ages. The AFT ages from Guatemala and Honduras show positive age–versus–elevation correlations both in the central Maya block and the central and eastern parts of the northern Chortís block (Fig. 6A); exhumation rates, if significant, are similar and slow for Maya and Chortís blocks (~0.038 and 0.035 mm/a, respectively), and possibly slightly more rapid along the western Ulúa-graben flank (~0.046 mm/a). The Chuacús-complex ages depict a cluster at ~30 Ma, low elevation ages from the Las Ovejas complex at ~12 Ma (Fig. 6A). Despite high elevation, the youngest ages of the Chuacús complex occur in western Guatemala along the Polochic fault in a small, ~15 Ma granite body and the mylonitic augengneiss it intrudes (samples GM13s, GM14s, Fig. 7A). The ~2 Ma age difference between crystallization and cooling through ~100°C of the granite reflects quenching at high crustal levels. The ~11.5 Ma TFT and the ~4.8 Ma AFT ages from low-T mylonite approximate the age of ductile–brittle to brittle Polochic faulting. The outcrop conditions prevent assessment of whether the apparently undeformed granite is locally affected by mylonitization but both mylonite and granite show E-trending, sinistral faults. The oldest ages at high

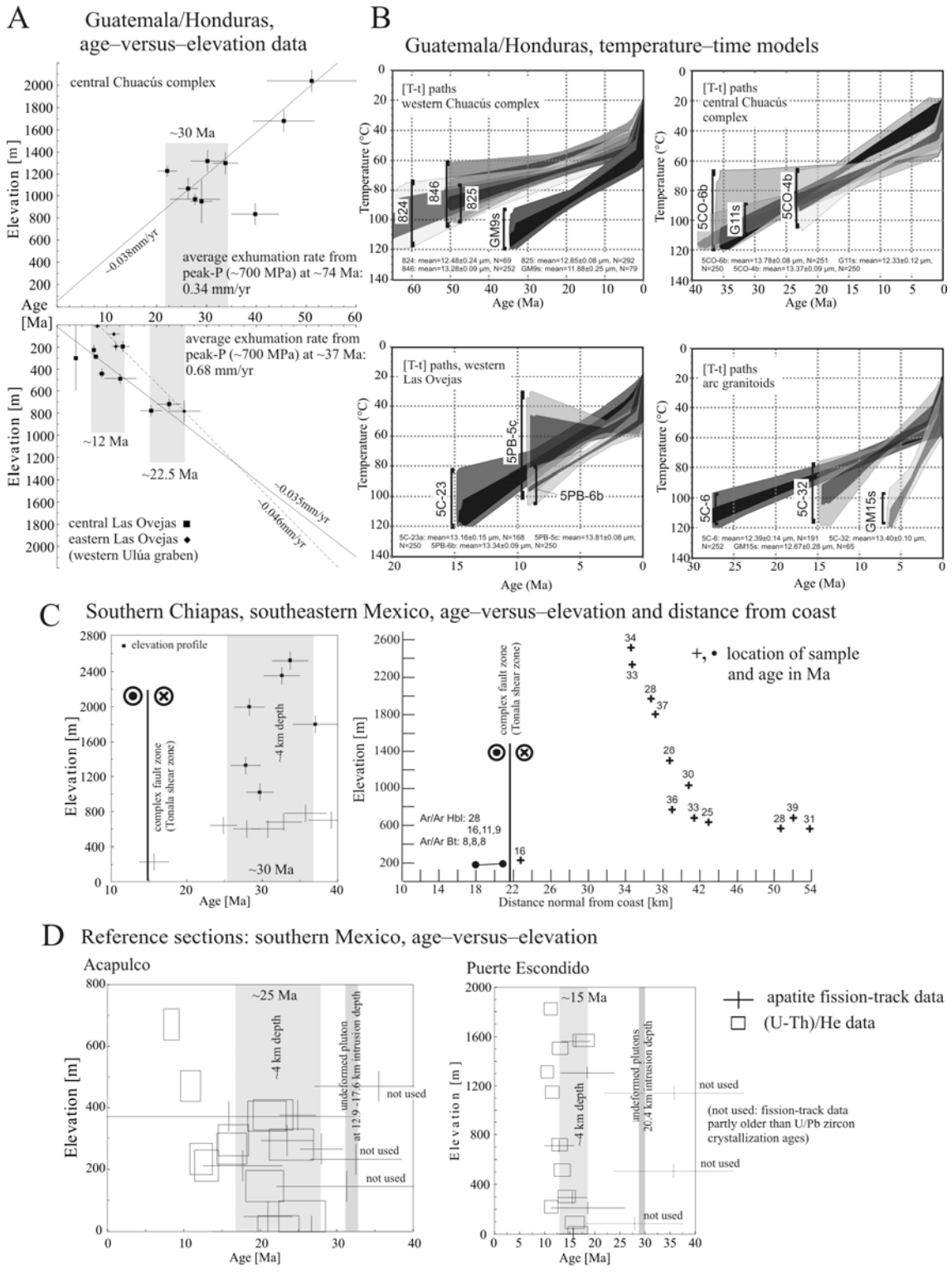

Figure 6. Low-temperature thermochronology data. (A) Apatite fission-track (AFT) age–versus–elevation plots for the central Chuacús complex (top) and the Las Ovejas complex and granitoids. Locations and fission-track parameters are given in Tables 6 and 7. (B) AFT temperature–time (T-t) paths for rocks of the Chuacús (western and central area) and Las Ovejas (western area) complexes and three arc granitoids; the latter are: 5C-6, Chiquimula batholith in the Las Ovejas complex; 5C-32, small granite east of the Chiquimula batholith; GM15s, augengneiss of the westernmost Chuacús complex overprinted by ~15 Ma granite. Good-fit solutions (all T-t paths with a merit function value of at least 0.5, Ketcham et al., 2000) are dark grey or black; acceptable-fit solutions (all T-t paths with a merit-function

elevation in the Chortís block cluster at ~22.5 Ma. The trend in the northern Chortís block for AFT ages to become younger toward major fault zones (Motagua fault, Ulúa graben), with ages as young as 7.8–3.8 Ma, (Figs. 6A and 7A), may be apparent, as these samples also occupy the lowest elevations and thus are certainly also an expression of the age–versus–elevation trend. The presence of these ages at low elevations along the Motagua fault suggests that its current activity (e.g., M7.5 1976 Guatemala earthquake, incorporating strike-slip and normal components; Plafker, 1976) extended at least into the latest Miocene–Pliocene.

The track-length distributions of our samples are unimodal, narrow, and symmetric. Modeled T-t paths give monotonous continuous-cooling type solutions (Fig. 6B). All of our T-t models (except the ~15 Ma granite from western Guatemala, see above) show a phase of rapid cooling in the last few Myr that is an artifact caused by annealing at ambient temperatures acting over geologic time. Low-T track-length reduction has been described for fossil tracks in age standards (e.g., Donelick et al., 1990) and borehole samples (Jonckheere and Wagner, 2000). This reduction is not incorporated into the annealing equations derived from laboratory experiments on induced fission tracks, which account for annealing processes that take place within the partial annealing zone (Jonckheere, 2003a, b).

Our samples from the Chiapas massif comprise a ≥1.5 km elevation profile (Fig. 6C) and two swaths separated by <40 km with little elevation difference; no apparent major fault separates these samples. The youngest sample is at ~15.7 Ma, close to the Tonala shear zone and the ~11 Ma tonalite (Fig. 6C); it is most likely thermally influenced, supporting the Miocene magmatism and deformation along this shear zone. The remaining samples range from ~25 to ~39 Ma without a clear age–versus–elevation trend and a weighted average age of 30.4 ± 2.5 Ma; we suggest that these samples indicate relatively rapid cooling at ~30 Ma.

---

value of at least 0.05) are light grey. (C) AFT age–versus–elevation plot and elevation–age–distance from the coast diagram for a vertical profile and regional samples of the south-central Chiapas massif, southern Mexico. The Tonala shear zone, associated granitoids, metamorphic rocks, and mylonites, and their ages (in Ma) are indicated (Hbl, hornblende; Bt, biotite); note their influence on one AFT sample. (D) AFT and apatite (U-Th)/He data for two coast-normal sections in southern Mexico from Ducea et al. (2004b) plotted in age–versus-elevation diagrams; these data are reference sections for our own data and are discussed in the text. Dark grey vertical bars give age range (U/Pb zircon) and intrusion depth of granitoids from about the same area as the thermochronology data. Light grey bars give interpreted closure through 70–100°C or ~4 km depth.

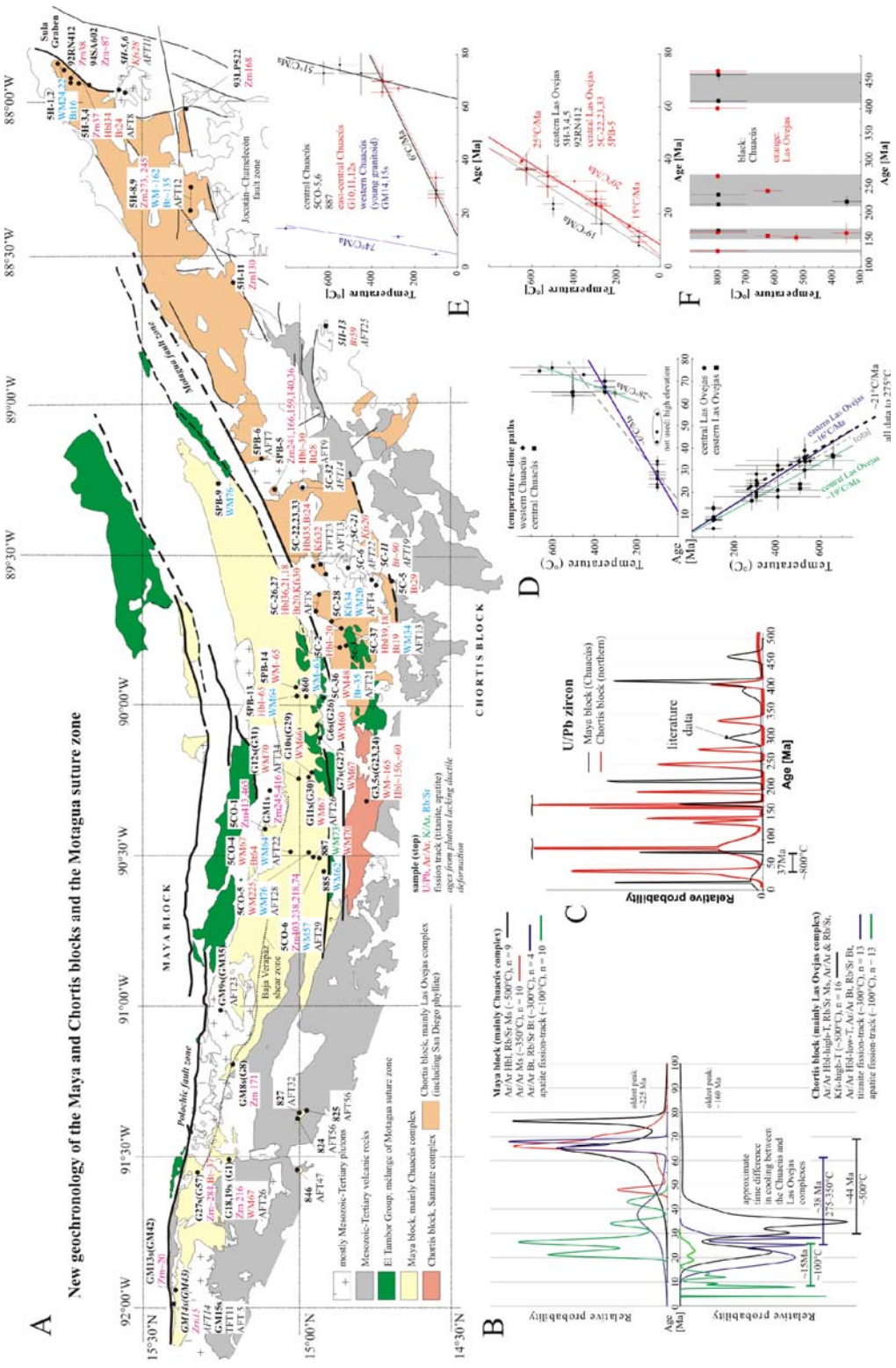

Figure 7. (A) Major geologic units of the Motagua suture zone, distribution of Paleozoic–Cenozoic igneous rocks and new geochronologic ages. Abbreviations: Zrn, zircon; WM, white mica; Bt, biotite; Hbl, hornblende; Kfs, potassium-feldspar; TFT, titanite fission-track; AFT, apatite fission-track. Numbers in italic denote undeformed granitoids. (B) Definition of mineral cooling and (C) zircon crystallization-age groups in relative probability plots, (D) Temperature–time diagrams of all data and (E) selected localities/samples (closing temperatures see text). (F) Single sample temperature–time diagrams illustrating age groups common in the Chuacús complex (Maya block) and the Las Ovejas complex (Chortis block).

5.4. Interpretation of new geochronology

Our U/Pb zircon geochronology outlines Early Paleozoic–Late Cenozoic high-T metamorphism and magmatism (Figs. 3 and 7C). In the Chuacús complex, we resolved prolonged Ordovician–Silurian (~410–485 Ma, age groups at 415 and 465 Ma), Permotriassic (~215–270 Ma, age groups at 238 and 220 Ma) and Middle Jurassic (~163–177 Ma, age group at 171 Ma) events; these are partly supported by Ar/Ar cooling ages (~225–238 Ma) and reflect magmatism (Fig. 3A). The U/Pb data also demonstrate metamorphic zircon growth at ~70–78 Ma (Th/U<0.03, age group at 74 Ma; Fig. 3A) about coeval with pegmatite emplacement at ~74 Ma (Rb/Sr and K/Ar on very coarse-grained white-mica). Miocene (~15 Ma) granite intruded into shallow crustal levels (nearly identical AFT age) in the western Chuacús complex. Both in the Las Ovejas complex and the central Chortís block, we resolved Early Permian (~264–283 Ma, age group at 273 Ma) magmatism followed by Early Triassic (~242–253 Ma, age group at 245 Ma) high-grade metamorphism that is also reflected by a K/Ar biotite cooling age (222 ± 8 Ma; MMAJ, 1980) and Middle to Late Jurassic (~140–191 Ma, age groups at 159 and 166 Ma) magmatism and subsequent cooling (Rb/Sr and Ar/Ar ages at ~155 Ma). Overwhelmingly, the northern margin of the Las Ovejas complex is dominated by Late Eocene high-grade metamorphism, migmatization, and plutonism at 40–35 Ma (age group at 37 Ma). Cooling ages related to this event also come from Roatán Island (~36 Ma Ar/Ar hornblende; see above). Our geochronology also supports an Ordovician–Silurian event in the Chortís block. Based on U/Pb zircon geochronology, the Maya and Chortís blocks share Ordovician to Jurassic events (Fig. 7F; the evident Proterozoic similarity is not addressed here). At least the northern and central Chortís block is distinctly different from the Maya block in the Late Cretaceous and early Tertiary.

The most striking, first-order result showcased by our Ar/Ar and Rb/Sr geochronology is the clear-cut separation of the southern Maya and northern Chortís blocks reflected in all cooling ages (Figs. 7A and B): the Chuacús complex, rimmed by the Polochic and the Motagua fault zones, cooled through ~500°C and through 275–350°C ~40 Myr earlier than the Las Ovejas complex south of the Motagua fault zone; cooling through ~100°C occurred ~15 Myr earlier in the Chuacús than the Las Ovejas complex. Obviously, the sampled block margins experienced distinctly different thermal evolutions during the Late Cretaceous and Tertiary: the Chuacús complex was heated to high amphibolite-facies metamorphism (see below) and cooled relatively rapidly (~28°C/Myr) to upper crustal temperatures during the Late Cretaceous (Fig. 7D); subsequently, cooling (~6°C/Myr) and exhumation was apparently slow (~0.038mm/a; see Figs. 6A and 7D). Multi-mineral T-t paths from central and east-central Chuacús samples (Fig. 7E) support this two-stage history. The Las Ovejas complex lacks Cretaceous regional metamorphism; its cooling from ≥40 Ma appears steady-state at ~16°C/Myr (Fig. 7D and E). Our geochronology does not prove whether slow cooling actually occurred, thus potentially reflecting long-term

strike-slip deformation, or represents deformation and cooling at 40–35 Ma and reactivation at 25–18 Ma. As we found clear syn-kinematic mineral growth defining both age groups (see below), we favor the latter scenario. Along the southern margin of the Chiapas massif, U/Pb and Ar/Ar geochronology demonstrates Tertiary plutonism (~29, ~16, ~11 Ma) and sinistral strike-slip at ~8 Ma along the Tonala shear zone.

Most AFT ages within the Chuacús complex of the southern Maya block group around ~30 Ma and thus correspond to the ~30 Ma age cluster in the Chiapas massif. We suggest that these ages indicate a thermal disturbance at ≥30 Ma induced by Tertiary arc magmatism and sinistral displacement between the Maya and Chortís blocks along and across this arc (see below). The young TFT and AFT ages along the Polochic fault zone relate its sinistral strike-slip deformation to the Late Miocene–Recent deformation along the Tonala shear zone, thus supporting their connection (Fig. 1C). These ages also support Burkart's (1983) estimate of major displacement (~130 km) along the Polochic fault between 10 and 3 Ma. The presence of very young AFT ages along the Motagua fault zone extends its neotectonic activity into the latest Miocene–Pliocene. The cluster of AFT ages at ~22.5 Ma in the northern Chortís block likely reflects continuation of the cooling from Late Eocene–Early Oligocene magmatism and metamorphism; the ~12 Ma cluster is attributed to a thermal event that is connected with the flare-up of magmatism (ignimbrite event) along Central America (see below).

Taking the peak-P conditions of ~0.7 GPa (see petrology below) reached in the Chuacús and Las Ovejas complexes during their Cretaceous (Chuacús, ~75 Ma) and Tertiary (Las Ovejas, ~40 Ma) metamorphism, it appears that (i) early average exhumation rates were at least one order of magnitude more rapid than those derived from the AFT age–versus–elevation relationship (Fig. 6A); (ii) the presence of AFT ages at high elevations, which approach those of the Ar/Ar and Rb/Sr biotite geochronometers, suggest that the change from relatively rapid to relatively slow rates occurred relatively early in the exhumation process (~60 Ma in the Chuacús complex; ~20 Ma in the Las Ovejas complex). The fact that the late-stage exhumation rates (AFT age–versus–elevation data) are grossly similar in the Chuacús and Las Ovejas complexes suggests, given the strongly different cooling rates, much hotter crust in the Las Ovejas complex.

The difference between the southern Maya and northern Chortís blocks during the Cretaceous–Tertiary is emphasized by the distinctly different P-T-d-t conditions encountered in the North and South El Tambor Group allochtons (Harlow et al., 2004; Tsujimori et al., 2004): extremely low-T lawsonite eclogites experienced blueschist-facies retrogression at ~120 Ma south of the Motagua fault, whereas higher-T zoisite eclogites show blueschist-facies retrogression at ~76 Ma north of the fault. These P-T-d-t conditions illustrate differences in tectonic evolution

and time of the emplacement of these subduction–accretion complexes. Significantly however, in the high-P/low-T case, the region south of the Motagua fault zone cooled earlier and cooling in the North El Tambor Group is coeval with the onset of cooling in the Chuacús complex.

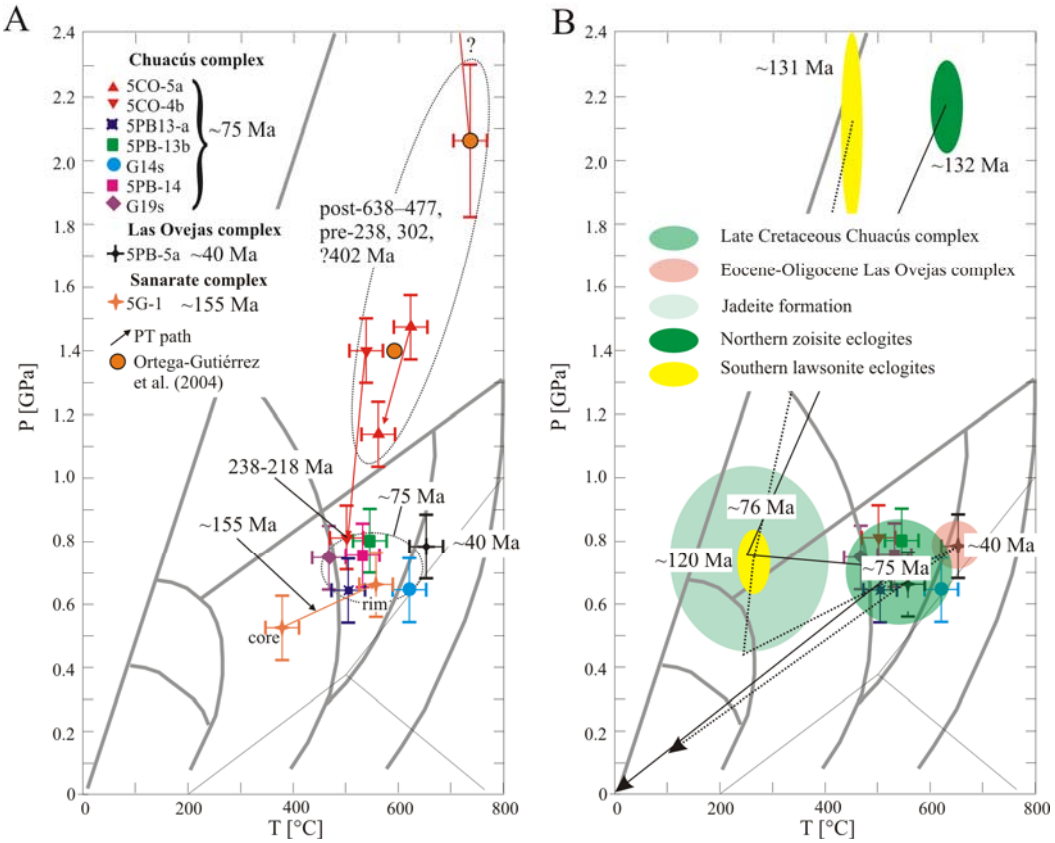

Figure 8. Pressure–temperature–time diagrams: (A) Pressure–temperature–time space of our new petrology and geochronology, and literature data of Ortega-Gutiérrez et al. (2004). A few Chuacús complex samples (Maya block) plot in the eclogite field. They follow an isothermal decompression path to amphibolite facies. The Chuacús eclogite-facies metamorphism is at best constrained to between 477 and 402 Ma and at worst to between 638 and 238 Ma. The retrograde amphibolite-facies metamorphism is dated at 238–218 Ma, the eclogite-facies metamorphism is pre-238 Ma (see text). Most of the Chuacús complex passed through epidote–amphibolite facies metamorphism and subsequent retrogression to greenschist facies. This event is well-dated ~~at~~ as Late Cretaceous (≤75 Ma). The Sanarate complex of the northwestern Chortís complex gives Jurassic (~155 Ma) epidote–amphibolite-facies metamorphism that evolved prograde out of the greenschist facies. The Las Ovejas complex (Chortís block) shows Tertiary (≤40 Ma) epidote–amphibolite to amphibolite facies. (B) Motagua suture zone pressure–temperature–time evolution from this study and Tsujimori et al. (2004, 2005, 2006), Harlow (1994), Harlow et al. (2004), and Brueckner et al. (2005). The Late Cretaceous Chuacús complex and mid-Tertiary Las Ovejas complex pressure–temperature fields are from this study. The northern zoisite eclogites (on Maya block) formed at ~132 Ma and reached mid-crustal conditions at about the same time as the Chuacús rocks experienced reheating at epidote–amphibolite-facies conditions accompanied by local magmatism. We suggest that the two are linked to the same oceanic–to–continental subduction zone (see text). The southern lawsonite eclogites (on Chortís block) formed at ~131 Ma and were at mid-crustal conditions already by ~120 Ma. Their emplacement is not genetically linked to the high-grade metamorphism and magmatism of the Las Ovejas rocks, which is a result of the Caribbean-plate translation and the formation of the Cayman trough (see text).

6. New Petrology

We selected twelve representative thin sections of magmatic and metamorphic rocks from both sides of the MSZ for electron microprobe analysis. Table 8 lists mineral assemblages and summarizes the P-T-t estimates, and Figure 8 visualizes the PT space of our and literature data.

6.1. Chiquimula batholith within Las Ovejas complex

Coarse-grained granodiorite 5C-13 is part of the Chiquimula batholith with the mineral assemblage quartz + K-feldspar + plagioclase + biotite + hornblende. Subhedral and anhedral plagioclase crystals are typically altered to sericite and have An-contents of 35-55 mole-% with normal zoning patterns. Twinning is in part deformational. Subhedral orthoclase has a K-feldspar component of 80-90 mole-% and displays perthitic unmixing. Prismatic amphibole is magnesiohornblende (classification of Leake et al., 1997) with relicts of augite in the cores. Reddish-brown biotite contains up to 4.6 wt.-% TiO_2, has an X_{Mg} of ~0.45 and is partly transformed to chlorite. Accessories are opaque minerals, apatite, and zircon. Anderson and Smith's (1995) Al-in-hornblende geobarometer yields 100–180 MPa at 740–860°C, calculated with the Ti-in-hornblende and plagioclase–hornblende geothermometers (Colombi, 1988; Blundy and Holland, 1990; Holland and Blundy, 1994). Our Ar/Ar geochronology demonstrates that the Chiquimula granite is a composite batholith (~90 Ma biotite–chlorite age, 5C-11; ~20 Ma K-feldspar, 5C-13); assuming that the 20 Ma K-feldspar age of 5C-11, adjacent to 5C-13, is close to the intrusion age of this shallow granodiorite (3–5.5 km), the average exhumation rate is 0.15–0.27mm/a. This supports our inference (see above) that relatively rapid exhumation in the Las Ovejas complex is pre-20 Ma.

6.2. Intrusive sequence, Juan de Paz ophiolite, North El Tambor Group

Fine- to medium-grained microdiorite 5PB-8 shows agglomeration of hornblende and plagioclase. Plagioclase shows normal zoning with An-content decreasing from 85 to 55 mole-% from core to rim. Calcic amphibole (magnesiohornblende) is slightly brownish and short prismatic. A few clinopyroxene relicts yield 95-98 mole-% augite (end member calculation after Banno, 1959) and are mantled by hornblende. Opaque minerals and apatite are common accessories. Anderson and Smith's (1995) Al-in-hornblende geobarometer indicates ~140 MPa at 730–860°C, calculated with the Ti-in-hornblende and the plagioclase–hornblende geothermometers. Bertrand et al. (1978) dated a likely metamorphic overprint in related dolerites from the Baja Verapaz (Fig. 1C) at ~75 Ma (see above).

6.3. Western Chuacús complex

Strongly foliated hornblende–epidote schist G19s contains phengite (Si-content ~3.3 p.f.u.), green amphibole (edenite to ferro-edenite associated with magnesio- to ferro-hornblende), epidote ($X_{Ps} \geq 0.15$; cf. Dahl and Friberg, 1980), and saussuritized plagioclase with an An-content

of 0–2 mole-%. Biotite forms post-tectonic, topotactic flakes on phengite. Accessory minerals are opaques and titanite. Phengite geobarometry yielded >0.7 GPa at 500°C (Massonne and Szpurka, 1997). The calibrations of Spear (1981) and Plyusnina (1982) gave 0.7–0.8 GPa at 450-500°C, which are reproduced by Colombi's (1988) Ti-in-hornblende geothermometer. Our 67 ± 1 Ma Ar/Ar phengite age demonstrates latest Cretaceous exhumation through the middle crust with an average rate ~0.37 mm/a. Epidote schist G21s is mylonitic with numerous porphyroclasts of epidote (X_{Ps}core = 0.295, X_{Ps}rim = 0.215), albite ($An_{0.3-0.9}$), and microcline ($Kfs_{98}Ab_{1-2}Cel_{1-2}An_{<0.5}$). The feldspars lack recrystallization but quartz recrystallized dynamically by subgrain rotation. Greenish biotite (X_{Mg}~0.47) and phengite (~3.3 Si p.f.u.) are common; opaques, titanite, apatite, and zircon are accessories. Strong mineral chemical disequilibria between the phases preclude PT estimates; the Si-content of phengite suggests ~0.8 GPa (Massonne and Szpurka, 1997).

6.4. Central Chuacús complex

Garnet gneiss 5CO-4b is dominated by orthoclase ($Kfs_{93}Ab_5Cel_1An_{<0.5}$) and minor, partly saussuritized plagioclase ($An_{0.2-1.4}$). Quartz shows subgrain-rotation recrystallization. Chloritized biotite (X_{Mg}=0.17) and phengite have epidote ($X_{Ps=}$0.23) and plagioclase inclusions. Phengite has elevated Si-contents of up to 3.50 p.f.u. in the core, indicating high-P conditions, whereas Si-contents as low as 3.27 p.f.u. occur in the rim sections. Garnet forms porphyroblasts with inclusions of plagioclase, quartz, minor ferro-hornblende/ferro-tschermakite, omphacite (10 mole-% jadeite) and rutile. It displays compositional zoning with a bell-shaped spessartine curve (core $Alm_{43}GAU_{44}Sps_{10}Prp_{0.5}$; rim $Alm_{47}GAU_{48}Sps_5Prp_{0.5}$). Carbonate, zircon, and titanite form accessory minerals in the matrix. Relict phases highlight the polymetamorphic evolution of 5CO-4b. Compositional zoning of garnet and omphacite inclusions in the core demonstrate high-P. For the garnet cores, ~525°C is calculated (Krogh, 2000) at ≥0.8 GPa (jadeite barometry of Holland, 1980, 1990). The highest-P conditions (highest $a_{prp}*a_{grs}^2$) are preserved near the garnet rim. 'Garnet–phengite' thermometry (Green and Hellman, 1982) using the garnet rim data and high-P phengite yields 550°C at minimum pressures of 1.4 GPa (phengite barometer of Massonne and Szpurka, 1997). The strong retrograde overprint is indicated by pervasive growth of matrix biotite and low-Si phengite; outermost garnet rims (highest X_{Prp}) and adjacent biotite yielded ~510°C (geothermometer of Hodges and Spear, 1982) at 0.7 GPa (barometry of Massonne and Szpurka, 1997 using paragenetic phengite), demonstrating re-equilibration under epidote–amphibolite-facies conditions. Due to this overprint and late retrograde processes, feldspar thermometry (Fuhrman and Lindsley, 1988) on coexisting plagioclase ($An_{0.2-1.4}$) and K-feldspar (integrated analysis with a 50 μm beam diameter) indicate cooling temperatures of 400–440°C. The lower intercept U/Pb zircon age indicates that high-P metamorphism is <638–477 Ma and

our Ar/Ar and Rb/Sr phengite and biotite ages date the latest portion of the retrograde path at 68–64 Ma.

Garnet amphibolite (eclogite) 5CO-5a contains minor quartz showing subgrain-rotation recrystallization and foliation-defining, large calcic amphibole (pargasite to edenite). Omphacite with 35 mole-% jadeite at the rim to 40 mole-% in the core is present as relicts in garnet and hornblende cores and less commonly in the matrix. Si-content of well-aligned phengite slightly decreases from core (3.32 p.f.u.) to rim (3.27 p.f.u.) and is the dominant sheet silicate. Garnet is almandine-rich with elevated grossular and pyrope contents. Remarkably flat zonation patterns may be due to the small crystal size; the average composition is $Alm_{60}GAU_{22}Sps_{0.5}Prp_{16}$. Plagioclase ($An_{2–4}$) is secondary, forming along the rims of garnet and hornblende; irregular spots of $An_{10–12}$ are also present. Late-stage biotite (X_{Mg}~0.53) grew at the expense of phengite. Apatite, rutile, ilmenite, and pyrrhotite are accessories. The mineral assemblage garnet + phengite + omphacite permits the application of the Waters and Martin (1993) barometer, which calculates pressures of 1.4–1.5 GPa for omphacite inclusions in the garnet core and core sections of phengite. A temperature estimate for this mineral assemblage using garnet-clinopyroxene geothermometry of Krogh (2000) is problematic due to the uncertainty of the ferric iron estimate in the silicates. Since garnet usually contains only small amounts of ferric iron, any error is predominately caused by the estimate of ferric iron in clinopyroxene. A useful approach is the assumption of 50% Fe^{3+} of total iron in clinopyroxene (Carswell et al., 2000; Schmid et al., 2000), which leads to temperatures of 600–625°C for garnet and omphacite inclusions. Similar temperatures are calculated using the hornblende–clinopyroxene geothermometer of Perchuk et al. (1985). Omphacite in the matrix likely was affected by retrograde processes and consequently shows a wide range of temperatures (490–590°C). Temperatures for retrograde overprint of the eclogite were estimated at about 560°C using the garnet–hornblende thermometer of Graham and Powell (1986) for garnet rims and adjacent hornblende. The GRIPS geobarometer of Bohlen and Liotta (1986) calculates pressures of ~1.1 GPa for these minerals and associated plagioclase, rutile, and ilmenite. These estimates indicate isothermal decompression during exhumation of the eclogite. Ortega-Gutiérrez et al.s' (2004) ~302 Ma lower intercept zircon age from a leucosome interbedded with relict eclogite from the area of 5CO-5 was interpreted to provide a minimum age for the Chuacús high-P event. We interpret our ages from this location as reflecting Triassic cooling during post-high-P, amphibolite-facies retrogression and Cretaceous reheating associated with regional metamorphism and local magmatism (see above).

The strong foliation of garnet-bearing micaschist 5PB-13a is formed by alternating mica- and quartz-rich layers; quartz shows subgrain-rotation and grain-boundary-migration recrystallization. Small, almandine-rich and spessartine-poor garnet grains ($Alm_{70}GAU_{10}Sps_1Prp_{18}$) are

included in large albite porphyroblasts ($An_{0.2-0.7}$), and larger garnet porphyroblasts with $Alm_{74}GAU_2Sps_{13}Prp_8$ crystallized within the matrix; the garnets are slightly inhomogeneous without regular zonation patterns. Green to brownish biotite (X_{Mg}~0.58) is partly altered to oxychlorite. Si-content in phengite decreases from core (3.3 p.f.u.) to rim (<3.2 p.f.u.). This correlates with decreasing Ti-content and indicates a retrograde evolution. Due to the lack of critical mineral assemblages, only few thermobarometers can be used to evaluate the PT conditions of these schists. The Si-content of phengite yields ≥0.6-0.8 GPa; the garnet–biotite geothermometer (Hodges and Spear, 1982) and the garnet–phengite geothermometer (Green and Hellman, 1982) point to 560-580°C for the garnet inclusions in albite and 460–475°C for the matrix garnets. Our Rb/Sr phengite age suggests metamorphism at ~65 Ma.

Garnet amphibolite 5PB-13b is well foliated, medium- to coarse-grained, and comprises large, pale-green calcic amphibole (magnesiohornblende to edenite) with numerous garnet and quartz inclusions; the matrix has also phengite and clinozoisite. Phengite Si-content (3.3–3.15 p.f.u.) and X_{Mg} (0.76–0.66) decrease toward the rims. Clinozoisite (X_{Ps}=0.08–0.09) forms large prisms. Quartz shows both dynamic subgrain-rotation and grain-boundary-migration recrystallization. Albite (An_{2-6}) has numerous quartz inclusions. Small, euhedral garnet yields $Alm_{55}GAU_{35}Sps_5Prp_4$ in the core and $Alm_{54}GAU_{30}Sps_5Prp_{11}$ in the rim and has increasing X_{Mg} values from core to the rim, indicative of prograde growth. One garnet differs compositionally, with high X_{Mg} in the core and abruptly increasing almandine content at the expense of grossular and spessartine towards the rim; this may indicate an earlier, prograde metamorphic evolution. Retrograde chlorite is widespread; apatite, zircon, and titanite are accessories. Pressures of ≥0.7 GPa (Massonne and Szpurka, 1997) at 530–550°C (garnet–hornblende geothermometer of Graham and Powell, 1986) are obtained; the Ti-in-hornblende thermometer of Colombi (1988) provides ~590°C. Our Ar/Ar amphibole and Rb/Sr phengite ages suggest metamorphism at ~65 Ma.

Hornblende–mica–chlorite schist 5PB-14 shows distinct layering with amphibole–mica and quartz that is dynamically recrystallized by subgrain rotation and grain-boundary migration. Pseudomorphs of chlorite (ripidolite after Hey, 1954) after relict garnet and lamellae of oligoclase (An_{12}) within albite ($An_{0.5-2}$) demonstrate retrograde overprint. Green amphibole (tschermakite to magnesiohastingsite) and clinozoisite (X_{Ps}~0.13) are subordinate. White mica shows increasing Si-content from the core to the rim (3.12–3.20 p.f.u.). Pale brown biotite is rare. Carbonate is Fe-bearing dolomite. Opaque minerals, rutile, and titanite form accessory phases. PT conditions of 500–550°C at ~0.8 GPa are suggested by the geothermobarometer of Plyusnina (1982). This estimate is reproduced by the phengite geobarometry (Massonne and Szpurka, 1997) and the amphibole–plagioclase geothermometers of Spear (1981), Blundy and Holland

(1990), and Holland and Blundy (1994). 600–630°C is indicated by the Ti-in-hornblende geothermometer of Colombi (1988), likely due to the high bulk Ti-content of the rock. This may, however, also indicate an early stage of medium- to high-grade, amphibolite-facies metamorphism. Our 65 ± 1 Ma Ar/Ar white mica age dates cooling during greenschist-facies retrogression.

Gneiss G14s is inhomogeneous with alternating plagioclase–quartz and mica–hornblende layers. Plagioclase is albite ($An_{0.5–2}$); epidote (X_{Ps}=0.2) and chlorite are present in the mafic layers. Phengite has Si-contents of 3.27–3.34 p.f.u. Biotite yields X_{Mg} of ~0.51. Green amphibole is magnesio- and ferro-hornblende. Small garnet within the mafic layers and as tiny inclusions in plagioclase has a bell-shaped spessartine curve and rimward decreasing X_{Fe} and X_{Mn}; cores and rims are $Alm_{40}GAU_{31}Sps_{25}Prp_1$ and $Alm_{48}GAU_{37}Sps_{13}Prp_2$, respectively. Accessories are carbonate, opaques, and titanite. Triboulet's (1992) geothermobarometer calculates ~610°C at ~0.62 GPa for the rim composition of the minerals, supported by phengite geobarometry at 0.6–0.7 GPa at 500–600°C. About 550°C are obtained by the garnet–hornblende (Graham and Powell, 1986) and the garnet–chlorite geothermometer (Ghent et al., 1987). These PT estimates indicate peak conditions at the transition from epidote-amphibolite– to amphibolite-facies metamorphism.

6.5. Sanarate complex

Chlorite–epidote–amphibole schist 5G-1a contains albite ($An_{1-3.5}$), clinozoisite (X_{Ps}≥0.1), chlorite (ripidolite), amphibole (edenite), and phengite (3.2–3.3 Si p.f.u.). The application of the geothermobarometer of Triboulet (1992) yields peak PT conditions of ~550°C at ~0.65 GPa for the rims of the minerals. The cores indicate ~380°C at ~0.55 GPa, outlining a prograde metamorphic loop. These data highlight the transition from lower greenschist to epidote–amphibolite facies and are supported by the geothermometry of Colombi (1988) and Holland & Blundy (1994), which provide ~415°C for the core and ~560°C for the rim of the amphibole. Si-contents of syn-tectonic phengite accordingly yield 0.6–0.65 GPa (Massonne and Szpurka, 1997). A likely age of this metamorphism is Middle Jurassic, given by the hornblende and white mica ages from adjacent locations G23, G24, which comprise similar rocks.

6.6. Las Ovejas complex

Garnet amphibolite 5PB-5a displays a fine- to medium-grained matrix with syn-kinematic biotite, amphibole and large, poikiloblastic garnet. Matrix quartz shows numerous subgrains. Biotite is Ti-rich (up to 4.1 wt.-% TiO_2) and has an X_{Mg} of about 0.24. The green amphibole is hastingsite. Large plagioclase grains are chemically homogeneous with An-content of ~35 mole-%. Garnet cores show $Alm_{69}GAU_{19}Sps_8Prp_4$; X_{Fe} and X_{Mn} increase towards the rims, indicating retrograde overprint. Accessories are opaques and apatite. Garnet–hornblende geother-

mometry (Graham and Powell, 1986) in combination with garnet–amphibole–plagioclase–quartz geobarometry (Kohn and Spear, 1990) yields 627–655°C at 0.7–0.8 GPa. Comparable temperatures are calculated with garnet–biotite thermometers of Hodges and Spear (1982), Indares and Martignole (1985), and Perchuk and Lavrent´eva (1983). Ar/Ar hornblende and biotite ages out of shear bands date deformation and rapid cooling through the middle crust at 30-28 Ma.

6.7. Interpretation of new petrology

Garnet amphibolite and felsic gneiss of the central Chuacús complex in the El Chol area preserve, in accordance with Ortega-Gutiérrez et al. (2004), a high-P event. Our data emphasize Ortega-Gutiérrez et al.s' "decompression and melting event" (550–650°C at 1.4 GPa). Garnet gneiss 5CO-4b likely records part of a prograde path. A first overprint is at ≥550°C and ~1.1 GPa, a second in the epidote–amphibolite-facies (~550°C at ~0.7 GPa). Only restricted areas of the Chuacús complex escaped the regional third overprint at 450–625°C at 0.7–0.8 GPa. The age of the high-P event is certainly pre-238 Ma, the age of two-mica orthogneiss intrusion (U/Pb ages) and high-T metamorphism (Ar/Ar ages) in the El Chol region, that we relate to the second overprint in the El Chol area dated as Triassic (238-215 Ma). The high-P event is syn- or post-638–477 Ma, the lower intercept U/Pb zircon age of high-P garnet–K-feldspar gneiss at location 5CO-4. It is likely older than the ~302 Ma lower intercept age of a leucosome interpreted to be associated with eclogite decompression (Ortega-Gutiérrez et al., 2004) and possibly syn- to pre-402 Ma, the age of metamorphic zircon incorporated in the Triassic two-mica orthogneiss. The regional ≥450°C and 0.7–0.8 GPa overprint is Late Cretaceous and the most outstanding feature of most of the Chuacús complex. This regional Cretaceous reheating is associated with local magmatism; deformation is syn-kinematic within the transition zone of amphibolite- to greenschist-facies metamorphism and continued during subsequent cooling. Characteristically, pressure estimates of the Cretaceous event are similar throughout the Chuacús complex but >100°C higher temperatures and somewhat higher pressures occur in the central Guatemala than in western Guatemala. The microdiorite from the Juan de Paz ultramafic sheet of the North El Tambor Group likely records seafloor hydrothermal overprint followed by low-grade Cretaceous metamorphism.

Our reconnaissance petrology of the northern Chortís block identifies Tertiary amphibolite-facies metamorphism, migmatization, local magmatism, and associated deformation for the Las Ovejas complex starting at ≥40 Ma. Peak PT conditions are ~650°C at 0.7–0.8 GPa, veiling earlier high-grade metamorphism associated with magmatism and migmatization that is Permo-triassic and Jurassic (age groups at 273, 245, 166, and 158 Ma). Distinctly different, Middle Jurassic (~155 Ma) prograde, lower greenschist- to epidote–amphibolite-facies metamorphism is preserved in the non-migmatitic Sanarate complex of southern Guatemala, west and outside of

the Cenozoic-shaped Las Ovejas complex. The latest Cretaceous–Tertiary Chiquimula batholith is a composite, shallow crustal level intrusion (3-6 km). Sub-volcanic ~20 Ma intrusives in this batholith demonstrate exhumation from ~25 km during 40–20 Ma, supporting a two-stage deformation–exhumation history within the Las Ovejas complex; i.e. relative rapid pre-20 Ma followed by slower post-20 Ma exhumation (see above).

Figure 8A summarizes the available P-T-t data from the Chuacús, Sanarate, and Las Ovejas complexes. The intricate metamorphic evolution in the Chuacús complex apparently is related to Early Paleozoic high-P metamorphism and its retrogression still in the eclogite field, further epidote–amphibolite-facies retrogression associated with Triassic magmatism/metamorphism, and regional Cretaceous epidote–amphibolite to amphibolite-facies reheating. The northern Chortís block contains a part dominated by Jurassic epidote–amphibolite metamorphism, only weakly overprinted by a Cenozoic event; the latter defines the Las Ovejas complex, which is characterized by epidote–amphibolite to amphibolite-facies reheating. Figure 8B compares the P-T-t evolutions of the mélange complexes (North and South El Tambor Groups) and the continental blocks onto which they were emplaced. Jurassic–Early Cretaceous North El Tambor Group oceanic and immature arc rocks incorporated ~131 Ma eclogite into an accretionary wedge that reached crustal levels in the Late Cretaceous (~76 Ma) and was incorporated as the roof nappe into the southern Maya block imbricate stack that initiated contemporaneously (~75 Ma). Mostly Cretaceous South El Tambor Group oceanic rocks incorporated ~132 Ma eclogite into an accretionary wedge, reached crustal levels at ~120 Ma, and were emplaced onto the Chortís block, whose last thermal overprint was during the Middle Jurassic. Locally and variably, the South El Tambor Group was affected by the Cenozoic deformation and metamorphism characterizing the La Ovejas complex.

7. Structure and kinematics

We organized our structural–geometry and kinematic data according to tectonic position and region (western, northern, and central Chuacús complex; central and eastern Las Ovejas).

7.1. Chuacús complex and Late Paleozoic cover, western Guatemala

Figures 9 and 10 compile structural and kinematic field and laboratory data and Figure 11 shows representative deformation features and dated syn-kinematic minerals. The western Chuacús complex shows regional, heterogeneously distributed, low-grade deformation (D_2) that overprints high-grade, partly migmatitic flow structures (D_1). Most pronounced is a deflection of the first foliation, s_1, into ubiquitous, sub-vertical, sinistral, D_2 shear zones. In this study, we concentrated on the Late Cretaceous (see below) greenschist-facies event D_2; its low-grade is distinct, as the same event reaches amphibolite facies in the central Chuacús complex of southern Guatemala and is coeval with magmatism. Another distinct map-scale feature is a NW struc-

tural trend (foliation, stretching lineation, shear planes), oblique to the ~E trend of the Polochic fault zone; the latter is clearly younger (see above).

The basement mainly comprises migmatitic paragneiss and (locally) orthogneiss, amphibolite and (hornblende)–epidote schist, augen gneiss of magmatic protolith, pegmatite, and variably strained granitoids. We also studied localities of Late Paleozoic metasediments (often conglomerate; Chicol and Sacapulas Formations). D_1 shows high-T plasticity, dominant coaxial flattening (s fabrics), and intrafolial and isoclinal folds, which refold an even earlier, relict foliation. D_1 is accompanied by local migmatization, traced by feldspar layers. D_1 quartz LPO shows medium- to high-T prism <a> glide (G20s of stop G45; Fig. 9, bottom right) that contrasts with D_2 low-T quartz LPO (see below). Quartz is coarse-grained and recrystallized by grain-boundary migration. D_1 is Late Triassic (~215 Ma), suggested by our U/Pb zircon age of phyllonitic (due to D_2) migmatitic gneiss (G18s of stop G1). D_2 formed 10–80 cm wide, chlorite- and carbonate-bearing shear zones that boudinaged s_1 (e.g., G1), imposed locally well developed augen- to ultra-mylonites that evolved during decreasing temperature into ductile–brittle mylonite with clinozoisite-, epidote-, and quartz-bearing faults (e.g., G3) and late fracturing (e.g., G45). These discrete shear zones widen into belts of mylonite, transforming the basement gneisses into biotite–chlorite schist and epidote–hornblende phyllite. Strain is locally prolate (dominant l-fabrics; e.g., G56/57). D2 quartz LPO indicates basal <a> slip (G1) with a strong coaxial flow component (c-axis cross-girdles). Quartz recrystallization mechanisms are variable but typically low-T and dynamic; subgrain rotation is dominant (e.g., G21s of stop G46; Fig. 11A-2) but evolves out of bulging recrystallization occur in quartz ribbons (e.g., G25s of stop G56, Fig. 11A-2, inset). Hornblende and feldspar are broken. Plagioclase shows rare incipient stages of recrystallization along twin planes; thus, deformation occurred mostly below ~450°C, evolving to very low-grade (≤300°C). Sinistral shear criteria are ubiquitous: flow folds, σ clasts, shear bands, and sc-fabrics in layers of quartz recrystallization (Fig. 9). Epidote (±hornblende) schists G19s (stop G1) and G21s (stop G3) provide quantitative PT estimates for the initial, higher-T stages of D2 at 450–500°C and 0.7–0.8 GPa. D2 is precisely dated at 67 ± 1 Ma by syn-kinematic white mica (G19s of stop G1; Fig. 11A-2). D2 also developed in the Paleozoic metasediments and is more pronounced (sinistral) transpressional (e.g., G4, Fig. 9) than in the underlying basement. Location GM36 shows stretched conglomerate (Fig. 9) cut by aplitic veins with the same ~E-W extension that stretched the pebbles; low-T plasticity with dynamic subgrain rotation occurred in quartz clasts. The basement rocks are variably overprinted by faults that are related to the Polochic fault zone (Fig. 10); the principal faults strike WNW (Polochic-parallel) and N. Faulting is ≤20 Ma, given by the ~20 Ma U/Pb zircon lower intercept of samples GM13s and GM14s (stops GM42, GM43) and the ~23 Ma AFT age of stop GM35 (sample GM9s); it is best constrained by the TFT and AFT ages along the Polochic fault (11.5–4.8 Ma, see above).

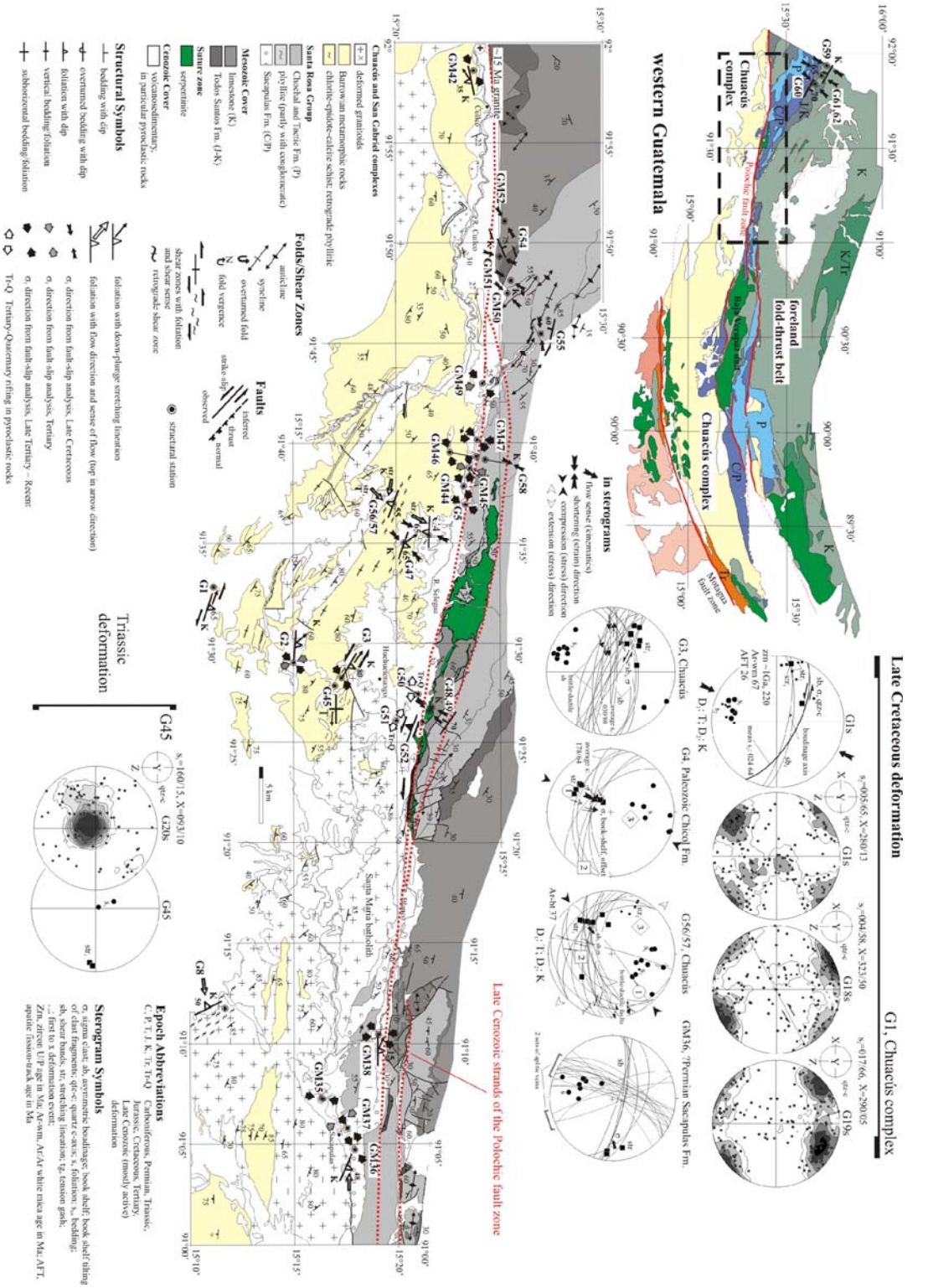

Figure 9. Overview map (top left) locates geologic-structural map (bottom) in the Maya block of western Guatemala. The latter compiles and reinterprets available 1:50.000 geologic maps and plots the main structural features both on map and in stereonets (lower hemisphere, equal area); it also serves as legend for the following structural data maps. S, foliation; str, stretching lineation; sb, shear band; ab, asymmetric boudinage; σ, δ, sigma and delta clasts; qtz-c,

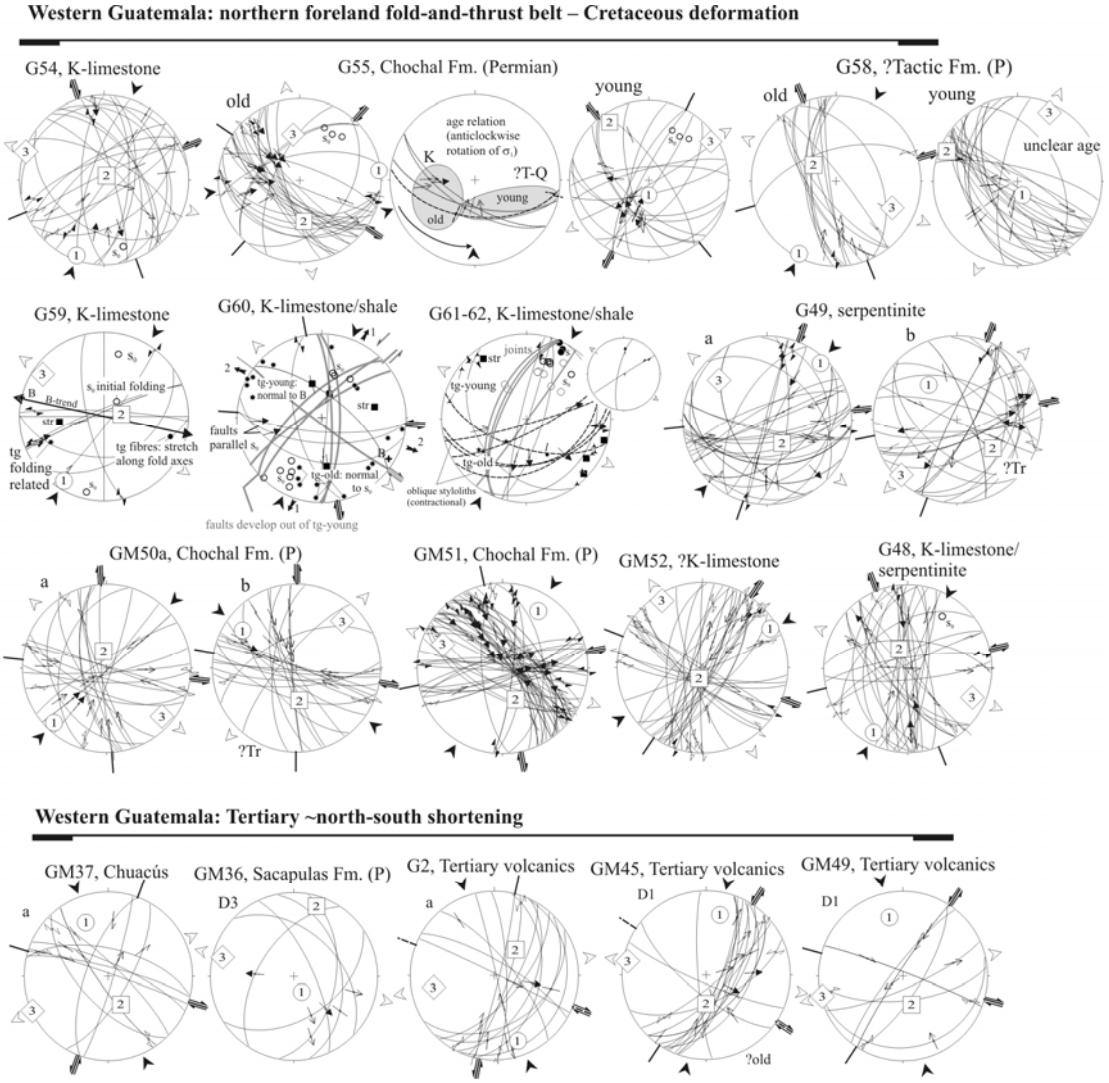

Figure 10. Additional structural data from the Maya block of western Guatemala. Legend for structural symbols as in Fig. 9. S0, bedding; tg, tension gash; ccw, counterclockwise.

(Figure 9, continued) LPO of quartz c-axis; subscripts $_{1,\ 2,}$ first, second deformation fabric element; D, deformation event; X, Y, Z, principal axes of finite strain. Fault-slip data and principal stress orientations 1–3: faults are drawn as great circles and striae are drawn as arrows pointing in the direction of displacement of the hanging wall. Confidence levels of slip-sense determination are expressed in the arrowhead style: solid, certain; open, reliable; half, unreliable; without head, poor. Arrows around the plots give calculated local orientation of subhorizontal principal compression and tension. Mineral abbreviations for geochronologic data obtained at the same location (below some stereonets) are those of Fig. 5. Ages are in Ma, except as otherwise noted.

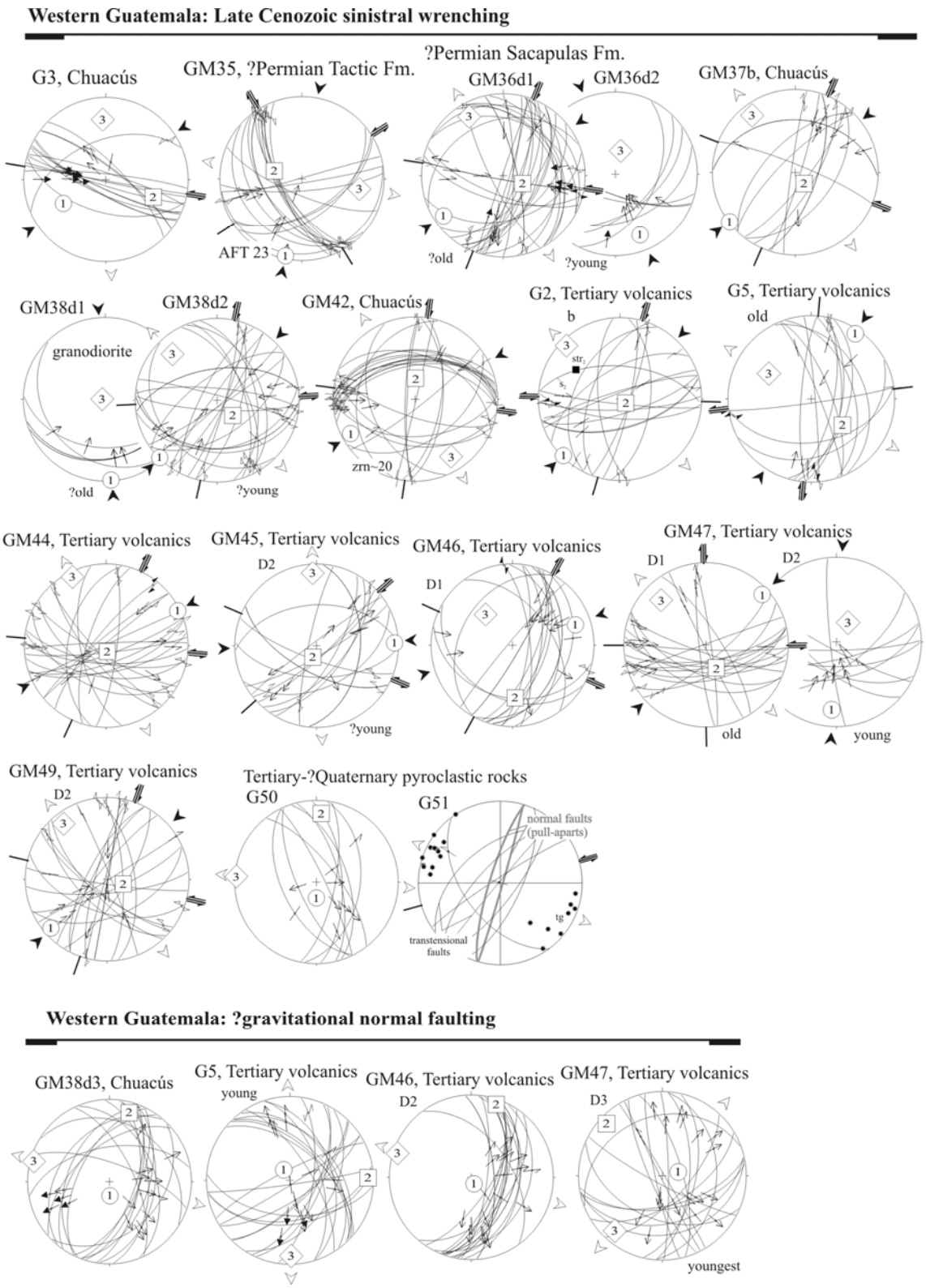

Figure 10. (continued)

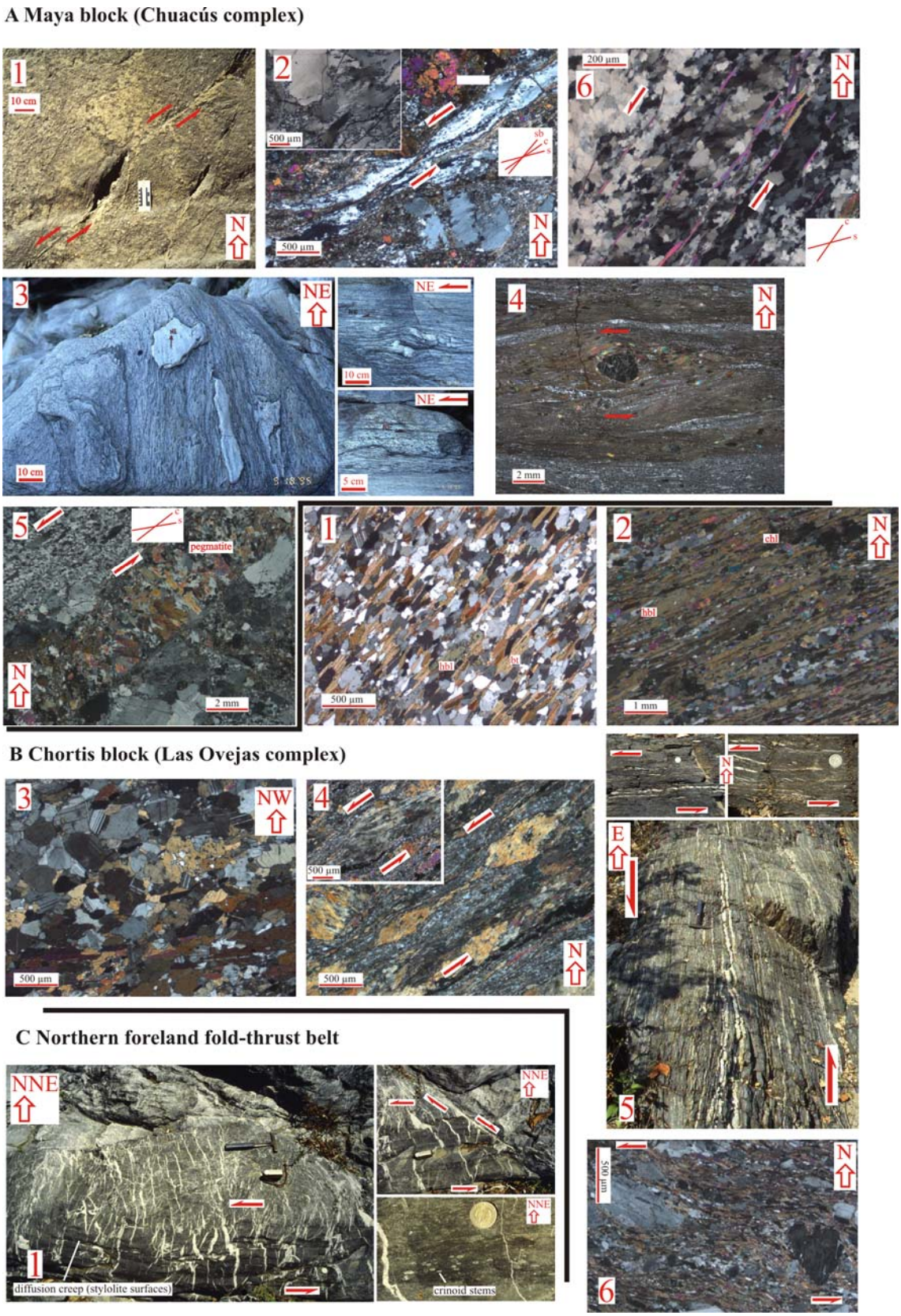

Figure 11. Representative dated minerals and deformation-geometry and kinematic structures. A: Chuacús-complex (Maya block) rocks. 1, stop G27, sample G7s: weathered retrograde biotite gneiss with sinistral brittle-ductile faults and pull-apart-type tension gashes that were locally filled with pseudotachylite (~70 Ma Ar/Ar whole rock). 2, western Guatemala: stop G46, sample G21s, partly mylonitic epidote schist; epidote and feldspar are brittle, quartz is

7.2. Chuacús complex, central Guatemala

Central Guatemala exposes the deepest part of the Chuacús complex studied by us (Figs. 12, 13) and allows insight into pre-Cretaceous deformation–metamorphism–magmatism. The Cretaceous structural overprint increases both toward south and north, i.e. the North El Tambor Group of the hanging wall. Typical Chuacús-complex rocks are garnet-bearing para- and orthogneiss, garnet amphibolite that is partly retrograde eclogite (see petrology), and marble (e.g., stops 880-884, 886, 5CO-4–6). Felsic and mafic rocks are often concordantly interlayered and resemble a bimodal volcanic sequence dominated by metasediments. The layering is accentuated by felsic sills (dominant) and dikes that crop out as partly pegmatitic orthogneiss and locally comprise 50% of the rock volume. They are associated with the main high-T metamorphism. Our new geochronology assigns them to the Triassic (see above). This rock association is sheared, folded, and thermally overprinted by syn- to post-tectonic feldspar + hornblende + white mica + garnet (± kyanite in quartz veins) growth. Locally, but increasingly abundant to the south, a second type of pegmatite is observed (e.g., stop 884). It is muscovite-rich, crosscuts the sills/dikes, and is associated with lower amphibolite- to upper greenschist-facies metamorphism. These pegmatites are undeformed where massive but sheared along quartz-rich layers.

---

ductile with subgrain-rotation recrystallization; quartz layers show syn-recrystallization sc fabric and strain concentration in shear bands (sb); phengite (~0.8 GPa) dates deformation at 67 ± 1 Ma (stop G1, Ar/Ar); inset (top-left, stop G8, sample GM8s) shows bulging recrystallization in quartz of mid-Jurassic granitoid that is locally mylonitized along discrete Cretaceous low-temperature shear zones. 3, stop 5CO-6: Triassic orthogneiss with pegmatite dikes and pods deformed top-to-NE during amphibolite-facies, ~70 Ma (U/Pb zircon) flow. 4, stop 854: Second deformation, likely Cretaceous, sinistral shear zones anastomose around relict garnet and white mica microlithons. 5, stop 856: undeformed pegmatite dikelet (quartz + plagioclase, plagioclase mostly converted to epidote) intrudes parallel to c planes of second deformation, recrystallized sc-fabric in quartz-rich layers of orthogneiss; pegmatite is Late Cretaceous (e.g., samples 885, 5CO-6b). Feldspar in orthogneiss is broken but locally recrystallized. 6, stop 5PB-9, eastern Guatemala: high-strain, sinistral shear zone dated by syn-kinematic white mica at ~76 Ma (Ar/Ar and Rb/Sr). B: Chortís block rocks. 1, stop 5PB-5, Las Ovejas complex: syn-kinematic amphibole (hastingsite) and biotite in ~650°C, 0.75 GPa (garnet) amphibolite date rapid cooling at ~30 Ma. 2, stop G24, sample G5s, Sanarate complex: ~155 Ma syn-kinematic amphibole and chlorite in amphibolite. 3, stop 5C-26, Las Ovejas complex: weakly deformed, migmatitic amphibolite, hornblende is syn-kinematic at ~35 Ma (Ar/Ar) with slow cooling to or reheating at ~20 Ma (Ar/Ar hornblende and biotite). 4, stop 5C-2, Las Ovejas-complex amphibolite: ~20 Ma syn-kinematic hornblende in mylonite. 5, stop 5C-37, Las Ovejas complex: retrograde amphibolite-biotite gneiss sequence with mostly foliation-parallel leucogranite dikes and quartz-segregation veins. Part of the high strain zone (bottom) and details (insets top) show sub-vertical, greenschist-facies, second deformation under sinistral wrenching. Hornblende dates beginning of deformation at ~39 Ma and biotite retrogression at ~20 Ma (Ar/Ar). Hammer and coins for scale. 6, stop 5H-4, Las Ovejas complex, Honduras: greenschist-facies, sinistral shear in diorite; hornblende and biotite date deformation between 38 and 25 Ma (Ar/Ar). C: Northern foreland fold-thrust belt. 1, stop G60: Cretaceous limestone; NE–SW shortening and NW–SE extension indicated by pressure-solution surfaces, fold-axis parallel tension gashes, and faults. Ductile strain is recorded by elliptical shape of crinoid stems; foliation dips steeply into the picture, bedding is sub-parallel to the outcrop surface. Hammer, compass, and coin for scale.

They are Late Cretaceous as indicated by ~74 Ma metamorphic overprint in the host rocks (U/Pb zircon, stop 5CO-6) and their 74–62 Ma white mica ages (see above).

The relict eclogite-facies metamorphism was at ~600°C and 1.4–1.5 GPa (see above) with a retrograde overprint at ~560°C and ~1.1 GPa. The latter metamorphism and associated magmatism is Triassic (see geochronology). Other garnet amphibolites are coarse-grained with variably developed but mostly strong foliation and 550–610°C at 0.6–0.7 GPa, thus transitional from amphibolite to the epidote–amphibolite facies. ~570°C and ~0.7 GPa conditions for formation of garnet inclusions and ~470°C for matrix garnets in well-foliated micaschists concur with PT estimates from the garnet amphibolites but likely trace progressive later stages of continuous metamorphic evolution. 500–550°C at ~0.7 GPa conditions characterize the latest stages of retrograde overprint in hornblende–mica–chlorite schists. Local, large-scale fluid flow is indicated by up to 1 m thick quartz-segregation veins and ubiquitous albite growth. The regional amphibolite- to epidote–amphibolite-facies overprint in the garnet amphibolites and schists is Late Cretaceous (see geochronology).

Where preserved Triassic deformation is distinct. Foliation is sub-vertical and folded tight-isoclinally to ptygmatically with axes parallel to the mineral stretching lineation (F_1 <a> type folds) that trends NNW (Fig. 12, stops 5CO-5, 880–886) and thus is clearly different from the overall trend of the Cretaceous deformation (~ENE). F_1 verge mostly (N)E and are locally sheath folds. At these locations, overprinting Cretaceous F_2 folds are steeply plunging, open, NE-vergent, and associated with dextral and sinistral (conjugate) shear bands (Fig. 12). Garnet–K-feldspar gneiss (5CO-4), resembling Rabinal augen gneiss (see below), has old garnet with an internal foliation that is 90° to the external (Cretaceous) foliation. Overall, Triassic deformation appears coaxial and the structures are annealed (widespread albite overgrowth, see above).

Structural geometry and kinematics of the regionally dominant Cretaceous deformation appear simple (Figs. 12, 13, 11A-3): the stretching lineation consistently trends ~ENE and parallels the ubiquitous B_2 axes; where s_1 is sub-vertical, it is transposed by sinistral shear zones/bands; where s_1 is sub-horizontal, shear zones/bands record sinistral transpressive, top-to-NE flow. Late faults have huge fibers and indicate N-S shortening (e.g., stop G29). This Cretaceous high-strain, NE–SW stretching is suggested by various features. Stop G31, for example, shows relatively idiomorphic, inclusion-free, pre-Cretaceous garnet that is fractured and connected with chlorite; a second generation of garnet and chlorite is co-genetic. Quartz shows transition from subgrain-rotation to grain-boundary-migration recrystallization (e.g., stop G31). At stops 880–886 late, mostly unfoliated/unfolded dikes/veins are exposed; some of these quartz + feldspar + muscovite + biotite pegmatites show high-strain boudinage. At stop 887 a several meters thick, weakly foliated pegmatite crosscuts the major (Triassic) foliation but deflects it si-

nistrally. F_3 refold F_2 openly. Where F_3 is not developed l tectonites are common. Our interpretation is that folding is represented by prolate strain (e.g., stop 887). Our geochronology constrains cooling from ~550 to 275°C and thus deformation at 75–65 Ma (see above).

Stations 854 and 856 reveal Chuacús complex that is dominated by orthogneiss (Figure 12). At 856, <0.5 m thick, D_1 mylonite–ultramylonite shear zones cut augen gneiss, biotite granite, and aplite dikes. The host rock is weakly deformed at high-T preserving NW trending str_1. Discrete ultramylonite shear zones that differ in degree of localization—the younger are more strongly localized—overprint a first, E striking, dextral, high-T shear zone fabric. D_1 is syn-migmatitic, F_1 are isoclinal. D_2 imprints ENE trending ultramylonitic–mylonitic, Ramsay–Graham-type shear zones with late chlorite–quartz veins, in which quartz is fibrous tracing the NW–SE str_2. Quartz and plagioclase in the sinistral, often anastomosing shear zones (Fig. 11A-4) show subgrain-rotation recrystallization and reaction softening by transfer to sericite and epidote, respectively; locally feldspar is recrystallized (~500°C). At 854 and 856, undeformed pegmatite and aplite dikes/dikelets cut migmatitic, sillimanite- and white mica-bearing ortho- and paragneiss and are younger than the D_2 fabric (Fig. 11A-5). Pure quartz layers show prism <a> slip and subgrain-rotation with transitions to grain-boundary migration recrystallization. Common F_2 refold both s_1 and D_2 shear zones, imposing prolate strain. We do not have direct age control on these deformations; however, structural geometry, kinematics, and associated metamorphism suggest a Cretaceous age for D_2.

We also studied the Chuacús complex along a section at its easternmost outcrop at the base of the Juan de Paz ophiolite unit (Fig. 12). The structural trend changes to ENE, from WNW in western and E in central Guatemala. Deformation is continuous from greenschist facies to brittle (boudinaged quartz rods) and heterogeneous. At station 5PB-9, deformation is high-strain, mostly coaxial with sinistral and dextral shear bands and <5 cm-thick mylonite zones, shows coaxial, basal <a> slip in quartz, and open <a> folds. The whole rock–syn-kinematic white mica (Fig. 11A-6), Rb/Sr isochron at 76.5 ± 0.6 Ma precisely dates deformation. At station 5PB-10 (Fig. 12), ubiquitous vertical, sinistral shear bands, a single- to type-I cross-girdle quartz c-axis orientation and strong preferred orientation of a-axis and m-planes indicate dominant rhomb and prism <a> slip under somewhat higher deformation temperatures than at station 5PB-9 and dominant non-coaxial flow.

7.3. Metasomatized southern Chuacús complex rocks below the North El Tambor Group, central Guatemala

The immediate footwall of the North El Tambor serpentinites comprises imbricates that stack Chuacús-complex rocks, Chuacús rocks with low-grade sedimentary rocks (Jones Forma-

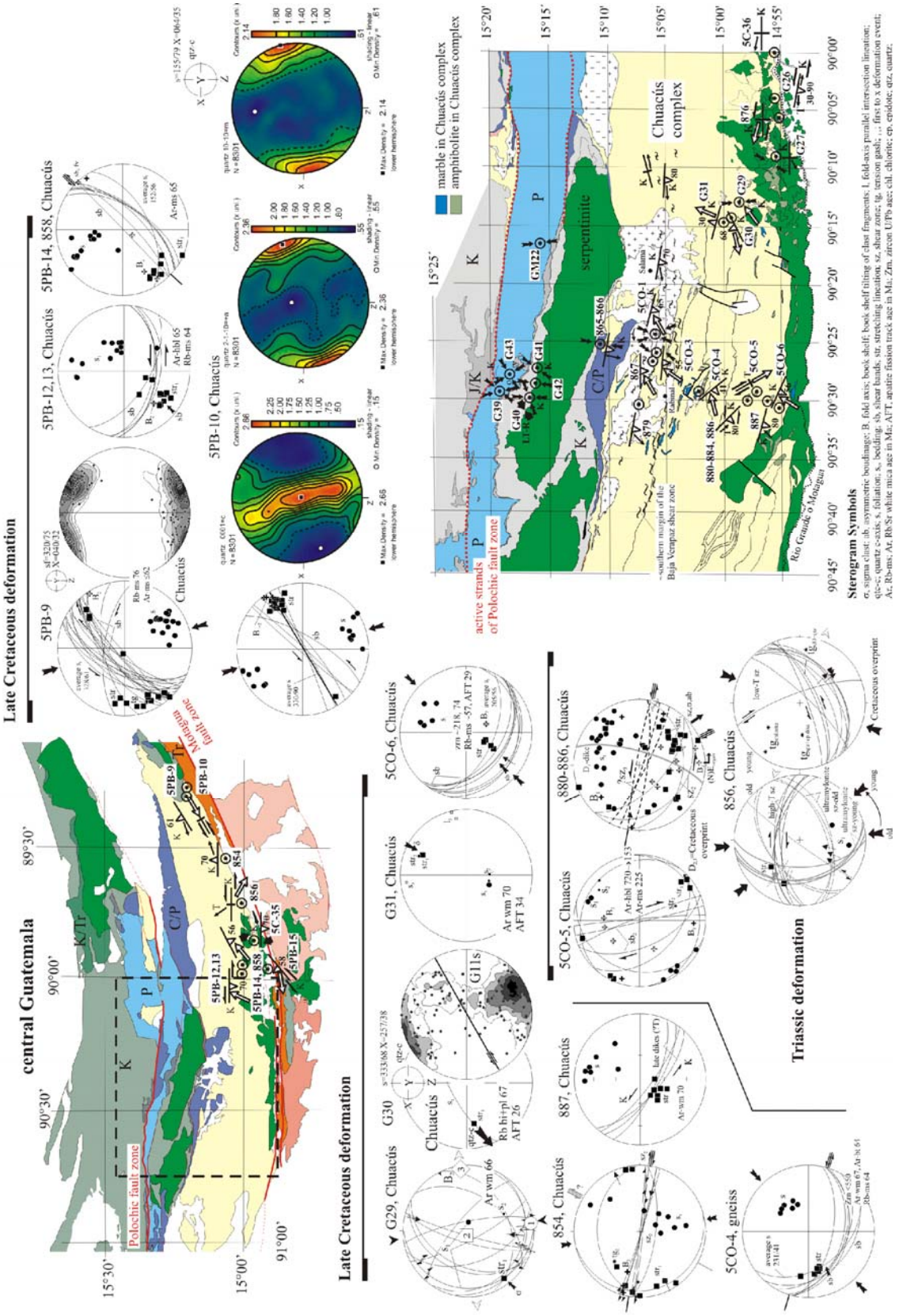

Figure 12. Overview map (top left) locates geologic–structural map (bottom right) in the Maya block of central Guatemala. Main structural features are plotted both on map and in stereonets (lower hemisphere, equal area). See Figs. 9 and 10 for legend; B, fold axis.

tion and San Lorenzo marble), and these rocks with serpentinite (Figs. 12, 13). Rocks that are imbricated are phyllite (retrograde biotite gneiss), epidotized biotite gneiss, (±garnet)–actinolite–clinozoisite–chlorite phyllite, marble, and low-grade siltstone. These rocks show neocrystallization of calcite, quartz, Mg-chlorite, and albite (e.g., stops 5PB-15, 860) depending on the surrounding lithology. The boundary between serpentinite and Chuacús-complex rocks is, where exposed, a shallow-dipping breccia zone with serpentinite and marble clasts (stop G26, Fig. 13). Nearly all of the stations (Fig. 13) show relict, mostly sub-horizontal, high-grade foliation (s_1) that is folded (e.g., G26, G27, 5C-36). During D_2 sinistral ductile–brittle shear bands developed where s_1 was steeply dipping (e.g., 5PB-15, 860). Stretching is WSW–ENE and exemplified by s_1 boudinage. Quartz-filled tension gashes are ubiquitous (e.g., G26, 5PB-15) and testify to fluid flow. F_2 flexural-glide folds are N(E)-vergent and show lengthening along B_2 (e.g., G26, 5C-36). Quartz deformed by subgrain-rotation recrystallization (e.g., G26) and basal <a> glide (5C-36). The LPO indicates dominantly coaxial flow. White mica at stop G26 is sericite and its Ar/Ar age dates deformation at ≥60 Ma. This corresponds to the Rb/Sr white mica–whole rock isochron at ~63 Ma from a chlorite phyllite. Faulting started in the ductile–brittle regime with a dominant NE striking set. At station G27 pseudotachylite (Figs. 11A-1, 13, sample G7s) fills pull-apart tension fractures. These are again involved in continuous deformation, as E-trending quartz fibers formed as strain shadows. The pseudotachylite dates D_2 at ~67 Ma.

7.4. North-central Chuacús complex, Rabinal granitoids and low-grade metasediments, central Guatemala

The northern Chuacús complex comprises paragneiss that typically resembles metagreywacke (coarse-grained feldspar and white mica) and K-feldspar porphyroblastic granitoid (U/Pb zircon ages at 485–410 Ma, stop 5CO-1) that were transformed to quartz phyllite and augen gneiss. The distinction between ortho- and paragneiss is problematic at many locations and makes mapped lithologic boundaries questionable (e.g., BGR, 1971, Fig. 12). Marble and amphibolite intercalations resemble those of the southern Chuacús complex. The major deformation, attributed to the WNW trending Baja Verapaz shear zone by Ortega-Gutiérrez et al. (2004), is locally mylonitic and low-grade. Foliation dips intermediate to steeply S(W) and the stretching lineation (str_1) plunges intermediate to the SW (Figs. 12, 13). A continuous kinematic evolution from ductile shear bands to ductile–brittle faults and quartz-filled, en-echelon tension gashes (e.g., stops 5CO-1, 5CO-3, 867) indicates sinistral transpression. At station 5CO-1, typical Rabinal augen gneiss, shear bands evolve into ductile–brittle faults (quartz ductile), and faults with large quartz–white mica fibers that are conjugate to kink bands that are partly faulted and indicate N–S shortening and E–W extension along str_1. Quartz shows typical low-T plasticity with subgrain-rotation recrystallization. K-feldspar is brittle. Local ultramylonite (<1 m thick, stop 867) has cogenetic chlorite + sericite and quartz ribbons that show weak bulging- and do-

minant subgrain-rotation recrystallization. Late kink folds are interpreted as flow heterogeneities at the end of deformation. Quartz fibers in the strain shadow of pyrite are un-recrystallized. The post-245 Ma (see above) Sacapulcas conglomerate (mostly intermediate volcanic rock pebbles, stops 865–866) records identical, low-T structural geometries and kinematics. Paragneiss (stop 867) preserves pre-Cretaceous deformation with large white mica and pre-existing foliation and felsic veins that are cut by orthogneiss that is typical Rabinal gneiss.

7.5. Northern foreland fold–thrust belt, Guatemala

The 'Laramide' foreland fold–thrust belt north of the Polochic fault zone and the overlying North El Tambor Group allow comparisons of structural geometries and kinematics with those recorded in the Chuacús basement in the south. The stratigraphic range observed at our structural stations ranges from Permian to Upper Cretaceous, i.e., Permian Chochal and Tactic Formation limestone and shale, and Lower and Upper Cretaceous Coban and Campur Formation dolomite and limestone (BGR, 1971). In the following, we give an overview but emphasize that the stereoplots (Figs. 10, 13) contain a cornucopia of structural detail, e.g., geometries, deformation evolution, and changes in the paleostress field. Deformation age is difficult to constrain directly. It is certainly Late Cretaceous–Tertiary. Structural and kinematic compatibility with the well-dated deformation in the Chuacús complex (see above) and that in the Sierra Madre Oriental–Yucatan fold belt (e.g., Gray et al., 2001) suggest the major deformation, sinistral transpression, is latest Cretaceous–early Tertiary.

In western Guatemala, stations G59 to G61 within Cretaceous limestone and minor shale record folding with well developed ductile–brittle, NW–SE extension along the regional fold trend (Figs. 10, 11C-1). Deformation starts during layer-parallel shortening before buckling with vertical extension by tension gashes (tg_{old}) and continues with buckling and layer-internal ductile flow with foliation development, foliation boudinage, and creation of a fold axis-parallel stretching lineation. Later stages develop conjugate but mostly sinistral faults and oblique stylolites that show strong volume-loss by pressure solution; dissolved material is partly deposited in veins that comprise up to 20-vol% of the rock. Fold axis-parallel extension is accentuated by a second set of tension gashes (tg_{young}) and conjugate faults that represent tilted horst-graben structures; the latter exactly constrain extension at 128° (inset stop G61-62, Fig. 10). Abundant crinoids in the limestone record up to 50% shortening due to volume reduction that is mostly accommodated by bedding-parallel stylolites (Fig. 11C-1). Other stations, both in limestone and serpentinite, show less ductile flow but more pronounced faulting. Folding is mostly gliding in bedding; the slip direction is oblique to the fold axes (e.g., stop G55). Common to most stations is rotation of σ_1 from E–W to N–S in time and sinistral transpression.

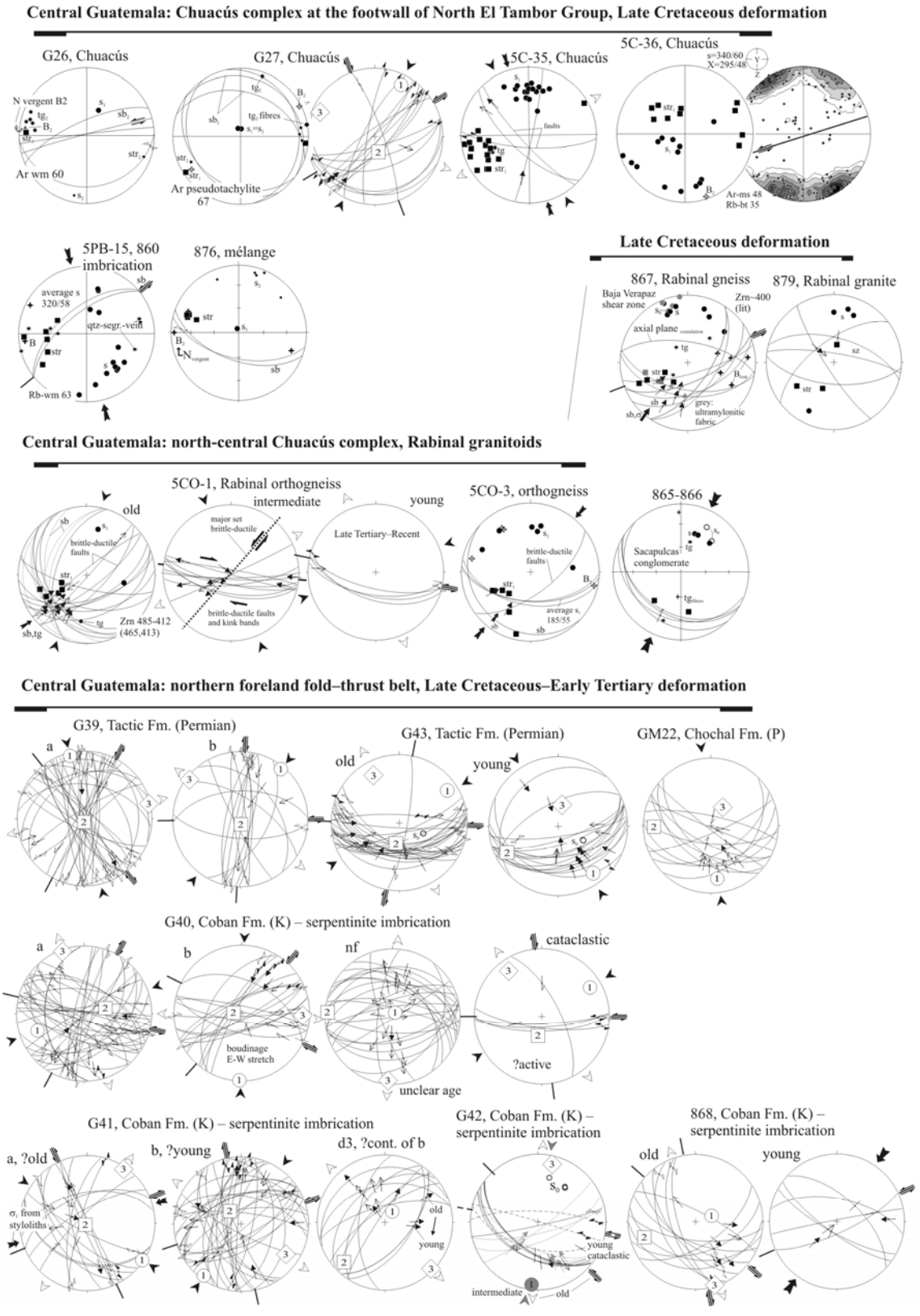

Figure 13. Additional structural data from the Maya block and the early Tertiary Subinal Formation in central Guatemala. Legend for structural symbols see Figs. 9, 10, 12.

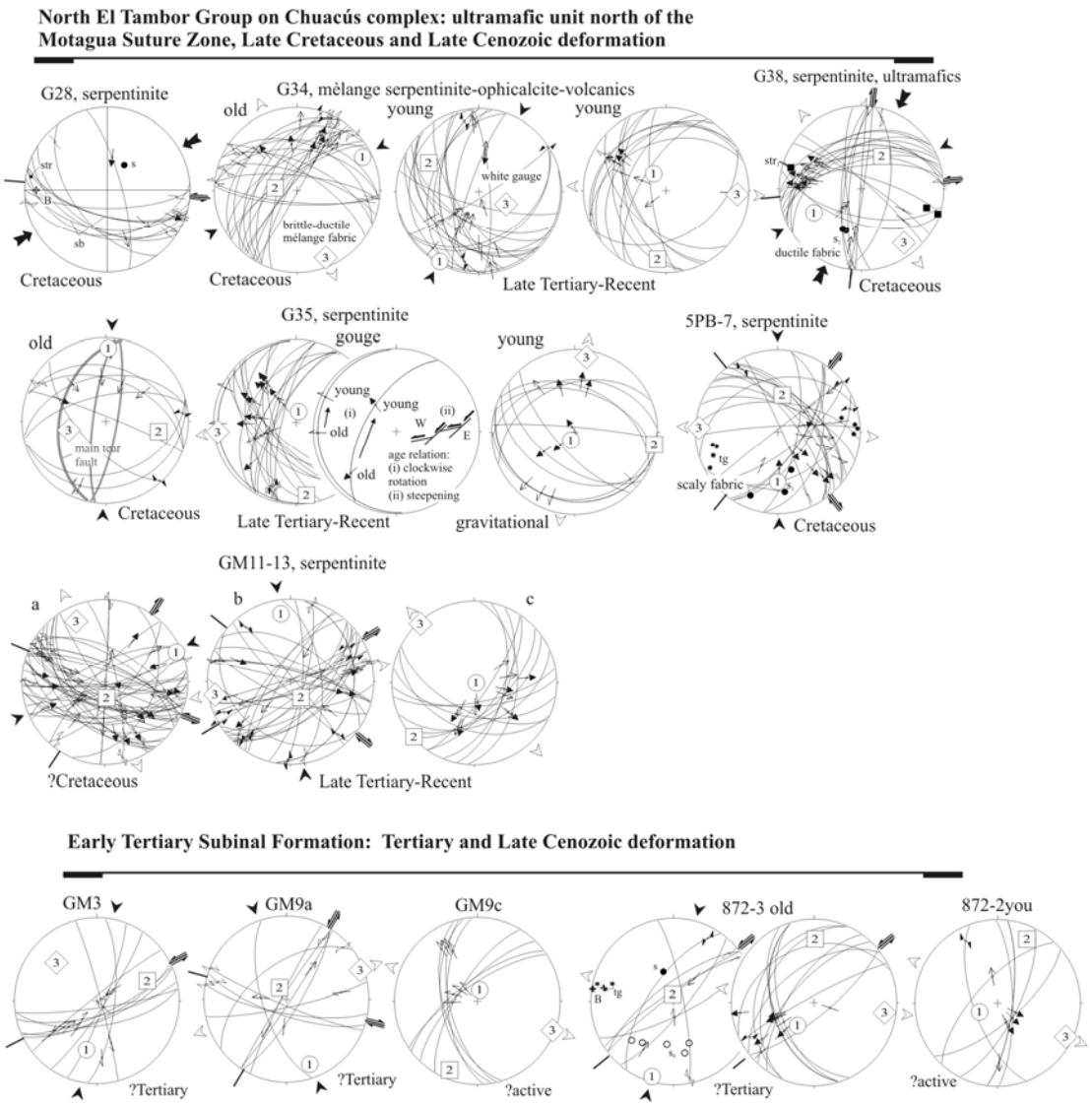

Figure 13. (continued)

In central Guatemala, Permian limestone and the contact zone between Cretaceous limestone and serpentinite provide a similar albeit less complete deformation history. Sinistral transpression and rotation of σ_1 imply increased shortening and less strike-slip over time (e.g., G43, Fig. 13). The weak structural record of serpentinite emplacement and the overall paucity of shallowly dipping faults are notable. Early fault sets indicate ~NE–SW shortening along conjugate strike-slip faults (e.g., G39). At station G40, ~N–S shortening along mostly strike-slip faults formed anastomosing fault zones with boudinage and E–W extension. Normal faults may be topographically induced, and late cataclastites likely record active sinistral wrenching along a strand of the Polochic fault zone. The normal faulting observed at station G41 could also be gravitationally induced or, alternatively, a transtensional continuation of sinistral wrenching.

7.6. North El Tambor Group on Chuacús complex, central Guatemala

We analyzed imbrications of serpentinite, ophicalcite, and felsic volcanic rocks (stop G34) and serpentinites (stops G28, G35, G38, GM11-13, 5PB-7; Figs. 13 and 14). All stations show a low-grade, ductile–brittle fabric with shear bands and faults that slipped sinistrally, coeval with shortening indicated by folding and oblique-slip faulting. White mica ages (~65 Ma) of greenschist-facies rocks (Chuacús complex, stops G26, G29, see above) in the immediate footwall of these El Tambor rocks suggest latest Cretaceous deformation. At several stations, tectonic mélange occurs along major N-dipping detachments that contain foliated, moderately serpentinized ultramafic rocks (G34, G38) and pure serpentinite (G35; Figs. 13 and 14) with brittle–ductile s–c fabrics. The ultramafic bodies are surrounded by an anastomosing, lenticular, scaly foliation that records overall coaxial deformation. Shortening is NNE–SSW and extension is WNW–ESE. Most stations contain a younger fabric with unclear age relations: sinistral shear and normal faulting both with NW–SE extension. Late-stage, flattening-type extension is possibly caused by topographic collapse.

7.7. Tertiary volcanic rocks and early Tertiary Subinal-Formation red beds, western and central Guatemala

In western Guatemala, Tertiary pyroclastic rocks, welded tuffs and, locally, sedimentary rocks cover the Chuacús complex and are exposed along the Polochic fault zone. Our data (Figs. 9, 10) highlight three strike-slip dominated events. From older to younger these are: (i) ~N–S shortening and ~E–W extension. (ii) ~NE–SW shortening and ~NW–SE extension, mostly along ~E-trending sinistral strike-slip faults. This is by far the dominant set and traces the Polochic fault-zone deformation. The strata dip up to 80°, indicating strong local shortening. A similar stress field but dominated by normal faults also occurs in subhorizontal pyroclastic rocks that likely are part of the Tertiary ignimbrite province of Central America (~15 Ma; e.g., Jordan et al., 2007); we thus attribute this major event to the currently active stress field. (iii) Normal faulting with widely dispersed slip directions. This event likely records topographic collapse.

Deformation of the Subinal-Formation red beds started with ~N–S shortening that tilted beds (open to tight folds) and produced a fracture cleavage (Figs. 13 and 14). At stops 872–873, two sets of older faults have constant ENE–WSW extension (σ_3) but σ_1 and σ_2 permutated. The strike-slip faults have oblique lineations so that faulting likely started during late stages of folding. Faulting recorded at all stations has a clear sinistral-transpressive component. Late normal faulting is interpreted as prolongation of folding-related deformation with extension along the fold axes becoming dominant.

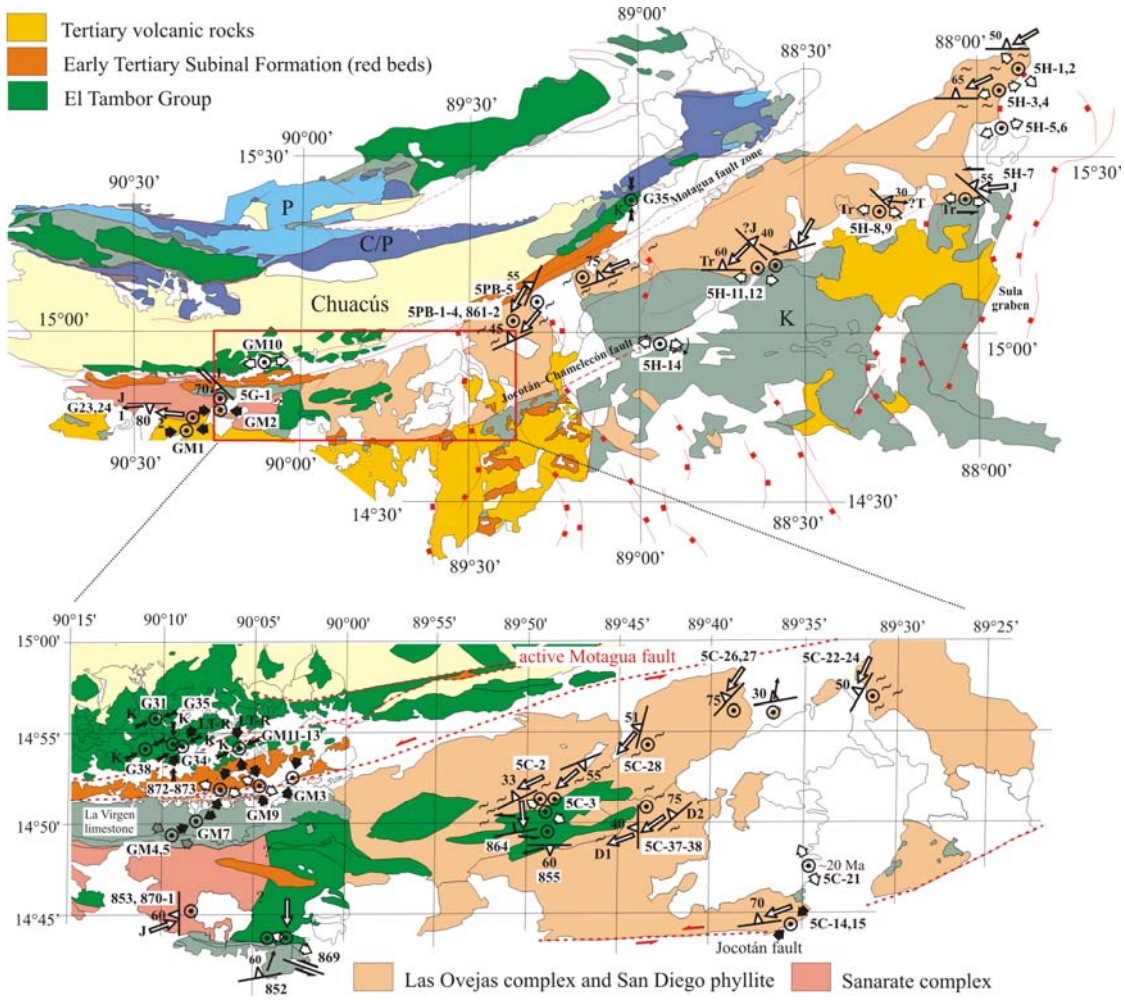

Figure 14. Geologic map (bottom) of the Motagua suture zone with structural data from the northern Chortís block, the North and South El Tambor Groups and the Sanarate complex; the outline of the latter is conjectural. In addition structural data of Cretaceous to late Tertiary sedimentary and magmatic rocks straddling the suture are shown. Main structural features are plotted both on map (this figure) and in stereonets (lower hemisphere, equal area, Fig. 15). See Figs. 9 and 10 for legend.

7.8. Sanarate complex, central Guatemala

The Sanarate complex, the westernmost basement outcrop south of the MSZ, comprises retrograde amphibolite, chlorite–epidote–hornblende schist, micaschist, and chlorite phyllite with peak PT conditions at ~550°C and ~0.65 GPa. The basement is in fault contact with Tertiary andesite and red beds (stops G23, G24, 5G-1; Figs. 14 and 15). Foliation and relict isoclinal folds constitute D_1. D_2 shows low-T, partly mylonitic quartz–white mica fabrics along an E trending, vertical foliation; shear sense is sinistral. Quartz is post-tectonically annealed. D_3 occurs both in the red beds/volcanics and the basement. ENE–WSW shortening thrust the basement in a sinistral-oblique sense onto the red beds. Two generations of hornblende exist in the studied amphibolite. The dominant syn-kinematic younger generation (Fig. 11B-2) and also syn-kinematic white mica in the micaschist/phyllite date D_2 as Middle Jurassic (samples G3s, G5s, stations G23, G24, Fig. 5E). The reheating (quartz weakly annealed) is likely Tertiary

(low-T steps in G5s). Adjacent stations 853 and 870–871 comprise massive amphibolite and rare garnet amphibolite and leucogabbro close to the boundary with the South El Tambor mélange rocks. Their apparently lower-grade metamorphism distinguishes them from the Las Ovejas complex amphibolites. Asymmetric boudinage of hornblende–quartz veins, σ clasts, and late biotite-rich shear bands associated with kink bands record top-to-NE flow with a slight dextral component along W-dipping foliations. Tight to isoclinal flow folds are present in high-strain zones (Fig. 15). This deformation remains to be dated.

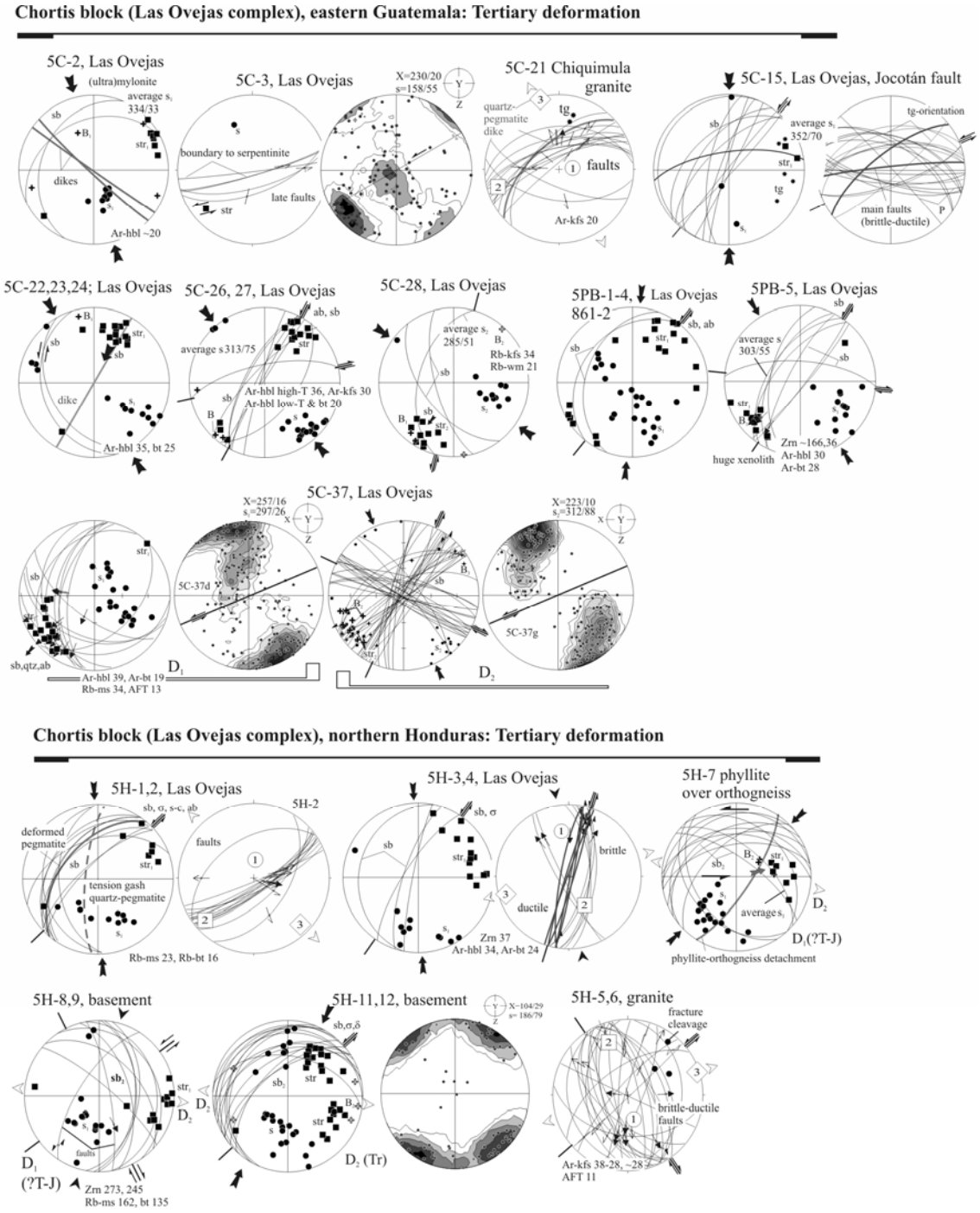

Figure 15. (figure caption see next page)

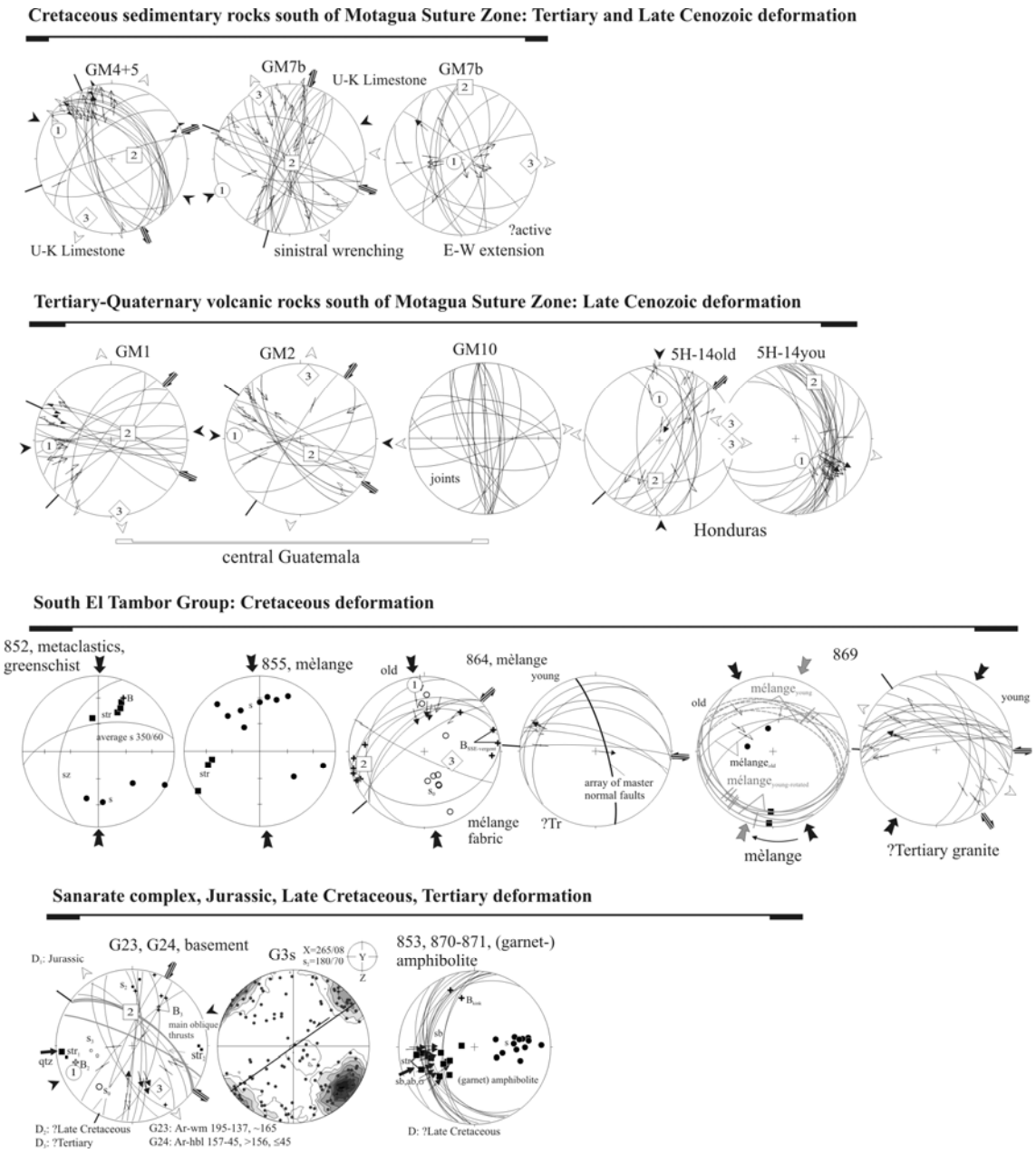

Figure 15. (continued) Structural data from the Chortís block and Cretaceous to late Tertiary sedimentary and magmatic rocks straddling the Motagua suture zone. Legend for structural symbols as in Figs. 9, 10, 12.

7.9. Las Ovejas complexes and San Diego phyllite, Guatemala and western Honduras

Stations 5C-2, 5C-28, 5C-26,27, and 5C-22–24 are in basement lacking retrograde metamorphism of the Las Ovejas complex south of the central Motagua valley and north(east) of serpentinite and mélange rocks of the South El Tambor Group (Figs. 14, 15). This area comprises biotite granite with diorite xenoliths, gabbro-amphibolite, migmatitic biotite gneiss, and garnet-bearing leucosome. The main deformation is of variable intensity, from weakly foliated to locally mylonitic–ultramylonitic but constant in orientation. Foliation has intermediate dips toward the NW, kinematically-related shear bands trend NE and dip, in general, steeper than the

foliation, and the stretching lineation is sub-horizontal NE–SW, parallel to axes of <a> type folds. These structures overprint relict earlier deformation fabrics and began syn-migmatically (Fig. 11B-3) with melt locally concentrated along shear bands; shear is overwhelmingly sinistral. Dikes intrude parallel to the foliation (5C-22, sub-volcanic granite), mostly normal to the stretching lineation (5C-2, diorite), thus indicating syn-tectonic magmatism, or crosscut irregularly (5C-28, pegmatite). Syn-kinematic hornblende and white mica date deformation as pre-to syn-35 Ma; a cluster of ~10 Myr younger ages (mostly cooling through 300°C) indicates later structural reactivation, as suggested by locally well defined, syn-kinematic mineral fabrics (e.g., stop 5C-2, Fig. 11B-4).

Paragneiss and micaschist at stop 5C-3 bound South El Tambor serpentinite and show syn-tectonic, greenschist-facies retrograde metamorphism. Late sinistral faults juxtapose these rocks with the serpentinite. Stations 5C-37, 38 at the southeastern edge of the same South El Tambor allochthon comprise migmatitic biotite gneiss, amphibolite, and leucogranite and their retrograde products. D_1 syn-amphibolite-facies deformation with local migmatites is overprinted by localized but pervasive greenschist-facies D_2 (Fig. 11B-5). The biotite gneiss and the amphibolite are in part extremely deformed and often l tectonites; s_1 and sinistral-transtensional shear bands dip intermediate to NW and str_1 plunges shallowly. The tourmaline–garnet–white mica leucogranites postdate the migmatitic gneiss, intrude mostly as sills, and are locally deformed syn-intrusive with high strain. D_2 induced vertical sinistral shear zones, <a> folds, foliation boudinage, and syn- and mostly antithetic faulting of leucogranite dikes and quartz segregation veins (Fig. 11B-5). The transition from shallowly dipping D_1 shear bands to vertical, ductile-brittle D_2 ones is abrupt (within ~10 m). Hornblende (amphibolite) and white mica (leucogranite) date the initiation of deformation and syn-tectonic intrusion at 40–35 Ma. The likely kinematic evolution from ductile (≤40 Ma) to ductile-brittle (~20 Ma, biotite) could be interpreted in this outcrop as long-lasting progressive deformation instead of structural reactivation (see above). Stations 5PB-1–5 and 861,862 expose unretrogressed Las Ovejas complex migmatitic biotite gneiss, intercalations of (garnet) amphibolite, biotite–white mica–garnet–tourmaline pegmatite, marble, and calcsilicate. Locally these rocks are post-tectonically annealed due to their proximity to granitoids (Fig. 14). At location 5PB-5 massive migmatite is enclosed in granite. Garnet amphibolite contained in the migmatite yielded ~650°C at 0.7–0.8 GPa peak metamorphic conditions and preserves pre-migmatitic garnet relicts. Deformation started prior to migmatization, is locally high-strain with migmatitic biotite-gneiss mylonite, and is sinistral-transpressive with local s–c mylonites. It continued with sinistral ductile-brittle faulting. Migmatization was at ~36 Ma (U/Pb zircon and Ar/Ar hornblende, see above). Station 5C-15 shows the Jocotán fault as a ductile–brittle sinistral fault zone. N–S ductile shortening with well devel-

oped sinistral shear bands changed to NE–SW compression in the brittle field. Low-T plasticity is recorded by bulging to dominant subgrain-rotation recrystallization in quartz.

7.10. Las Ovejas complex of northern Honduras

Stations 5H-1–6 characterize deformation of the western footwall of the Ulúa graben in northern Honduras (Figs. 14, 15). The Las Ovejas complex rocks and their deformation are similar to those in Guatemala. Partly migmatitic biotite gneiss, biotite granite, diorite, micaschist, and small white mica- and garnet- or hornblende-bearing pegmatite pods and sills deformed under sinistral transpression that started during the migmatitic stage. Deformation continued into the ductile–brittle field with sinistral-transtensive, SE-dipping shear zones/normal faults that we relate to opening of the Ulúa graben. The pegmatites either show strain concentration with well developed mylonite and ultramylonite or are variably but mostly weakly deformed, forming irregular pods. In comparison with Guatemala, foliation is rotated, dipping moderately to steeply N with the stretching lineation NE–SW; shear bands dip NW. Our 40–36 Ma U/Pb zircon ages from migmatitic biotite gneiss and the ~38 Ma Ar/Ar hornblende age from hornblende pegmatite constrain small-scale magmatism and deformation (see above). Syn-kinematic hornblende and biotite (Fig. 11B-6) and rapid cooling of K-feldspar in greenschist-facies, ductile–brittle shear zones related to the Ulúa graben suggest its initiation at ~28 Ma. At stop 5H-7, a top-to-E shear/normal fault zone separates orthogneiss from phyllite and is likely related to the Ulúa graben. The orthogneiss shows a relict older fabric (D_1) with NE dipping foliation. Greenschist facies with up to mylonitic deformation is present both in phyllite and orthogneiss. Shear bands show sinistral transpression (NE–SW shortening) with transition to brittle–ductile fabrics. Quartz shows subgrain-rotation recrystallization. Stations 5H-8,9 comprise orthogneiss and migmatite with mostly Permotriassic U/Pb zircon ages and Jurassic–Cretaceous cooling ages. These rocks are distinctly different from the Las Ovejas complex rocks along the MSZ. Migmatization is pervasive and thus different from the ~40 Ma event. D_1 is coeval with migmatization. Again, NE-dipping s_1 is overprinted by discrete ductile–brittle shear bands/zones that probably are Tertiary. Stations 5H-11,12 comprise low-T, mylonitic orthogneiss (likely a rhyolitic protolith) interlayered with thin paragneiss and marble (?metavolcanic sequence). A relict high-T deformation, again with the characteristic NE dipping foliation, is cut by greenschist-facies mylonite (locally chlorite out of biotite and sericite on mylonitic shear bands) with <3 cm chlorite-bearing ultramylonite layers. Overall deformation is top-to-SW sinistral transpression and likely related to the Jocotán fault zone.

7.11. Late Cretaceous and Tertiary–Quaternary sedimentary and magmatic rocks south of the Motagua suture zone, central Guatemala

Conjugate strike-slip fault sets that indicate ~E–W shortening dominate Upper Cretaceous limestones (stops GM4,5,7; Figs. 14 and 15). The quality of the field exposures do not allow us

to discriminate among subgroups representing a deformation sequence or to assess block rotations. The lack of a dominant E-trending set of sinistral strike-slip faults, which we attribute to the active stress field along the Motagua fault, distinguishes these stations from the Tertiary–Quaternary rocks (stops GM1,2,10; Figs. 14 and 15) but ties them to the deformation recorded in Subinal-Formation red beds. The latest increment of deformation in all these stations is E–W extension by normal faulting. Biotite granite (≥37 Ma) at stations 5H-5,6 within the footwall block of the Ulúa graben shows brittle–ductile normal faults and fracture cleavage related to graben formation dated by rapid cooling at ~28 Ma (Ar/Ar K-feldspar). Conjugate strike-slip faulting with N–S compression was followed by normal faulting (σ_3 of both events trends E) in red beds and volcanic rocks at station 5H-14 within the Jocotán fault zone.

7.12. South El Tambor Group on Las Ovejas complex and San Diego phyllite, central Guatemala

Stations 852, 855, 864, 869 comprise rare unfoliated blueschist, serpentinite, graphite-bearing meta-siltstone to phyllite with quartzite layers, and greenschist of the southern South El Tambor mélange. The meta-siltstones show ductile–brittle, heterogeneous fracture cleavage formed by pressure solution (diffusion creep), and quartz veins in meta-sandstone layers. D_1 shows open–tight, ~S vergent folds and thrust imbricates with associated fold–bend folds. We do not have age information on this mélange-forming event. These rocks are cut by sub-volcanic andesite dikes and sub-volcanic granite stocks, which we interpret as apophyses of the Chiquimula batholith. D_2 affects the mélange rocks and these dikes/granitoids by ~E trending (transtensional) strike-slip and normal faults. Their low-T nature and the presence of ~20 Ma sub-volcanic granite in the Chiquimula batholith (see above) suggest Tertiary faulting.

7.13. Interpretation of new structural geology

Our work along the MSZ focused on the Cretaceous–Cenozoic deformation. Clearly, however, older events occurred. In the Chuacús complex, Triassic deformation, studied superficially, shows high-T ductile flow and is distinct in structural geometry and kinematics: (N)W striking foliation, NW trending stretching directions, tight–isoclinal <a> folds. Shortening appears coaxial N(E)–S(W) with strong along strike lengthening. Associated high-T metamorphism, migmatization, and magmatism are Late Triassic (238–215 Ma, major group at ~220 Ma). Foliation trajectories of the Late Cretaceous, Maya-block deformation change from WNW in western, to W in central, and SW in eastern Guatemala. Using the (W)NW-strike of the Late Cretaceous–Paleocene Mexican thrust belt as a reference frame (e.g., Nieto-Samaniego et al., 2006), this implies large-scale sinistral shear. The southern Maya block in Guatemala apparently comprises a ductile–brittle nappe stack, whose detailed geometry remains to be established. The North El Tambor Group allochton in the hanging wall, itself an accretionary stack of rocks of variable tectonostratigraphic origin and subduction depth, is underlain by an up to several 100 m

thick carapace of imbricated rocks, containing Chuacús basement and cover, altered by fluid infiltration and metasomatism. The central Chuacús complex may either constitute a Late Cretaceous antiformal stack or, our preferred model, an antiform above a blind thrust, exposing pre-Cretaceous metamorphic and magmatic products in its core. The Baja Verapaz shear zone is the sole thrust to this stack. The northern El Tambor sheets (Baja Verapaz, Sierra des Santa Cruz) are cut by out-of-sequence thrusts that are part of the foreland fold–thrust belt. The relatively high-P (0.7–0.8 GPa) and relatively low-T (≥450°C) metamorphism in the Chuacús complex suggests subduction of oceanic crust transitioning to continental crust (the Chuacús geothermal gradient is ≥18°C/km from our data) and steep continental subduction; this is supported by the nearly coeval blueschist (~76 Ma, North El Tambor Group) and epidote–amphibolite- to amphibolite-facies (≤75 Ma, Chuacús complex) metamorphism in the accretion stack and the sinistral-transpressive deformation. Penetration of deformation and overburden (PT conditions) appear to increase from western to eastern Guatemala. Although in detail variable, meso-scale Late Cretaceous deformation is simple: N–S shortening by reverse shear zones and up to two generations of folds are accompanied by sinistral strike-slip shearing and major E–W lengthening. Tangential stretching is dominant in most cases, as deduced from the mostly shallowly plunging stretching lineation. In detail, overall sinistral transpression is typically partitioned between oblique stretching within the foliation and strike-slip along steeper dipping shear zones/bands transecting the foliation. Flow has a dominant non-coaxial component, most clearly expressed by quartz LPOs, developed during dynamic, subgrain-rotation dominated recrystallization. There is a clear kinematic continuity from ductile to brittle deformation. Although dominated by diffusion creep, deformation is on first-order identical within the northern foreland fold–thrust belt, the sole thrust carapace below the North El Tambor Group sheet, and within it. Emplacement of the El Tambor allochton, poorly constrained by our data, appears to change from tangential to frontal over time (strike-slip before thrusting).

Structural trends in the northern foreland fold–thrust belt and the Chuacús complex of western Guatemala are NW and oblique to the Polochic fault zone, testifying to the younger age of this fault. Polochic mylonitic deformation appears to be younger than ~15 Ma (apparent post-tectonic pluton), although our only Tertiary age (~37 Ma) from western Guatemala (G27s, stop G57), from a discrete low-T mylonite zone in gneiss close to the Polochic fault zone, may hint at a late Eocene slip history. Ductile to brittle slip along the Polochic is dated as late Neogene–Recent in western Guatemala (TFT and AFT ages) and at ~8 Ma (Ar/Ar chronology) along the, likely kinematically related, Tonala shear zone in southeastern Mexico.

Tertiary volcanic rocks record a phase of pronounced N–S shortening along the western Polochic fault zone. Its active deformation is by a kinematically-related combination of strike-slip and normal faulting. We interpret the Subinal-Formation red beds as intra-continental molasse

related to late-stage, erosional unroofing of the Chuacús complex. Its deformation was developed during N–S shortening by folding and fold-axis parallel extension, accompanied by sinistral shear. The latest stage indicates N trending graben formation.

Our study indicates that the Las Ovejas complex of the northern Chortís block is less a lithologically defined unit than distinguished from the other basement units by its Tertiary metamorphism, magmatism, and deformation. It forms a westward narrowing belt of overall sinistral transtension along ~NW-dipping foliations. Deformation penetration apparently increases toward north, the MSZ, and seems to be more localized and to die out southward and westward. The belt of Tertiary shear thus appears to trend oblique to the Motagua fault. Deformation interacts with amphibolite-facies metamorphism, widespread migmatization, and local magmatism, demonstrated most clearly by small syn- to post-tectonic pegmatites. The close special and temporal interaction between high-strain deformation and Tertiary metamorphism, migmatization, and magmatism is confined to the northern Chortís block. It appears that arc magmatism/metamorphism provided the heat input localized deformation. Deformation started premigmatitic and occurred in a kinematic continuity from ductile to brittle. Batholiths are posttectonic. Tertiary sinistral-transtensional wrenching appears, like the Cretaceous deformation of the Chuacús complex, partitioned between oblique stretching along a shallower dipping foliation and strike-slip along steeper dipping shear zones/bands. Deformation began prior to 40 Ma and we suggest that there were two major phases, ≥40–35 Ma and 25–18 Ma. This reactivation interpretation still must be tested. The Ulúa graben started in temporal and kinematic continuity with wrenching along the Las Ovejas complex at ~28 Ma. The topographically well developed active grabens, however, are a neotectonic feature. Also the Jocotán-Chamelecón fault zone was part of this deformation system, albeit mostly ductile–brittle. The Tertiary event veils pre-Cenozoic tectonometamorphic–magmatic events, with distinct structural orientation and kinematics. The latest preserved is Jurassic and has a NW structural trend. The South El Tambor Group was emplaced by S-vergent thrusting and associated folding. It is involved with the Tertiary sinistral wrench deformation.

The Sanarate complex with its distinct lithology, metamorphism, and age of metamorphism is affected by the Tertiary deformation but has a characteristic W dipping foliation and top-to-E flow in its dominant amphibolite lithology. This deformation is Jurassic or younger. Late Cenozoic deformation, preserved in Late Cretaceous and Tertiary–Quaternary rocks on the Chortís block, is by distributed sinistral strike-slip. The latest event we recognized in the Chortís block and the Subinal Formation is E–W extension by normal faulting. The entire MSZ area shows gravitationally induced faulting due to the large topographic relief.

8. Discussion

Here we return to the principal questions this paper aims to address: (i) which crustal sections of the MSZ accommodated the large-scale sinistral offset along the northern Caribbean plate boundary, when did it occur, and in which kinematic framework, and (ii) what Paleozoic–Tertiary geologic correlations exist between the Maya block, the Chortís block, the tectonostratigraphic complexes ("terranes") of southern Mexico, and the arc/subduction complexes of the northern Caribbean. First we focus on geologic correlations proceeding from Paleozoic to Recent, then we refine Caribbean tectonic models for the Cretaceous and Cenozoic.

8.1. Appalachian–Caledonian orogeny in the Maya block

The central and northern Chuacús complex contains a paragneiss-dominated sequence in which meta-basalts prevail among the magmatic rocks, and quartzite and calcsilicate/marble are minor constituents. The sequence may be divided into the hanging Rabinal complex and the lower Chuacús complex *s.s*. (Fig. 2C and D). Their boundary is a Cretaceous shear zone but this may represent reactivation of an older structure. Both complexes contain Middle Proterozoic crust (U/Pb zircon), the Rabinal complex is dominated by 485–400 Ma (age groups at 465 Ma and 413 Ma) mega-crystic K-feldspar augen gneiss and apparently lacks meta-basalts. The lower Chuacús complex shows high-P (perhaps ultrahigh-P) metamorphism that is, at best, constrained in age to between 477 Ma and 402 Ma, and conservatively to between 638 and 302 Ma (Figs. 2D, 16A; see above). Due to multiple magmatic–metamorphic overprints, post-high-P retrogression is mostly undated. The early stage of migmatization, interpreted as decompression melting, is at ~302 Ma (Ortega-Gutiérrez et al., 2004). The Rabinal complex apparently lacks high-P metamorphism but this has to be confirmed by quantitative petrology. Lower Carboniferous (≤350 Ma) Santa Rosa Group sediments cover the complexes unconformably (Fig. 2C). We correlate this sequence with the Acatlán complex of the Mixteca terrane of southern Mexico.

The Acatlán complex comprises a nappe stack containing Middle Proterozoic to Paleozoic units imbricated during the Paleozoic. To date, seven nappes containing distinctive stratigraphy have been discriminated (Fig. 2I; Talavera-Mendoza et al., 2005). The entire stack shares a ~325 Ma regional metamorphism (Vega-Granillo et al., 2007). The Xayacatlán suite comprises eclogite-facies, mafic and pelitic rocks (Ortega-Gutiérrez et al., 1999) and is intruded by Ordovician leucogranites (478 ± 5 to 461 ± 9 Ma; Talavera-Mendoza et al., 2005), postdating high-P metamorphism. Peak PT conditions were at 490–610°C and 1.2–1.3 GPa, reached during Early Ordovician (~490–477 Ma, U/Pb zircon; Vega-Granillo et al., 2007). The suite re-equilibrated in greenschist facies during the Mississippian (~332–318 Ma, Vega-Granillo et al., 2007; Yañez et al., 1991). The hanging Esperanza suite is dominated by Early Silurian (442 ± 5 to 440 ± 14

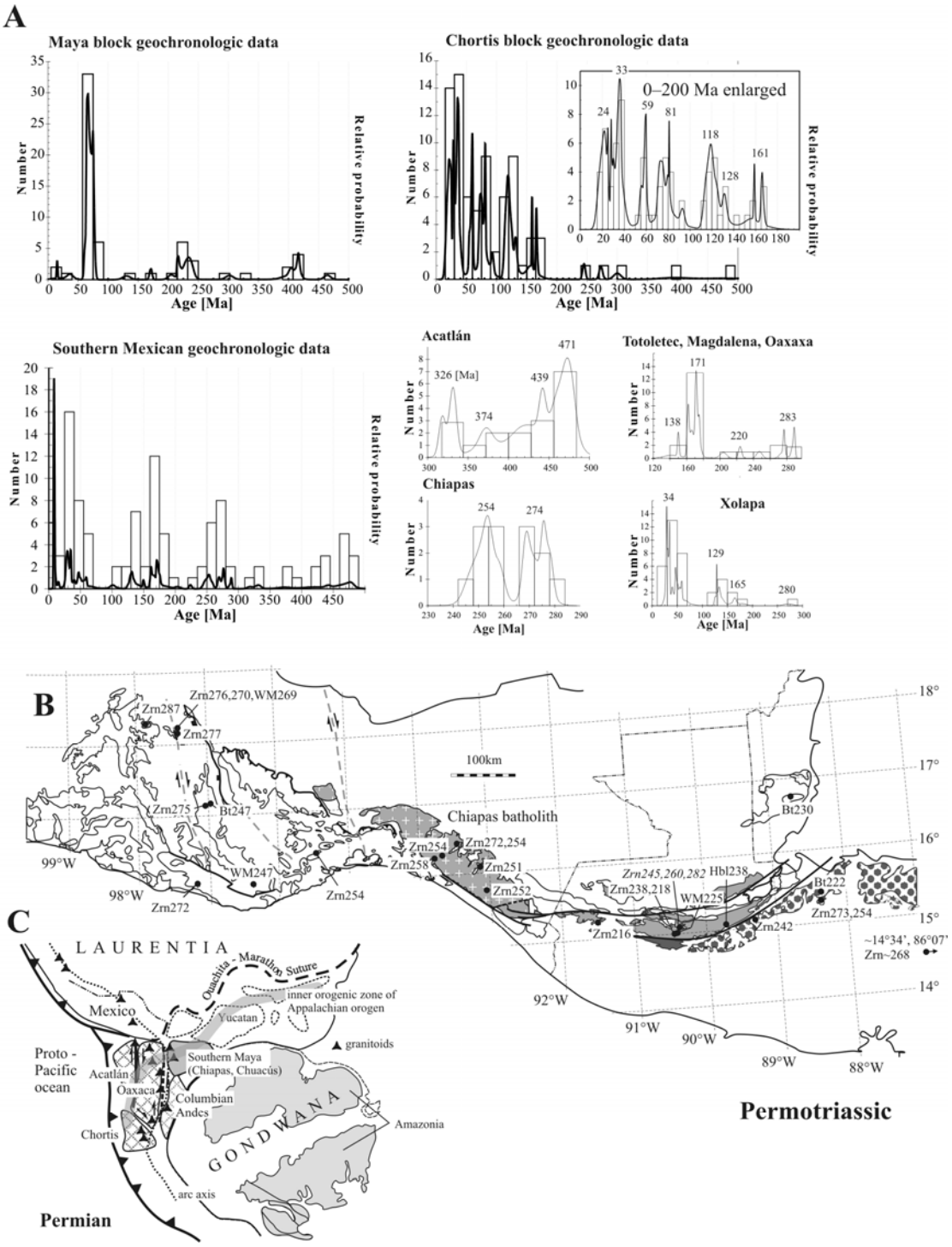

Figure 16. Tectonic–paleogeographic evolution models for the northern Caribbean plate boundary and Paleozoic–Cenozoic correlations between southern Mexico and the Chortís block. (A) Overview of our new and published geochronology from the Maya block, the Chortís block, and southern Mexico. Data are referenced in the captions of Fig. 1 and the text. (B) Permotriassic ages of southern Mexico and northern Central America. Ages in italics refer to detrital zircons. (C) Paleogeographic model for the Permian modified from Weber et al. (2006) and Vega-Granillo et al. (2007) emphasizing arc magmatism along the margins of Laurentia and Gondwana and a common position of the Acatlán complex and the Maya block in the inner orogenic zone of the Appalachian orogen.

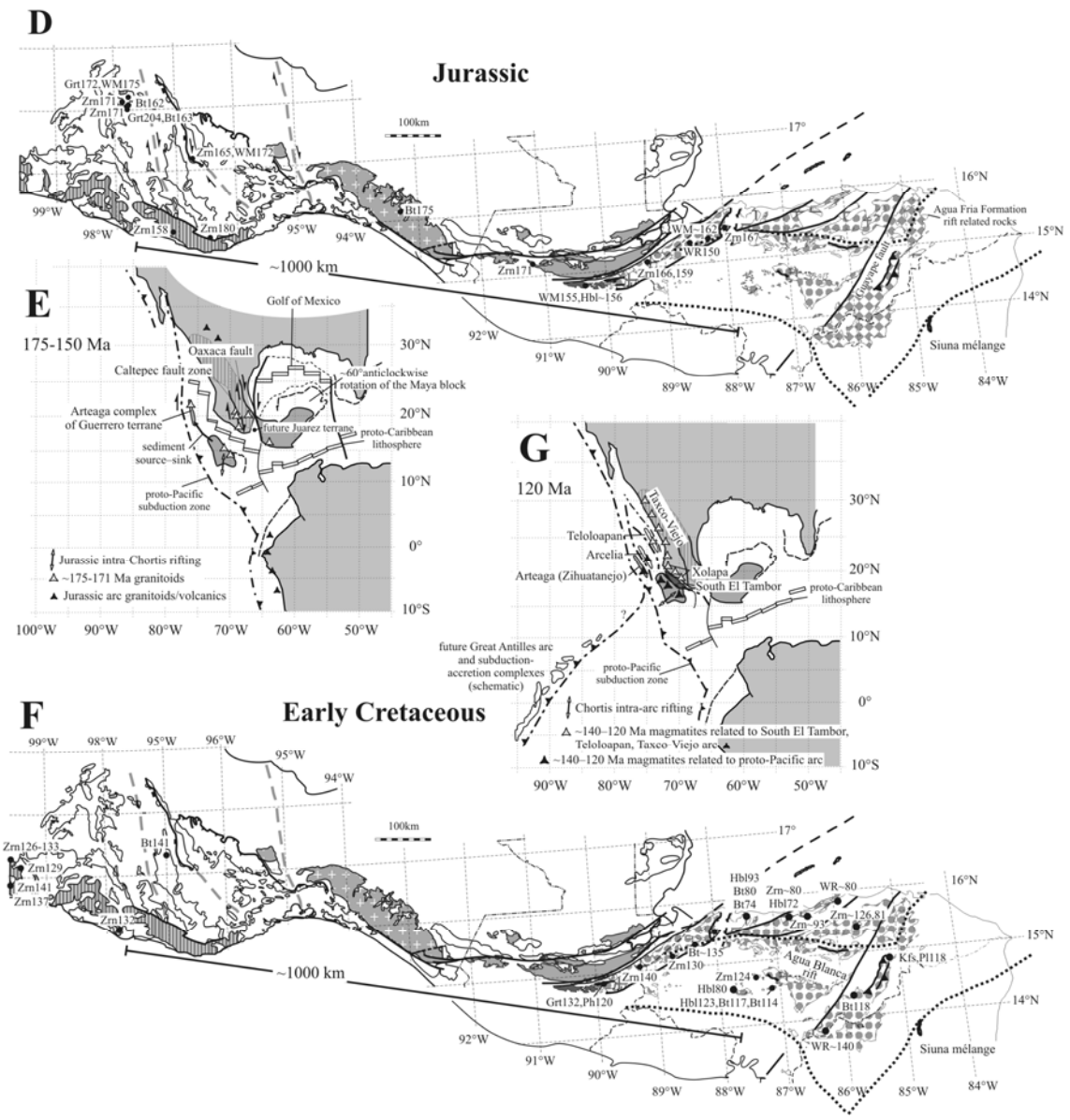

Figure 16. (continued) (D) Jurassic ages along the northern Caribbean plate boundary. Subdivision of the Chortís block follows Roger et al. (2007c). (E) Middle to Late Jurassic tectonics of the Caribbean emphasizing rifting of the Chortís block from southern Mexico and its connection with the Arteaga complex of the Zihuatanejo terrane of southwestern Mexico. (F) Early Cretaceous ages of southern Mexico and northern Central America. (G) Late Early Cretaceous tectonics of the Caribbean underlining emplacement of the South El Tambor Group rocks onto the Chortís block and the existence of continuous arcs off southwestern and southern Mexico: Chortís–Xolapa–Taxco–Viejo; South El Tambor Group–Teloloapan; Arteaga (Zihuatanejo)–Sanarate (Chortís).

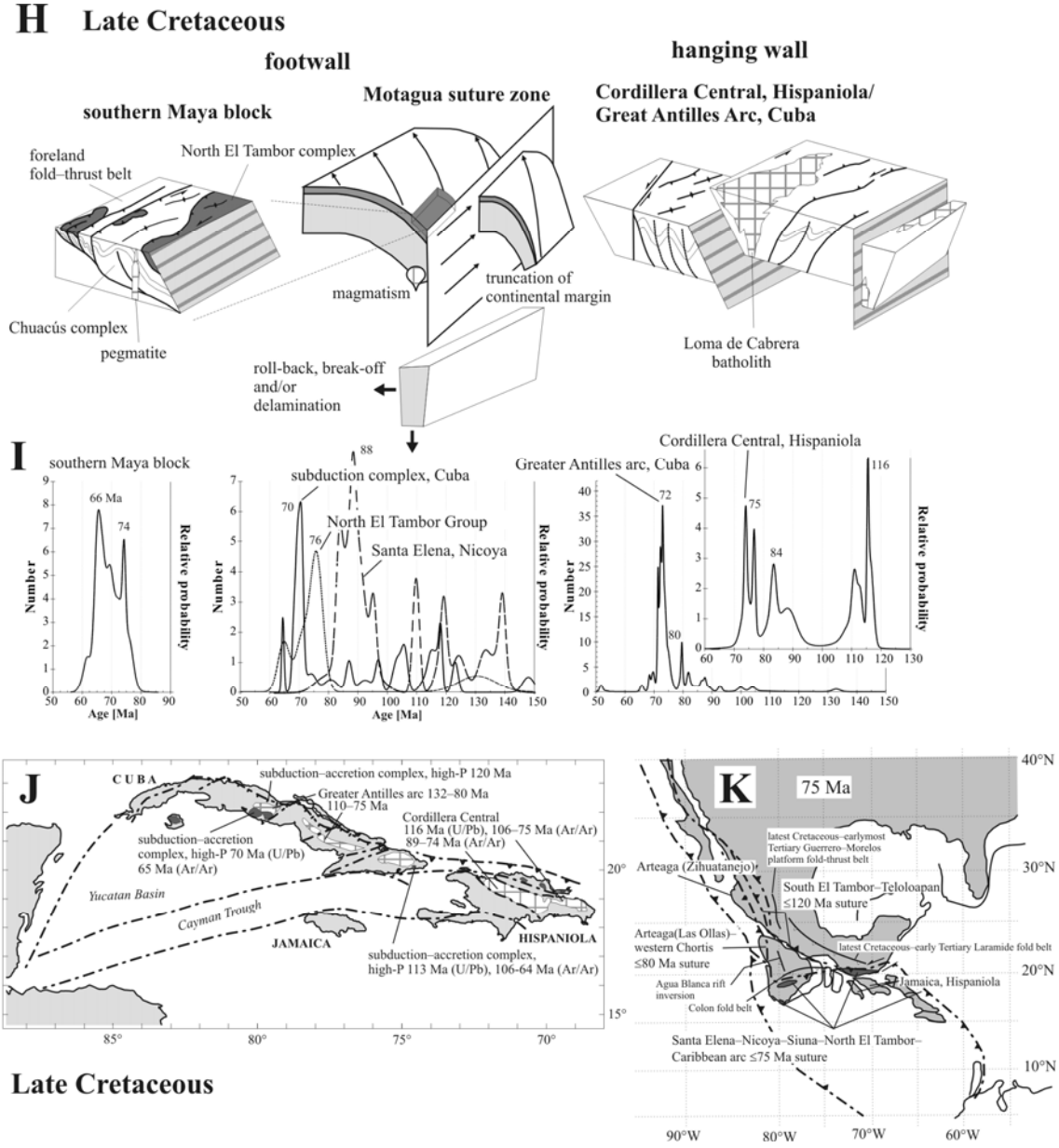

Figure 16. (continued) (H) Block diagrams illustrating a N–S swath across the Motagua suture zone at ~70 Ma. The southern Maya block is imbricated by sinistral transpression. Roll-back and break-off of the North El Tambor Group (Caribbean) slab may have caused magmatism in the southern Maya block. Truncation of the continental margin by sinistral transpression; hanging wall arc magmatism terminated contemporaneously to slightly after (reflecting transfer to the Bahamas continental margin) their collision with the southern Maya and southern Chortís blocks (see text for further discussion). Hanging-wall arc diagram modified from the Cordillera Central, Hispaniola, situation (Escuder-Viruete et al., 2006a). (I) Geochronology of the footwall and hanging wall of the Motagua suture zone: left, ages of imbrication and associated metamorphism in the southern Maya block (this paper); center, ages in the North El Tambor Group (see references in the text) and the subduction–accretion complexes in Cuba (Garcia-Casco et al., 2002, 2007; Schneider et al., 2004; Krebs et al., 2007); right, ages from the Greater Antilles arc, Cuba, and Cordillera Central arc, Hispaniola (Grafe et al., 2001; Hall et al., 2004; Stanek et al., 2005; Rojas-Agramonte et al. 2006; Kesler et al., 2005; Escuder Viruete et al., 2006b). (J) Subduction–accretion and arc complexes of Cuba and Hispaniola and major age groups emphasizing the evolution of the hanging wall of the Motagua suture zone. (K) Late Cretaceous tectonics of the northern Caribbean highlighting the two Late Cretaceous suture zones on the Chortís block.

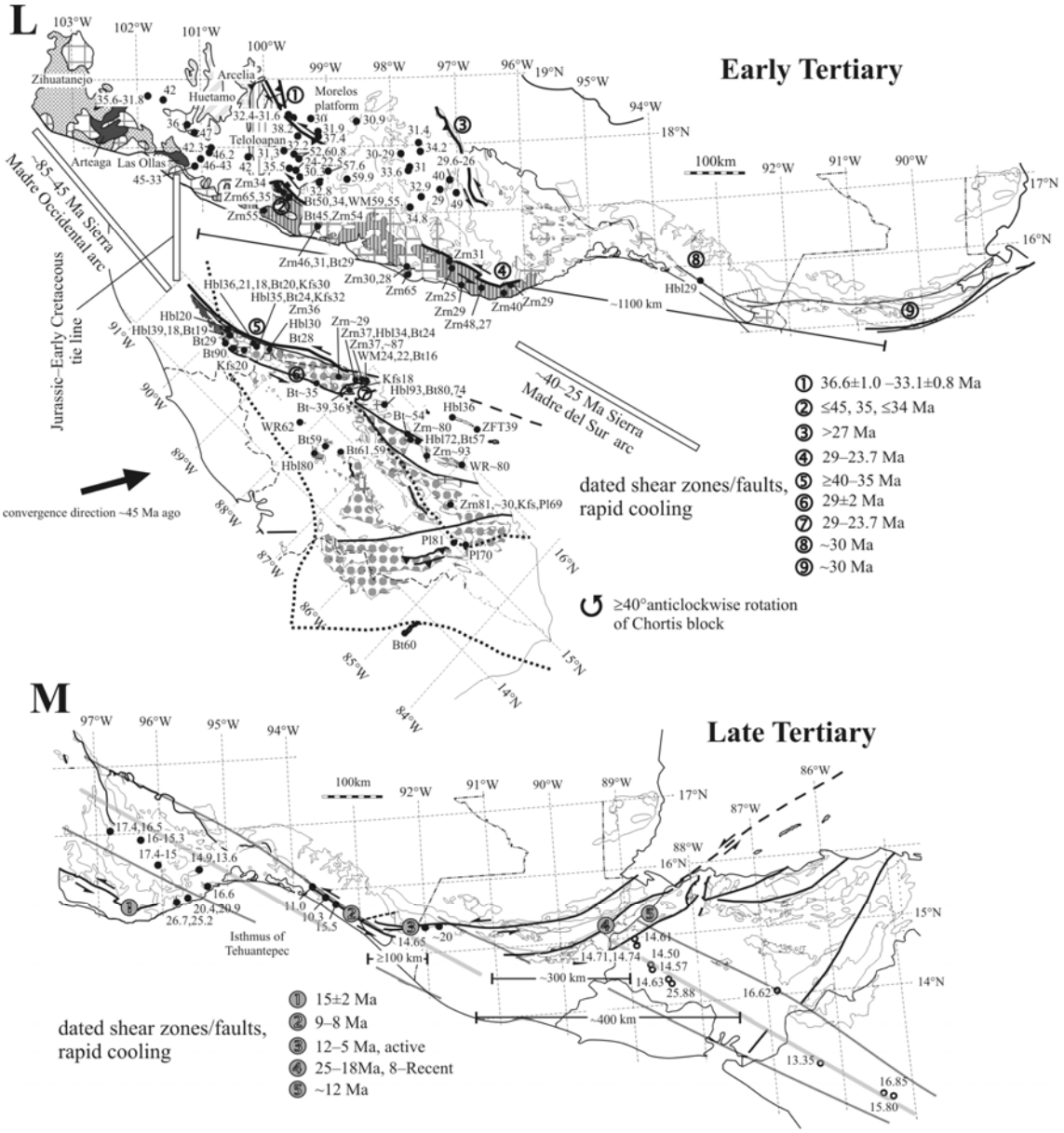

Figure 16. (continued) (L) Late Cretaceous and early Tertiary ages along the northern Caribbean plate boundary bringing the Chortís block to its pre-~40 Ma position off southern Mexico. Geochronologic data compiled from Herrmann et al. (1994), Morán-Zenteno et al. (1999), Ducea et al. (2004), Cerna et al. (2007) and references therein. Deformation zones (numbers 1–9) and their ages are discussed in the text. Convergence direction at ~45 Ma is from Pindell et al. (1988). (M) Middle Miocene ages along the northern Caribbean plate boundary. Geochronology is from this paper, Morán-Zenteno et al. (1999), and Jordan et al. (2007) and references therein. Deformation zones (numbers 1–5) and their ages are discussed in the text.

Ma; Ortega-Gutiérrez et al., 1999; Talavera-Mendoza et al., 2005) mega-crystic, K-feldspar augen gneiss and contains meta-sediments and meta-basalts transformed to eclogite. The entire suite records peak PT at 730–830 °C and 1.5–1.7 GPa reached at ~430–420 Ma. Partial overprinting occurred at 640–690°C and 1.0–1.4 GPa prior to ~375 Ma. The high-P nappes were stacked before the Early Carboniferous (Figs. 2G; 16A-Acatlan; Vega-Granillo et al., 2007).

A possible correlation equates the lower Chuacús and Rabinal complexes of the southern Maya block with the Esperanza suite of the Mixteca terrane, based on comparable lithology, time, and values of high-P metamorphism (Fig. 2C, D and I; 16A). In this scenario the Rabinal gneisses must contain high-P relicts. Due to the abundance of mafic rocks in the lower Chuacús complex, its correlation with the Xayacatlán suite is preferred. In this scenario the Rabinal gneisses would represent post-high-P intrusions (Fig. 2I).

Although our data from the Chortís block are sparse, U/Pb analysis identified ~480, ~400, and ~329 Ma zircons in the basement rocks, suggesting that this block also experienced Ordovician–Devonian–Carboniferous magmatism/metamorphism. We propose that the southern Maya block was part of the Alleghanian–Appalachian orogen and due to its high-P metamorphism and extensive Ordovician–Silurian magmatism was located together with the Acatlán complex within the orogenic interior along the southern margin of North America. It is likely that the Chortís block also belonged to this orogen (Fig. 16C).

8.2. Permotriassic arc on Maya and Chortís blocks

Gneiss of the Chuacús complex of western Guatemala was migmatized at ~216 Ma. In central Guatemala, orthogneiss intruding high-P paragneiss and garnet amphibolite records two zircon-crystallization events at 238 and 219 Ma. Regional magmatism/metamorphism is demonstrated by similar hornblende and white mica cooling ages (238–225 Ma; Fig. 16A and B). Phyllite interlayered with conglomerate of the Sacapulcas member of the Santa Rosa Group contains detrital zircons at ~282, ~260, and ~245 Ma. Volcanic pebbles dominate the conglomerate. Triassic deformation in the Chuacús complex shows high-T flow with N(E)–S(W) shortening and both sub-vertical and along-strike, NW–SE extension. In the Chortís block, migmatitic orthogneiss crystallized at ~273 Ma and underwent high-T metamorphism at ~245 Ma. Inherited ~241 Ma zircon in Jurassic orthogneiss and biotite cooling ages support regional Triassic magmatism/metamorphism (Fig. 16A and B).

Permotriassic granitoids are documented along the length of Mexico and probably extend into northwestern South America (e.g., Centeno–García, 2005). Their apparent linear arrangement likely traces an active continental margin that originated after final amalgamation of Pangea during the Ouachita–Marathon orogeny at ~290 Ma (Fig. 16C; Torres et al., 1999). Isotopic

ages of these granitoids span 287–210 Ma with reliable U/Pb zircon ages at 287–270 Ma (Figs. 1C, 16A-Ttoletec/Magdalena/Oaxaxa, 16B; Yañez et al., 1991; Solari et al., 2001; Elías-Herrera and Ortega-Gutiérrez, 2002; Ducea et al., 2004a). In contrast to these mostly undeformed granitoids, the Chiapas-massif batholith rocks (Fig. 16B) are deformed and metamorphosed (Weber et al., 2006a). Rock types include orthogneisses that are intruded by calc-alkaline rocks varying from granite to gabbro, meta-sedimentary rocks (metapelite/psammite, calcsilicate; Sepultura unit) and mafic rocks (hornblende gneiss; Custepec unit). Zircons from orthogneiss yielded a concordia age at 271.9 ± 2.7 Ma, and three samples from migmatitic paragneiss and leucosome yielded 254.0 ± 2.3 to 251.8 ± 3.8 Ma ages (Fig. 16A-Chiapas). The latter ages date the most prominent event in the Chiapas massif—partial anatexis in metapelite/psammite and, locally, orthogneiss. High-grade metamorphism is contemporaneous with ~N–S shortening (Weber et al., 2006a).

Our new ages indicate that during the Permotriassic the southern Maya and the northern Chortís blocks were part of a continuous magmatic arc from northeastern Mexico to northern South America (e.g., Dickinson and Lawton, 2001), which initiated after the formation of Pangea along the western continental margin of Gondwana (Fig. 16C). Sample 5H-9a zircons of migmatitic orthogneiss in the north-central Chortís block have within error the same intrusion and high-grade metamorphic ages as the Chiapas-massif rocks (Fig. 16A). This identical geologic history suggests a direct correlation between the Chiapas massif and the northern Chortís block along the Permotriassic arc prior to the opening of the Gulf of Mexico (Fig. 16B and C). The ages in the Chuacús complex are ~30 Ma younger than those in the Chiapas massif and also younger than most Permotriassic ages in southern Mexico. We speculate that the Chuacús complex occupied, together with the Maya Mts. of Belize, an easterly position along the main Chiapas–Chortís arc (Fig. 16C). The younger ages may reflect an episode of flat-slab subduction that shortened the main arc (Weber et al., 2006a) and caused a younger episode of magmatism/metamorphism in its hinterland. Shortening directions are similar in the Chuacús complex and the Chiapas massif. Associated with the shortening there is likely a dextral-transpressional component, widespread in southern Mexico (e.g., Malone et al., 2002), which is consistent with tangential stretching in the Triassic Chuacús complex.

Above, we correlated the lower Chuacús and Rabinal complexes of Guatemala with the Acatlán complex of the Mixteca terrane of southern Mexico (Fig. 2C, D and I). Although strongly overprinted by magmatism/metamorphism, the Sepultura and Custepec units of the Chiapas massif show similarities with the meta-sedimentary and meta-basaltic units of southern Mexico and Guatemala. Ties are also provided by the cover sequences; for example, ~420 Ma detrital zircons are found in the Chiapas-massif Santa Rosa Group (Weber et al., 2006b) and the Sacapulcas rocks of Guatemala (Fig. 2B and C). Pan-African zircons occur in the Santa Rosa

Group and as inherited zircons in the Chortís-block rocks and suggest proximity of both the Maya and Chortís blocks to Gondwana (Fig. 16C). Conglomerate clasts that are predominantly sourced from intermediate volcanic rocks, and ~245, ~260, and ~280 Ma detrital zircons make the Chiapas–Chortís-arc massif the likely source of the Sacapulcas rocks.

8.3. Jurassic rifting and arc magmatism

Granite intruded into the Chuacús complex of western Guatemala at ~171 Ma (164–177 Ma zircons; Fig. 16A). Most of the Maya block was probably emergent during the Triassic–Jurassic with the likely Middle Jurassic–Early Cretaceous Todos Santos Formation reflecting rifting during Jurassic separation of North and South America (Fig. 2B; e.g., Donnelly et al., 1990). Granites also intruded the northern Chortis block during the Middle Jurassic (~159 and 166 Ma, zircons at 140–191 Ma; 167 Ma; ~168 Ma; Fig. 16D). The Middle Jurassic, clastic, partly greenschist-facies Agua Fria Formation (Fig. 2J) thickens from the central to the eastern Chortís block and is interpreted to be related to transtension and rifting during the Jurassic opening between North and South America; e.g., the Guayape fault zone may have originated as a Jurassic normal fault (Fig. 16D; e.g., James, 2006; Gordon 1993). The rocks of the Agua Fria Formation were deformed during the Late Jurassic (Viland et al., 1996).

Early–Middle Jurassic magmatism–metamorphism affected the Chazumba and Cosoltepec units of the Acatlán complex and produced the Magdalena migmatites of southern Mexico (Figs. 2I, 16A-Totoletec, Magdalena, Oaxaca; e.g., Talavera-Mendoza et al., 2005; our new ~162 Ma cooling age); inferred metamorphic conditions were low-P/high-T (~730°C at ~0.55 GPa; Keppie et al., 2004). Anatectic granitic dykes of the San Miguel unit (175–172 Ma; e.g. Yañez et al., 1991) cut the former units. These events have been interpreted as the result of a plume breaking up Pangea, opening of the Gulf of Mexico, and Triassic–Middle Jurassic magmatic arc activity (e.g., Keppie et al., 2004). ~ Approximately 165 Ma, NNW trending, dextral transtension shear, kinematically compatible with opening of the Gulf of Mexico, occurred along the Oaxaca fault (Alaniz-Alvarez et al., 1996), and NW-trending, Jurassic earliest Cretaceous dextral transpression took place within the northern Oaxaca complex (Solari et al., 2004). The Xolapa complex (Fig. 2L) also shows 165–158 Ma magmatic–metamorphic ages (Fig. 16A-Xolapa; Herrmann et al., 1994; Ducea et al., 2004a). The Zihuatanejo and Huetamo mature arc sections of the Guerrero terrane rest unconformably on the Arteaga–Las Ollas basement, which comprises ocean-floor–continental-slope–subduction complexes that were deposited in the Late Triassic–Early Jurassic, intruded by 187 ± 7 Ma granite, and deformed in the Middle Jurassic (Fig. 2M). Major late Middle–Late Proterozoic–Phanerozoic detrital zircon populations from these complexes are ~247, ~375, ~475, 575, ~975 Ma. The overlying Cretaceous arc has major zircon populations at ~160, ~258, ~578, ~983 Ma (Fig. 2M; Talavera-Mendoza et al., 2007).

Our tectonic model (Fig. 16E) integrating the Jurassic evolution of the Maya and Chortís blocks with the magmatic–tectonic evolution of southern Mexico is modified from Mann (2007). Onset of rifting in the Gulf of Mexico and between North and South America reduced Triassic (see above) to Jurassic volcanic eruption rate in southern Mexico and the Maya and the Chortís blocks. Late intrusion into active dextral (Mexico) fault zones may explain the concentration of magmatism at 175–166 Ma (Fig. 16D). Rifting of the Chortís block from southern Mexico likely initiated along the arc and developed either as back-arc extension above the proto-Pacific subduction zone, a failed arm of the proto-Caribbean rift, or a combination. Additionally, the Arteaga–Las Ollas basement units rifted from southern Mexico, as they likely shared the Late Triassic–Jurassic history of southern Mexico (Fig. 2M; e.g., Talavera-Mendoza et al., 2007). Our model requires rifting the Chortís block from southern Mexico and creation of oceanic crust, because MORB oceanic crust and mélange of the South El Tambor Group is present between the Chortís block and southern Mexico. This must predate 132 Ma, the age of eclogite formation in the South El Tambor Group and is likely pre-Late Jurassic, the probable age of the oldest radiolarians in the South El Tambor cherts (Chiari et al., 2004). Rifting affected also the interior of the Chortís block (Agua Fria Formation; Fig. 16D). These rift structures trend ~NE (present coordinates), sub-parallel to the northwestern and southeastern margins of the Chortís block and the Guayape fault. This rifting is distinctly different from the WNW trending mid–Cretaceous intra-arc rifting (Roger et al., 2007a; see below). The Late Jurassic regional metamorphism (165–150 Ma; Fig. 16A) and deformation (Viland et al., 1996) may be rift and strike-slip related.

Several likely connections exist between the Chortís block, the Xolapa complex, and the Guerrero composite terrane. The Sanarate complex (Fig. 2E), the westernmost basement outcrop of the Chortís block south of the MSZ, was included with the South El Tambor Group because of its metamorphism (lower metamorphic grade than that of the Las Ovejas unit) and rock assemblage (dominated by mafic and clastic rocks) (e.g., Tsujimori et al., 2004, 2006); however, the Jurassic age for the metamorphism precludes such a correlation. Here we suggest a correlation of this complex with the Arteaga–Las Ollas units (Figs. 2M and 16E) based on lithology, likely proximity to the Jurassic continental margin of Mexico, and distinct Jurassic metamorphism (Fig. 2E and M). The Sanarate complex likely also includes parts of the Cretaceous Zihuatanejo and Huetamo volcanic and clastic units (Fig. 2M). Both the Arteaga–Las Ollas units and the overlying Cretaceous arc contain zircons that may have originated from the Chortís block. The ~247, ~257, and 475 Ma clusters, particularly in the ≥85 Ma arc rocks are especially difficult to derive from North America because of intervening spreading ridges and subduction zones (Figs. 2M and 16E, see below). The pre-migmatitic basement of the Xolapa complex, containing evidence for a Grenville crustal component (Herrmann et al., 1994) and Permian

magmatism (see above) in an alternation of meta-greywacke and meta-basic rocks, probably correlate to the Permian and Jurassic section of the Mixteca terrane (Fig. 2M, Olinalá unit). Finally, connecting the Jurassic magmatic–metamorphic rocks of southern Mexico and the northern Chortís block implies a ~1000 km post-Jurassic offset.

8.4. Early Cretaceous subduction, top-to-S emplacement of the South El Tambor Group, and proto-Pacific arc formation

Spreading between the Chortís block and southern Mexico must have reverted to subduction before 132 Ma (see above). The ~120 Ma phengite ages of the South El Tambor Group blueschists are interpreted as marking fluid infiltration during retrogression from eclogite facies conditions (see above) and likely date exhumation during emplacement of the South El Tambor Group mélange onto the Chortís block (Fig. 8B). The El Tambor rocks are emplaced top-to-S (present coordinates). Aptian–Albian calc-alkaline, arc volcanic rocks of the Manto Formation and volcanoclastic rocks of the Tayaco Formation, sandwiched between shallow water carbonates, were deposited in a zone of intra-arc extension in the central Chortís block, the Agua Blanca rift (Roger et al., 2007a; Fig. 16F). The strike of the rift is WNW (present coordinates), oblique to the northern margin of the Chortís block and the Jurassic extensional structures (see above). Cretaceous (peaks at ~128, ~118, ~81 Ma; Figs. 16A and 5H) magmatic rocks are widespread on the Chortís block (Fig. 16F) and likely mark continuous arc formation above the proto-Pacific subduction zone (Fig. 16G). The Xolapa complex, the largest plutonic and metamorphic mid-crustal basement unit in southern Mexico preserves abundant migmatites that were produced during a single metamorphic event with peak prograde conditions at 830–900°C and 0.63–0.95 GPa. This occurred within a continental magmatic arc and overprinted a pre-migmatitic metamorphic assemblage (Corona-Chávez et al., 2006). Deformation, likely (N)NE–(S)SW shortening (Corona-Chávez et al., 2006), associated with low-P metamorphism and migmatization predates 129 ± 0.5 Ma in the Tierra Colorada area of the western Xolapa complex (Solari et al., 2007). The migmatites have been directly dated at 131.8 ± 2.2 Ma (Herrmann et al., 1994) and 130–140 Ma (Ducea et al., 2004a). The structural top of the migmatized sequences is the 126–133 Ma Chapolapa Formation (Campa and Iriondo, 2004; Hernández-Treviño et al., 2004) that mostly comprises meta-andesite/rhyolite. The hanging wall Albian–Cenomanian Morelos Formation shelf limestone is in tectonic contact (Figs. 2L, 16A-Xolapa; e.g., Riller et al., 1992; Solari et al., 2007).

Roger et al. (2007a) suggested several features and piercing lines that convincingly tie the Chortís block to southern Mexico; here we elaborate on the tectonic model explaining the correlation (Fig. 16G). We suggest that the 141–126 Ma migmatization–magmatism of the Xolapa complex represents arc magmatism related to subduction of the South El Tambor Group lithosphere. Characteristically, no Cretaceous ages younger than ~126 Ma have been found in Xolapa

complex, so the end of arc magmatism in the South El Tambor subduction zone is likely contemporaneous with emplacement of the South El Tambor Group onto the Chortís block (≤120 Ma, see above). Laterally, Xolapa-complex magmatism is correlated with that in the Taxco–Viejo unit of the Mixteca terrane, also an arc on continental crust (e.g., Centeno-García et al., 1993) and dated at 130.0 ± 2.6 and 131.0 ± 0.85 Ma (Campa and Iridono, 2004). This correlation is supported by the, within error, identical ages of the Chapolapa Formation meta-andesite/rhyolite (Xolapa complex) and the volcanic flows of the Taxco–Viejo unit (Fig. 2L and M). Magmatism in the Teloloapan intra-oceanic arc ended at ~120 Ma. Magmatism in the oceanic arc and back-arc region of the Arcelia units, outboard (southwesterly) of the Teloloapan unit continued into the Cenomanian (Fig. 2M). The youngest detrital zircon fractions in the clastic rocks above the volcanic succession in the Teloloapan and Taxco–Viejo units, comprising magmatic zircons from local sources, are ~124 and ~132 Ma, respectively (Talavera-Mendoza et al., 2007), thus contemporaneous with the Xolapa-complex zircons. Again, these ages indicate that magmatism terminated at that time and suggest a close spatial relationship of the Taxco–Viejo–Xolapa–Teloloapan arcs (Figs. 2M and 16G). The NE dipping subduction zone of the South El Tambor Group may have ended at a transform fault at the eastern end of the Maya block (Fig. 16G).

The Teloloapan, Taxco–Viejo, and Olinalá units and the Xolapa complex are covered by Albian–lower Cenomanian Morelos shelf limestones (Fig. 2L and M). These limestones may correspond to the massive La Virgen limestone atop the South El Tambor Group (Fig. 2K). Carbonate passive margin strata (Coban–Campur Formations; Fig. 2B) were deposited on the Maya block. The post-suturing deposits on the Chortís block are probably the red beds and foreland-basin deposits of the Valle de Angeles and Gualaco Formations. The latter is typically intercalated with Upper Cretaceous volcanic rocks indicating establishment of the Sierra Madre Occidental arc in Late Cretaceous, also on the Chortís block (see below). Characteristically, proto-Pacific subduction continued beneath the Chortís block and the Zihuatanejo unit far into the Late Cretaceous (Fig. 2J and M). In our interpretation the Agua Blanca rift and the Manto volcanic rock intercalations are related to proto-Pacific subduction and intra-arc extension. We attribute the inversion of the Agua Blanca intra-arc rift to the accretion of the Zihuatanejo–Huetamo units–Sanarate complex to southern Mexico and the western Chortís block. Top-to-E shear in the greenschist facies, meta-basaltic/clastic Sanarate complex of the western Chortís block reflects this accretion of the Guerrero terrane/Sanarate complex.

Why were so many individual arcs and subduction–accretion complexes developed along the southwestern margin of Mexico (the Guerrero composite terrane) and the Chortís block (the Sanarate complex) during the late Early and Late Cretaceous (e.g., Talavera-Mendoza et al., 2007)? If rifting between the Chortís block–Arteaga unit and southern Mexico was mostly re-

lated to spreading between the two Americas and formation of the Gulf of Mexico (Fig. 16E), spreading was likely N–S with ~N trending transform faults. Transformation of this rift to convergence along the ~NNW-trending proto-Pacific subduction zone may have allowed activation of some transform faults as subduction zones.

8.5. Late Cretaceous North El Tambor Group subduction and Maya block–Caribbean arc collision

Our structural, petrologic, and geochronologic data demonstrate sinistral transpressive collision along the southern margin of the Maya block during Late Cretaceous. Collision transferred the southern Maya block into a nappe stack with the North El Tambor Group ophiolitic mélange at top. Characteristically, deformation involved N–S shortening and E–W lengthening. Sinistral transpression was partitioned on all scales between oblique stretching along the foliation and sinistral strike-slip along steeply-dipping shear zones (Fig. 16H). To a first-order, deformation is identical in the North El Tambor Group, Chuacús complex, and the northern foreland fold–thrust belt. 450–550°C and 0.7–0.8 GPa regional Cretaceous reheating within the Chuacús complex, associated with local magmatism, is syn-kinematic. Penetration of deformation and overburden (PT conditions) increase from west to east along the collision zone. The relatively high-P/low-T metamorphism and nearly coeval blueschist- (North El Tambor Group) and amphibolite-facies metamorphism (Chuacús complex) suggest a cold geotherm and steep continental subduction (Fig. 16H). Southern Maya block imbrication is dated at 75–65 Ma (Fig. 16I) and cooling to upper crustal levels (~100°C) was attained by early Tertiary (AFT results at high elevation, see above). The Jurassic–Early Cretaceous North El Tambor Group oceanic and immature arc rocks incorporated ~131 Ma eclogite into an accretionary wedge that reached crustal levels by Late Cretaceous (~76 Ma).

What collided with the southern Maya block in the latest Cretaceous? We follow and broaden the model of Mann (2007) and Rogers et al. (2007b) and suggest that the Maya block–North El Tambor Group suture extends toward the west into the footwall of the Siuna terrane of the southern Chortís block and the Nicaragua Rise and to the east into the subduction–accretion and arc complexes of Jamaica, Hispaniola (Dominican Republic), and Cuba (Figs. 16J and K). In comparison with the North El Tambor Group (Fig. 2A), the Siuna mélange (Fig. 2F) contains similar lithology (ultramafic rocks, radiolarites, meta-andesite, volcanic arenites) of proven Late Jurassic age, high-P phengites at ~139 Ma, blueschist and eclogite, and Aptian–Albian turbiditic sequence. These rocks are overlain by the Atima Formation and intruded by diorite (~60 Ma) and andesite dikes (~76 Ma; Fig. 2F; Flores et al., 2007; Venable, 1994). The poorly dated (post-80 Ma) Colon fold belt of the eastern Chortís block and the Nicaragua Rise likely reflects imbrication along the footwall of the Siuna terrane (Roger et al., 2007b). The Siuna terrane likely extends westward into the ocean igneous complexes of the Santa Elena and Nicoya peninsu-

las of Costa Rica; these complexes contain ~165–83 Ma pillow lavas, sills and flows, radiolarian chert, basalt breccias, and gabbro and plagiogranite. They are unconformably capped by ≤75 Ma reef limestones (Figs. 2G and 16I; e.g., Hoernle and Hauff, 2005). The Cuban subduction–accretion complex contains ~148–65 Ma high-P rocks (major peaks at ~116 Ma, ~70 Ma; Figs. 16I and J; Krebs et al., 2007, Schneider et al., 2004). The Greater Antilles arc of Cuba was active at 133–66 Ma (Fig. 16I and J; major peaks at ~72 Ma, ~80 Ma, Stanek et al., 2005; Rojas et al., 2005; Grafe et al., 2001; Hall et al, 2004), and the Cordillera Central arc (Dominican Republic) spanned ~117–74 Ma (Figs. 16H,I and J; major peaks at ~75 Ma, ~84 Ma, and ~116 Ma, Kesler et al., 2005; Escuder Viruete et al., 2006b). Thus these subduction–accretion complexes and arcs cover time ranges comparable to that of the North El Tambor Group, with subduction and arc formation terminated ~10 Myr after collision along the southern Maya block. This indicates the time span required to transfer these subduction–accretion and arc complexes to the Bahamas-platform collision zone when the southern Maya block acted as a sinistral transform fault zone. Accordingly, termination of pronounced magmatism in the Santa Elena–Nicoya subduction-accretion complexes approximately 10 Myr earlier (Fig. 16I) reflects their earlier collision with the southwestern Chortís block. Based on the termination of magmatism at 74 Ma within the Cordillera Central arc and its well developed sinistral transpressive deformation (Escuder Viruete et al., 2006a,b), we speculate this arc was the immediate hanging wall of the collision zone along the southern Maya block.

What was the origin of the ≤75 Ma pegmatitic magmatism in the southern Maya block, post-dating North El Tambor Group emplacement and folding–thrusting in the Chuacús complex? Causes might include Pacific-arc magmatism, local anatexis due to crustal thickening, or break-off of the Siuna terrane–North El Tambor Group–Caribbean arc slab. We favor the latter (Fig. 16H), as entry of the Nicoya–Siuna–North El Tambor–Caribbean slab into the proto-Caribbean sea must have induced its rapid anticlockwise rotation, rapid along-strike length reduction, and thus slab fracturing and roll-back. In contrast, contemporaneous Pacific arc subduction occurred far to the west on the Chortís block (Fig. 16K) and the thermal overprint due to crustal stacking was likely insufficient and too early in the Chuacús complex to cause anatexis (see above).

Cerna et al. (2007) hypothesized a mostly E vergent, partly sinistral transpressive, N trending fold-thrust belt along the western Mixteca terrane, the Guerrero–Morelos platform that originated during the Coniacian (≤90 Ma; Cenomanian, ≤100 Ma, after Talavera-Mendoza et al., 2005) and was active into the Tertiary. They related this E–W shortening to the collision of the Caribbean plate with the Chortís block. Roger et al. (2007b) and our data show, however, that this collision is ~N–S and ≤76 Ma on the southern Chortís and Maya blocks (see above). Probably, the Laramide fold–thrust belt orocline on the Guerrero–Morelos platform, along the Sierra

de Juárez (Cerca et al., 2007), and within the southern Maya block (this study) is a composite structure, related to accretion of the most outboard Guerrero-terrane units, Pacific subduction, and collision of the Siuna terrane–North El Tambor Group–Caribbean plate. We suggest that shortening in the Guerrero–Morelos platform and its continuation into the Chortís block (Agua Blanca rift inversion) is mainly related to the ≤80 Ma Arteaga–western Chortís (Sanarate complex) suture and Pacific subduction and the Sierra de Juárez–southern Maya block shortening due to the ≤76 Ma Caribbean plate collision (Fig. 16K). Structural superpositions must have occurred mostly in the Mixteca–Oaxaca basement terrane area.

8.6. Late Eocene–Recent eastward displacement of the Chortís block

Most tectonic models place the Chortís block opposite southern Mexico during Late Cretaceous–early Tertiary (e.g., Mann, 2007; see above). Roger et al. (2007a,b) summarized features and piercing lines that support this connection. Here we summarize additional evidence and trace the eastward displacement of the Chortís block to its present position. Approximately 80–45 Ma magmatic rocks of the Sierra Madre Occidental crop out along the coast of southwestern Mexico and inland up to ~99°W (Fig. 16L; Schaaf et al., 2005; Morán-Zenteno et al., 1999). This magmatic arc continued into the central Chortís block. Lining up the NW trend of these rocks in Mexico (the arc continues northwest of the area shown in Fig. 16L) and on the Chortís block yields ~1100 km sinistral displacement and ≤40° anticlockwise rotation of the Chortís block (Figs. 1C, 16L). Based on one data point from the central Chortís block, the paleomagnetically determined anticlockwise post-60 Ma rotation is ~32° (Gose, 1985). During the Oligocene, eastward migration of Chortis induced a northeastward migration of the trench (Herrmann et al., 1994) and the associated Sierra Madre del Sur arc shifted inland and eastward into southeastern Mexico. The arc trends ESE (Morán-Zenteno et al., 1999), which is particularly evident on the Chortís block (Fig. 16L).

When did the Chortís block break away from southern Mexico? In the Chortís block, high-grade and high-strain deformation began at ≥40 Ma and we suggested above that there were major deformation phases at ~40–35 Ma and possibly at 25–18 Ma. Sinistral transtension in the La Venta–Tierra Colorada shear zone along the northwestern margin of the Xolapa complex is low-grade at ~300°C (low-T quartz ductility; Riller et al., 1992; Solari et al., 2007) and started at ≤45 Ma (Solari et al., 2007). Local high-strain flow occurred at ~35 Ma (see above). Post-tectonic intrusions are 34 ± 2 Ma (Tierra Colorado granite, Herrmann et al., 1994); however, brittle, sinistral transtension continued during cooling of this granite (Riller et al., 1992). The distinctly different exposure level of the continuous Early Cretaceous Taxco–Viejo (west; up to greenschist facies) and Xolapa arc (east; amphibolite facies and migmatization) is ascribed to major exhumation of the latter. Large-scale sinistral transtension along the northwestern Xola-

pa-complex margin certainly contributed to this difference. Robinson et al. (1990) obtained a ~40 Ma age for syn-kinematic tonalite north of Acapulco. Sinistral shear occurred along the northern margin of the eastern Xolapa complex between 29 and 24 Ma (Chacolapa shear zone, point 4 in Fig. 16L; Tolson, 2005). Other sinistral transtensive deformation zones in southern Mexico outside the Xolapa complex are dated to between ~37 and ~27 Ma (points 1 and 3 in Fig. 16L). Corona-Chávez et al. (2006) estimated that about 70% of the eastern Xolapa complex was affected by discontinuous mylonitic–cataclastic, post-migmatitic deformation. We conclude that the migration of the Chortís block initiated ≥40 Ma and was fully active at 40–35 Ma. This is compatible with the chronology of spreading in the Cayman trough pull-apart basin (see above).

Using (U-Th)/He thermochronology, Ducea et al. (2004b) estimated average exhumation rates for the Xolapa complex. A western segment at Acapulco yielded ages between 26 and 8.4 Ma and a rate of 0.22 mm/a; an eastern profile at Puerto Escondido gave 17.7–10.4 Ma ages and 0.18 mm/a. This slow Neogene exhumation contrasts with petrologic data that suggest exhumation from ≥25 km (migmatites; Corona-Chávez et al., 2006) and 20–13 km (granitoids; Morán-Zenteno et al., 1996) since 34–27 Ma, the age of the granitoids; therefore, most exhumation must have taken place before the Miocene. Pooling the (U-Th)/He and AFT data of Ducea et al. (2004b) and excluding outliers (e.g., ages older than crystallization and those with very large errors) indicate that most samples of the western profile cooled through 70–100°C or were exhumed from ~4 km at ~25 Ma. Except for three outliers most samples of the eastern profile have identical ages over 2 km elevation and thus suggest rapid cooling at ~15 Ma (Fig. 6D). Using the three plutons for which U/Pb zircon ages are available (Herrmann et al., 1994), we obtained exhumation rates of ~1.5 mm/a between 31 and 25 Ma (12.9 km depth at 31 Ma and ~4 km at ~25 Ma) and ~1.9 mm/a between 32 and 25 Ma (17.9 km depth at 32 Ma and ~4 km at ~25 Ma) for the western section, and 1.2 mm/a (20.4 km depth at 29 Ma and ~4 km at ~15 Ma) for the eastern profile. For the western section, Herrmann et al. (1994) obtained two ~47 Ma migmatization ages; this yields ~0.8 mm/a between 47 and 31 Ma (~26 km depth at 47 Ma and 12.9 km at 31 Ma). Along the northern rim of the Chortís block our data indicate an exhumation rate of ~1 mm/a between 36 and 9 Ma (~28 km depth at 36 Ma and ~3 km at 9 Ma). These data indicate that the early stages of Chortís-block migration were associated with rapid exhumation due to sinistral transtension and erosion.

The early stage of distributed sinistral displacement and erosion that affected a broad zone in southern Mexico and the northern Chortís block also must have affected the southern Maya block, as its eastern extension, the Nicaragua Rise, was located off the western edge of the Maya block (Fig. 16K). We interpret our AFT data from the southern Chiapas massif and the

Chuacús complex, both clustering at ~30 Ma (Fig. 6A and C), to record this distributed transtension–transpression–sinistral migration and erosion phase.

Why did the Chortís block break away at ≥40 Ma? Following Ratschbacher et al. (1991) and Riller et al. (2002), we propose that the contemporaneous change in several plate tectonic boundary conditions triggered break away. During Eocene, shear stresses across the arc were high due to rapid convergence of relatively young lithosphere under an angle of ~45° to a pre-existing lithospheric weakness, the South El Tambor suture. Most importantly, sinistral break away started in an area that had been an arc at least since Late Cretaceous (see above) and thus was thermally weakened. This is a common process in oblique subduction settings. Consequently, the largest volume (Morán-Zenteno et al., 1999) and the concentration in time (~33 Ma Chortís block, ~34 Ma Xolapa complex; Fig. 16A) of magmatism and metamorphism seems to have been controlled by the NW–SE shear zones associated with transtensional–transpressional tectonics at the boundary between southern Mexico and the Chortís block (Herrmann et al., 1994; Fig. 16L).

Early and middle Miocene (~20–10 Ma) volcanic rocks are distributed around the Isthmus of Tehuantepec (Fig. 16M). In this region it is evident that volcanism in the inland regions was active after cessation of Oligocene plutonism in the Xolapa complex (Morán-Zenteno et al., 1999). The earliest manifestations of magmatic activity along the eastern and central Trans-Mexican volcanic belt are as old as middle Miocene (~17 Ma; Ferrari et al., 1994) and thus this belt may form a direct continuation of the volcanism around the Isthmus of Tehuantepec. To the east coeval magmatism occurred along the western part of the Polochic fault zone in westernmost Guatemala (Fig. 16M), indicating ≥100 km offset along the Polochic fault since then. This is similar to the ~130 km offset proposed along this fault between 10 and 3 Ma (Burkart, 1983; Burkart et al., 1987). Still further east, the ~16.9–13.4 Ma ignimbrite province strikes NW–SE across the Chortís block (Fig. 16M, e.g., Jordan et al., 2007). Aligning the southeastern Mexican and Chortís-block volcanic provinces yields ~400 km displacement since ~15 Ma and ~300 km offset along the Motagua fault (Fig. 16M). Several elements trace the displacement during this time (Fig. 16M): tectonic and stratigraphic features northwest of the Isthmus of Tehuantepec indicate sinistral transtension with ~N-trending pull-apart basins coeval with volcanism (Morán-Zenteno et al., 1999); the easternmost part of the Xolapa complex experienced rapid cooling at ~15 Ma (Fig. 6D); the Chacolapa shear zone was reactivated at ~15 Ma; the Tonala and Polochic shear zones were active at 9–8 Ma and 12–5 Ma, respectively; and most of the AFT ages in the Chortís block closed at ~12 Ma (all data from this study).

8.7. Variations in the Late Cenozoic stress field

N–S rifts that disrupt the ignimbrite province in western Honduras and southeastern Guatemala commenced after ~10.5 Ma (Gordon and Muehlberger, 1994). They are related to plateau uplift following slab break-off underneath Central America (Rogers et al., 2002). Our 11.2–7.9 Ma AFT data from the western flank of the Ulúa graben support the late Miocene onset of rifting, although extension structures formed as early as ~28 Ma, contemporaneous with and kinematically related to sinistral wrenching along the northern margin of the Chortís block. Numerical modeling suggests that presently the western edge of the Chortís block is pinned against North America, making the triple junction between the Cocos, North American, and Caribbean plates a zone of diffuse deformation (Álvarez-Gómez et al., 2008). Our late Cenozoic deformation" structural event (Figs. 10, 13, and 15), reflecting sinistral slip along ~E-striking strike-slip faults locally interacting with ~N-striking normal faults, is distributed across the entire plate boundary from the northern foreland to south of the Jocotán–Chamelecón fault zone. The transition from older dominant strike-slip to younger, prevailing normal faulting, proposed by Gordon and Muehlberger (1994), also is evident from our data. However, normal faulting exemplified by the grabens in southern Guatemala and western Honduras (Fig. 15), extends northward across the Motagua fault zone into the Tertiary Subinal Formation (Fig. 13), the North El Tambor Group rocks on the central Chuacús complex (Fig. 13), and the Chuacús complex and Tertiary–Quaternary volcanic rocks of western Guatemala (Fig. 10). This indicates that today the Polochic fault constitutes the major plate boundary fault. This is compatible with termination of the active strike-slip and reverse fault province of eastern Chiapas north of the Polochic fault zone (Andreani et al., 2008). Furthermore, our data support additional salient features of the late Cenozoic stress distribution: shortening directions trend ~NW–SE in western and west-central Guatemala and in particular in western Guatemala south of the Polochic fault ("Late Cenozoic deformation"; Figs. 10, 13 and 15) and outline the dextral, WNW trending Jalpatagua fault zone along the active volcanic arc (Gordon and Muehlberger, 1994; Álvarez-Gómez et al., 2008).

9. Conclusions

New geochronologic, petrologic, and structural data constrain the pressure–temperature–deformation–time (P-T-d-t) history of the northern Caribbean plate boundary in southern Mexico, central Guatemala, and northwestern Honduras. In particular, we investigated which crustal sections of the Motagua suture zone accommodated the large-scale sinistral offset along the plate boundary, and the chronologic and kinematic framework of this process. Correlations between the Maya and Chortís blocks, tectonostratigraphic complexes of southern Mexico, and arc/subduction complexes of the northeastern Caribbean constrain models for the early Paleozoic to Recent evolution of the northern Caribbean plate boundary. Our findings constrain major tectonic, magmatic and metamorphic episodes in these areas:

(1) During early Paleozoic, southern Mexico (Acatlán complex of the Mixteca terrane), the southern Maya block (Chuacús complex), and likely also the Chortís block were part of the Alleghanian–Appalachian orogen along the southern margin of North America. The Chuacús complex felsic gneiss–amphibolite association and relict high-P metamorphism probably matches those of the Xayacatlán suite in the Acatlán complex; the Ordovician, mega-crystic K-feldspar Rabinal gneiss may be equivalent to post-high-P intrusions in this suite.

(2) After the final amalgamation of Pangea, an arc developed along its western margin, causing magmatism and regional amphibolite-facies metamorphism in southern Mexico (~290–250 Ma), the Chuacús complex of the southern Maya block (270–215 Ma), and the Chortís block (283–242 Ma). Identical intrusion and metamorphic ages (273 and 254 Ma) in the Chiapas massif of the southwestern Maya block and the northern Chortís block suggest a similar position within the arc. Younger ages in the southern Maya block (Chuacús complex) are attributed to its position in the hinterland of the main arc and a speculative episode of flat-slab subduction.

(3) The Jurassic opening of the Gulf of Mexico separated the Maya block from North America. Granite intruded the Chuacús complex (Maya block) of western Guatemala at 164–177 Ma. Most of the Maya block was probably emergent during Triassic–Jurassic with the likely Middle Jurassic–Early Cretaceous Todos Santos Formation reflecting rifting during separation of North and South America. Dextral shear along ~NNW trending shear zones within southern Mexico is kinematically related to opening the Gulf of Mexico and may account for the concentration of magmatism at ~175–166 Ma in southern Mexico. Granites also intruded the northern Chortís block during Middle Jurassic time (~168–159 Ma). The Middle Jurassic Agua Fria Formation records upper crustal transtension and rifting. Rifting of the Chortís block from southern Mexico likely initiated within the thermally weakened proto-Pacific arc, possibly as a failed arm of the proto-Caribbean rift. This rifting separated the northern Chortís block from the Xolapa complex of southern Mexico and also parts of the Guerrero terrane from parts of southwestern Mexico that have Jurassic-aged basement. The Sanarate complex of the northwestern Chortís block correlates with the Arteaga–Las Ollas units of the Guerrero terrane, sharing a dominantly mafic lithology and Jurassic metamorphism. Rifting produced the Late Jurassic–Early Cretaceous oceanic crust of the South El Tambor Group and terminated before 132 Ma, the age of eclogite-facies metamorphism in that Group.

(4) Rifting between Chortís block and southern Mexico reverted to subduction in the Early Cretaceous. Arc magmatism and high-T/low-P metamorphism (141–126 Ma) along the Xolapa complex of southern Mexico is likely related to subduction of South El Tambor Group lithosphere, which was emplaced southward onto the Chortís block at or after ~120 Ma. Laterally,

Xolapa-complex magmatism is correlated with that in the Taxco–Viejo unit of the Mixteca terrane. While collision of the Chortís block with southern Mexico terminated arc magmatism in the Xolapa complex, proto-Pacific subduction continued on the Chortís block and the Zihuatanejo unit of the Guerrero terrane to its northwest. This unit and the Sanarate complex of the Chortis block amalgamated to southern Mexico during Late Cretaceous.

(5) Spectacular sinistral transpressive collision occurred along the southern margin of the Maya block during Late Cretaceous (≤76 Ma). Collision transferred the southern Maya block into a nappe stack with the North El Tambor Group at top. Sinistral transpression was partitioned on all scales ~~in~~ between oblique stretching along the foliation and sinistral strike-slip along steeply-dipping shear zones. To first order, deformation is identical in the North El Tambor Group, Chuacús complex, and the Laramide, northern foreland fold–thrust belt. The relatively high-P/low-T metamorphism and nearly coeval blueschist- (North El Tambor Group) and lower amphibolite-facies metamorphism (Chuacús complex) suggest a cold geotherm and steep continental subduction. The Maya block–North El Tambor Group suture extends westward into the footwall of the Santa Elena–Nicoya complexes, the Siuna terrane of the southern Chortís block, and the Nicaragua Rise and to the east into the subduction–accretion and arc complexes of Cuba and Hispaniola. Postulated break-off of the North El Tambor Group slab may account for ≤75 Ma magmatism in the southern Maya block.

(6) High shear stress across the Caribbean–North American plate boundary during the Eocene triggered breakaway of the Chortís block from southern Mexico at ≥40 Ma, coeval with initiation of the Cayman trough pull-apart basin. Sinistral break away started in an area, the Xolapa complex and the northern Chortís block, that had been an arc at least since Late Cretaceous and thus was thermally weakened. The Las Ovejas complex of the northern Chortís block forms a westward narrowing belt of distributed sinistral transtension and represents the southern part of the high-strain displacement zone along which the Chortís block migrated eastward. Deformation interacted with amphibolite-facies metamorphism, widespread migmatization, and local magmatism, illustrated most clearly by small syn- to post-tectonic pegmatites. The close spatial and temporal interaction between high-strain deformation and Tertiary metamorphism, migmatization, and magmatism is confined to the northern Chortís block. It appears that arc magmatism provided the heat input to localize deformation. Consequently, the largest volume and the concentration in time (40–20 Ma) of magmatism and metamorphism seems to have been controlled by shear zones associated with transtensional–transpressional tectonics at the boundary between southern Mexico and the Chortís block. The Ulúa graben, and possibly other N trending grabens of southern Guatemala and northern Honduras, started in temporal and kinematic compatibility with wrenching along the Las Ovejas complex. The topographically well expressed active grabens, however, are neotectonic features. Also the Jocotán-Chamelecón fault

zone was part of this deformation system. Breakaway and early eastward translation of the Chortís block induced exhumation rates of 0.8–1.9 mm/a in the Xolapa complex and the northern Chortis block. Initial eastward translation is also recorded by rapid cooling within the southern/southwestern Maya block at ~30 Ma. Approximately 175, ~130, and ~40 Ma magmatic belts both in southern Mexico and on the Chortís block consistently argue for ~1100 km offset since ≥40 Ma along the northern Caribbean plate boundary. Post-40 Ma structures and a ~15 Ma magmatic belt indicate that ~700 km of that offset occurred prior to 40 Ma. The Tonala shear zone, bounding the Chiapas massif to the southwest, and Polochic shear zones were major deformation zones at 9–8 Ma and 12–5 Ma, respectively.

(7) N–S rifts in western Honduras and southeastern Guatemala are related to plateau uplift following slab break-off underneath Central America. 11.2–7.9 Ma apatite-fission track ages from the western flank of the Ulúa graben support the late Miocene onset of rifting. Presently, the triple junction between the Cocos, North American, and Caribbean plates is a zone of diffuse deformation. Normal faulting, exemplified by the grabens in southern Guatemala and western Honduras, extends northward across the Motagua fault zone into the Chuacús complex, indicating that today the Polochic fault constitutes the major plate boundary fault. Distributed, dextral, WNW trending fault zones are active along the active volcanic arc.

Acknowledgements

This work grew out of our research in southern Mexico in the early 1990s and was started by Gabriel Dengo (Guatemala City) in 1993. Stimulating discussions with Claude Rangin and Xavier LePichon and their groups at College de France, Paris and Aix-en-Provence, and the inspiring work and papers of our Mexican colleagues prompted the first author to put together the data that always seemed to be less bright than those from Asia; we hope that this paper proves otherwise. Bastian Wauschkuhn (Freiberg) compiled Fig. 1B. Gareth Seward (UCSB) contributed the EBSD LPO measurement of sample 5PB-10. Peter Bock (Freiberg and CICESE) collected the elevation profile samples from Tres Picos and did a preliminary fission-track analysis on the samples from southern Mexico. Eva Enkelmann (Lehigh) supported the AFT work. Wolfgang Frisch (Tübingen), Gero Michel (Bermuda), and Ulrich Riller (Toronto) helped in the field. LR thanks Bradley Hacker (UCSB) for endless support in the Ar-lab when both were at Stanford in the mid 1990s. Michael Kozuch collected sample SF1D, and Athena Andrews Rodbell and Jose Maria Gutierrez sample 86TA100. Funded by DFG grants RA442/6 and 25 to LR, NSF grant EAR 9219284 to MG, and awards from DAAD and Studienstiftung des Deutschen Volkes to KS.

References

Alaniz-Alvarez, S., Van der Heyden, P., Nieto-Samaniego, A.F., and Ortega-Gutiérrez, F., 1996, Radiometric and kinematic evidence for Middle Jurassic strike-slip faulting in southern Mexico related to the opening of the Gulf of Mexico: Geology, v. 24, p. 443–446, doi: 10.1130/0091-7613(1996)024<0443: RAKEFM>2.3.CO;2.

Álvarez-Gómez, J. A., Meijer, P. T., Martínez-Diaz, J. J., and Capote R., 2008, Constraints from finite element modeling on the active tectonics of northern Central America and the Middle America Trench: Tectonics, doi:10.1029/2007TC002162.

Anderson, J. L., and Smith, D. R., 1995, The effects of temperature and fO_2 on the Al-in-hornblende barometer: American Mineralogist, v. 80, p. 549–559.

Andreani L., Le Pichon X., Rangin C., Martínez–Reyes J., in press, The Southern Mexico Block : Main boundaries and new estimation for its Quaternary motion. Bulletin de la 3 Société Géologique de France, T. 179.

Avé Lallemant, H.G., and Gordon, M.B., 1999, Deformation history of Roatán Island: Implications for the origin of the Tela Basin (Honduras), *in* Mann, P., ed., Caribbean Basins. Sedimentary Basins of the World, 4: Elsevier Science B.V., Amsterdam, The Netherlands, p. 197–218.

Bachmann, R., 2003, 'Megashears' and the early evolution of the Caribbean – structural geology and petrology of deformation zones in Guatemala and Honduras: Diploma thesis, TUBA Freiberg, Germany, 99 pp.

Banno, S., 1959, Aegirinaugites from crystalline schists in Sikoku: J. Geol. Soc. Japan, v. 65, p. 652–657.

Bargar, K.E., 1991, Fluid inclusions and preliminary studies of hydrothermal alteration in core hole PLTG-1, Platanares geothermal area, Honduras: Journal of Volcanology and Geothermal Research, v. 45, p. 147–160.

Bateson, J.H., 1972, New interpretation of geology of Maya Mountains, British Honduras, American Association of Petroleum Geologists, Bulletin, v. 56, p. 956–963.

Beccaluva, L., Bellia, S., Coltorti, M., Dengo, G., Guinta, G., Mendez, J., Romero, J., Rotolo, S., and Siena, F., 1995, The northwestern border of the Caribbean plate in Guatemala: new geological and petrological data on the Motagua ophiolitic belt: Ofioliti, v. 20, p. 1–15.

Bertrand, J., and Vuagnat, M., 1975, Données chimiques diverses sur des ophiolites du Guatémala : Bulletin Suisse de Minéralogie Pétrographie, v. 57, p. 466–483.

Bertrand, J., Delaloye, M., Fontignie, D., and Vuagnat, M., 1978, Ages (K/Ar) sur diverses ophiolites et roches associées de la Cordillère centrale du Guatémala: Bulletin Suisse de Minéralogie Pétrographie, v. 58, p.405–412.

Bohlen, S., and Liotta, J., 1986, A barometer for garnet amphibolites and garnet granulites: Journal of Petrology, v. 27, p. 1025–1034.

Brueckner, H. K., Hemming, S., Sorensen, S., and Harlow, G. E., 2005, Synchronous Sm-Nd mineral ages from HP terranes on both sides of the Motagua Fault of Guatemala: Convergent suture and strike-slip fault?: AGU Fall Meeting, Suppl., 86 (52).

Bundesanstalt für Bodenforschung (BGR), 1971, Geologische Übersichtskarte 1:125000, Baja Verapaz und Südteil der Alta Verapaz (Guatemala): D-3 Hannover-Buchholz.

Burkart, B., 1983, Neogene North America–Caribbean plate boundary across northern Central America: offset along the Polochic fault: Tectonophysics, v. 99, p. 251–270, doi: 10.1016/0040-1951(83)90107-5.

Burkart, B., 1994, Northern Central America, *in* Donovan, S., and Jackson, T., eds., Caribbean Geology, an introduction: Kingston, U.W.I. Publ. Assos., pp. 265–283.

Burkart, B., Deaton, B. C., Dengo, C., Moreno, G., 1987, Tectonic wedges and offset Laramide structures along the Polochic fault of Guatemala and Chiapas, Mexico: Reaffirmation and large Neogene displacement, Tectonics, v. 6, p. 411–422.

Campa, M.F., and Iriondo, A., 2004, Significado de dataciones cretácicas de los arcos volcánicos de Taxco, Taxco Viejo y Chapolapa, en la evolución de la plataforma Guerrero Morelos: IV Reunión Nacional de Ciencias de la Tierra, Juriquilla, Querétaro, p. 338.

Carswell, D., O'Brian, P., Wilson, R., Zhai, M., 2000, Metamorphic evolution, mineral chemistry and thermobarometry of schists and orthogneisses hosting ultra-high pressure eclogites in the Dabie Shan of Central China: Lithos, v. 52, p. 121–155.

Centeno-García, E., Ruiz, J., Coney, P.J., Patchett, P.J., and Ortega, G.F., 1993, Guerrero terrane of Mexico: Its role in the Southern Cordillera from new geochemical data: Geology, v. 21, p. 419–422, doi: 10.1130/0091-7613(1993)021<0419:GTOMIR>2.3.CO;2.

Cerca, M., Ferrari, L., López-Martínez, M., Martiny, B., and Irondo, A., 2007, Late Cretaceous shortening and early Tertiary shearing in the central Sierra Madre des Sur, southern Mexico: Insights into the evolution of the Caribbean–North American plate interaction, Tectonics, v. 26, TC3007, doi:10.1029/2006TC001981.

Chiari, M., Dumitrica, P., Marroni, M., Pandolfi, L., and Principi, G., 2004, Paleontological evidences for a late Jurassic age of the Guatemala ophiolites, Abstract 32nd IGC – Florence.

Clemons, R.E., 1966, Geology of the Chiquimula quadrangle, Guatemala, Central America: PhD Thesis, University of Texas, Austin, 1966.

Colombi, A., 1988, Métamorphisme et géochimie des roches mafigues des Alpes onest centrals (géoprofil Viége–Domodossola–Lacarno): PhD Thesis, University Lausanne, Switzerland, 216 pp.

Corona-Chávez, P., Poli, S., and Bigioggero, B., 2006, Syn-deformational migmatites and magmatic-arc metamorphism in the Xolapa Complex, southern Mexico: Journal of metamorphic Geology, v. 24, p. 169–191, doi:10.1111/j.1525–1314.2006.00632.x.

Dahl, P.S., and Friberg, L.M., 1980, The occurrence and chemistry of epidote-clinozoisites in mafic gneisses from the Ruby Range, southwestern Montana: Contr. Geol. Univ. Wyoming, v. 18, p. 77–82.

DeGraaff-Surpless, K., Graham, S. A., Wooden, J. L., and McWilliams M.O., 2002, Detrital zircon provenance analysis of the Great Valley Group, California: Evolution of an arc-forearc system: Geological Society of America Bulletin, v. 114, p. 1564 – 1580.

DeMets, C., 2001, A new estimate for present-day Cocos–Caribbean plate motion: Implications for slip along the Central American volcanic arc: Geophysical Research Letters, v. 28, p. 4043–4046.

Dickinson, W. R., and Lawton, T. F., 2001, Carboniferous to Cretaceous assembly and fragmentation of Mexico: Geological Society of America Bulletin, v. 113, p. 1142–1160.

Donelick, R.A., Roden, M.K., Mooers, J.D., Carpenter, B.S., and Miller, D.S., 1990, Etchable length reduction of induced fission tracks in apatite at room temperature (=23°C): Crystallographic orientation effects and 'initial' mean lengths: Nuclear Tracks and Radiation Measurements, v. 17, p. 261–265, doi: 10.1016/1359-0189(90)90044-X.

Donnely, T. W., Horne, G. S., Finch, R. C., and López-Ramos, E., 1990, Northern Central America: The Maya and Chortis blocks, *in* Dengo, G., and Case, J., eds., The Caribbean Region: Geology of North America, Geological Society of America, v. H., The Caribbean Region, The Geological Society of America, p. 37–76.

Drobe, J., and Oliver, D., 1998, U-Pb age constraints on Early Cretaceous volcanism and stratigraphy in central Honduras: Geological Society of America, Cordilleran section meeting, v. 30, p. 12.

Ducea, M., Gehrels, G.E., Shoemaker, S., Ruíz, J., and Valencia, V.A., 2004a, Geologic evolution of the Xolapa Complex, southern Mexico: Evidence from U-Pb zircon geochronology: Geological Society of America Bulletin, v. 116, p. 1016–1025, doi: 10.1130/B25467.1.

Ducea, M., Valencia, V.A., Shoemaker, S., Reiners, P.W., DeCelles, P.G., Campa-Uranga, M.F., Morán-Zenteno, D.J., and Ruíz, J., 2004b, Rates of sediment recycling beneath the Acapulco trench: Constraints from (U-Th)/He thermochronology: Journal of Geophysical Research, v. 109, doi: 10.1029/2004JB003112.

Elías-Herrera, M., and Ortega-Gutiérrez F., 2002, Caltepec fault zone: an early Permian dextral transpressional boundary between the Proterozoic Oaxacan and Paleozoic Acatlán complexes, southern Mexico, and regional tectonic implications: Tectonics, v. 21, p. 1–19.

Elías-Herrera, M., Ortega-Gutiérrez, F., Sánchez-Zavala, J.L., Macías-Romo, C., Ortega-Rivera, A., Iriondo, A., 2005, La falla de Caltepec: raíces expuestas de una frontera tectónica de larga vida entre dos terrenos continentales del sur de México: Boletín de la Sociedad Geológica Mexicana, v. LVII, p. 83–109.

Emmet, P., 1983, Geology of the Agalteca Quadrangle, Honduras, Central America: M.S. thesis, The University of Texas at Austin, 201p.

Escuder Viruete, J., Contreras, F., Stein, G., Urien, P., Joubert, M., Ullrich, T., Mortensen, J., and Pérez-Estaún, A., 2006a, Transpression and strain partitioning in the Caribbean Island-arc: Fabric development, kinematics and Ar-Ar ages of syntectonic emplacement of the Loma de Cabrera batholith, Dominican Republic: Journal of Structural Geology, v. 28, p. 1496–1519.

Escuder Viruete, J., Díaz de Neira, A., Hernáiz Huerta, P.P., Monthel, J., García Senz, J., Joubert, M., Lopera, E., Ullrich, T., Friedman, R., Mortensen, J., and Pérez-Estaún, A., 2006b, Magmatic relationships and ages of Caribbean Island arc tholeiites, boninites and related felsic rocks, Dominican Republic: Lithos, v. 90, p. 161–186.

Ferrari, L., Garduño, V.H., Pasquaré , G., Tibaldi, A., 1994, Volcanic and tectonic evolution of central Mexico: Oligocene to Present: Geofísica Internacional, v. 33, p. 91–105.

Flores, K., Baumgartner, P.O., Skora, S., Baumgartner, L., Cosca, M., and Cruz, D., 2007, The Siuna serpentinite mélange: an Early Cretaceous subduction/accretion of a Jurassic arc: EOS Trans. AGU, v. 88(52), Fall Meet. Suppl., Abstract T11D-03.

Fourcade, E., Piccioni, L., Escriba, J., and Rosselo, E., 1999, Cretaceous stratigraphy and palaeoenvironments of the Southern Petén Basin, Guatemala: Cretaceous Research, v. 20, p. 793–811.

Fuhrman, M.L., and Lindsley, D.H., 1988, Ternary feldspar modeling and thermometry: Amer. Mineral., v. 73, p. 201-215.

García-Casco, A., Torres-Roldán, R.L., Millán, G., Monié, P., and Schneider, J., 2002, Oscillatory zoning of eclogitic garnet and amphibole, Northern Serpentinite melange, Cuba: a record of tectonic instability during subduction: Journal of Metamorphic Geology, v. 20, p. 581–598.

Garcia-Casco, A., Lazaro, C., Rojas Agramonte, Y., Kröner, A., and Neubauer, F., 2007, From Aptian onset to Danian demise of subduction along the northern margin of the Caribbean plate (Sierra del Convento Melange, Eastern Cuba): EOS Trans. AGU, 88(52), Fall Meet. Suppl., Abstract T11D-06.

Ghent, E.D., Stout, M.Z., Black, P.M., and Brothers, R.N., 1987, Chloritoid bearing rocks with blueschists and eclogites, northern New Caledonia: Journal of metamorphic Petrology, v. 5, p. 239–254.

Gomberg, D.N., Banks, P.O., and McBirney, A.R., 1968, Guatemala: preliminary zircon ages from the Central Cordillera: Science, v. 162, p.121–122.

Gordon, M.B., 1993, Revised Jurassic and Early Cretaceous (pre-Yojoa Group) stratigraphy of the Chortis block: paleogeographic and tectonic implications, GCSSEPM Foundation 13th Annual Research Conference, Proceedings: p. 143–154.

Gordon, M. B., and Muehlberger, W. R., 1994, Rotation of the Chortis block causes dextral slip of the Guayape fault: Tectonics, v. 13, p. 858–872.

Gose, W.A., 1985, Paleomagnetic results from Honduras and their bearing on Caribbean tectonics: Tectonics, v. 4, p. 565–585.

Grafe, F., Stanek, K.P., Baumann, A., Maresch, W., Hames, W.E., Grevel, C., and Millan, G., 2001, Rb-Sr and 40Ar/39Ar mineral ages of granitoid intrusives in the Mabujina unit, Central Cuba: thermal exhumation history of the Escambray Massif: Journal of Geology, v. 109, p. 615–631.

Graham, C. M., and Powell, R., 1986, A garnet-hornblende geothermometer: Calibration, testing, and application to the Pelona Schists, Southern California: Journal of metamorphic Geology, v. 2, p.13–31.

Gray, G.G., Pottorf, R.J., Yurewicz, D.A., Mahon, K.I., Pevear, D.R., and Chuchla, R.J., 2001, Thermal and chronological record of syn- to post-Laramide burial and exhumation, Sierra Madre Oriental, Mexico, *in* Bartolini, C., Buffler, R.T., and Cantú-Chapa, A., eds., The western Gulf of Mexico Basins: Tectonics, sedimentary basins, and petroleum systems, AAPG Memoir, v. 75, p. 159–181.

Green, T. H., and Hellman, P. L., 1982, Fe-Mg partitioning between coexisting garnet and phengite at high pressure, and comments on a garnet-phengite geothermometer: Lithos, v. 15, p. 253–266.

Grimmer, J.C., Ratschbacher, L., McWilliams, M.O., Franz, L., Gaitzsch, I., Tichomirowa, M., Hacker¸ B.R., and Y. Zhang, 2003, When did the ultrahigh-pressure rocks reach the surface? A $^{207}Pb/^{20}6Pb$ zircon, $^{40}Ar/^{39}Ar$ white mica, Si-in-white mica, single-grain provenance study of Dabie Shan synorogenic foreland sediments: Chemical Geology, v. 197, p. 87–110.

Grimmer J.C., Jonckheere, R., Enkelmann, E., Ratschbacher, L., Hacker, B.R., Blythe, A., Wagner, G.A., Liu, S., and Dong, S., 2002, Cretaceous–Tertiary history of the southern Tan-Lu fault zone: Apatite fission-track and structural constraints from the Dabie Shan: Tectonophysics, v. 359, p. 225–253.

Guzmán-Speziale, M., 2001, Active seismic deformation in the grabens of northern Central America and its relationship to the relative motion of the North America-Caribbean plate boundary: Tectonophysics, v. 337, p. 39–51.

Hacker, B. R., Mosenfelder, J. L., and Gnos, E., 1996, Rapid emplacement of the Oman ophiolite: Thermal and geochronologic constraints: Tectonics, v. 15, p. 1230–1247.

Hall, C.M., Kesler, S.E., Russel, N., Piñero, E., Sanchez, R., Perez, M., Moira, J., and Borges, M., 2004, Age and tectonic setting of the Camagüey volcanic-intrusive arc, Cuba: evidence for rapid uplift of the western Greater Antilles: Journal of Geology, v. 112, p. 521–542.

Harlow, G.E., 1994, Jadeitites, albitites and related rocks from the Motagua Fault Zone, Guatemala: Journal of Metamorphic Geology, v. 12, p.49–68.

Harlow, G.E., Hemming, S.R., Avé Lallemant, H.G., Sisson, V.B., and Sorensen, S.S., 2004, Two high-pressure–low-temperature serpentinite-matrix mélange belts, Motagua fault zone, Guatemala: A record of Aptian and Maastrichtian collisions: Geology, v. 32, p.17–20.

Hernández-Treviño, T., Torres de León, R., Solís-Pichardo, G., Schaaf, P., Hernández-Bernal, M.S., and Morales-Contreras, J.J., 2004, Edad de la Formación Chapolapa en la localidad del Río Cochoapa al este del Ocotito, estado de Guerrero: IV Reunión Mexicana de Ciencias de la Tierra, Juriquilla, Querétaro, pp. 338.

Herrmann, U., Nelson, B.K., and Ratschbacher, L., 1994, The origin of a terrane: U-Pb systematics and tectonics of the Xolapa complex (southern Mexico): Tectonics, v. 13, p. 455–474.

Hey, M., 1954: A new review of the chlorites: Mineralogical Magazine, v. 30, p. 225–234.

Hodges, K. V., and Spear, F. S., 1982, Geothermometry, geobarometry and the Al2SiO5 triple point at Mt. Moosilauke, New Hampshire: Am. Mineral., v. 67, p. 1118–1134.

Hoernle, K., and Hauff, F., 2005, Chapter 20. Oceanic igneous complexes, *in* Bundschuh, J., and Alvarado, G., eds., Central America: Geology, Resources, and Natural Hazards: A.A.Balkema Publishers, Lisse, The Netherlands, p. 523–547.

Holland, T. J. B., 1980, The reaction albite = jadeite + quartz determined experimentally in the range of 600°C –1200°C: Am. Mineral., v. 65, p. 129–134.

Holland, T. J. B., 1990, Activities of components in omphacitic solid solution: Contrib. Mineral. Petrol., v. 105, p. 446–453.

Holland, T. J. B., and Blundy, J. D., 1994, Non-ideal interactions in calcic amphiboles and their bearing on amphibole-plagioclase thermometry: Contrib. Mineral. Petrol., v. 116, p. 208–224.

Horne, G., Atwood, M., and King, A., 1974, Stratigraphy, sedimentology, and paleoenvironment of Esquias Formation of Honduras: American Association of Petroleum Geologists Bulletin, v. 58, p. 176–188.

Horne, G., Clark, G., and Pushkar, P., 1976a, Pre-Cretaceous rocks of northwestern Honduras: basement terrane in Sierra de Omoa: American Association of Petroleum Geologists Bulletin, v. 60, p. 566–583.

Horne, G., Pushkar, P. and Shafiqullah, M., 1976b, Laramide plutons on the landward continuation of the Bonacca ridge, northern Honduras: Publicaciones Geologicas del ICAITI (Guatemala), v. 5, p.84–90.

Indares, A., and Martignole, J., 1985, Biotite garnet geothermometry in the granulite facies: The influence of Ti and Al in biotite: Am. Mineral., v. 70, p. 272–278.

Instituto Geográfico Nacional (IGN): Mapa Geológico de Guatemala Escala, 1978, 1:50.000, Hoja Río Hondo, Guatemala.

Jackson, T.A., Duke, M.J.M., Scott, P.W., Smith, F., and Wilkinson, F.C.F., 1995, Petrology and inferred tectonic setting of the Mountain Pine Ridge Granitoids, Maya Mountains, Belize: International Geology Review, v. 37, p. 26–38.

James, K., 2006, Arguments for and against the Pacific origin of the Caribbean Plate: Discussion, finding for an inter-American origin: Geological Acta, v. 4, p. 279–302.

Jarosewich, E., Nelen, J. A., and Norberg, J. A., 1980, Reference samples for electron microprobe analysis: Geostandard Newsletter, v. 4, p. 43–47.

Jonckheere, R., 2003a, On the densities of etchable fission tracks in a mineral and co-irradiated external detector with reference to fission-track dating of minerals: Chemical Geology, v. 200, p. 41–58, doi: 10.1016/S0009-2541(03)00116-5.

Jonckheere, R., 2003b, On the methodical problems in estimating geological temperature and time from measurements of fission tracks in apatite: Radiation Measurements, v. 36, p. 43–55, doi: 10.1016/S1350-4487(03)00096-9.

Jonckheere, R., and Wagner, G.A., 2000, The KTB apatite fission-track profile: The significance of bore-hole data in fission-track analysis: Geological Society of Australia Abstracts, v. 58, p. 193–194.

Jordan, B.R., Sigurdsson, H., Carey, S., Lundin, S., Rogers, R.D., Singer, B., and Barguero-Molina, M., 2007, Petrogenesis of Central American Tertiary ignimbrites and associated Caribbean Sea tephra, *in* Mann, P., ed., Geologic and tectonic development of the Caribbean plate boundary in northern Central America: Geological Society of America Special Paper 428, p. 151–179, doi:10.1130/2007.2428(07).

Keppie, D. J., 2004, Terranes of Mexico revisited: A 1.3 billion year odyssey, International Geology Review, v. 46, p. 765–794.

Keppie, D. J., Nance, R.D., Dostal, J., Ortega-Rivera, A., Miller, B.V., Fox, D., Muise, J., Powell, J.T., Mumma, S.A., and Lee J.W.K., 2004, Mid-Jurassic tectonothermal event superposed on a Paleozoic geological record in the Acatlán complex of southern Mexico: hotspot activity during the breakup of Pangea, Gondwana Research, v. 7, p. 239–260.

Kesler, S.E., Campell, I.H., Allen, Ch.M., 2005, Age of the Los Ranchos Formation, Dominican Republic: Timing and tectonic setting of primitive island arc volcanism in the Caribbean region: Geological Society of America Bulletin, v. 117, p. 987–995.

Ketcham, R.A., Donelick, R.A., and Donelick, M.B., 2000, AFTSolve: A program for multikinetic modeling of apatite fission-track data: Geological Materials Research, v. 2, p. 1–32.

Kohn, M., and Spear, F., 1990, Two new geobarometers for garnet-amphibolites, with application to southeastern Vermont: American Mineralogist, v. 75, p. 89–96.

Krebs, M., Stanek, K.P., Scherer, E., Maresch, W., Grafe, F., Idleman, B., and Rodionov, N., 2007, Age of high pressure metamorphism from the Escambray Massif, Cuba: Abstract, Goldschmidt Conference Cologne 2007, Cambridge Publications, A522.

Kretz, R., 1983, Symbols for rock-forming minerals: American Mineralogists, v. 68, p. 277–279.

Krogh, E. J., 2000, The garnet-clinopyroxene Fe/Mg geothermometer: an updated calibration: Journal of Metamorphic Geology, v. 18, p. 211–219.

Leake, B. E., Wooley, A. R., Arps, C., Birch, W., Gilbert, M., Grice, J., Hawthorne, F., Kato, A., Kisch, H., Krivovichev, V., Linthout, K., Mandariona, J. L. J., Maresch, V., Nickel, E., Rock, N., Schumacher, J., Smith, D., Stephenson, N., Ungaretti, L., Whittaker, E., and Youzhi, G., 1997, Nomenclature of amphiboles. Report of the subcommittee on amphiboles of the Intern. Mineral. Association Commission on new minerals and mineral names, European Journal of Mineralogy, v. 9, p. 623–665.

Ludwig, K.R., 2003, Isoplot 3.01. A geochronological toolkit for Microsoft Exel: Berkeley Geochronology Center Special Publication, v. 4, p. 1–70.

Machorro, R., 1993, Geology of the northwestern part of the Granados Quadrangle, Central Guatemala, MSc Thesis, University of Texas, El Paso.

Malone, J.R., Nance, R.D., Keppie, J.D., and Dostal, J., 2002, Deformational history of part of the Acatlán Complex: Late Ordovician Early Permian orogenesis in southern Mexico: Journal of South American Earth Sciences, v. 15, p. 511–524, doi: 10.1016/S0895-9811(02)00080-9.

Mann, P., 2007, Overview of the tectonic history of northern Central America, *in* Mann, P., ed., Geologic and tectonic development of the Caribbean plate boundary in northern Central America: Geological Society of America Special Paper 428, p. 1–19, doi:10.1130/2007.2428(01).

Manton, W.I., 1996, The Grenville of Honduras: Geological Society of America, Annual Meeting Abstracts with Program, p. A–493.

Manton, W.I, and Manton, R.S, 1984, Geochronology and Late Cretaceous–Tertiary tectonism of Honduras: Direccion General de Minas e Hidrocarburos, Honduras, 55 p.

Manton, W.I, and Manton, R.S, 1999, The Southern flank of the Tela basin, Republic of Honduras, *in* Mann, P., ed., Caribbean Basins. Sedimentary Basins of the World, 4: Elsevier Science B.V., Amsterdam, The Netherlands, p. 219–236.

Martens, U., Ortega-Obregón, C., Estrada, J., and Valle, M., 2005, Chapter 19. Metamorphism and metamorphic rocks, *in* Bundschuh, J., and Alvarado, G., eds., Central America: Geology, Resources, and Natural Hazards: A.A.Balkema Publishers, Lisse, The Netherlands, p. 485–522.

Massonne, H.-J., and Szpurka, Z., 1997, Thermodynamic properties of white micas on the basis of high-pressure experiments in the system K_2O-MgO-Al_2O_3-SiO_2-H_2O and K_2O-FeO-Al_2O_3-SiO_2-H_2O: Lithos, v. 41, p. 229–250.

Meschede, M., and Frisch, W., 1998, A plate-tectonic model for the Mesozoic and Early Cenozoic history of the Caribbean plate: Tectonophysics, v. 296, p. 269–291.

Meschede, M., Frisch, W., Herrmann, U., and Ratschbacher, L., 1996, Stress transmission across an active plate boundary: An example from southern Mexico: Tectonophysics, v. 266, p. 81–100, doi: 10.1016/S0040-1951(96)00184-9.

Metal Mining Agency of Japan (MMAJ), 1980, Report on geology survey of the western area (Olancho): v. 5, Japan International Copperation Agency, Government of Japan, 138p.

Morán-Zenteno, D., 1992, Investigaciones isotópicas de Rb-Sr y Sm-Nd en rocas cristalinas de la eregión de Tierra Colorada-Acapulco-Cruz-Grande, Estado de Guerrero: Unpublished PhD Thesis, Universidad Autonoma de Mexico, Mexico, DF, 175 pp.

Morán-Zenteno, D.J., Corona-Chávez, P., and Tolson, G., 1996, Uplift and subduction erosion in southwestern Mexico since the Oligocene: Pluton geobarometry constraints: Earth and Planetary Science Letters, v. 141, p. 51–65, doi: 10.1016/0012-821X(96)00067-2.

Morán-Zenteno, D.J., Tolson, G., Martínez-Serrano, R.G., Martiny, B., Schaaf, P., Silva-Romo, G., Macías-Romo, C., Alba-Aldave, L., Hernández-Bernal, M.S., and Solís-Pichardo, G.N., 1999, Tertiary arc-magmatism of the Sierra Madre del Sur, Mexico, and its transition to the volcanic activity of the Trans-Mexican Volcanic Belt: Journal of South American Earth Sciences, v. 12, p. 513–535.

Nieto-Samaniego, A.F., Alaniz-Álvarez, S.A., Silva-Romo, G., Eguiza-Castro, M.H., and Mendoza-Rosales, C.C., 2006, Latest Cretaceous to Miocene deformation events in the eastern Sierra Madre del Sur, Mexico, inferred from the geometry and age of major structures: Geological Society of America Bulletin, v. 118, p. 238–252, doi: 10.1130/B25730.1.

Ortega-Gutiérrez, F., Elías-Herrera, M., Macías-Romero, C., and López, R., 1999, Late Ordovician–Early Silurian continental collisional orogeny in southern Mexico and its bearing on Gondwana-Laurentia connections: Geology, v. 27, p. 719–722, doi: 10.1130/0091-7613(1999)027<0719:LOESCC>2.3.CO;2.

Ortega-Gutiérrez, F., Solari, L.A., Solé, J., Martens, U., Gómez-Tuena, A., Morán-Ical, Reyes-Sala, M., and Ortega-Obregón, C., 2004, Polyphase, high-temperature eclogite-facies metamorphism in the Chuacús complex, Central Guatemala: Petrology, geochronology, and tectonic implications: International Geology Review, v. 46, p. 445-470.

Ortega-Obregón, C., Solari, L., Keppie, J.D., Ortega-Gutiérrez, F., Solé, J., and Morán, S., 2008, Middle-Late Ordovician magmatism and Late Cretaceous collision in the southern Maya block, Rabinal-Salamá area, central Guatemala: implications for North America-Caribbean plate tectonics: Geological Society of America Bulletin, in press.

Ortega-Obregón, C., Solari, L., Ortega-Gutiérrez, F., Solé-Viñas, J., and Gómez-Tuena, A., 2004, Caracterización estructural, petrológica y geocronológica de la zona de cizalla "Baja Verapaz", Guatemala. Libro de Resúmenes, IV Reunión Nacional de Ciencias de la Tierra, Juriquilla—México, 2004, p. 204.

Perchuk, L.L., and Lavrent´eva, J.V., 1983, Experimental investigations of exchange equilibria in the system cordierite-garnet-biotite, *in* Saxena S. K., ed., Kinematics and equilibria in mineral reactions: Springer, Berlin, p. 199-239.

Perchuk, L.L., Aranovich, L.Y., Podlesskii, K.K., Lavrent´eva, J.V., Gerasimov, V.Y., Fed'kin, V.V., Kitsul, V.I., Karsakov, L.P., and Berdnikov, N.V., 1985, Precambrian granulites of the Aldan shield, eastern Siberia, USSR: Journal of Metamorphic Geology, v. 3, p. 265–310.

Pindell, J.K., Cande, S.C., Pitman II, W.C., Rowley, D.B., Dewey, J.F., Labrecque, J., and Haxby, W., 1988, A plate-kinematic framework for models of Caribbean evolution: Tectonophysics, v. 155, p. 121–138.

Pindell, J.L., Kennan, L., Stanek, K.P., Maresch W., and Draper G., 2006, Foundations of Gulf of Mexico and Caribbean evolution: eight controversies resolved: Geologica Acta, v.99, no.4, p. 303–341.

Plafker, G., 1976, Tectonic aspects of the Guatemala earthquake of 4 February 1976: Science, v. 193, p. 1201–1208.

Plyusnina, L. P., 1982, Geothermometry and geobarometry of plagioclase-hornblende bearing assemblages: Contrib. Mineral. Petrol., v. 80, p. 140–146.

Ratschbacher, L., Riller, U., Meschede, M., Herrmann, U., Frisch, W., 1991, Second look at suspect terranes in southern Mexico: Geology, v. 19, p. 1233–1236.

Ratschbacher, L., Franz, L., Enkelmann, E., Jonckheere, R., Pörschke, A., Hacker, B.R., Dong, S., and Zhang, Y., 2006, The Sino-Korean–Yangtze suture, the Huwan detachment, and the Paleozoic–Tertiary exhumation of (ultra)high-pressure rocks along the Tongbai–Xinxian–Dabie, *in* Hacker, B.R., McClelland, W.C., and Liou, J.G., eds., Ultrahigh-pressure metamorphism: Deep continental subduction: Geological Society of America, Special Paper, v. 403, p. 45–75, doi 10.1130/2006.2403(03).

Riller, U., Ratschbacher, L., and Frisch, W., 1992, Left-lateral transtension along the Tierra Colorada deformation zone, northern margin of the Xolapa magmatic arc of southern Mexico: Journal of South American Earth Sciences, v. 5, p. 237–249, doi: 10.1016/0895-9811(92)90023-R.

Robinson, K.L., Gastil, R.G., Campa, M.F., and Ramirez-Espinosa, J., 1989, Geochronology of basement and metasedimentary rocks in southern Mexico and their relation to metasedimentary rocks in Peninsular California: Geological Society of America Abstracts with Programs, v. 21, no. 5, p. 135.

Rogers, R.D., 2003, Jurassic–Recent tectonic and stratigraphic history of the Chortis block of Honduras and Nicaragua (northern Central America): PhD Thesis, University of Texas, Austin, 265pp.

Rogers, R. D., Kárason, H., and van der Hilst, R. D. , 2002, Epeirogenic uplift above a detached slab in northern Central America: Geology, v. 30, 1031–1034.

Rogers, R.D., Mann, P., Scott, R.W., and Patino, L., 2007a, Cretaceous intra-arc rifting, sedimentation, and basin inversion in east-central Honduras, *in* Mann, P., ed., Geologic and tectonic development of the Caribbean plate boundary in northern Central America: Geological Society of America Special Paper 428, p. 89–128, doi:10.1130/2007.2428(05).

Rogers, R.D., Mann, P., Emmet, P.A., and Venable, M.E., 2007b, Colon fold belt of Honduras: Evidence for Late Cretaceous collision between the continental Chortis block and intra-oceanic Caribbean arc, *in* Mann, P., ed., Geologic and tectonic development of the Caribbean plate boundary in northern Central America: Geological Society of America Special Paper 428, p. 129–149, doi:10.1130/2007.2428(06).

Rogers, R.D., Mann, P., and Emmet, P.A., 2007c, Tectonic terranes of the Chortis block based on integration of regional aeromagnetic and geologic data, *in* Mann, P., ed., Geologic and tectonic development of the Caribbean plate boundary in northern Central America: Geological Society of America Special Paper 428, p. 65–88, doi:10.1130/2007.2428(06).

Rojas-Agramonte, Y., Kröner, A., García-Casco, A., Iturralde-Vinent, M.A., Wingate, M.T.D., and Liu, D.Y., 2006, Geodynamic implications of zircon ages from Cuba: Geophysical Research Abstracts, v. 8, 04943, 2006, SRef-ID: 1607-7962/gra/EGU06-A-04943.

Rosencrantz E., Ross, M.I., and Slater, J.G., 1988, Age and spreading history of the Cayman Trough as determined from depth, heat flow, and magnetic anomalies: J. Geophys. Res., v. 93, 2141–2157.

Sánchez-Zavala, J.L., Ortega-Gutiérrez, F., Keppie, J.D., Jenner, G.A., and Belousova, E., 2004, Ordovician and Mesoproterozoic zircon from the Tecomate Formation and Esperanza granitoid, Acatla´n Complex, southern Mexico: local provenance in the Acatlán and Oaxacan complexes: International Geology Review, v. 46, 1005–1021.

Schaaf, P., Morán-Zenteno, D., Hernández-Bernal, M.S., Solis-Pichardo, G., Tolson, G., and Köhler, H., 1995, Paleogene continental margin truncation in southwestern Mexico: Geochronological evidence: Tectonics, v. 14, p. 1339–1350.

Schaaf, P., Weber, B., Weis, P., Groß, A., Ortega-Gutiérrez, F., and Köhler, H., 2002, The Chiapas Massif (Mexico) revised: new geologic and isotopic data for basement characteristics, *in* Miller, H., ed., Contributions to Latin-American geology: Neues Jahrbuch Geologie Paläontologie, Abhandlungen, v. 225, p. 1–23.

Schmid, R., Franz, L., Oberhänsli, R., and Dong, S., 2000, High Si-phengite, mineral chemistry and P-T evolution of ultra-high-pressure eclogites and calc-silicates from the Dabie Shan, eastern PR China: Geological Journal, v. 35, p. 185–207.

Schneider, J., Bosch, D., Monié, P., Guillot, S., García-Casco, A., Lardeaux, J. M., Luís Torres-Roldán, R., and Millán Trujillo, G., 2004, Origin and evolution of the Escambray Massif (Central Cuba): an example of HP/LT rocks exhumed during intraoceanic subduction: Journal of Metamorphic Geology, v. 22, 227–247.

Schwartz, D.P, 1976, Geology of the Zacapa quadrangle and vicinity, Guatemala, Central America: PhD Thesis, State University of New York, Binghamton, 1976.

Solari L.A., Dostal J., Ortega-Gutiérrez F., and Keppie J.D., 2001, The 275 Ma arc-related La Carbonara stock in the northern Oaxacan Complex of southern Mexico: U–Pb geochronology and geochemistry: Revista Mexicana de Ciencias Geológicas, v. 18, p. 149–161.

Solari, L.A., Keppie, J.D., Ortega-Gutiérez, F., Ortega-Rivera, A., Hames, W.E., and Lee, J.K.W., 2004, Phanerozoic structures in the Grenville complex, southern Mexico: Result of thick-skinned tectonics: International Geology Review, v. 46, p. 614–628.

Solari, L.A., Torres de León, R., Hernández Pineda, G., Solé, J., Solís-Pichardo, Hernández-Treviño, G., 2007, Tectonic significance of Cretaceous–Tertiary magmatic and structural evolution of the northern margin of the Xolapa Complex, Tierra Colorada area, southern Mexico: Geological Society of America Bulletin, v. 119, p. 1265–1279; doi: 10.1130B26023.1.

Solari, L. A., Ortega-Gutiérrez, F., Elías-Herrera, M., Schaaf, P., Norman, M., Torres de León, R., Ortega-Obregón, C., Chiquín, M., and Morán-Ical, S., 2008, U-Pb zircon geochronology of Paleozoic units in Western and Central Guatemala: insights into the tectonic evolution of Middle America, *in* Pindell, J., and James, H. J. K., eds., The Geology of the Caribbean Plate: Geological Society of London, Special Publication, in press.

Spear, F. S., 1981, NaSi=CaAl exchange equilibrium between plagioclase and amphibole: Contrib. Mineral. Petrol., v. 72, p. 33–41.

Spear, F. S., 1995, Metamorphic phase equilibria and pressure-temperature-time paths: Mineralogical Society of America Monograph, Washington, D. C., 799 pp.

Sperner, B., Ratschbacher, L., and Ott, R., 1993, Fault-striae analysis: A Turbo Pascal program package for graphical presentation and reduced stress tensor calculation: Computers & Geosciences, v. 19, p. 1361–1388.

Sperner, B. and Ratschbacher, L., 1994, A Turbo Pascal program package for graphical representation and stress analysis of calcite deformation: Zeitschrift deutsche Geologische Gesellschaft, v. 145, p. 414-423.

Stanek, K.P., Rißе, A., Renno, A., Romer, R., and Grafe, F., 2005, The history of the Great Antillean Island Arc: example from Central Cuba: Abstract, Colloquium on Latin American Geosciences 2005, Potsdam, Terra Nostra, Nr. 1,

Steiner, M.B., and Walker, J.D., 1996, Late Silurian plutons in Yucatan: J. Geophys. Res., v. 101, p. 17727–17735.

Stipp, M., Stünitz, H., Heilbronner, R., and Schmid, S.M., 2002, The eastern Tonale fault zone: a natural laboratory for crystal plastic deformation of quartz over a temperature range from 250 to 700°C: Journal of Structural Geology, v. 24, p. 1861–1884.

Sutter, J. F., 1979, Late Cretaceous collisional tectonics along the Motagua fault zone, Guatemala: Geological Society of America Abstracts with Programs, v. 11, p. 525–526.

Talavera-Mendoza, O., Ruiz, J., Gehrels, G.E., Meza-Figueroa, D., Vega-Granillo, R., Campa-Uranga, M.F., 2005, U-Pb geochronology of the Acatlán complex and implications for the Paleozoic paleogeography and tectonic evolution of southern Mexico, Earth and Planetary Science Letters, v. 235, p. 682–699.

Talavera-Mendoza, O., Ruiz, J., Gehrels, G.E., Valencia, V.A., and Centeno-García, E., 2007, Detrital zircon U/Pb geochronology of southern Guerrero and western Mixteca arc successions (southern Mexico): New insights for the

tectonic evolution of southwestern North America during the late Mesozoic: Geological Society of America Bulletin, v. 119, p. 1052–1065, doi: 10.1130/B26016.1.

Tolson, G., 2005, La falla Chacalapa en el sur de Oaxaca: Boletín de la Sociedad Geológica Mexicana, v. 57, p. 111–122.

Torres R., Ruiz J., Patchett P.J., and Grajales J.M., 1999, Permo-Triassic continental arc in eastern Mexico: tectonic implications for reconstructions of southern North America, *in* Bartolini, C.W., Wilson J.L., Lawton T.F., eds., Mesozoic sedimentary and tectonic history of North-Central Mexico: Geological Society of America Special Paper, v. 340, pp. 191–196.

Triboulet, C., 1992, The (Na-Ca)amphibole-albite-chlorite-epidote-quartz geothermobarometer in the system S-A-F-M-C-N-H_2O. 1. An empirical calibration: Journal of metamorphic Geology, v. 10, p. 545–556.

Tsujimori, T., Liou, J.G., and Coleman, R.G., 2004, Comparison of two contrasting eclogites from the Motagua fault zone, Guatemala: southern lawsonite eclogite versus northern zoisite eclogite, Geological Society of America Abstracts with Programs, v. 36, p.136.

Tsujimori, T., Liou, J.G., and Coleman, R.G., 2005, Coexisting retrograde jadeite and omphacite in a jadeite-bearing lawsonite eclogite from the Motagua Fault Zone, Guatemala: American Mineralogist, v. 90, p. 836–842.

Tsujimori, T., Sisson, V.B., Liou, J.G., Harlow, G.E., and Sorensen, S.S., 2006, Petrologic characterization of Guatemalan lawsonite eclogite: Eclogitization of subducted oceanic crust in a cold subduction zone, *in* Hacker, B.R., McClelland, W.C., and Liou, J.G., eds., Ultrahigh-pressure metamorphism: Deep continental subduction: Geological Society of America Special Paper, v. 403, p. 147–168, doi: 10.1130/2006.2403(09).

van den Boom, G., 1972, Petrofazielle Gliederung des metamorphen Grundgebirges in der Sierra de Chuacús, Guatemala: Beihefte Geologisches Jahrbuch, v. 122, pp. 5–49.

Vega-Granillo, R., Talavera-Mendoza, O., Meza-Figueroa, D., Ruiz, J., Gehrels, G.E., López-Martínez, M., and de la Cruz-Vargas, J.C., 2007, Pressure-temperature-time evolution of Paleozoic high-pressure rocks of the Acatlán Complex (southern Mexico): Implications for the evolution of the Iapetus and Rheic Oceans: Geological Society of America Bulletin, v. 119. p. 1249–1264, doi: 10.1130/B226031.1.

Venable, M., 1994, A geological, tectonic, and metallogenetic evaluation of the Siuna terrane (Nicaragua): Ph.D. disseration, University of Arizona, Tucson, 154 p.

Viland, J., Henry, B., Calix, R., and Diaz, C., 1996, Late Jurassic deformation in Honduras: Proposals for a revised regional stratigraphy: Journal of South American Earth Sciences, v. 9, p. 153–160.

Von Blanckenburg, F. V., Villa, I., Baur, H., Morteani, G., and Steiger, R.H. , 1989, Time calibration of a PT-path in the Western Tauern Window, Eastern Alps: The problem of closure temperatures: Contributions to Mineralogy and Petrology, v. 101, p. 1–11.

Waters, D.J., and Martin, H.N., 1993, Geobarometry in phengite-bearing eclogites: Terra Abstracts, v. 5, p. 410–411; updated calibration of 1996 at: http://www.earth.ox.ac.uk/~davewa/ecbar.html.

Watkins, J. S., 1989, The Middle America trench off southern Mexico, *in* Winterer, E. L., Hussong, D. M., and Decker, R. W., eds., The Eastern Pacific Ocean and Hawaii: The Geology of North America, v. N, pp. 523–533.

Wawrzyniec, T., Molina-Garza, R.S., Geissman, J., and Iriondo, A., 2005, A newly discovered. Relic, transucrrent plate boundary – the Tonala shear zone and paleomagnetic evolution of the western Maya block, SW Mexico: Geological Society of America Abstract with Programs, v. 37, p.68.

Weber, B., Cameron, K.L., Osorio, M., Schaaf, P., 2005, A late Permian tectonothermal event in Grenville crust of the Southern Maya terrane; U-Pb zircon ages from the Chiapas massif, Southeastern México: International Geology Review, v. 47, p. 509–529.

Weber, B., Iriondo, A., Premo, W.R., Hecht, L., Schaaf, P., 2006a, New insights into the history and origin of the southern Maya Block, SE México; U-Pb-SHRIMP zircon geochronology from metamorphic rocks of the Chiapas Massif, International Journal of Earth Sciences, DOI 10.1007/s00531-006-0093-7.

Weber, B., Schaaf, P., Valencia, V.A., Iriondo, A., and Ortega-Gutiérrez, F., 2006b, Provenance ages of late Paleozoic sandstones (Santa Rosa Formation) from the Maya block, SE Mexico. Implications on the tectonic evolution of western Pangea: Revista Mexicana de Ciencias Geológicas, v. 23, p. 262–276.

Weiland, T., Suayah, W., and Finch, R., 1992, Petrologic and tectonic significance of Mesozoic volcanic rocks in the Río Wampú area, eastern Honduras: Journal of South American Earth Sciences, v. 6, p. 309–325.

Williams, I.S., 1998, U-Th-Pb geochronology by ion microprobe, *in* McKibben, M.A., Shanks III, W.C., and Ridley, W.I., eds., Applications of microanalytical techniques to understanding mineralizing processes: Reviews in Economic Geology, v. 7, p. 1–35.

Wilson, H.H., 1974, Cretaceous sedimentation and orogeny in nuclear Central America: American Association of Petroleum Geologists, v. 58, p. 1348–1396.

Yañez, P., Ruiz, J., Patchett, P. J., Ortega-Gutierrez, F., Gehrels, G. E., 1991, Isotopic studies of the Acatlán complex, southern Mexico: Implications for Paleozoic North American tectonics: Geological Society of America Bulletin, v. 103, p. 817–828.

Appendix

TABLE 1. SAMPLE DESCRIPTIONS AND STOP LOCATIONS

Sample	Stop	Rock	N latitude	W longitude	Elevation (m)
Western Chuacús complex					
G1s	G1	quartzitic paragneiss	15°11.2’	91°32.7’	1990
G18s	G1	phyllonitic migmatitic gneiss	15°11.2’	91°32.7’	1990
G19s	G1	hornblende-epidote schist	15°11.2’	91°32.7’	1990
G20s	G45	quartz-rich migmatitic augengneiss	15°17.4’	91°29.0’	–
G21s	G3=G46	epidote schist	15°18’[1]	91°29.6’[1]	–
G27s	G56, G57	biotite-granite gneiss	15°19.9’	91°37.2’	–
GM8s	GM33=G8	greenschist-grade granite mylonite	15°12.2’	91°11.8’	–
	GM37	phyllonite	15°17.2’[1]	91°05.8’[1]	–
	GM38	granodiorite	15°19.061’	91°10.374’	–
GM13s	GM42	(?ortho)gneiss	15°23.977’	91°58.790’	1100[1]
Central Chuacús complex					
G10s	G29	calcsilicate layer in marble	14°57.2’	90°13.2’	–
G11s	G30	migmatitic two-mica orthogneiss	14°58.0’	90°14.3’	1070
G12s	G31, G19	retrograde mylonitic orthogneiss	15°00.3’	90°14.7’	1300
G14s	G32	augengneiss	15°01.8’	90°13.1’	–
5PB-8	5PB-8	micro-diorite	15°15.06’	89°11.51’	–
5PB-9b	5PB-9	phyllitic para- and orthogneiss intercalation	15°14.02’	89°15.51’	–
	5PB-10	marble mylonite	15°13.08’	89°14.58’	–
5PB-13a	5PB-13	garnet-bearing mica schist	15°00.41’	89°58.22’	–
5PB-13b	5PB-13	garnet amphibolite	15°00.41’	89°58.22’	–
5PB-14	5PB-14	hornblende-mica-chlorite schist	15°00.37’	89°57.56’	480
5CO-1	5CO-1	two-mica orthogneiss	15°06.05’	90°24.03’	–
	5CO-3	orthogneiss	15°06.09’	90°27.05’	–
5CO-4b	5CO-4	two mica, garnet ?paragneiss	15°02.43’	90°29.41’	1229
5CO-5a	5CO-5	garnet amphibolite (eclogite) with two mica schist intercalations	14°57.05’	90°29.11’	970
5CO-5b	5CO-5	deformed meta-pegmatite	14°57.05’	90°29.11’	970
5CO-6b	5CO-6	garnet orthogneiss	14°55’[1]	90°31’[1]	950[1]
824	824	two-mica gneiss	15°00.9246’	90°22.8978’	2038
825	825	garnet-muscovite gneiss	14°58.8036’	90°20.0832’	823
827	827	quartz-rich micaschist	15°00.0930’	90°20.2200’	1319
846	846	garnet amphibolite (eclogite)	15°00.0612’	90°32.4480’	1681
	854	(ultra)mylonitic gneiss, pegmatite	15°03.954’	89°36.118’	284
	856	augengneiss, biotite granite, aplite	15°00.715’	89°43.997’	–
	876	intercalation of low-grade meta-sedimentary rocks with schists and serpentinite	14°55.115’	90°05.952’	360
885A	885	pegmatite	14°53.989’	90°33.211’	883
	880-886	variegated Chuacús gneisses along the El Chol and Aqua Caliente rivers	14°58°992’ to 14°54°813°	90°28.882’ to 90°31.423’	
887C	887	quartzo-feldspatic paragneiss	14°56.090’	90°30.101’	864
Metasomatized southern Chuacús complex					
G6s	G26	metasomatized basement (phyllonite)	14°55.4’	90°04.4’	–
G7s	G27	metasomatized, retrogressed biotite gneiss, pseudotachylite vein in pull-apart tension gash	14°55.0’	90°08.1’	–
	5C-35	chlorite phyllite (metasomatic basement)	14°57.13’	89°49.45’	–
5C-36a	5C-36	metasomatized biotite gneiss (phyllonite),	14°55.47’	89°59.27’	372
860B	860, 5PB-15	metasomatized garnet micaschist (phyllonite)	14°57.344’	89°57.774’	378
	876	intercalation of low-grade meta-sedimentary rocks with schists and serpentinite	14°55.115’	90°05.952’	360
Sanarate complex					
G3s	G23	retrograde basement imbricated with phyllite, epidote schist	14°45’[2]	90°20’[2]	–
G5s	G24	amphibolite	14°47.3’[1]	90°17’[1]	–
5G-1a	5G-1	chlorite-epidote-hornblende schist	14°47.46’	90°15.17’	–
	853	amphibolite	14°45.254’	90°08.307’	855

	870, 871	amphibolite	14°45.3’	90°08.5’	880
North and South El Tambor complexes					
	G28	serpentinite	14°56.3’[1]	90°11.2’[1]	–
	G34=GM14	mélange of serpentinite, ophicalcite, volcanics	14°54.38’	90°09.39’	–
	G35	serpentinite	14°54.3’[1]	90°09.4’[1]	–
	G38	serpentinite	14°54.2’[2]	90°11’[2]	–
	5PB-7	serpentinite	15°23.04’	89°01.16’	–
	GM11 to GM13	serpentinite	1.5 km outcrop stretch		
			14°54.801’	90°07.911’	–
	852	mélange of clastics and greenschist	14°44.487’	90°04.892’	766
	855	mélange of phyllite, serpentinite, blueschist	14°49.635’	89°48.008’	686
	864	meta-siltstone, serpentinite, granite dike	14°51.492’	89°48.725’	349
	869	meta-clastics; granite dikes	14°43.620’	90°03.842’	990
Foreland fold-and-thrust belt; Paleozoic to Tertiary cover; south and north of Motagua fault zone					
	G2	pyroclastics and welded tuff	15°15’[2]	91°29’[2]	–
	G4	meta-conglomerate; Chicol Formation	15°21.6’[1]	91°35.6’[1]	–
	G5	intercalation of volcanics and clastics	15°22.6’[1]	91°37.3’[1]	–
	G39=GM23	massive limestone	15°18.5’[1]	90°29.1’[1]	–
	G40=GM25	serpentinite–Coban limestone contact	15°18.55’	90°29.11’	–
	G41=GM26	serpentinite–Coban limestone contact	15°16.4’[1]	90°28.58’[1]	–
	G42	serpentinite–Coban limestone contact	15°16.449’	90°28.585’	–
	G43	Cretaceous limestone	15°18.5’[1]	90°28’[1]	–
	G48	boundary limestone to serpentinite	15°22’[1]	91°27’[1]	–
	G49	serpentinite	15°22’[1]	91°27.5’[1]	–
	G50	pyroclastics	15°21.3’[1]	91°29.35’[1]	–
	G51	pyroclastics	15°21.45’[1]	91°26.5’[1]	–
	G54	Cretaceous limestone	15°24.7’[1]	91°49’[1]	–
	G55	Permian Chochal limestone	15°29.6’[1]	91°45.5’[1]	–
	G58	cataclastic, dark limestone, dolomite	15°24.3’[1]	91°39.8’[1]	–
	G59	Cretaceous thick-bedded limestone	15°38’[1]	91°58.6’[1]	–
	G60	Late Cretaceous limestone	15°36.1’	91°51.5’	–
	G61,62	slate-limestone intercalation	close to G60		–
	GM1	rhyolite	14°43,6’[1]	90°32.3’[1]	–
	GM2	volcanics	14°46.951’	90°17.509’	–
	GM3	Subinal red beds	14°51.807’	90°04.706’	–
	GM4,5	?Cretaceous limestone	14°49.065’	90°09.301’	–
	GM7	?Cretaceous limestone	14°50.387’	90°07.966’	–
	GM9	Subinal red beds	14°53.003’	90°03.632’	–
	GM10	pyroclastics	14°54.891’	90°05.297’	–
GM1s	GM15	quartz phyllite	15°06’[1]	90°18’[1]	–
	GM22	Permian Chochal limestone	15°16’[2]	90°17’[2]	–
GM9s	GM35	phyllite of ?Permian Tactic Fm.	15°17.7’[1]	91°04.7’[1]	1250[1]
	GM36	meta-conglomerate (Sacapulas Fm.)	15°19’[1]	91°03.2’[1]	–
	GM44	volcanics	15°23.4’[1]	91°38.1’[1]	–
	GM45	volcanics	15°14.3’[1]	91°38.3’[1]	–
	GM46	volcanics	15°24.35’	91°38.3’	–
	GM47	volcanics	15°25.148’	91°38.799’	–
	GM49	volcanics	15°24’[2]	91°42.8’[2]	–
	GM50	Permian Chochal limestone	15°25’[2]	91°47’[2]	–
	GM51	Permian Chochal limestone	west of GM50		–
	GM52	Permian Chochal limestone	15°25’[2]	91°51’[2]	–
	5H-14	red beds and volcanic	14°55.52’	88°58.18’	–
	865	meta-conglomerate (Sacapulas Fm.)	15°11.117°	90°25.527’	852
	866	meta-conglomerate (Sacapulas Fm.)	15°08.919°	90°24.352’	895
	868	ultramafic rocks and Coban limestone	15°16.601’	90°29.246’	935
	872	Subinal red beds	14°51.619’	90°07.796’	434
	873	Subinal red beds	14°51.633’	90°07.079’	452
Western Las Ovejas complex, Guatemala					
5C-2c	5C-2	amphibolite	14°51.46’	89°48.79’	–
	5C-3	phyllitic paragneiss	14°50.38’	89°48.35’	–
5C-5	5C-5	phyllite, ?San Diego phyllites	14°43.13’	89°35.16’	–
	5C-15	mylonitic paragneiss	14°43.14’	89°35.55’	–
5C-23a	5C-23	granite	14°57.35’	89°32.30’	194

5C-23c	5C-23	biotite gneiss (migmatite)	14°57.35’	89°32.30’	194
5C-23d	5C-23	hornblende-biotite gneiss	14°57.35’	89°32.30’	194
5C-26c	5C-26	garnet amphibolite	14°56.17’	89°37.53’	194
5C-26d	5C-26	migmatitic biotite gneiss, amphibolite	14°56.17’	89°37.53’	194
5C-27a	5C-27	garnet-bearing migmatite, leucosome	14°57.18’	89°40.32’	286
5C-28b	5C-28	biotite gneiss with deformed pegmatite dike	14°54.32’	89°43.44’	~300
5C-33	5C-33	biotite gneiss	14°57.29’	89°32.38’	–
5C-37a	5C-37	migmatitic biotite gneiss	14°51.32’	89°44.25’	488
5C-37b	5C-37	phyllitic biotite-granite gneiss (migmatite in Chiquimula granite)	14°51.32’	89°44.25’	488
5C-37d	5C-37	garnet micaschist	14°51.32’	89°44.25’	488
5C-37e	5C-37	leucogranite injected into shear zone	14°51.32’	89°44.25’	488
	5PB1-4	gneiss, marble, leucogranite, amphibolite	15°02.12’ to 15°05.34’	89°18.11’ to 89°21.15’	
5PB-5a	5PB-5	amphibolite in migmatite	15°05.17’	89°17.05’	440
5PB-5c	5PB-5	orthogneiss (large xenolith in granite)	15°05.17’	89°17.05’	440
5PB-6b	5PB-6	granite close to augengneiss	15°08.36’	89°11.11’	226
Eastern Las Ovejas complex, Honduras					
	5H-1	micaschist, migmatitic biotite gneiss	15°45.25’	87°52.20’	–
5H-2a	5H-2	leucogranite with localized shear zones	15°43.56’	87°53.54’	–
5H-3a	5H-3	tonalitic granite with local shear zones	15°41.09’	87°56.18’	16
5H-4b	5H-4	biotite–amphibolite pegmatite in leucogranite	15°39.08’	87°56.57’	–
5H-4c	5H-4	greenschist facies shear zone in amphibolite	15°39.08’	87°56.57’	–
5H-4d	5H-4	undeformed amphibolite	15°39.08’	87°56.57’	–
	5H-7	phyllite over orthogneiss	15°25.48’	88°01.22’	–
	5H-8	migmatitic orthogneiss	15°19.50’	88°18.07’	–
5H-9a	5H-9	migmatitic orthogneiss	15°20.38’	88°21.54’	199
5H-11a	5H-11	greenschist-grade orthogneiss	15°12.83’	88°36.58’	–
	5H-12	paragneiss, marble	15°12.09’	88°37.37’	–
92RN412	92RN412	granitic gneiss	15°40.4’[1]	87°56.7’[1]	–
93LP522	93LP522	granite	15°28.3’	88°02.4’	–
94SA602	94SA602	amphibolite	15°39.1’	87°56.9’	–
Metamorphic basement of the central Chortis block, Honduras					
SF1D	SF1D	weakly deformed granite	14°33.85’[1]	86°07.09’[1]	–
92QO404	92QO404	tonalitic granite-gneiss	14°47.35’[1]	87°01.73’[1]	–
86TA100	86TA100	(?ortho) augen schist	14°40.22’[2]	86°56.0’[2]	940
Granitoids of the arc complex					
	5H-5, 6	granite	15°35.39’ to 15°33.50’	87°57.05’ to 87°58.04’	
5C-6	5C-6	granite (Chiquimula batholith)	14°46.58’	89°34.55	719
5C-11	5C-11	granodiorite (Chiquimula batholith)	14°47.03’	89°35.40’	779
5C-13	5C-13	granodiorite (Chiquimula batholith)	14°47.21’	89°34.21’	–
5C-21	5C-21	subvolcanic granite (Chiquimula batholith)	14°52.95’	89°30.95’	–
5C-32	5C-32	granite	14°59.57’	89°17.22’	~870
5H-5	5H-5	granite	15°35.39’	87°57.05’	88
5H-13	5H-13	subvolcanic granite	14°55.15’	88°45.44’	789
GM14s	GM43	Miocene granite	15°24.429’	91°59.951’	~1100
GM15s	GM43	augengneiss mylonite; float	15°24.4’	91°59.9’	~1100
Southern Mexico					
ML-18		migmatite	18°00’[1]	97°50’[1]	–
ML-37		mylonitic gneiss	15°52’[1]	96°29’[1]	–
MU-12		Cruz Grande migmatitic gneiss	16°48.00’	99°07.88’	76
MU-13		La Palma = Las Piñas gneiss mylonite	17°04.9’	99°29.7’	359
ML-39		Pochutla mylonitic gneiss	15°51.8’	96°29.78’	275
PA3-4		mylonitic gneiss	15°40’[1]	93°10’[1]	50[1]
CB35		mylonitic gneiss	15°42.29’	93°10.40’	80[1]
CB31		diorite	15°43.87’	93°14.32’	57[1]
CA34		tonalite	16°06.05’	93°40.45	230[1]
PI28-1		mylonitic gneiss	15°42’[1]	93°12’[1]	65[1]
CB-8		meta-psammite	16°16.891’	93°36.877’	770
CB-12		orthogneiss	16°20.35’	93.32.66’	690
CB-16		orthogneiss	16°05.51’	93°11.01’	590
CB-17		orthogneiss	16°04.38’	93°12.35’	590

CB-28	orthogneiss	16°07.15’	93°41.56’	220
CMP-5	orthogneiss	16°06.60’	93°26.33’	670
CMP-13	orthogneiss	16°02.47’	93°13.62’	630
TP-1016	granodiorite	16°13.95’	93°35.20’	1016
TP-1320	granodiorite	16°12.56’	93°35’	1320
TP-1800	granite	16°12’	93°36.1’	1800
TP-1990	granite	16°11.8’	93°36.06’	1990
TP-2347	tonalite	16°11.6’	93°36.6’	2347
TP-2513	granodiorite	16°11.7’	93°36.68’	2513

[1] imprecise coordinates determined with GPS in the 1990s; [2] imprecise coordinates determined from maps

TABLE 2. U/Pb TIMS ANALYTICAL DATA

Fraction	Size, μm	Weight, mg	U (ppm)	Pb (ppm)	Measured Isotope Ratios			Calculated Radiogenic Ratios						Calculated Ages (Ma)			
					$^{206}Pb/^{204}Pb$	$^{206}Pb/^{207}Pb$	$^{206}Pb/^{208}Pb$	$^{206}Pb^*/^{238}U$	±2σ %	$^{207}Pb^*/^{235}U$	±2σ %	$^{207}Pb^*/^{206}Pb^*$	±2σ %	$^{206}Pb^*/^{238}U$	$^{207}Pb^*/^{235}U$	$^{207}Pb^*/^{206}Pb$	±2σ (Ma)
G 27s (stop G57), biotite-granite gneiss, west of Huehuetenango, Chuacús complex, western Guatemala																	
3 F	40-75	1.30	1118	154.2	6179	13.831	20.5008	0.14267	0.51	1.37847	0.52	0.070076	0.05	859.7	879.8	930.6	1.1
2 E	75-125	2.10	734	105.6	14509	14.018	17.2502	0.14803	0.11	1.43766	0.12	0.070436	0.04	889.9	904.7	941.1	0.9
2 F	75-125	4.59	652	94.1	9282	13.915	16.5138	0.14777	0.14	1.43465	0.14	0.070412	0.04	888.5	903.5	940.4	0.9
3 F	40-75	2.99	627	89.7	9655	13.942	16.6208	0.14670	0.10	1.42261	0.11	0.070335	0.04	882.4	898.5	938.2	0.9
3 F	40-75	2.51	497	70.0	6330	13.812	16.8847	0.14438	0.12	1.39809	0.12	0.070232	0.04	869.4	888.1	935.2	0.9
G18s (stop G1), phyllonitic migmatitic gneiss, west of Huehuetenango, Chuacús complex, western Guatemala																	
2 F	75-125	1.31	43	3.1	99.6	4.981	1.8954	0.03936	0.31	0.29711	1.43	0.054749	1.33	248.9	264.1	402.0	30
2 F	75-125	1.01	145	7.6	664.7	12.223	4.7287	0.04582	0.18	0.37998	0.27	0.060145	0.19	288.8	327.0	608.8	4.2
2 E	75-125	1.47	33	1.3	516.2	12.821	3.6002	0.03400	0.11	0.23339	0.83	0.049781	0.77	215.6	213.0	184.8	18
2 F	75-125	1.31	83	6.7	91.1	4.713	1.8081	0.04249	0.18	0.30489	1.99	0.052047	1.90	268.2	270.2	287.5	43
GM14s (station GM43), granite, west of Cuilco, western Guatemala																	
2 F I	75-125	1.83	281	7.7	2584	13.958	8.2501	0.02657	0.37	0.24250	0.37	0.066185	0.08	169.1	220.5	812.2	1.6
3 F	40-75	2.50	206	1.3	1056	13.845	5.4244	0.00590	0.13	0.04768	0.20	0.058594	0.14	37.9	47.3	552.1	3.1
2 F	75-125	1.00	690	11.4	2387	13.723	7.6330	0.01589	0.76	0.14671	0.77	0.066951	0.10	101.7	139.0	836.2	2.2
2 F A	75-125	3.00	303	6.7	847.4	12.022	6.1905	0.02022	0.36	0.18495	0.75	0.066350	0.65	129.0	172.3	817.4	14
2 F B	75-125	2.50	281	4.3	511.7	11.318	5.2317	0.01348	0.19	0.11184	1.55	0.060196	1.52	86.3	107.7	610.6	33
GM13s (GM42), gneiss, west of Cuilco, western Guatemala																	
3 F B	40-75	2.22	291	2.0	879.0	13.308	5.0503	0.00647	0.11	0.05247	0.51	0.058801	0.47	41.6	51.9	559.7	10
2 F AL	75-125	1.93	102	15.6	7532	13.801	8.6004	0.14982	0.43	1.45957	0.44	0.070656	0.06	900.0	913.8	947.5	1.3
2 F A	75-125	2.92	86	12.5	1483	12.732	7.2665	0.14178	0.11	1.34954	0.32	0.069033	0.28	854.7	867.4	899.7	5.9
2 F II	75-125	3.50	111	16.9	5275	13.700	8.7096	0.14878	0.13	1.44367	0.15	0.070378	0.07	894.1	907.2	939.4	1.4
2 F B	75-125	3.00	58	9.0	3230	13.368	7.8328	0.15215	0.12	1.47884	0.21	0.070493	0.17	913.0	921.8	942.7	3.5
2 F III	75-125	3.03	88	13.9	1323	12.374	7.3711	0.14828	0.10	1.43352	0.31	0.070119	0.29	891.3	903.0	931.8	5.9
3 F	40-75	2.04	189	1.0	739.0	13.245	5.0393	0.00490	0.13	0.03781	0.52	0.055945	0.49	31.5	37.7	450.2	11
GM8s (stop G8=GM33), mylonitic monzonite, south of Sacapulas, Chuacús complex, western Guatemala																	
2 F	75-125	2.30	206	7.3	863.8	14.042	5.3669	0.03197	0.15	0.23992	0.18	0.054426	0.10	202.9	218.4	388.7	2.3
2 F	75-125	0.58	249	8.9	203.2	8.281	2.7404	0.02565	0.21	0.17217	0.50	0.048686	0.43	163.3	161.3	132.7	10
3 F	40-75	1.17	263	7.7	1092	15.955	4.2309	0.02588	0.33	0.17603	0.37	0.049332	0.15	164.7	164.6	163.6	3.4
3 F	40-75	1.00	408	13.1	361.2	11.136	3.4385	0.02561	0.32	0.17406	0.36	0.049293	0.17	163.0	162.9	161.8	3.9
86TA100, augenschist, Orica-Guayape sheet, basement of central Honduras																	
2 F	75-125	1.10	237	23.8	1583	13.350	10.1768	0.09856	0.44	0.89580	0.44	0.065922	0.05	605.9	649.5	803.9	1.1
3 F	40-75	1.50	210	19.7	7519	14.793	12.0367	0.09467	0.45	0.85853	0.46	0.065770	0.08	583.1	629.3	799.0	1.6
2 F	75-125	2.50	296	32.0	4249	13.841	11.9282	0.10834	0.60	1.03029	0.60	0.068969	0.06	663.1	719.1	897.8	1.3
2 F B	75-125	1.62	290	28.7	2576	13.789	11.7882	0.09878	0.87	0.91309	0.88	0.067042	0.14	607.2	658.7	839.2	2.9
2 F B	75-125	2.20	248	27.5	13269	14.181	12.9874	0.11242	0.42	1.07765	0.42	0.069523	0.05	686.8	742.5	914.3	1.0

TABLE 2. U/Pb TIMS ANALYTICAL DATA (continued)

Fraction	Size, μm	Weight, mg	U (ppm)	Pb (ppm)	Measured Isotope Ratios			Calculated Radiogenic Ratios						Calculated Ages (Ma)			
					$^{206}Pb/^{204}Pb$	$^{206}Pb/^{207}Pb$	$^{206}Pb/^{208}Pb$	$^{206}Pb^*/^{238}U$	±2σ %	$^{207}Pb^*/^{235}U$	±2σ %	$^{207}Pb^*/^{206}Pb^*$	±2σ %	$^{206}Pb^*/^{238}U$	$^{207}Pb^*/^{235}U$	$^{207}Pb^*/^{206}Pb$	±2σ (Ma)
92RN412, granitic gneiss, Baracoa sheet, northern Honduras																	
3 F	40-75	1.20	1074	6.4	1371	17.283	9.2133	0.00593	1.43	0.03863	1.45	0.047216	0.26	38.1	38.5	60.2	6.1
2 F	75-125	1.10	982	6.1	1476	17.136	9.1728	0.00616	0.93	0.04116	0.99	0.048490	0.33	39.6	40.9	123.2	7.7
2 F N	75-125	1.11	1013	5.9	1210	16.811	8.3185	0.00569	0.58	0.03716	0.60	0.047410	0.13	36.5	37.1	69.9	3.0
2 F S	75-125	1.46	651	4.6	1238	15.789	8.2230	0.00689	0.94	0.04899	0.95	0.051608	0.13	44.2	48.6	268.1	3.0
92QO404, tonalitic granite-gneiss, El Porvenir sheet, basement of central Honduras																	
F N idio	75-125	2.87	275	21.6	7354	16.369	9.0881	0.07806	0.31	0.63709	0.32	0.059197	0.06	484.5	500.5	574.4	1.3
F idio	75-125	2.05	291	22.3	2262	15.507	7.8409	0.07411	0.18	0.59426	0.19	0.058153	0.08	460.9	473.6	535.5	1.7
2 F	75-125	2.50	172	16.6	363.2	10.011	4.6698	0.08093	1.94	0.67134	1.94	0.060160	0.13	501.7	521.5	609.3	2.9
3 F	40-75	2.01	292	22.3	5698	16.414	8.0612	0.07410	0.98	0.59531	0.99	0.058270	0.12	460.8	474.3	539.9	2.6
3 F G	40-75	1.14	349	31.7	430.2	10.685	5.1172	0.07827	0.31	0.64820	0.33	0.060067	0.09	485.8	507.4	606.0	1.9
F 1 idio	75-125	1.05	245	18.9	8687	16.530	8.9748	0.07685	0.53	0.62417	0.53	0.058904	0.07	477.3	492.5	536.6	1.4
94SA602, amphibolite, Choloma sheet, Las Ovejas complex, northern Honduras																	
2 F w.s.	75-125	0.50	173	2.7	1647	17.628	4.2180	0.01402	0.09	0.09256	0.15	0.047884	0.11	89.7	89.9	93.6	2.6
2 F b.p.	75-125	2.01	130	2.1	1527	17.353	3.5184	0.01413	0.18	0.09369	0.28	0.048088	0.21	90.5	90.9	103.6	5.1
2 F idio	75-125	4.56	142	2.3	1164	16.546	3.3240	0.01377	0.64	0.09096	0.68	0.047899	0.21	88.2	88.4	94.3	4.9
SF1D, weakly deformed granite, San Francisco de Becerra sheet, basement of east-central Honduras																	
2 F	75-125	1.03	531	22.7	3352	15.759	17.0621	0.04406	0.20	0.35970	0.23	0.059212	0.10	277.9	312.0	574.9	2.2
2 F sm.I.	75-125	1.41	559	28.2	6864	15.017	16.0751	0.05185	0.33	0.46168	0.33	0.064574	0.05	325.9	385.4	760.5	1.1
2 F cl.	75-125	1.69	514	23.3	8823	16.569	18.1984	0.04713	1.03	0.38200	1.03	0.058786	0.06	296.9	328.5	559.2	1.2
2 F sm ii	40-75	0.86	480	22.0	7109	16.502	19.1226	0.04739	1.87	0.38309	1.87	0.058633	0.05	298.5	329.3	553.5	1.0
2 F f.sm.	40-75	1.01	683	34.0	5084	14.737	15.6789	0.05103	0.14	0.45812	0.15	0.065112	0.07	320.8	383.0	778.0	1.3
93LP522, granite, Valle de Naco sheet, northwestern Honduras																	
2 F n.icl.	75-125	1.95	510	13.2	5784	19.307	12.1596	0.02642	0.26	0.17965	0.30	0.049323	0.14	168.1	167.8	163.2	3.2
2 F SM.	75-125	1.74	532	14.7	7023	18.008	12.4501	0.02824	0.14	0.20839	0.16	0.053523	0.06	179.5	192.2	351.0	1.3
3 F cl.	75-125	1.80	511	13.2	6456	19.214	12.3173	0.02643	0.38	0.18159	0.39	0.049838	0.05	168.1	169.4	187.4	1.3
3 F n.cl	40-125	1.30	693	18.7	4295	18.040	12.2107	0.02744	0.21	0.19713	0.22	0.052098	0.06	174.5	182.7	289.7	1.3

TABLE 3. U/Pb SHRIMP ANALYTICAL DATA

Spot	$\%^{206}Pb_c$	U ppm	Th ppm	$^{232}Th/^{238}U$	$^{206}Pb^*$ ppm	$^{206}Pb/^{238}U$ Age(1)	$^{206}Pb/^{238}U$ Age (2)	$^{206}Pb/^{238}U$ Age(3)	$^{207}Pb/^{206}Pb$ Age(1)	%disc.	total $^{238}U/^{206}Pb$ ±%	total $^{207}Pb/^{206}Pb$ ±%	$^{238}U/^{206}Pb^{*(1)}$ ±%	$^{207}Pb^*/^{206}Pb^{*(1)}$ ±%	$^{207}Pb^*/^{235}U^{(1)}$ ±%	$^{206}Pb^*/^{238}U^{(1)}$ ±%	err corr
Maya block																	
G18S-1	0.07	1426	85	0.06	161.4	797.0 ± 2.2	790.9 ± 2.4	797.9 ± 2.2	985 ± 11	24	7.59 ± 0.3	.0726 ± 0.5	7.60 ± 0.3	.0720 ± 0.56	1.31 ± 0.6	.1316 ± 0.3	.455
G18S-2	0.00	115	86	0.77	3.5	224.2 ± 3.1	224.7 ± 3.1	223.9 ± 3.6	137 ± 93	-39	28.26 ± 1.4	.0488 ± 4.0	28.26 ± 1.4	.0488 ± 4.0	0.24 ± 4.2	.0354 ± 1.4	.332
G18S-3	2.43	46	40	0.90	1.4	216.8 ± 5.3	221.8 ± 4.8	223.2 ± 5.7	-1011 ± 1010	-566	28.52 ± 2.2	.0517 ± 6.0	29.23 ± 2.5	.0315 ± 34.0	0.15 ± 34.1	.0342 ± 2.5	.072
G18S-4	-0.34	134	67	0.52	17.9	935.9 ± 7.7	931.3 ± 7.9	935.0 ± 8.2	1049 ± 46	12	6.42 ± 0.9	.0715 ± 1.5	6.40 ± 0.9	.0743 ± 2.3	1.60 ± 2.5	.1562 ± 0.9	.358
G18S-5	0.00	78	42	0.56	9.8	882.5 ± 9.5	881.2 ± 9.9	884.6 ± 10.4	919 ± 41	4	6.82 ± 1.1	.0697 ± 2.0	6.82 ± 1.1	.0697 ± 2.0	1.41 ± 2.3	.1467 ± 1.1	.496
G18S-6	0.00	40	23	0.60	1.2	224.8 ± 5.2	225.0 ± 5.3	222.4 ± 5.9	189 ± 152	-16	28.18 ± 2.4	.0499 ± 6.5	28.18 ± 2.4	.0499 ± 6.5	0.24 ± 7.0	.0355 ± 2.4	.338
G18S-7	0.00	83	74	0.92	2.3	205.2 ± 3.4	204.3 ± 3.4	204.1 ± 4.1	375 ± 103	83	30.91 ± 1.7	.0541 ± 4.6	30.91 ± 1.7	.0541 ± 4.6	0.24 ± 4.9	.0323 ± 1.7	.343
G18S-8	-0.21	45	21	0.47	1.3	218.2 ± 4.8	218.0 ± 4.9	217.8 ± 5.2	250 ± 150	15	29.11 ± 2.2	.0495 ± 6.4	29.05 ± 2.2	.0512 ± 6.5	0.24 ± 6.9	.0344 ± 2.2	.323
G18S-9R	0.13	1203	202	0.17	128.8	756.3 ± 2.1	751.1 ± 2.3	754.7 ± 2.2	933 ± 14	23	8.02 ± 0.3	.0712 ± 0.5	8.03 ± 0.3	.0701 ± 0.7	1.20 ± 0.8	.1245 ± 0.3	.391
G18S-10	2.38	45	25	0.57	1.4	218.6 ± 5.1	222.8 ± 5.0	224.1 ± 5.5	-726 ± 646	-432	28.30 ± 2.2	.0545 ± 6.0	28.99 ± 2.4	.0348 ± 23.1	0.17 ± 23.2	.0345 ± 2.4	.103
GM1S-1	8.10	644	270	0.43	24.5	260.4 ± 2.9	257.0 ± 7.9	262.3 ± 3.4	684 ± 848	163	22.60 ± 0.7	.1163 ± 18.1	24.26 ± 1.1	.0623 ± 39.7	0.35 ± 39.7	.0412 ± 1.1	.028
GM1S-2	0.10	145	40	0.28	21.9	1037.8 ± 9.3	1040.8 ± 9.7	1039.7 ± 9.7	967 ± 48	-7	5.70 ± 1.0	.0748 ± 1.5	5.72 ± 1.0	.0714 ± 2.4	1.72 ± 2.5	.1747 ± 1.0	.381
GM1S-3	0.41	111	35	0.33	17.3	1075.5 ± 10.7	1073.5 ± 11.2	1075.7 ± 11.2	1119 ± 42	4	5.50 ± 1.1	.0787 ± 1.6	5.51 ± 1.1	.0769 ± 2.1	1.93 ± 2.3	.1816 ± 1.1	.460
GM1S-4	-0.05	843	112	0.14	131.4	1074.5 ± 9.6	1075.6 ± 10.1	1075.0 ± 9.8	1050 ± 21	-2	5.51 ± 1.0	.0748 ± 1.0	5.51 ± 1.0	.0743 ± 1.0	1.86 ± 1.4	.1814 ± 1.0	.683
GM1S-5	-0.05	202	141	0.72	46.8	1536.5 ± 10.6	1541.6 ± 11.6	1538.2 ± 11.7	1477 ± 29	-4	3.70 ± 0.8	.0952 ± 0.9	3.72 ± 0.8	.0925 ± 1.6	3.43 ± 1.7	.2692 ± 0.8	.448
GM1S-6	-0.25	489	151	0.32	88.0	1225.1 ± 6.4	1228.4 ± 6.9	1225.3 ± 6.7	1166 ± 16	-5	4.78 ± 0.6	.0791 ± 0.8	4.78 ± 0.6	.0788 ± 0.8	2.27 ± 1.0	.2093 ± 0.6	.580
GM1S-7	0.04	677	553	0.84	26.1	282.2 ± 1.7	282.6 ± 1.8	285.4 ± 2.2	232 ± 46	-18	22.31 ± 0.6	.0522 ± 1.7	22.35 ± 0.6	.0508 ± 2.0	0.31 ± 2.1	.0447 ± 0.6	.303
GM1S-8	0.08	3664	43	0.01	210.3	416.5 ± 1.6	416.5 ± 1.6	416.7 ± 1.6	412 ± 19	-1	14.97 ± 0.4	.0557 ± 0.8	14.98 ± 0.4	.0550 ± 0.9	0.51 ± 0.9	.0667 ± 0.4	.410
GM1S-9	0.14	145	51	0.36	27.4	1283.6 ± 10.6	1282.8 ± 11.4	1283.6 ± 11.2	1296 ± 26	1	4.54 ± 0.9	.0848 ± 1.2	4.54 ± 0.9	.0842 ± 1.3	2.56 ± 1.6	.2203 ± 0.9	.570
GM1S-10	0.29	199	126	0.66	6.7	245.1 ± 2.9	245.9 ± 2.9	243.6 ± 3.4	127 ± 149	-48	25.65 ± 1.2	.0534 ± 3.1	25.81 ± 1.2	.0486 ± 6.3	0.26 ± 6.5	.0388 ± 1.2	.188
GM8S-1	-0.04	133	49	0.38	18.4	965.7 ± 8.7	966.9 ± 9.1	967.6 ± 9.2	935 ± 32	2.2	6.18 ± 1.0	.0710 ± 1.5	6.19 ± 1.0	.0702 ± 1.6	1.56 ± 1.8	.1616 ± 1.0	.523
GM8S-2R	0.82	143	28	0.20	3.3	169.4 ± 2.4	169.8 ± 2.4	170.0 ± 2.5	85 ± 186	14.5	37.16 ± 1.4	.0560 ± 3.9	37.55 ± 1.4	.0477 ± 7.8	0.18 ± 8.0	.0266 ± 1.4	.181
GM8S-3R	0.44	1065	206	0.20	25.6	176.4 ± 1.0	176.9 ± 1.0	176.5 ± 1.0	68 ± 119	9.2	35.79 ± 0.5	.0531 ± 1.6	36.04 ± 0.6	.0474 ± 5.0	0.18 ± 5.1	.0277 ± 0.6	.119
GM8S-3C	-0.22	864	309	0.37	128.6	1029.7 ± 10.1	1032.2 ± 10.6	1030.8 ± 10.7	970 ± 12	1.8	5.77 ± 1.1	.0718 ± 0.6	5.77 ± 1.1	.0715 ± 0.6	1.71 ± 1.2	.1732 ± 1.1	.876
GM8S-4C	0.30	143	49	0.35	15.8	777.3 ± 9.8	777.3 ± 10.1	779.9 ± 10.4	775 ± 47	3.4	7.78 ± 1.3	.0675 ± 1.7	7.80 ± 1.3	.0650 ± 2.2	1.15 ± 2.6	.1281 ± 1.3	.513
GM8S-4R	0.27	632	197	0.32	14.6	170.3 ± 1.1	170.1 ± 1.1	170.5 ± 1.2	226 ± 50	2.5	37.30 ± 0.7	.0517 ± 1.9	37.35 ± 0.7	.0507 ± 2.1	0.19 ± 2.2	.0268 ± 0.7	.295
GM8S-5R	1.10	1336	363	0.28	32.3	176.2 ± 1.0	176.9 ± 0.9	176.6 ± 0.9	9 ± 147	8.0	35.55 ± 0.5	.0584 ± 1.3	36.10 ± 0.6	.0462 ± 6.1	0.18 ± 6.1	.0277 ± 0.6	.091
GM8S-5C	0.61	76	74	1.01	1.7	164.6 ± 3.4	167.3 ± 3.3	166.2 ± 4.2	-614 ± 581	8.0	37.81 ± 1.9	.0543 ± 5.3	38.67 ± 2.1	.0362 ± 21.3	0.13 ± 21.4	.0259 ± 2.1	.098
GM8S-6	0.11	645	30	0.05	15.1	173.5 ± 1.1	173.3 ± 1.2	173.4 ± 1.2	214 ± 44	5.6	36.67 ± 0.7	.0504 ± 1.9	36.67 ± 0.7	.0504 ± 1.9	0.19 ± 2.0	.0273 ± 0.7	.329
GM8S-7	0.42	137	110	0.83	3.2	172.3 ± 2.4	171.6 ± 2.5	170.8 ± 2.9	323 ± 91	3.2	36.92 ± 1.4	.0529 ± 4.0	36.92 ± 1.4	.0529 ± 4.0	0.20 ± 4.2	.0271 ± 1.4	.334
GM8S-8	0.36	241	214	0.92	5.5	169.1 ± 1.9	169.1 ± 1.9	168.2 ± 2.3	177 ± 108	2.7	37.50 ± 1.1	.0523 ± 3.5	37.63 ± 1.1	.0496 ± 4.6	0.18 ± 4.8	.0266 ± 1.1	.234
5CO1-1	0.15	444	208	0.48	25.3	413.0 ± 2.3	413.7 ± 2.4	414.7 ± 2.6	358 ± 35	-13	15.09 ± 0.6	.0549 ± 1.4	15.11 ± 0.6	.0537 ± 1.5	0.49 ± 1.6	.0662 ± 0.6	.354
5CO1-2	0.49	122	32	0.27	8.0	471.1 ± 4.8	471.2 ± 5.0	468.3 ± 5.1	462 ± 66	-2	13.12 ± 1.1	.0602 ± 2.3	13.19 ± 1.1	.0562 ± 3.0	0.59 ± 3.1	.0758 ± 1.1	.338
5CO1-3	0.15	454	105	0.24	27.7	441.1 ± 2.3	441.6 ± 2.4	441.1 ± 2.5	401 ± 32	-9	14.10 ± 0.5	.0559 ± 1.3	14.12 ± 0.6	.0547 ± 1.4	0.53 ± 1.5	.0708 ± 0.6	.357
5CO1-4	0.00	238	60	0.26	26.3	781.1 ± 15.5	769.1 ± 15.8	768.2 ± 16.3	1141 ± 23	46	7.76 ± 2.1	.0778 ± 1.1	7.76 ± 2.1	.0778 ± 1.1	1.38 ± 2.4	.1288 ± 2.1	.878
5CO1-5	0.03	686	170	0.26	92.1	935.7 ± 3.3	934.5 ± 3.5	936.3 ± 3.4	967 ± 14	3	6.40 ± 0.4	.0716 ± 0.7	6.40 ± 0.4	.0713 ± 0.7	1.54 ± 0.8	.1562 ± 0.4	.477
5CO1-6	0.26	1883	222	0.12	125.5	480.3 ± 4.1	478.5 ± 4.2	480.1 ± 4.2	598 ± 22	25	12.89 ± 0.9	.0619 ± 0.7	12.93 ± 0.9	.0598 ± 1.0	0.64 ± 1.4	.0774 ± 0.9	.655
5CO1-7R	0.07	1179	284	0.25	161.5	953.4 ± 2.6	953.4 ± 2.8	953.7 ± 2.7	951 ± 11	0	6.27 ± 0.3	.0713 ± 0.5	6.27 ± 0.3	.0708 ± 0.5	1.56 ± 0.6	.1594 ± 0.3	.481

5CO1-8	0.05	871	555	0.66	55.5	461.3 ± 1.8	461.3 ± 1.8	462.0 ± 2.0	460 ± 21	0	13.48 ± 0.4	.0566 ± 0.9	13.48 ± 0.4	.0562 ± 1.0	0.57 ± 1.0	.0742 ± 0.4	.386
5CO1-9	0.48	64	58	0.92	12.1	1265.5 ± 14.3	1260.3 ± 15.3	1273.3 ± 16.6	1342 ± 48	6	4.59 ± 1.2	.0899 ± 1.7	4.61 ± 1.2	.0861 ± 2.5	2.58 ± 2.8	.2169 ± 1.2	.447
5CO1-10	0.00	332	282	0.88	18.7	410.6 ± 4.6	409.8 ± 4.6	408.6 ± 5.4	469 ± 34	14	15.21 ± 1.1	.0564 ± 1.5	15.21 ± 1.1	.0564 ± 1.5	0.51 ± 1.9	.0658 ± 1.1	.596
5CO1-11	1.24	608	94	0.16	39.2	461.4 ± 2.0	462.5 ± 1.9	462.0 ± 1.9	381 ± 76	-17	13.31 ± 0.4	.0643 ± 1.4	13.48 ± 0.4	.0542 ± 3.4	0.55 ± 3.4	.0742 ± 0.4	.130
5CO1-12R	0.25	78	25	0.34	4.7	437.3 ± 4.8	437.9 ± 4.9	434.7 ± 5.1	394 ± 97	-10	14.21 ± 1.1	.0566 ± 3.5	14.25 ± 1.1	.0546 ± 4.3	0.53 ± 4.5	.0702 ± 1.1	.253
5CO1-12C	0.13	98	33	0.34	14.1	995.8 ± 7.2	997.0 ± 7.7	994.8 ± 7.7	968 ± 40	-3	5.98 ± 0.8	.0724 ± 1.8	5.99 ± 0.8	.0714 ± 1.9	1.64 ± 2.1	.1670 ± 0.8	.374
5CO1-13R	0.01	1691	109	0.07	98.9	424.3 ± 1.2	423.3 ± 1.2	423.8 ± 1.3	499 ± 17	18	14.70 ± 0.3	.0573 ± 0.8	14.70 ± 0.3	.0572 ± 0.8	0.54 ± 0.8	.0680 ± 0.3	.357
5CO1-14C	0.11	171	57	0.34	23.0	937.6 ± 16.9	940.7 ± 18.3	938.6 ± 18.1	857 ± 132	-9	6.38 ± 1.9	.0685 ± 6.3	6.39 ± 1.9	.0676 ± 6.4	1.46 ± 6.7	.1566 ± 1.9	.291
5CO1-14R	0.09	630	595	0.98	42.3	484.4 ± 1.8	484.6 ± 1.9	339.4 ± 31.7	473 ± 30	-2	12.80 ± 0.4	.0573 ± 1.2	12.81 ± 0.4	.0565 ± 1.4	0.61 ± 1.4	.0780 ± 0.4	.278
5CO1-15C	0.08	326	151	0.48	38.9	836.9 ± 4.1	833.4 ± 4.3	836.0 ± 4.4	940 ± 24	12	7.21 ± 0.5	.0710 ± 1.1	7.21 ± 0.5	.0704 ± 1.2	1.35 ± 1.3	.1386 ± 0.5	.404
5CO1-16C	0.04	188	60	0.33	27.4	1010.7 ± 5.2	1009.5 ± 5.6	1010.3 ± 5.5	1037 ± 26	3	5.89 ± 0.6	.0742 ± 1.3	5.89 ± 0.6	.0738 ± 1.3	1.73 ± 1.4	.1697 ± 0.6	.398
5CO1-16R	0.05	1024	83	0.08	66.1	467.0 ± 1.3	467.1 ± 1.4	467.4 ± 1.4	457 ± 22	-2	13.30 ± 0.3	.0565 ± 0.9	13.31 ± 0.3	.0561 ± 1.0	0.58 ± 1.0	.0751 ± 0.3	.290
5CO1-17C	0.00	267	78	0.30	38.6	1003.4 ± 4.5	1002.8 ± 4.8	1002.1 ± 4.7	1017 ± 22	1	5.94 ± 0.5	.0731 ± 1.1	5.94 ± 0.5	.0731 ± 1.1	1.70 ± 1.2	.1684 ± 0.5	.403
5CO1-18R	0.95	101	61	0.63	5.7	410.1 ± 4.3	413.2 ± 4.2	408.9 ± 4.6	135 ± 177	-67	15.08 ± 1.0	.0565 ± 3.1	15.22 ± 1.1	.0487 ± 7.5	0.44 ± 7.6	.0657 ± 1.1	.142
5CO1-19C	0.47	246	75	0.31	30.1	853.6 ± 4.6	841.4 ± 4.6	846.6 ± 4.9	1178 ± 34	38	7.03 ± 0.6	.0830 ± 1.1	7.06 ± 0.6	.0792 ± 1.7	1.55 ± 1.8	.1416 ± 0.6	.312
5CO1-19R	0.66	381	106	0.29	22.5	426.6 ± 2.5	426.5 ± 2.5	425.5 ± 2.9	433 ± 70	2	14.52 ± 0.6	.0608 ± 1.5	14.62 ± 0.6	.0555 ± 3.1	0.52 ± 3.2	.0684 ± 0.6	.190
5CO1-20C	0.05	217	52	0.25	32.8	1043.5 ± 4.8	1038.3 ± 5.4	1044.0 ± 5.1	1149 ± 41	10	5.69 ± 0.5	.0785 ± 2.1	5.69 ± 0.5	.0781 ± 2.1	1.89 ± 2.1	.1757 ± 0.5	.234
5CO1-21C	0.06	194	67	0.36	27.6	987.2 ± 5.0	987.5 ± 5.4	988.1 ± 5.4	980 ± 27	-1	6.04 ± 0.5	.0723 ± 1.3	6.04 ± 0.6	.0718 ± 1.3	1.64 ± 1.4	.1655 ± 0.6	.384
5CO6b-1R	0.17	1720	9	0.01	17.1	74.0 ± 0.7	74.1 ± 0.7	74.1 ± 0.7	3 ± 52	-95	86.52 ± 0.9	.0475 ± 1.8	86.66 ± 0.9	.0461 ± 2.1	0.07 ± 2.3	.0115 ± 0.9	.392
5CO6b-2R	0.31	1876	62	0.03	22.3	88.3 ± 0.4	88.6 ± 0.4	88.1 ± 0.4	-49 ± 52	-155	72.30 ± 0.5	.0477 ± 1.5	72.52 ± 0.5	.0451 ± 2.1	0.09 ± 2.2	.0138 ± 0.5	.223
5CO6b-3R	0.39	870	5	0.01	8.0	68.4 ± 0.6	68.6 ± 0.6	68.6 ± 0.6	-53 ± 98	-177	93.34 ± 0.8	.0483 ± 2.9	93.71 ± 0.8	.0451 ± 4.0	0.07 ± 4.1	.0107 ± 0.8	.198
5CO6b-3C	0.75	134	153	1.18	3.9	212.6 ± 2.8	214.2 ± 2.8	214.3 ± 3.5	-91 ± 150	-143	29.60 ± 1.3	.0505 ± 3.6	29.82 ± 1.3	.0444 ± 6.1	0.21 ± 6.3	.0335 ± 1.3	.210
5CO6b-4R	0.17	382	7	0.02	3.6	70.3 ± 0.9	70.3 ± 0.9	70.2 ± 0.9	73 ± 146	4	91.08 ± 1.3	.0489 ± 4.6	91.24 ± 1.3	.0475 ± 6.1	0.07 ± 6.3	.0110 ± 1.3	.204
5CO6b-4C	1.06	138	3	0.02	7.7	400.6 ± 3.9	402.9 ± 4.0	404.0 ± 3.9	197 ± 110	-51	15.43 ± 1.0	.0587 ± 2.3	15.60 ± 1.0	.0500 ± 4.7	0.44 ± 4.9	.0641 ± 1.0	.209
5CO6b-5R	0.47	1064	5	0.01	10.7	74.4 ± 0.5	74.7 ± 0.5	74.7 ± 0.5	-98 ± 85	-232	85.71 ± 0.7	.0481 ± 2.2	86.11 ± 0.7	.0442 ± 3.5	0.07 ± 3.5	.0116 ± 0.7	.199
5CO6b-5C	0.00	138	38	0.29	16.0	815.0 ± 7.2	812.7 ± 7.5	814.1 ± 7.6	889 ± 31	9	7.42 ± 0.9	.0687 ± 1.5	7.42 ± 0.9	.0687 ± 1.5	1.28 ± 1.8	.1348 ± 0.9	.527
5CO6b-6R	0.96	520	6	0.01	4.8	68.8 ± 0.8	69.4 ± 0.7	69.4 ± 0.7	-303 ± 242	-540	92.30 ± 1.0	.0487 ± 3.2	93.19 ± 1.1	.0408 ± 9.5	0.06 ± 9.5	.0107 ± 1.1	.116
5CO6b-7R	0.22	1029	5	0.01	10.8	77.8 ± 0.5	78.1 ± 0.6	78.0 ± 0.5	-57 ± 65	-173	82.12 ± 0.7	.0468 ± 2.2	82.31 ± 0.7	.0450 ± 2.7	0.08 ± 2.8	.0121 ± 0.7	.254
5CO6b-8R	0.00	563	5	0.01	5.4	71.5 ± 0.7	71.6 ± 0.7	71.4 ± 0.7	18 ± 78	-75	89.60 ± 1.0	.0464 ± 3.2	89.60 ± 1.0	.0464 ± 3.2	0.07 ± 3.4	.0112 ± 1.0	.295
5CO6b-9C	0.10	768	492	0.66	24.8	237.3 ± 1.2	237.7 ± 1.3	237.4 ± 1.4	171 ± 37	-28	26.64 ± 0.5	.0503 ± 1.5	26.67 ± 0.5	.0495 ± 1.6	0.26 ± 1.7	.0375 ± 0.5	.316
5CO6b-10R	0.25	364	231	0.65	10.7	216.3 ± 1.7	216.7 ± 1.7	213.3 ± 2.0	140 ± 78	-35	29.24 ± 0.8	.0508 ± 2.2	29.31 ± 0.8	.0488 ± 3.3	0.23 ± 3.4	.0341 ± 0.8	.233
5CO6b-10C	0.76	277	151	0.57	9.0	237.7 ± 2.1	238.6 ± 2.2	239.0 ± 2.4	91 ± 95	-62	26.42 ± 0.9	.0540 ± 2.4	26.62 ± 0.9	.0478 ± 4.0	0.25 ± 4.1	.0376 ± 0.9	.221
5CO6b-11C	0.00	327	339	1.07	9.7	218.0 ± 1.8	217.6 ± 1.8	217.4 ± 2.3	289 ± 53	32	29.07 ± 0.8	.0521 ± 2.3	29.07 ± 0.8	.0521 ± 2.3	0.25 ± 2.5	.0344 ± 0.8	.342
5CO6b-12C	1.49	67	50	0.77	1.9	209.9 ± 5.7	211.2 ± 5.7	209.4 ± 6.6	-36 ± 306	-117	29.76 ± 2.7	.0575 ± 4.8	30.21 ± 2.8	.0454 ± 12.6	0.21 ± 12.9	.0331 ± 2.8	.214
5CO6b-12R	0.00	1413	6	0.00	14.0	74.0 ± 0.5	73.9 ± 0.5	74.0 ± 0.5	133 ± 46	80	86.58 ± 0.6	.0487 ± 2.0	86.58 ± 0.6	.0487 ± 2.0	0.08 ± 2.0	.0116 ± 0.6	.303
5CO6b-13C	0.33	54	25	0.48	8.8	1119.5 ± 13.5	1120.9 ± 14.3	1120.7 ± 14.5	1094 ± 53	-2	5.26 ± 1.3	.0785 ± 2.0	5.27 ± 1.3	.0760 ± 2.6	1.99 ± 3.0	.1897 ± 1.3	.445
5CO6b-14R	0.00	284	6	0.02	2.8	74.7 ± 1.1	74.2 ± 1.1	74.3 ± 1.1	333 ± 102	346	85.80 ± 1.5	.0531 ± 4.5	85.80 ± 1.5	.0531 ± 4.5	0.09 ± 4.7	.0117 ± 1.5	.317
5CO6b-15R	0.65	504	6	0.01	5.1	74.6 ± 0.8	75.1 ± 0.8	74.9 ± 0.8	-262 ± 165	-451	85.40 ± 1.1	.0467 ± 3.5	85.95 ± 1.1	.0414 ± 6.5	0.07 ± 6.6	.0116 ± 1.1	.170
5CO6B-15C	1.24	58	34	0.60	1.7	217.4 ± 4.1	218.9 ± 3.8	218.9 ± 4.2	-62 ± 420	-128	28.79 ± 1.7	.0551 ± 5.9	29.15 ± 1.9	.0449 ± 17.2	0.21 ± 17.3	.0343 ± 1.9	.111
5CO6B-16C	1.33	61	33	0.55	1.8	217.6 ± 3.9	220.2 ± 3.6	219.7 ± 4.0	-298 ± 481	-237	28.74 ± 1.6	.0518 ± 5.7	29.13 ± 1.8	.0408 ± 18.8	0.19 ± 18.9	.0343 ± 1.8	.097
5CO6B-17C	0.21	106	30	0.30	11.3	753.8 ± 5.7	746.2 ± 6.0	754.4 ± 6.0	1005 ± 52	33	8.04 ± 0.8	.0744 ± 2.2	8.06 ± 0.8	.0727 ± 2.6	1.24 ± 2.7	.1240 ± 0.8	.302
5CO6B-18C	0.08	2261	2494	1.14	73.0	237.8 ± 0.6	238.0 ± 0.6	235.3 ± 0.8	195 ± 24	-18	26.59 ± 0.3	.0506 ± 0.9	26.62 ± 0.3	.0500 ± 1.0	0.26 ± 1.1	.0376 ± 0.3	.246
5CO6B-19C	0.00	229	240	1.08	6.9	222.2 ± 1.9	222.0 ± 2.0	221.3 ± 2.5	248 ± 112	12	28.52 ± 0.9	.0512 ± 4.9	28.52 ± 0.9	.0512 ± 4.9	0.25 ± 4.9	.0351 ± 0.9	.173
5CO6B-20C	0.21	64	13	0.21	11.4	1220.4 ± 12.0	1239.1 ± 13.6	1222.0 ± 12.4	885 ± 93	-27	4.79 ± 1.1	.0703 ± 4.1	4.80 ± 1.1	.0686 ± 4.5	1.97 ± 4.6	.2084 ± 1.1	.233
5CO6B-21C	0.00	1348	4	0.00	12.8	70.8 ± 0.4	71.0 ± 0.4	70.8 ± 0.4	-11 ± 55	-116	90.51 ± 0.6	.0458 ± 2.3	90.51 ± 0.6	.0458 ± 2.3	0.07 ± 2.4	.0110 ± 0.6	.241
GM14S-1	9.66	82	58	0.72	0.2	14.5 ± 0.8	13.1 ± 0.8	13.2 ± 1.0	1995 ± 220	13674	444.64 ± 5.6	.1226 ± 12.4	444.64 ± 5.6	.1226 ± 12.4	0.04 ± 13.6	.0022 ± 5.6	.415

GM14S-2	12.66	76	41	0.56	0.2	14.0 ± 1.5	15.2 ± 0.9	15.1 ± 1.2		-100	369.79 ± 5.3	.1464 ± 11.8	460.72 ± 10.7			.0022 ± 10.7	
GM14S-3	2.52	339	244	0.74	0.7	13.6 ± 0.6	14.8 ± 0.3	14.4 ± 0.4		-100	424.92 ± 2.2	.0662 ± 8.8	472.05 ± 4.1			.0021 ± 4.1	
GM14S-4	2.94	281	280	1.03	0.6	14.9 ± 0.5	15.5 ± 0.4	15.7 ± 0.5	-2636 ± 0	-17734	402.66 ± 2.4	.0696 ± 9.2	430.81 ± 3.5			.0023 ± 3.5	
GM14S-5	6.80	90	52	0.59	0.2	15.3 ± 0.6	14.3 ± 0.7	14.0 ± 0.8	1625 ± 253	10521	420.97 ± 4.2	.1000 ± 13.6	420.97 ± 4.2	.1000 ± 13.6	0.03 ± 14.2	.0024 ± 4.2	.298
GM14S-6	3.64	132	100	0.78	0.3	16.0 ± 0.6	15.4 ± 0.6	15.1 ± 0.7	1071 ± 249	6592	402.10 ± 3.4	.0751 ± 12.4	402.10 ± 3.4	.0751 ± 12.4	0.03 ± 12.9	.0025 ± 3.4	.268
GM14S-7	6.94	101	74	0.76	0.2	14.1 ± 0.9	14.5 ± 0.6	14.2 ± 0.8	-2636 ± 0	-18829	412.77 ± 4.0	.1011 ± 13.0	457.60 ± 6.6			.0022 ± 6.6	
GM14S-8	9.26	62	55	0.92	0.1	14.5 ± 0.8	13.2 ± 0.8	13.3 ± 1.0	1948 ± 283	13302	442.96 ± 5.4	.1195 ± 15.8	442.96 ± 5.4	.1195 ± 15.8	0.04 ± 16.7	.0023 ± 5.4	.324
GM14S-9	3.94	235	178	0.78	0.5	12.8 ± 0.7	13.8 ± 0.4	13.8 ± 0.5		-100	447.59 ± 2.8	.0774 ± 10.3	503.23 ± 5.3			.0020 ± 5.3	
GM14S-10	9.83	77	43	0.58	0.2	15.9 ± 0.7	14.4 ± 0.8	14.9 ± 0.9	2014 ± 236	12530	403.70 ± 4.6	.1240 ± 13.3	403.70 ± 4.6	.1240 ± 13.3	0.04 ± 14.1	.0025 ± 4.6	.326
GM14S-11	7.92	122	89	0.76	0.3	13.9 ± 0.8	14.4 ± 0.6	14.1 ± 0.8	-2636 ± 0	-19082	411.79 ± 3.8	.1089 ± 11.6	463.79 ± 5.6			.0022 ± 5.6	
GM14S-12	0.23	64	36	0.57	8.9	968.2 ± 10.6	967.8 ± 11.2	969.2 ± 11.7	978 ± 53	1	6.16 ± 1.2	.0733 ± 2.3	6.17 ± 1.2	.0717 ± 2.6	1.60 ± 2.9	.1620 ± 1.2	.412
GM14S-13	0.27	76	39	0.54	4.4	423.2 ± 6.1	425.5 ± 6.0	423.5 ± 6.5	235 ± 204	-45	14.62 ± 1.4	.0575 ± 4.1	14.74 ± 1.5	.0509 ± 8.8	0.48 ± 9.0	.0679 ± 1.5	.165
GM14S-14	8.20	135	82	0.63	0.3	16.2 ± 0.7	14.9 ± 0.7	14.7 ± 0.8	1818 ± 227	11110	396.90 ± 4.1	.1112 ± 12.5	396.90 ± 4.1	.1112 ± 12.5	0.04 ± 13.1	.0025 ± 4.1	.309
GM14S-15	8.95	92	71	0.80	0.2	14.1 ± 1.7	15.5 ± 0.9	15.2 ± 1.1		-100	378.80 ± 4.8	.1171 ± 16.2	458.31 ± 12.3			.0022 ± 12.3	
GM14S-16	10.41	98	62	0.65	0.2	11.0 ± 3.3	15.0 ± 0.8	14.1 ± 1.1		-100	385.75 ± 4.8	.1286 ± 13.9	587.16 ± 30.3			.0017 ± 30.3	
Chortis block																	
5H3a-1R	0.47	365	12	0.0350	1.8	35.4 ± 0.7	35.7 ± 0.7	35.8 ± 0.7	-404 ± 439	-1241	179.16 ± 1.9	.0505 ± 6.5	181.72 ± 2.1	.0392 ± 16.8	0.03 ± 16.9	.0055 ± 2.1	.121
5H3a-2R	-0.18	193	5	0.0268	1.0	37.3 ± 0.9	37.3 ± 1.0	37.2 ± 0.9	-39 ± 230	-205	172.55 ± 2.5	.0453 ± 9.5	172.55 ± 2.5	.0453 ± 9.5	0.04 ± 9.8	.0058 ± 2.5	.258
5H3a-3C	0.27	2101	5	0.0024	10.9	39.0 ± 0.5	38.9 ± 0.5	39.0 ± 0.5	145 ± 65	273	164.90 ± 1.2	.0489 ± 2.8	164.90 ± 1.2	.0489 ± 2.8	0.04 ± 3.0	.0061 ± 1.2	.391
5H3a-4C	-0.33	219	97	0.4595	1.1	35.2 ± 1.0	36.5 ± 0.9	36.0 ± 1.0			176.72 ± 2.4	.0441 ± 9.3	182.47 ± 2.9	.0183 ± 76.3	0.01 ± 76.4	.0055 ± 2.9	.038
5H3a-5C	-0.03	5793	685	0.1223	30.9	39.9 ± 0.4	40.0 ± 0.4	39.9 ± 0.4	-31 ± 49	-178	160.82 ± 1.0	.0465 ± 1.7	161.04 ± 1.0	.0455 ± 2.0	0.04 ± 2.3	.0062 ± 1.0	.454
5H3a-6C	0.78	117	34	0.2967	0.6	37.1 ± 1.1	36.8 ± 1.2	36.9 ± 1.2	324 ± 264	774	173.21 ± 3.1	.0529 ± 11.6	173.21 ± 3.1	.0529 ± 11.6	0.04 ± 12.0	.0058 ± 3.1	.257
5H3a-7C	0.00	332	73	0.2282	1.7	37.5 ± 0.8	37.5 ± 0.8	37.3 ± 0.8	37 ± 169	0	171.47 ± 2.0	.0468 ± 7.1	171.47 ± 2.0	.0468 ± 7.1	0.04 ± 7.4	.0058 ± 2.0	.273
5H3a-8C	0.18	2383	418	0.1813	12.4	38.8 ± 0.4	38.7 ± 0.4	38.7 ± 0.5	111 ± 62	185	165.76 ± 1.2	.0482 ± 2.6	165.76 ± 1.2	.0482 ± 2.6	0.04 ± 2.9	.0060 ± 1.2	.404
5H11a-1	2.03	71	26	0.37	1.2	124.6 ± 2.9	122.1 ± 3.0	122.9 ± 3.2	762 ± 153	511	51.23 ± 2.4	.0646 ± 7.2	51.23 ± 2.4	.0646 ± 7.2	0.17 ± 7.6	.0195 ± 2.4	.311
5H11a-2	-0.42	438	239	0.56	7.8	131.8 ± 1.7	132.6 ± 1.7	132.1 ± 1.8	-134 ± 106	-202	48.32 ± 1.3	.0453 ± 3.3	48.42 ± 1.3	.0436 ± 4.3	0.12 ± 4.5	.0207 ± 1.3	.286
5H11a-3	-0.19	196	121	0.64	3.4	129.0 ± 2.1	129.8 ± 2.1	128.8 ± 2.3	-141 ± 225	-209	49.26 ± 1.6	.0471 ± 6.7	49.49 ± 1.6	.0435 ± 9.1	0.12 ± 9.2	.0202 ± 1.6	.175
5H11a-4	-0.11	189	62	0.34	3.3	131.1 ± 2.1	131.3 ± 2.1	130.8 ± 2.2	88 ± 119	-33	48.66 ± 1.6	.0478 ± 5.0	48.66 ± 1.6	.0478 ± 5.0	0.14 ± 5.3	.0206 ± 1.6	.306
5H11a-5	-0.09	220	97	0.46	3.9	130.1 ± 2.0	130.2 ± 2.0	130.0 ± 2.1	95 ± 107	-27	49.04 ± 1.5	.0479 ± 4.5	49.04 ± 1.5	.0479 ± 4.5	0.13 ± 4.8	.0204 ± 1.5	.318
5H11a-6	-0.03	168	59	0.36	3.0	131.2 ± 2.2	131.2 ± 2.2	130.9 ± 2.3	121 ± 122	-7	48.65 ± 1.7	.0485 ± 5.2	48.65 ± 1.7	.0485 ± 5.2	0.14 ± 5.5	.0206 ± 1.7	.306
5H11a-7	-0.01	198	102	0.53	3.6	133.6 ± 2.1	134.7 ± 2.1	133.5 ± 2.3	-241 ± 252	-281	47.36 ± 1.6	.0486 ± 4.7	47.77 ± 1.6	.0418 ± 10.0	0.12 ± 10.1	.0209 ± 1.6	.160
5Pb-5c.1.1	0.30	2171	238	0.11	71.2	240.6 ± 1.0	239.6 ± 1.0	240.1 ± 1.0	389 ± 54	62	26.21 ± 0.42	0.05684 ± 1.3	26.29 ± 0.44	0.0544 ± 2.4	0.2854 ± 2.4	0.03803 ± 0.44	.181
5Pb-5c.1.2	0.00	1681	309	0.19	35.8	158.01 ± 0.82	157.87 ± 0.84	157.65 ± 0.86	193 ± 40	22	40.3 ± 0.53	0.04995 ± 1.7	40.3 ± 0.53	0.04995 ± 1.7	0.1709 ± 1.8	0.02481 ± 0.53	.290
5Pb-5c.1.3	1.65	617	61	0.10	13.1	155.3 ± 1.9	156.9 ± 1.4	157.4 ± 1.4	-302 ± 430	-295	40.34 ± 0.89	0.0539 ± 3.2	41.01 ± 1.2	0.0408 ± 17	0.137 ± 17	0.02438 ± 1.2	.072
5Pb-5c.2.1	0.00	318	87	0.28	53.3	1149.3 ± 5.6	1126.2 ± 5.9	1135.3 ± 6.0	1557 ± 17	35	5.124 ± 0.54	0.09651 ± 0.91	5.124 ± 0.54	0.09649 ± 0.91	2.596 ± 1.1	0.1952 ± 0.54	.506
5Pb-5c.2.2	0.07	578	128	0.23	88.9	1060.4 ± 4.8	1058.8 ± 5.0	1060.9 ± 4.9	1096 ± 20	3	5.589 ± 0.49	0.07662 ± 0.78	5.593 ± 0.49	0.07605 ± 1	1.875 ± 1.1	0.17879 ± 0.49	.437
5Pb-5c.2.3	0.69	1413	608	0.44	30.8	160.56 ± 0.85	160.8 ± 0.81	160.92 ± 0.89	105 ± 89	-35	39.37 ± 0.5	0.05363 ± 1.5	39.65 ± 0.54	0.0481 ± 3.8	0.1673 ± 3.8	0.02522 ± 0.54	.142
5Pb-5c.3.1	0.07	723	192	0.27	16.4	167.5 ± 1.3	167 ± 1.3	166.9 ± 1.4	279 ± 56	66	37.96 ± 0.78	0.0524 ± 2.2	37.99 ± 0.78	0.0519 ± 2.5	0.1882 ± 2.6	0.02633 ± 0.78	.303
5Pb-5c.3.2	1.22	606	131	0.22	13.7	165.6 ± 1.8	165.7 ± 1.5	166.1 ± 1.5	160 ± 290	-3	37.95 ± 0.84	0.059 ± 3.7	38.42 ± 1.1	0.0493 ± 12	0.177 ± 12	0.02603 ± 1.1	.090
5Pb-5c.4.1	0.04	765	311	0.42	17.4	168.1 ± 1.2	167.5 ± 1.3	166.3 ± 1.4	300 ± 59	78	37.84 ± 0.74	0.0527 ± 2.5	37.86 ± 0.74	0.0523 ± 2.6	0.1906 ± 2.7	0.02642 ± 0.74	.278
5Pb-5c.4.2	0.00	1635	855	0.54	37.1	168.2 ± 1.0	168.3 ± 1.1	168.4 ± 1.2	143 ± 43	-15	37.83 ± 0.63	0.04891 ± 1.8	37.83 ± 0.63	0.04889 ± 1.8	0.1782 ± 1.9	0.02643 ± 0.63	.325
5Pb-5c.5.1	0.13	577	250	0.45	13.1	167.8 ± 1.4	167.7 ± 1.5	167.9 ± 1.6	191 ± 77	14	37.88 ± 0.86	0.0509 ± 3	37.93 ± 0.86	0.0499 ± 3.3	0.1814 ± 3.4	0.02637 ± 0.86	.253
5Pb-5c.5.2	0.51	1192	165	0.14	26.7	165.2 ± 1.0	165.6 ± 1.0	165.8 ± 1.0	65 ± 84	-60	38.32 ± 0.61	0.0514 ± 2.1	38.52 ± 0.63	0.0473 ± 3.5	0.1694 ± 3.6	0.02596 ± 0.63	.176
5Pb-5c.5.3	0.33	351	56	0.17	7.78	163.7 ± 1.8	162.7 ± 1.8	162.7 ± 1.8	398 ± 100	143	38.74 ± 1.1	0.0573 ± 3.5	38.87 ± 1.1	0.0547 ± 4.7	0.1938 ± 4.8	0.02572 ± 1.1	.227
5Pb-5c.5.4	0.08	2855	830	0.30	64.2	166.54 ± 0.68	166.49 ± 0.69	166.35 ± 0.72	178 ± 34	7	38.18 ± 0.41	0.05026 ± 1.3	38.21 ± 0.41	0.04964 ± 1.5	0.1791 ± 1.5	0.02617 ± 0.41	.268
5Pb-5c.6.1	1.27	559	472	0.87	12.6	164.5 ± 1.6	166.2 ± 1.5	165.9 ± 1.8	-276 ± 260	-268	38.19 ± 0.87	0.0513 ± 3	38.68 ± 10	0.0412 ± 10	0.147 ± 10	0.02585 ± 10	.098

5Pb-5c.6.2	0.06	1879	168	0.09	41.9	164.99 ± 0.8	164.9 ± 0.83	164.91 ± 0.81	187 ± 56	14	38.55 ± 0.49	0.0503 ± 2.3	38.57 ± 0.49	0.0498 ± 2.4	0.1781 ± 2.4	0.02593 ± 0.49	.199
5Pb-5c.6.3	0.06	634	118	0.19	11.9	139.3 ± 1.2	138.8 ± 1.2	138.5 ± 1.3	269 ± 74	93	45.75 ± 0.87	0.0521 ± 3	45.77 ± 0.87	0.0516 ± 3.2	0.1555 ± 3.3	0.02185 ± 0.87	.262
5Pb-5c.7.1	0.72	290	65	0.23	5.54	140.8 ± 1.8	140.4 ± 1.8	136.8 ± 1.9	259 ± 170	84	44.94 ± 1.3	0.0571 ± 4.3	45.27 ± 1.3	0.0514 ± 7.4	0.157 ± 7.5	0.02209 ± 1.3	.175
5Pb-5c.7.2	0.95	769	173	0.23	3.81	36.72 ± 0.58	36.48 ± 0.54	36.63 ± 0.57	288 ± 250	686	173.4 ± 1.4	0.0597 ± 4.9	175 ± 1.6	0.0521 ± 11	0.041 ± 11	0.005712 ± 1.6	.143
5Pb-5c.7.3	7.88	173	52	0.31	0.771	30.8 ± 1.6	30.7 ± 1.9	31.2 ± 1.2	170 ± 1700	444	192.3 ± 3.1	0.1123 ± 8	209 ± 5.3	0.049 ± 72	0.033 ± 72	0.00479 ± 5.3	.074
5Pb-5c.8.1	0.03	4330	1208	0.29	112	190.6 ± 1.4	190.6 ± 1.4	189.8 ± 1.4	186 ± 25	-3	33.32 ± 0.72	0.05003 ± 0.98	33.33 ± 0.72	0.0498 ± 1.1	0.206 ± 1.3	0.03 ± 0.72	.557
5Pb-5c.8.2	0.23	3374	1024	0.31	75.8	166.02 ± 0.76	166.32 ± 0.76	166.44 ± 0.8	96 ± 45	-42	38.24 ± 0.46	0.04973 ± 1.2	38.33 ± 0.46	0.04794 ± 1.9	0.1725 ± 2	0.02609 ± 0.46	.236
5Pb-5c.8.3	0.23	800	73	0.09	17.1	158.6 ± 1.2	158.3 ± 1.2	158.7 ± 1.2	228 ± 100	44	40.06 ± 0.74	0.0525 ± 2.6	40.15 ± 0.77	0.0507 ± 4.4	0.1742 ± 4.5	0.02491 ± 0.77	.172
5Pb-5c.9.1	0.41	424	186	0.45	9.5	165.2 ± 1.7	164.8 ± 1.7	166.1 ± 1.8	251 ± 120	52	38.37 ± 0.99	0.0545 ± 3.3	38.53 ± 1	0.0512 ± 5.2	0.1833 ± 5.3	0.02595 ± 1	.194
5Pb-5c.9.2	0.77	1166	273	0.24	25.7	162.2 ± 1.1	163.3 ± 1.0	163.2 ± 1.1	-102 ± 150	-163	38.94 ± 0.62	0.0502 ± 2.1	39.24 ± 0.69	0.0442 ± 6	0.1552 ± 6	0.02548 ± 0.69	.115
5Pb-5c.10.1	0.35	682	95	0.14	16.3	175.8 ± 1.4	176 ± 1.4	176.2 ± 1.5	146 ± 110	-17	36.04 ± 0.8	0.0517 ± 2.7	36.17 ± 0.83	0.049 ± 4.6	0.1867 ± 4.7	0.02765 ± 0.83	.179
5Pb-5c.10.2	0.13	2151	946	0.45	47.3	162.68 ± 0.8	162.7 ± 0.81	163.02 ± 0.88	159 ± 48	-2	39.08 ± 0.49	0.05031 ± 1.6	39.13 ± 0.5	0.0492 ± 2.1	0.1735 ± 2.1	0.02556 ± 0.5	.236
5Pb-5c.11.1	0.00	2532	1089	0.44	55.9	163.41 ± 0.73	163.49 ± 0.75	163.14 ± 0.81	143 ± 35	-12	38.95 ± 0.45	0.04891 ± 1.5	38.95 ± 0.45	0.04891 ± 1.5	0.1731 ± 1.5	0.02567 ± 0.45	.295
5Pb-5c.12.1	0.01	105	29	0.28	2.48	174.2 ± 3.8	169.8 ± 3.9	170.4 ± 4.1	974 ± 150	459	36.5 ± 2.2	0.0717 ± 7.5	36.5 ± 2.2	0.0716 ± 7.5	0.27 ± 7.8	0.02739 ± 2.2	.285
5Pb-5c.12.2	0.31	1537	535	0.36	33.8	162.2 ± 1.0	162.6 ± 1.0	162.2 ± 1.1	74 ± 83	-54	39.11 ± 0.62	0.05 ± 2.1	39.24 ± 0.64	0.0475 ± 3.5	0.1669 ± 3.5	0.02549 ± 0.64	.180
5Pb-5c.13.1	2.58	229	83	0.37	1.17	37.2 ± 1.4	37.2 ± 1.0	36.5 ± 1.1	40 ± 1100	2	168.2 ± 2.7	0.0672 ± 8.2	172.6 ± 3.7	0.047 ± 46	0.037 ± 46	0.00579 ± 3.7	.081
5H-9a.1.1	0.68	256	190	0.77	9.4	267.7 ± 3.1	268.3 ± 3.0	269.3 ± 3.5	198 ± 180	-26	23.42 ± 1.1	0.0556 ± 3.1	23.58 ± 1.2	0.0501 ± 7.7	0.293 ± 7.8	0.0424 ± 1.2	.153
5H-9a.1.2	0.85	81	45	0.58	3.06	275.1 ± 4.9	274.7 ± 4.8	275.9 ± 5.4	328 ± 220	19	22.74 ± 1.7	0.0598 ± 5.5	22.93 ± 1.8	0.053 ± 9.7	0.318 ± 9.9	0.04359 ± 1.8	.183
5H-9a.1.3	0.78	373	2	0.01	12.4	242 ± 2.2	242.8 ± 2.1	243.3 ± 2.1	120 ± 160	-50	25.93 ± 0.87	0.0547 ± 2.8	26.13 ± 0.94	0.0484 ± 6.7	0.255 ± 6.8	0.03826 ± 0.94	.139
5H-9a.2.1	0.07	519	214	0.43	97.2	1269.9 ± 5.2	1273.9 ± 5.5	1269.9 ± 5.5	1206 ± 19	-5	4.589 ± 0.44	0.08096 ± 0.85	4.592 ± 0.45	0.08036 ± 0.96	2.413 ± 1.1	0.21774 ± 0.45	.423
5H-9a.2.2	0.10	300	73	0.25	56.4	1275.4 ± 6.5	1279.9 ± 7.0	1276.7 ± 6.7	1204 ± 27	-6	4.566 ± 0.56	0.08111 ± 1.2	4.57 ± 0.56	0.0803 ± 1.4	2.422 ± 1.5	0.2188 ± 0.56	.381
5H-9a.2.3	4.74	567	9	0.02	26.8	328.9 ± 4.0	329.2 ± 2.6	330.1 ± 2.8	347 ± 350	5	18.17 ± 0.72	0.0915 ± 2.6	19.08 ± 1.2	0.0534 ± 15	0.386 ± 16	0.05235 ± 1.2	.080
5H-9a.3.1	1.45	119	64	0.55	4.44	269.1 ± 4.3	270.9 ± 3.9	272.4 ± 4.4	11 ± 340	-96	23.12 ± 1.4	0.058 ± 4.6	23.46 ± 1.6	0.0463 ± 14	0.272 ± 14	0.04262 ± 1.6	.114
5H-9a.3.2	0.51	331	146	0.46	12.3	270.8 ± 3.0	271.4 ± 2.8	272.2 ± 3.0	202 ± 200	-25	23.18 ± 1	0.0542 ± 2.9	23.3 ± 1.1	0.0502 ± 8.6	0.297 ± 8.7	0.04291 ± 1.1	.131
5H-9a.4.1	0.71	271	166	0.63	10.5	283.2 ± 2.8	284.7 ± 2.7	285.9 ± 3.0	95 ± 170	-66	22.1 ± 0.94	0.0537 ± 3.1	22.26 ± 1	0.0479 ± 7	0.297 ± 7	0.04491 ± 1	.144
5H-9a.4.2	0.00	540	368	0.70	20.4	277.1 ± 1.9	276.6 ± 1.9	277.1 ± 2.2	346 ± 50	25	22.77 ± 0.69	0.0534 ± 2.2	22.77 ± 0.69	0.0534 ± 2.2	0.3234 ± 2.3	0.04392 ± 0.69	.297
5H-9a.4.3	0.21	1685	1934	1.19	62.4	271.4 ± 1.3	271.9 ± 1.4	272.6 ± 1.7	207 ± 42	-24	23.2 ± 0.5	0.05196 ± 1.3	23.25 ± 0.5	0.05025 ± 1.8	0.2979 ± 1.9	0.043 ± 0.5	.268
5H-9a.5.1	0.50	441	394	0.92	16.2	268.2 ± 2.2	269.2 ± 2.2	268.5 ± 2.7	130 ± 130	-52	23.42 ± 0.8	0.0527 ± 2.6	23.54 ± 0.86	0.0486 ± 5.6	0.285 ± 5.7	0.04248 ± 0.86	.151
5H-9a.5.2	0.64	169	26	0.16	5.83	252.6 ± 3.3	252.7 ± 3.3	251.9 ± 3.3	252 ± 170	0	24.86 ± 1.3	0.0564 ± 4.1	25.02 ± 1.3	0.0513 ± 7.4	0.282 ± 7.5	0.03997 ± 1.3	.177
5H-9a.5.3	8.07	98	59	0.63	3.82	263.9 ± 9.4	273.4 ± 4.3	275 ± 5.1			21.96 ± 1.5	0.0907 ± 4.1	23.89 ± 3.6			0.0418 ± 3.6	
5H-9a.6.1	0.24	261	92	0.36	43	1129.1 ± 7.5	1130.1 ± 7.9	1130.7 ± 7.9	1115 ± 42	-1	5.21 ± 0.71	0.0788 ± 1.6	5.223 ± 0.72	0.0768 ± 2.1	2.026 ± 2.2	0.1914 ± 0.72	.324
5H-9a.6.2	0.24	348	25	0.07	19.2	400.2 ± 3.5	396.9 ± 3.7	399.6 ± 3.5	660 ± 110	65	15.57 ± 0.88	0.0635 ± 4.6	15.61 ± 0.9	0.0616 ± 5.2	0.544 ± 5.3	0.06406 ± 0.9	.169
5H-9a.6.3	0.17	354	19	0.05	36.4	727.6 ± 5.2	724.7 ± 5.4	727.6 ± 5.2	842 ± 52	16	8.354 ± 0.75	0.0685 ± 2	8.368 ± 0.76	0.0672 ± 2.5	1.106 ± 2.6	0.11949 ± 0.76	.290
5H-9a.6.4	0.54	494	3	0.01	16.7	247 ± 2.3	246.9 ± 2.3	247 ± 2.3	268 ± 120	8	25.46 ± 0.92	0.0559 ± 2.9	25.59 ± 0.96	0.0516 ± 5.3	0.278 ± 5.3	0.03907 ± 0.96	.180
5H-9a.6.3-re	0.18	279	17	0.06	27.5	700.4 ± 9.7	696.1 ± 9.9	700.4 ± 9.8	871 ± 45	24	8.7 ± 1.5	0.0695 ± 1.8	8.71 ± 1.5	0.0681 ± 2.2	1.077 ± 2.6	0.1148 ± 1.5	.561
5H-9a.7.1	0.71	65	19	0.30	9.11	965 ± 12	970 ± 12	972 ± 12	850 ± 130	-12	6.142 ± 1.2	0.0733 ± 2.9	6.186 ± 1.3	0.0674 ± 6.4	1.501 ± 6.5	0.1616 ± 1.3	.202
5H-9a.7.2	0.20	467	3	0.01	15.4	242.7 ± 1.9	241.9 ± 1.9	242.5 ± 1.9	349 ± 90	44	26.01 ± 0.79	0.0551 ± 2.6	26.07 ± 0.81	0.0535 ± 4	0.283 ± 4	0.03836 ± 0.81	.201

Errors are 1-sigma; Pb_c and Pb^* indicate the common and radiogenic portions, respectively.

Error in Standard calibration was 0.34%

(1) Common Pb corrected using measured ^{204}Pb.

(2) Common Pb corrected by assuming $^{206}Pb/^{238}U$-$^{207}Pb/^{235}U$ age-concordance

(3) Common Pb corrected by assuming $^{206}Pb/^{238}U$-$^{208}Pb/^{232}Th$ age-concordance

TABLE 4. $^{40}AR/^{39}AR$ DATA

Sample	Stop	Mineral	*J*	Weight mg	Grain Size μm	Total Fusion Age, Ma	Weighted Mean Age, Ma	Isochron Age, Ma	MSWD	$^{40}Ar/^{36}Ar$	$\%^{39}Ar$ Used	Steps
Western Chuacús complex												
G19s	G1	Phe	0.003192	10.1	10-20	66.66±0.33	66.53±0.33	66.50±0.37	4.1/2.0	296±4	61	6-16/21
		Phe	0.003185	10.1	20-40	67.92±0.34	67.38±0.33	67.00±0.37	4.1/1.9	307±5	79	7-19/23
G27s	G57	Bt	0.004555	0.3	250	37.38±1.37	35.06±1.29	37.21±10.06	0.6/2.4	350±74	48	5-10/15
Central Chuacús complex												
G10s	G29	WM	0.004564	1.2	100-200	66.04±0.65	66.00±0.65	65.96±0.66	14.6/1.7	299±9	93	3-21/26
G12s	G31	WM	0.0007854	nd	nd	71.80±0.89	72.59±0.65	67.8±5.0	31	297±64	100	1-19/19
5CO-4b	5CO-4	Bt	0.004480	4.3	250	64.31±0.63	64.34±0.63	64.80±0.68	26.6/1.8	264±11	98	2-17/19
		WM	0.004590	2.9	250	67.77±0.67	67.51±0.66	67.56±0.73	174/1.7	286±17	100	1-17/17
5CO-5a	5CO-5	WM	0.004586	2.1	250	234.4±2.2	225.1±2.1	225.2±2.2	0.9/2.6	294±3	5	1-5/23
		Hbl	0.004581	8.9	250	670.61±5.60	–	–	–	–	100	1-20/20
5PB-9b	5PB-9	WM	0.004570	5.1	250	60.27±0.59	–	–	–	–	100	1-27/27
5PB-13b	5PB-13	Hbl	0.0007852	nd	nd	94±18	69.3±1.4	64.5±5.4	0.31	1283±270	35	5 of 12
5PB-14	5PB-14	WM	0.004568	2.9	250	64.67±0.63	65.01±0.64	64.93±0.64	1.2/2.3	297±1	68	14-20/20
887C	887	WM	0.014376	5.4	250	70.5±1.2	69.8±1.2	70.9±3.8	13	321±120	78	1-7/10
Metasomatized southern Chuacús complex												
G6s	G26	WM	0.004565	0.6	~63	71.40±0.80	62.01±0.69	59.55±2.37	2.2/2.3	497±367	48	6-12/16
G7s	G27	WR rhyolite	0.004446	20.0	na	68.37±0.94	69.91±1.06	63.66±9.19	9.5/3.0	305±15	59	2-5/7
5C-36a	5C-36	WM	0.004579	1.9	250	48.04±0.47	48.32±0.48	48.20±0.50	16.7/1.8	298±3	86	9-22/22
Sanarate complex												
G3s	G23	WM	0.004534	2.2	~63	168.05±1.61	170.56±1.63	151.2±13.22	80/2.4	1339±918	69	3-8/17
G5s	G24	Hbl	0.004519	9.5	250	128.08±1.29	155.85±1.50	155.92±1.91	75/2.7	291±8	36	13-17/17
Western Las Ovejas complex, Guatemala												
5C-2c	5C-2	Hbl	0.000786	nd	nd	22.1±6.6	19.2±1.5	20.1±6.4	0.32	280±36	73	1-4/6
5C-5	5C-5	Bt	0.004574	0.5	~63	29.21±0.29	29.18±0.29	29.90±0.33	3.4/2.6	255±6	88	2-6/7
5C-23d	5C-23	Hbl	0.004609	23.4	250	35.99±0.37	35.43±0.36	35.81±0.40	1.6/2.0	276±9	64	6-15/17
5C-23c	5C-23	Bt	0.004612	0.8	250	25.57±0.26	25.24±0.25	25.34±0.26	0.3/3.0	291±2	60	3-6/9
5C-26c	5C-26	Hbl low-T	0.004607	18.9	250	27.84±0.28	17.76±0.18	18.21±0.45	48.3/2.6	272±18	45	1-5/19

		medium-T					21.73±0.24	21.72±0.35	2.4/2.4	384±3	13	10-15/19
		high-T					38.01±0.38	35.78±2.28	43.8/3.8	314±18	17	15-17/19
		Bt	0.004605	2.9	250	13.84±0.62	20.49±0.24	21.08±0.84	18.1/2.0	294±2	76	4-9/11
5C-26d	5C-26	Kfs	0.004600	12.7	400	30.25±0.59	30.42±0.32	29.94±0.54	6.4/2.3	297±1	89	10-16/17
5C-33	5C-33	Bt	0.004597	2.5	250	22.42±0.24	23.04±0.23	22.80±0.26	2.2/2.1	297±1	58	6-13/17
		Kfs low-T	0.004524	26.8	400	129.9±2.0	7.4±1.1	6.7±3.2	1.7/2.6	298±25	23	6-10/21
		medium-T					31.38±2.78	32.98±10.47	0.1/3.8	292±7	7	11-13/21
5C-37b	5C-37	Hbl high-T	0.004566	8.6	250	41.06±0.43	39.11±0.55	39.10±3.93	1.2/2.1	512±117	37	8-11/12
		low-T					18.23±053	18.27±1.63	1.7/2.3	362±20	20	1-3/12
5C-37d	5C-37	Bt	0.004593	2.9	250	17.81±0.18	18.15±0.19	19.49±1.18	60/2.3	289±6	74	4-10/12
5PB-5a	5PB-5	Hbl	0.0007864	nd	250	30.4±1.0	31.03±0.70	29.9±1.4	67/–	243±77	96	2-13/15
		Bt	0.004572	1.6	250	28.22±0.28	28.20±0.28	28.29±0.32	18.2/2.1	289±6	100	1-8/8
Eastern Las Ovejas complex, Honduras												
5H-3a	5H-3	Bt (laser)	0.004420	sg	250	25.58±0.26	18.98±0.22	19.00±2.78	17.4/2.1	661±412	100	1-10/10
5H-4b	5H-4	Bt (laser)	0.004424	sg	250	25.58±0.34	25.70±0.34	23.05±1.86	1.6/3.0	314±13	100	1-4/4
		Hbl	0.004532	5.3	250	36.87±0.40	38.81±0.40	38.86±1.78	93.7/2.6	291±135	92	5-9/10
5H-4c	5H-4	Bt	0.004577	2.3	250	24.77±0.25	25.75±0.26	24.67±0.44	0.6/3.0	311±4	54	5-8/9
		Hbl	0.004527	7.5	250	32.57±0.40	31.53±0.32	31.44±0.65	52.3/2.1	297±6	98	4-11/11
5H-4d	5H-4	Hbl	0.0007881	nd	nd	28.6±2.0	30.0±1.5	26.1±3.6	6.1/–	334±16	100	1-17/17
Granitoids of the arc complex												
5C-11	5C-11	Bt+Chl	0.004422	sg	na	84.51±0.89	89.98±0.89	–	–	–	100	1-10/10
5C-21	5C-21	Kfs (laser)	0.004416	sg	400	20.03±0.23	19.09±0.25	18.80±0.45	0.3/3.0	297±1	58	5-9/9
5H-5	5H-5	Kfs low-T	0.004529	12.3	400	32.98±0.33	28.29±0.28	28.31±0.36	2.4/2.6	291±59	27	10-14/33
5H-13	5H-13	Bt (laser)	0.004425	3.0	250	57.71±0.70	60.89±0.61	61.95±0.86	9.7/2.4	265±14	100	1-6/6
Southern Mexico												
ML-18	ML-18	Bt	0.004540	1.1	250	148.82±1.43	162.2±0.8	–	–	–	10	19-21/21
ML-37	ML-37	WM high-T	0.004542	1.7	250	302.76±2.76	315.09±2.87	316.3±0.4	5/3	289±2	37	16-20/20
ML-37	ML-37	WM low-T	0.004542	1.0	250	302.76±2.76	246.70±2.76	255.39±22.70	68/3.8	289±14	2	1-3/20
MU-12	MU-12	Bt	0.0015255	1.0	250	29.69±0.35	28.60±0.29	28.62±0.40	0.02/3.8	295±2	58	13-16/17
MU-13	MU-13	Bt	0.0015249	1.2	250	35.06±1.24	34.38±0.39	35.12±0.70	0.5/3.0	275±12	56	11-15/16
ML-39	ML-39	Bt	0.0015307	1.5	250	15.22±0.46	14.57±0.59	13.81±1.90	1.6/2.6	300±10	51	1-5/15
PA3-4	PA3-4	Hbl	0.0042502	sg		–	8.1±0.6	8.8±1.5	1.9	290±27	100	1-5/5
PA3-4	PA3-4	Bt	0.0042502	203/sg		3 exp.	–	8.5±0.3	2.1	Forced	100	1-9/9
CB35	CB35	Hbl	0.0036469	198/320		2 exp.	–	28.4±1.3	3.0	293±25	–	1-7/9

CB35	CB35	Bt	0.0035870	35/203	2 exp.	–	8.2±0.1	0.57	297±3	100	1-12/12
CB31	CB31	Hbl	0.0049746	207/305	2 exp.	–	15.5±1.2	0.89	305±19	–	1-6/8
CB34	CB34	Hbl	0.0035870	195/306	2 exp.	–	11.0±1.8	0.33	307±6	100	1-9/9
PI28-1	PI28-1	Hbl	0.0042502	sg	–	8.1±0.3	–	–	–	100	1-4/4
PI28-1	PI28-1	Bt	0.0042502	191/sg	3 exp.	–	8.0±0.5	1.3	303±3	100	1-8/8

J is the irradiation parameter; MSWD is the mean square weighted deviation, which expresses the goodness of fit of the isochron; isochron and weighted mean ages are based on fraction of ^{39}Ar and steps listed in the last two columns. WM(P)A is the weighted mean (plateau) age. Abbreviations: sg, single-grains (laser total-fusion ages); Phe, phengite; WR, whole rock; WM, white mica; Hbl, amphibole; Kfs, potassium feldspar; Bt, biotite; Chl, chlorite; low-T, low-temperature steps; medium-T, intermediate-temperature steps; high-T, high-temperature steps; exp., heating or laser degassing experiments on different fractions of minerals from the same sample; na, not applicable; nd, not determined.

Age interpretation

Western Chuacús complex: G19s fine-grained phengite: unified age for two grain-size fractions: 67±1 Ma; G27s biotite: WMA calculated for $^{40}Ar/^{36}Ar = 350$; 37±5 Ma.

Central Chuacús complex: 5CO-4b biotite: 64.5±1.0 Ma; 5CO-4b white mica: 67.5±2.0 Ma.G10s white mica: 66±1 Ma; G12s white mica: 70±3 Ma; 5CO-5a white mica: hump-shaped spectrum indicates ^{40}Ar excess, 219-243 Ma; low-T plateau at 225±5 Ma; 5CO-5a hornblende: loss profile from ~720 Ma to ~153 Ma; 5PB-9b sericitic white mica: 52-62 Ma hump-shaped spectrum indicates ^{40}Ar excess; 5PB-13b hornblende: mixing of different age components; minimal age of old component 137 Ma, maximal age of young component 20 Ma; major age component at 65±6 Ma; 5PB-14 white mica: loss profile from ~65 Ma to ~50 Ma; mid and high-T 'plateau' at 65.2±0.8 Ma; 887C white mica: 70.0±1.5 Ma.

Metasomatized southern Chuacús complex: G6s white mica: U-shaped spectrum indicates ^{40}Ar excess; 60±5 Ma; G7s rhyolite gash filling: 67±5 Ma; 5C-36a white mica: 48±1 Ma.

Sanarate complex: G3s white mica: loss profile from ~195 Ma to ~137 Ma; mid-T 'plateau' at 155±10 Ma; G5s hornblende: loss profile from ~157 Ma to ~45 Ma; high-T 'plateau' at 156±5 Ma, low-T 'plateau' at 60±20 Ma;

Western Las Ovejas complex, Guatemala: 5C-2c hornblende: 20±2 Ma; 5C-5 biotite: loss profile from ~31 Ma to ~26 Ma; mid-T 'plateau' at 29±2 Ma; 5C-23c biotite: 25.3±0.5 Ma; 5C-23d hornblende: 35.5±1.0 Ma; 5C-26c hornblende: loss profile from ~64 Ma to 17 Ma; low-T 'plateau' at 18±2 Ma, intermediate-T 'plateau' at 21±2 Ma and high-T 'plateau' at 36±3 Ma; intermediate and low-T 'plateau' and chlorite-biotite ages are identical within error at 20±2 Ma; 5C-26c chlorite-biotite mixture: loss profile from ~28 Ma to ~3 Ma; mid-T 'plateau' at 20±2 Ma; 5C-26d potassium-feldspar: 30±1 Ma; 5C-33 biotite: loss profile from ~26 Ma to ~15 Ma; mid-T 'plateau' at 23±2 Ma; 5C-33 potassium-feldspar: loss profile from ~370 Ma to ~6 Ma, low-T ^{40}Ar excess, fast cooling at 32±4 Ma and 7±2 Ma; 5C-37b hornblende: high-T WMA calculated for $^{40}Ar/^{36}Ar = 553$; 39±3 Ma; low-T WMA calculated for $^{40}Ar/^{36}Ar = 362$; 18±3 Ma; 5C-37d biotite: loss profile from ~26 Ma to ~9 Ma; mid-T 'plateau' at 19±2 Ma; 5PB-5a hornblende: 30±2 Ma; 5PB-5a biotite: 28.2±0.4 Ma.

Eastern Las Ovejas complex, Honduras: 5H-3a biotite: single-grain laser-fusion age (10 grains); WMA calculated from $^{40}Ar/^{36}Ar = 661$; 22±4 Ma; 5H-4b biotite: single-grain laser-fusion age (4 grains) at 25±3 Ma; 5H-4c biotite: loss profile from ~28 Ma to ~18 Ma; minor ^{40}Ar excess; mid-T 'plateau' at 25±2 Ma; Integrated biotite age of stations 5H-3 and 5H-4 at 24±2 Ma; 5H-4b hornblende: 38±2 Ma; 5H-4c hornblende: 31±5 Ma; 5H-4d hornblende: 29±3 Ma; Integrated hornblende age of stations 5H-4 at 34±4 Ma.

Granitoids: 5C-11 chloritized biotite: single-grain laser-fusion age (10 grains) at 90±10 Ma; 5C-21 potassium-feldspar: single-grain laser-fusion age (8 grains)at 20±1 Ma; 5H-5 K-feldspar: loss profile from ~37 Ma to ~28 Ma, low-T 'plateau' indicates fast cooling at 28.3±0.5 Ma; 5H-13 biotite: single-grain laser-fusion age (6 grains) at 59±3 Ma.

Southern Mexico: ML-18 biotite: loss profile from 163 to 88 Ma, high-T 'plateau' at 162±2 Ma, low-T 'plateau' at 90±2 Ma; ML-37 white mica: loss profile from 316 to 238 Ma, high-T 'plateau' at 315±3 Ma, low-T 'plateau' at 247±3 Ma; MU-12 biotite: 29±1 Ma; MU-13 biotite: 35±1 Ma; ML-39 biotite: 15±2 Ma; PA3-4 hornblende: 8.5±1.5 Ma; PA3-4 biotite: 8.5±1.0 Ma; CB35 hornblende: 28.5±1.5 Ma; CB35 biotite: 8.2±0.5 Ma; CB31 hornblende: 15.5±1.5 Ma; CB34 hornblende: 11.2 Ma; PA28-1 hornblende: 8.1±0.5 Ma; PI28-1 biotite: 8.0±0.5 Ma

TABLE 5. RB/SR ANALYTICAL DATA

Sample (stop)	$^{87}Rb/^{86}Sr$	± (%)	$^{87}Sr/^{86}Sr$	± (%)	Age	±
Chuacús complex						
5CO-4b wr	3.646	1	0.7948	0.05	Wm 63.5	5.2
5CO-4b Pl	4.338	1	0.79482	0.01		
5CO-4b Wm1, 2min, W1	159.775	1	0.93532	0.05		
G11s(G30), Bt 10min	413.033	1	1.10289	0.05	Bt 67.4	0.7
G11s(G30), Pl	0.952	1	0.70819	0.02		
5PB-9b, wr	38.255	1	0.80174	0.03	Wm 76.5	0.59
5PB-9b, Wm3, 2 min, W1	527.228	1	1.33388	0.07		
5PB-9b, Wm6, 2 min, W2	393.719	1	1.18754	0.07		
5PB-13b, Pl	0.069	1	0.70913	0.01	Wm 63.6	2.4
5PB-13b, Wm 2min	2.899	1	0.7117	0.01		
5PB-13b, Wm4, 10min, W1	3.032	1	0.71171	0.03		
5CO-5b, Wr	0.056	1	0.70861	0.01	Wm 76.1	1.5
5CO-5b, Ms1, 2min, W1	4.952	1	0.7139	0.01		
5CO-5b, Ms2+4, 2min, W2	4.088	1	0.713	0.02		
5CO-6b, wr	0.545	1	0.70938	0.02	Wm 56.6	8
5CO-6b, Kfs	0.242	1	0.70898	0.02		
5CO-6b, Wm2, 2min, W1	30.81	1	0.73454	0.07		
5CO-6b, Wm4, 2min, W2	33.569	1	0.73504	0.07		
885A, wr	1.029763	1	0.709764	0.0005	Wm 65.2	1.4
885A, Wm, 1.0A	1.750590	1	0.710431	0.0005		
885A, Wm, 1.2A	1.867765	1	0.71054	0.0005		
885A, Wm, 0.8A	1.949947	1	0.710672	0.0005		
Metasomatized southern Chuacús complex						
5C-36a, wr	0.14	1	0.70576	0.01	Bt 35	14
5C-36a, Pl	0.09	1	0.7056	0.01		
5C-36a Bt 10min	7.562	1	0.70936	0.01		
860B, wr	2.847707	1	0.706266	0.0005	Wm 63	17
860B, Wm, 065A	3.101435	1	0.706552	0.0005		
860B, Wm, 085A	0.329555	1	0.704046	0.0005		
Las Ovejas complex						
5C-28b, wr	3.944	1	0.71209	0.01	Wm 20.7	3.1
5C-28b. Pl	1.422	1	0.71087	0.01		
5C-28b, Wm 10min	65.791	1	0.7293	0.01		
5C-28b, Wm2, 10min, W2	73.754	1	0.73293	0.01		
5C-28b, Kfs	8.906	1	0.7145	0.01	Kfs 34.2	1
5C-37e, wr	2.257	1	0.71298	0.05	Wm 33.7	1.6
5C-37e, Pl	2.243	1	0.71335	0.01		
5C-37e, Kfs	2.348	1	0.71338	0.01		
5C-37e Wm, 2min	73.269	1	0.74719	0.07		
5H-2c, wr	4.439	1	0.71896	0.01	Wm 23.7	0.3
5H-2c, Pl	3.501	1	0.71848	0.01		
5H-2c, Kfs	5.082	1	0.71914	0.01		
5H-2c, Wm, 1.5min	64.26	1	0.73751	0.02		
5H-2c, Wm, 2min	67.998	1	0.73853	0.02		
5H-2a, Bio 10min	215.869	1	0.75908	0.03	Bt 16.2	2.1
5H-2a, GG	8.204	1	0.71153	0.01	Wm 21.8	0.4
5H-2a, Plg	4.857	1	0.71027	0.03		
5H-2a, Wm, 10min	222.159	1	0.78344	0.05		
5H-9a, wr	1.775	1	0.71548	0.01	Wm 162	11
5H-9a, Pl	0.294	1	0.71207	0.05		
5H-9a, Wm, 2min	6.817	1	0.72728	0.01		
5H-9a, Wm1, 2min, W1	7.934	1	0.72906	0.04		
5H-9a, Wm2, 2min, W2	9.125	1	0.73272	0.02		
5H-9a, Bt, 2min	36.279	1	0.7827	0.01		
5H-9a, Bt4, 2min, W1	50.248	1	0.80718	0.02	Bt 135	8

Abbreviations see Table 2. Ages are mineral isochrons. Sample specifications include various grinding times, grain-size, and magnetic fractions.

TABLE 6. FISSON-TRACK DATA

Apatite													
Sample	Elevation [m]	Grains	Ns	Ni	ρ_D (10^6 cm^{-2})	ϕ (10^{15} cm^{-2})	Z (10^8 year)	ξ (year cm^2)	P (χ^2)	ϕ-age (Ma)	Z-age (Ma)	ξ-age (Ma)	z_0-age (Ma)
Western Chuacús complex, Guatemala													
GM9s	1250	147	1002	2848	0.428	2.184	1.182	350.3	0.080	23.3±0.9	20.8±0.8	26.3±1.2	22.6±1.0
GM14s	1100	32	211	1024	0.445	2.268	1.219	350.3	0.000	14.2±1.1	12.5±1.0	16.0±1.3	13.7±1.1
GM15s	1100	243	920	13121	0.445	2.268	1.219	350.3	0.000	4.8±0.2	4.3±0.2	5.5±0.2	4.7±0.2
G18s	1990	29	684	1772	0.428	2.184	1.182	350.3	0.000	25.6±1.2	22.8±1.1	28.9±1.5	24.8±1.2
Central Chuacús complex, Guatemala													
5C-36a	372	93	1029	3311	0.428	2.184	1.182	350.3	0.001	20.6±0.8	18.3±0.7	23.3±1.0	20.0±0.8
5CO-4b	1229	50	644	2012	0.379	2.280	1.271	350.3	0.993	22.1±1.0	20.3±1.1	21.2±1.2	21.5±1.1
5CO-5b	970	71	182	455	0.377	2.281	1.271	350.3	0.000	27.7±2.5	25.4±2.4	26.3±2.5	26.8±2.4
5CO-6b	~950	41	1067	2434	0.428	2.184	1.182	350.3	0.000	29.0±1.1	25.9±1.0	32.8±1.5	28.1±1.2
G11s	1070	50	1006	2539	0.428	2.184	1.182	350.3	0.000	26.3±1.0	23.4±0.9	29.7±1.4	25.4±1.1
G12s	1300	123	1069	2094	0.428	2.184	1.182	350.3	0.000	33.8±1.3	30.1±1.2	38.2±1.8	32.8±1.4
824	2038	20	289	391	0.432		1.389	350.3	0.000		51.1±4.5	55.7±4.6	
825	823	10	1491	2571	0.436		1.413	350.3	0.000		40.8±2.2	44.1±1.9	
827	1319	20	913	2206	0.442		1.461	350.3	0.242		30.2±1.7	32.0±1.6	
846	1681	31	501	853	0.456		1.556	350.3	0.001		45.5±3.1	46.7±2.9	
Western Las Ovejas complex													
5C-6	719	50	533	1636	0.388	2.279	1.271	350.3	1.000	22.5±1.2	20.7±1.2	22.1±1.3	21.8±1.2
5C-11	779	43	369	1350	0.386	2.279	1.271	350.3	0.999	18.9±1.1	17.3±1.2	18.5±1.2	18.3±1.2
5C-23a	194	50	392	2055	0.384	2.280	1.271	350.3	1.000	13.2±0.7	12.1±0.8	12.8±0.8	12.8±0.8
5C-27a	286	43	747	6660	0.382	2.280	1.271	350.3	0.998	7.8±0.3	7.1±0.4	7.5±0.4	7.5±0.3
5C-28b	300	41	1101	19348	0.428	2.184	1.182	350.3	0.000	3.8±0.1	3.4±0.1	4.3±0.2	3.7±0.1
5C-32	868	50	391	1995	0.380	2.280	1.271	350.3	0.377	13.6±0.8	12.4±0.8	13.0±0.8	13.1±0.8
5C-37a	488	9	76	397	0.428	2.184	1.182	350.3	1.000	12.7±1.6	11.3±1.4	14.3±1.8	12.2±1.6
5PB-5c	440	43	699	5407	0.375	2.281	1.271	350.3	1.000	9.0±0.4	8.2±0.4	8.5±0.4	8.7±0.4
5PB-6b	226	47	1100	10197	0.445	2.268	1.219	350.3	0.000	7.4±0.2	6.6±0.2	8.4±0.3	7.2±0.3
Eastern Las Ovejas complex													
5H-3a	16	135	1054	9144	0.445	2.268	1.219	350.3	0.000	7.9±0.3	7.0±0.3	9.0±0.4	7.7±0.3
5H-5	88	61	402	2472	0.445	2.268	1.219	350.3	0.000	11.2±0.6	9.9±0.6	12.7±0.8	10.9±0.6
5H-9a	199	29	1064	6322	0.445	2.268	1.219	350.3	0.000	11.6±0.4	10.2±0.4	13.1±0.6	11.2±0.4
5H-13	789	50	339	922	0.445	2.268	1.219	350.3	0.001	25.3±1.6	22.4±1.5	28.6±2.0	24.5±1.6

Southern Mexico													
CB-8	770	12	1092	1950	0.323	2.109	1.166	350.3	0.000	35.8±1.4	32.6±1.2	31.6±1.8	35.2±1.5
CB-12	690	14	1085	1767	0.323	2.104	1.163	350.3	0.042	39.2±1.5	35.6±1.4	34.6±2.0	38.5±1.7
CB-16	590	45	1246	2572	0.322	2.099	1.159	350.3	0.000	30.8±1.1	28.0±1.0	27.2±1.5	30.3±1.2
CB-17	590	51	1495	3397	0.321	2.094	1.155	350.3	0.000	28.0±0.9	25.4±0.8	24.7±1.3	27.5±1.0
CB-28	220	62	307	1243	0.320	2.089	1.152	350.3	0.963	15.7±1.0	14.2±0.9	13.8±1.1	15.4±1.0
CMP-5	670	11	1170	2241	0.319	2.079	1.144	350.3	0.331	32.9±1.2	29.8±1.1	29.1±1.7	32.3±1.3
CMP-13	630	11	1177	2975	0.318	2.074	1.141	350.3	0.114	24.9±0.9	22.5±0.8	22.0±1.2	24.4±1.0
TP-1016	1016	5	1686	3559	0.317	2.069	1.137	350.3	0.000	29.7±0.9	26.9±0.8	26.3±1.4	29.2±1.0
TP-1320	1320	11	1093	2440	0.314	2.044	1.118	350.3	0.001	27.8±1.0	25.0±0.9	24.6±1.4	27.3±1.1
TP-1800	1800	10	1066	1778	0.316	2.059	1.130	350.3	0.000	37.4±1.5	33.8±1.3	33.1±2.0	36.7±1.6
TP-1990	1990	6	1088	2398	0.315	2.054	1.126	350.3	0.071	28.3±1.0	25.5±0.9	25.0±1.5	27.8±1.2
TP-2347	2347	10	1113	2110	0.313	2.039	1.115	350.3	0.001	32.6±1.2	29.3±1.1	28.8±1.7	32.0±1.4
TP-2513	2513	5	1131	2084	0.314	2.049	1.122	350.3	0.002	33.7±1.2	30.4±1.1	29.8±1.7	33.1±1.4

Titanite

Sample	Elevation [m]	Grains	Ns	Ni	Z (10^6 year)	ξ (year cm^2)	P (χ^2)	Z-age (Ma)	z-age (Ma)
5C-23a	194	5	5141	4636	41.94	126.76	0.000	23.2±1.3	22.7±1.9
GM15s	1100	13	627	1158	42.06	126.76	0.000	11.4±0.8	11.0±1.1

See Table 1 for locations and rock descriptions. Ns: number of spontaneous tracks; Ni: number of induced tracks; ρ_D: track density on dosimeter; ϕ: neutron flux density; Z: Z calibration factor; ξ, ξ calibration factor; z: zCN5- calibration factor; P(χ)2 is the probability of obtaining χ2 value for v degrees of freedom (where v = number of grains - 1).

TABLE 7. CONFINED TRACK-LENGTH PARAMETER IN APATITE

Sample	N	MTL (μm)	Error	Std.
5C-6	191	12.39	0.14	1.99
5C-23a	168	13.16	0.15	1.92
5C-32	252	13.40	0.10	1.53
5CO-4b	250	13.37	0.09	1.34
5CO-6b	251	13.78	0.08	1.33
5PB-5c	250	13.81	0.08	1.20
5PB-6b	250	13.34	0.09	1.38
G11s	250	12.33	0.12	1.93
G12s	21	11.31	0.76	3.48
GM9s	79	11.88	0.25	2.20
GM13s	41	10.94	0.51	3.28
GM15s	65	12.67	0.28	2.30
824	69	12.48	0.24	1.98
825	292	12.85	0.08	1.42
846	252	13.28	0.09	1.37

N: number of tracks; MTL: mean track length; Std.: standard deviation.

TABLE 8. PETROLOGY

sample	stop	rock type	mineral content	description	PT method	P [GPa]	T [°C]	Age [Ma]
Western Chuacús complex								
G19s	G1	hbl-ep schist	hbl		Ti in hbl		462-555	Ar-phg 67±1
			ep	short prismatic blasts	pl-hbl		460-640	Rb-pgh 55±10
			phg		pl-hbl graph. Spear		450	
			pl	inner part saussuritizied	pl-hbl graph. Plyusnina	0.7 - 0.8	500	
					phg minimum pressure	0.7		
G21s	G46	epidote schist	bt		no equilibrium!			
			ep	porphyroblasts	phg pressure	0.8		
			phg					
			kfs	no recrystallization				
			pl					
			ttn	as accessory phase				
Central Chuacús complex								
5CO-5a	5CO-5	eclogite	bt	very infrequently	GRIPS	0.9-1.1		Ar-hbl ~720 to 153
			hbl	large crystals	grt-cpx			Ar-phg 225±5
			cpx		internal cpx		514-611	
			grt		external cpx		490-590	
			pl		grt-hbl	1.3-1.6	562-650	
			phg	show high pressure	cpx-hbl graph.		630-640	
			ilm	as accessory phase	cpx-bt graph.		630-640	
					phg pressure	1.0-1.1		
					jadeite barometry	1.1-1.2		
					phg pressure	1.4-1.5		
5CO-4b	5CO-4	garnet gneiss	bt	partly altered to chlorite	grt-cpx		525	Ar-phg 67.5±2.0
			grt	large crystals with inclusions	grt-phg	1.4	550	Ar-bt 64.5±1.0
			phg	show high pressure	grt-bio	0.7	500	U/Pb 638-477
			epi	very infrequently				
			pl	partly saussuritiicied				
			kfs					
			ttn	as accessory phase				
5PB-13a	5PB-13	garnet-bearing mica schist	bt	partly altered to chlorite	large grt		460	
			grt	as inclusions in pl	tiny grt		561	
			phg		grt-phg			
			pl	inclusions of grt	large grt		475	
					tiny grt		580	
					phg minimum pressure	0.6-0.8		
5PB-13b	5PB-13	garnet amphibolite	grt	small crystals	grt-hbl		530-550	Rb-phg 63.6±2.4
			hbl		grt-chl	0.8	400	Ar-hbl 137-20, 65±6
			chl		hbl-pl		530-630	
			phg		Ti in hbl		590	
			epi		plg-hbl graph. Spear		500	
			pl	large crystals, inclusion-free	pl-hbl graph. Plyusnina	0.7-0.8	480	
G14s	G32	garnet amphibolite	bt		grt-phg		455	
			grt	blasts in matrix, inlusions in pl	grt-hbl		470-495	
			hbl		Triboulet			
			phg		internal hbl	0.85	700	
			pl	inclusions	external hbl	0.62	610	
			ep	short prismatic blasts	phg minimum pressure	0.6-0.8		
			chl	anormal brown interferrence colors	pl-hbl graph. Spear		490	
			ttn	as accessory phase	pl-hbl graph. Plyusnina	0.83	450-460	
5PB-14	5PB-14	hbl-ms-chl	hbl	very infrequently	pl-hbl		540-550	Ar-phg 65-50, 65.2±0.8
			epi	infrequently	pl-hbl graph. Spear		510	
			phg		pl-hbl graph. Plyusnina	0.8	500	
			pl	hugh crystals	Ti in hbl		624	
			chl	pseudomorphs after grt	phg minimum pressure	0.6		

Las Ovejas complex								
5PB-5a	5PB-5	garnet amphibolite	bt	partly altered to chlorite	grt-hbl	0.7-0.8	627-655	Ar-hbl 30±2
			grt	poikiloblast, pressure shadows	pl-hbl graph. Spear		530	Ar-bt 28.2±0.4
			hbl	partly mantled by bt	pl-hbl graph. Plyusnina		530	U/Pb-zrn 36.2±2.1
			pl	partly saussuriticied, inclusions of bt, hbl, qtz	grt-bt		630	
Sanarate complex								
5G-1	5G-1a	chlorite-epidote hornblende schist	pl		phg minimum pressure	0.6-0.65	500	
			ep		Triboulet			
			hbl		core	0.55	380	
			phg		rim	0.65	550	
			chl		Ti in hbl			
					core		448	
					rim		499	
					pl-hbl			
					core		413	
					rim		560	
Intrusives								
5C-13	5C-13	granodiorite	bt	partly altered to chlorite	Al in hbl	0.1-0.175		
			hbl	heavily corroded, with biotite	Ti in hbl		741	
			kfs	with perthitic unmixing	pl-hbl		754-862	
			pl	partly altered to sericite				
5PB-8	5PB-8	microdiorite	hbl	prismatic crystals	Al in hbl	0.14		
			cpx	mantled by hbl	Ti in hbl		730	
			pl	partly altered to sericite	pl-hbl		747-862	
					cpx-hbl graph.		750	

Chapter 5

Syn-orogenic extension: late Miocene exhumation of the Shaxdara gneiss dome, Southern Pamirs

Abstract

The Shaxdara gneiss dome in South Pamirs, southern Tajikistan, is re-interpreted as Paleozoic–Mesozoic marine sediment sequence, metamorphosed in a Cretaceous Andean-type magmatic arc. Low-grade metamorphic equivalents crop out in the southeastern Pamirs and in the Wakhan corridor in easternmost Afghanistan. Continued post-collisional convergence between India and Asia caused transpression along the western Pamirs resulting in crustal thickening and *en echelon* formation of several gneiss domes. Thickening was compensated by synorogenic upper crustal extension confined to the thermally weakened gneiss domes. Apatite fission track data from the Shaxdara dome suggest a rolling-hinge model (Wernicke and Axen, 1988) of tectonic denudation, active from at least ~10 Ma to ~5 Ma. The dome-bounding normal fault is the South Pamir Fault, which is tentatively traced eastwards, implying that the low-grade rocks of southeastern Pamirs constitute fault-bound tilted blocks above a major low-angle detachment. The Shaxdara gneiss dome is thus the largest extensional gneiss dome in the entire India–Asia collision zone. (U-Th)/He data indicate a later episode of rapid cooling caused by incision of the Pamir River, likely starting in the late Pliocene or Pleistocene.

1. Introduction

Great advances in the understanding of collisional orogens have resulted from research in the Tibet–Himalaya system, but its westward continuation, the Pamir Mountains remains little studied (Fig. 1). For example, correlation of tectonic units and sutures between Tibet and the Pamirs is still disputed (Yin and Harrison, 2000; Schwab et al., 2004).

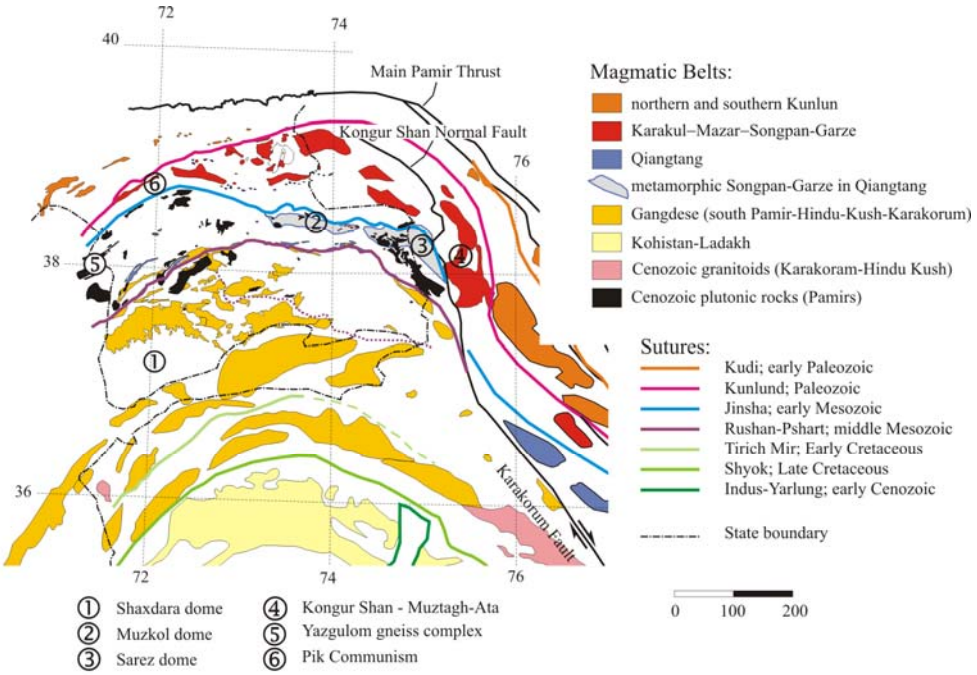

Figure 1. Simplified geologic map of the Pamirs, Hindu Kush, and Karakorum showing magmatic belts and sutures; after Schwab et al. (2004).

Objective of this study is the large (>100×300km) Shaxdara gneiss complex of the southwestern Pamirs, previously regarded as Archaean-Proterozoic basement accreted to Asia during Paleozoic or Mesozoic (Vlasov et al., 1991). We propose a Paleozoic-Mesozoic origin for the paragneisses metamorphosed by a Cretaceous active continental margin and overprinted by late Oligocene–?early Miocene crustal thickening. Structural observations and thermochronology reveal rapid Miocene exhumation to upper crustal depth under N-S extension, contemporaneous with the ongoing India–Asia convergence. Syn-orogenic extension to such extent entailing gneiss dome formation is unparalleled in the Himalaya–Tibet orogen. Exposure of deep crustal levels in the Pamirs provides insights into mid-crustal processes largely concealed in Tibet and thus offers new possibilities for the understanding of collisional orogenies.

Combined apatite fission track and (U-Th)/He data indicate post-Miocene river incision following a period of tectonic quiescence after cessation of doming in the South Pamirs. Disturbed river patterns suggest reorganisation of drainage systems during the Plio- or

Pleistocene. Future research supplementing the low-temperature thermochronology data set and implementing geomorphological criteria will unravel the neotectonic evolution and reveal possible links to deep seismicity located beneath the South Pamirs and Hindu Kush (e.g., Burtman and Molnar, 1993).

2. Geology of the Shaxdara gneiss dome

The Shaxdara gneiss dome is the largest outcrop of high-grade metamorphic rocks in the Pamirs; it encompasses most of southern Tajikistan and extends westward into Afghanistan (Fig. 2). The central part of the dome (southwest Tajikistan) consists of high-grade migmatitic gneisses and (garnet)-biotite-schists, locally kyanite- and sillimanite-bearing, and subordinate calc-silicates and marbles; lithologies are similar in the (western) Afghan part (Vlasov et al., 1991). Along the Afghan–Tajik border the dome is deeply incised by the Pjansch River, creating up to 2500m topographic relief.

The eastern continuation of the dome is partly covered by Quaternary sediments. Migmatitc gneisses outcrop as far south as the central Wakhan range (Afghan Pamirs in the Wakhan corridor of easternmost Afghanistan), where they are thrust southwards onto Late Paleozoic Wakhan slates (Zanchi et al., 2004). Gneisses pass upwards into late-Paleozoic Wakhan slates (e.g. Buchroithner, 1980), which occupy most of the Wakhan corridor, and Permo-Triassic clastic metasediments and minor carbonates. In the Wakhan range the succession is overprinted by the mid-Cretaceous Issik batholith (Rb/Sr biotite and muscovite ~102 Ma, Buchroithner and Scharbert, 1979).

The South Alichur range of south-central Tajikistan is made up of ortho- and paragneisses; to the north high-grade rocks pass into Triassic and Jurassic marine sediments and reef carbonates, which also outcrop widely in the southeastern Pamirs (Leven, 1995). Locally, Paleozoic (meta-) sediments have been mapped overlying the gneisses both in the central and eastern part of the dome. The northern margin of the dome is not well defined in the eastern part.

Cretaceous plutonic rocks are prevalent in the Southern Pamirs (Vlasov et al., 1991). Together with intrusives from Wakhan (Issik granodiorite) and northern Pakistan (Karakorum Axial Batholith) they form a continuous magmatic belt of ~200 km width ranging from the Shyok suture (closure of a mid-Cretaceous back-arc basin and accretion of the Kohistan-Ladakh island arc to Asia ~80 Ma; Rolland et al., 2000) to the Mesozoic Rushan-Pshart suture between Central and Southern Pamirs (Schwab et al., 2004; Fig. 1, 2); a few Cretaceous plutons also outcrop along the Rushan-Pshart suture and in the Central Pamirs. Geochemical and age data from the Karakorum batholith (Crawford and Searle, 1992 and references therein; Fraser et al.,

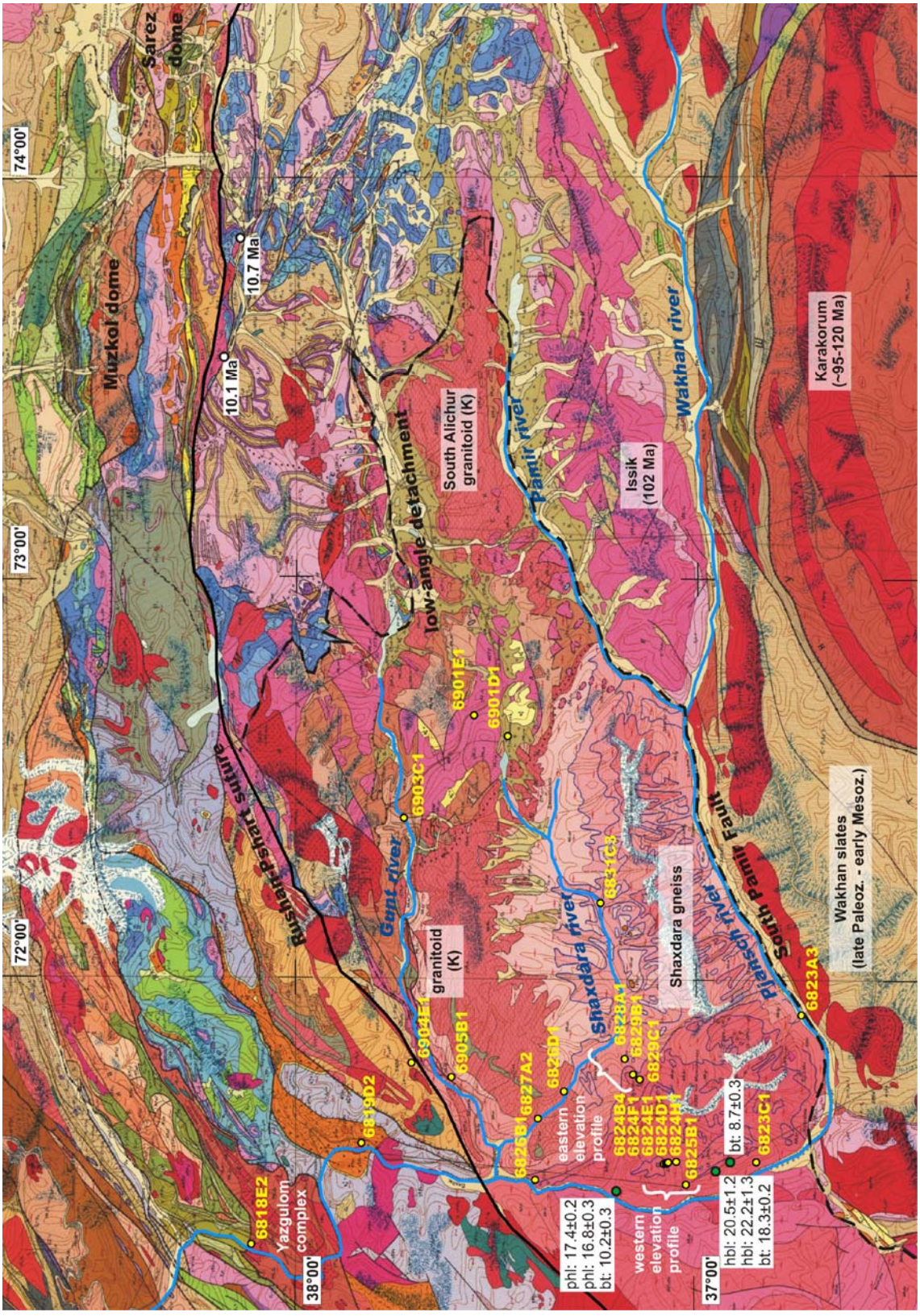

Figure 2. Detail of the geological map of Tajikistan (Vlasov et al., 1991) outlining major features mentioned in the text. Brown, purple and blue colors in the northeast show sedimentary sequences of the southeastern Pamirs. Yellow: sample number and location of apatite fission-track and (U-Th)/He-data; white: apatite fission-track ages from Schwab (2004); green: $^{40}Ar/^{39}Ar$ data from Hubbard et al. (1999); hbl: hornblende; phl: phlogopite; bt: biotite.

2001; Hildebrand et al., 2001) suggest mid-Cretaceous, calc-alkaline, subduction-related magmatism; minor Jurassic–Early Cretaceous magmatism is attributed to an active margin and suturing along the Tirich Mir fault (Hildebrand et al., 2001). Schwab et al. (2004) reported geochemical signatures from Mid and Late Cretaceous plutonic rocks from the Central and northernmost Southern Pamirs indicative for a mature arc to post-collisional setting. These authors attribute the widespread Cretaceous magmatism to flat-slab subduction of young oceanic lithosphere of the Shyok back-arc basin, and an Andean-type active margin that can be traced to the Lhasa block of southern Tibet (Gangdese arc). After accretion of the Kohistan-Ladakh arc continuous crustal thickening and shortening caused protracted sillimanite-grade metamorphism and magmatic activity with a major magmatic pulse in the Early Miocene (~24 Ma; Fraser et al., 2001).

3. Structural geology

The overall structure of the Shaxdara gneiss is subhorizontal layering of migmatitic paragneisses (Fig. 3a). Migmatization produced melts that formed granitoids of variable size (Fig. 3b). Both migmatization and intrusion of large intrusive bodies occurred syn-kinematic to N-S extension (Fig. 3c). Melt in necks of boudinaged mafic layers, in strain shadows of large clasts, and melt inclusions within garnet-porphyroblasts suggest coeval metamorphism, anatexis, and deformation (Fig. 3d). Syn-migmatitic ductile shear zones (Fig. 4, e.g., 6820B, 6827B, 6905A-B) indicate top-S to top-SW flow (Fig. 3e). The trend of stretching lineations associated with high-grade metamorphism (expressed by aligned amphibole, sillimanite, feldspar) varies between SW (e.g., 6820B, 6826A-B), S (6823B, 6827C) and SE (6829A). Where two lineations can be distinguished, the second one is generally closer to N-S (6822C, 6823C, 6826A, Fig. 3f). Mylonites occur throughout the dome; S–C-fabrics, σ- and δ-clasts, asymmetric boudinage (Fig. 3g), and mostly south-dipping ductile shear zones indicate top-S shear. Folding is isoclinal (6822C, 6904) to open (most other stations), fold axes are parallel to the (first) stretching lineation and trend generally NW-SE. Exceptions are the NE-trending fold axes of migmatites that developed coevally with the shear zones at stations 6904. In stations 6826A and 6826B, two generations of folds with unclear age relationship were documented; the more prominent set has fold axes parallel to the general NW trend of fold axes and stretching lineations.

Low temperature brittle–ductile shear zones and faults indicate N-S extension (Fig. 3h, 4); with the exception of stations 6829A and 6901A, late shear/fault planes dip S. Altogether, our structural observations suggest a continuous process of top-to-S deformation under N-S to NW-SE extension from high-temperature migmatization and granitoid emplacement to upper crustal brittle conditions.

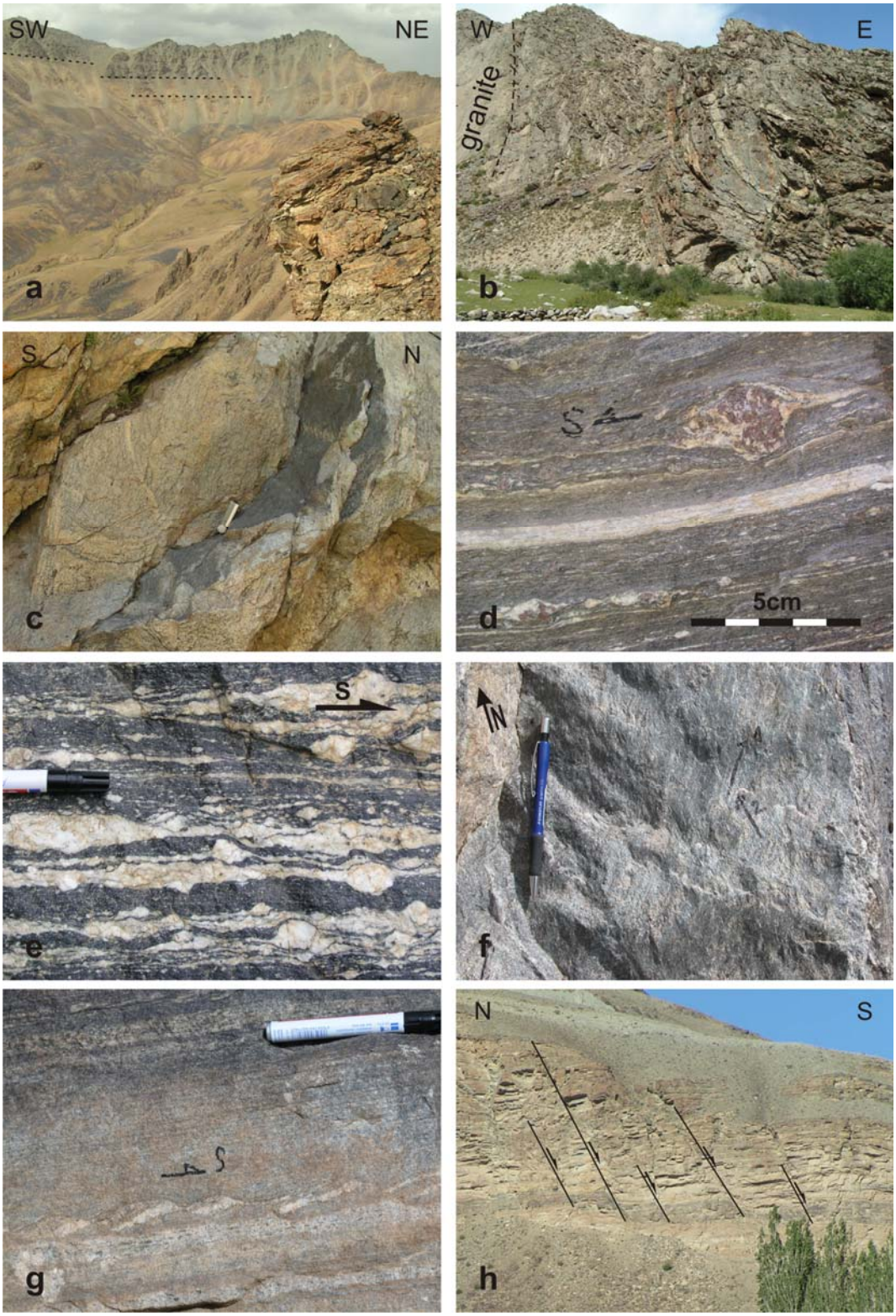

Figure 3. Representative deformation-geometry and kinematic structures. (a) West-central dome, view to the northwest. Note the regionally subhorizontal layering of paragneisses. (b) Syn-migmatitic intrusion of granitic body. (c) Same granite as Fig. 3b, foliated and cut by ductile shear zones; geologic compass for scale. (d) Syn-migmatitic garnet growth under top-S mylonitic deformation. (e) Mylonitic migmatite, top-S shear. (f) Amphibole- and feldspar-ductile older stretching lineation (1) overprinted by younger quartz ductile stretching lineation (2); station 6823C. (g) Synthetic asymmetric boundinage (top-to-S) close to station 6823A. (h) Brittle faulting; Shaxdara valley, view to the east.

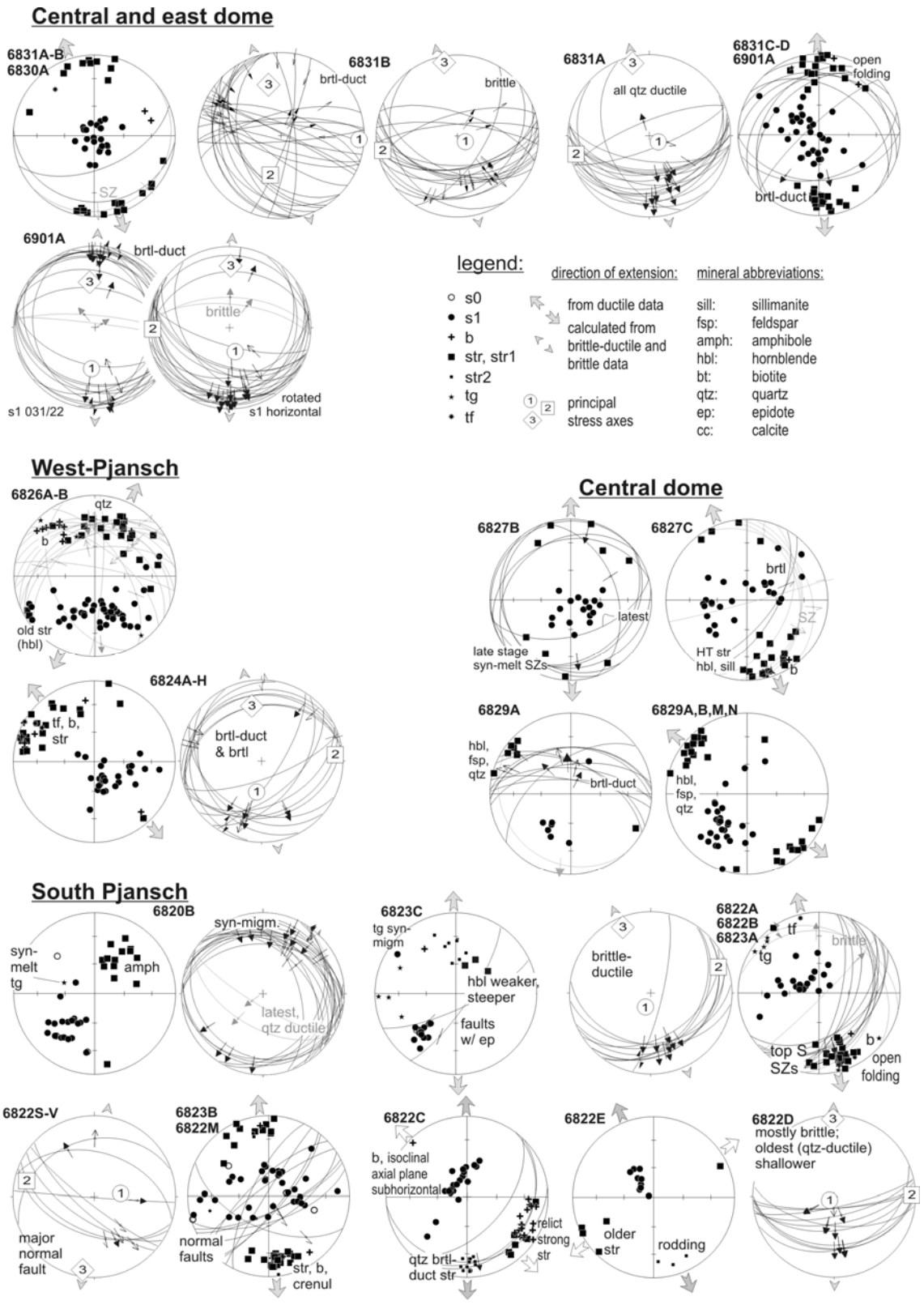

Figure 4. Summary of structural data (lower hemisphere, equal area stereoplots). Fault-slip data: faults are drawn as great circles and striae are drawn as arrows pointing in the direction of displacement of the hanging wall. Confidence levels of slip-sense determination are expressed in the arrowhead style: solid, certain; open, reliable; half, unreliable; without head, poor. Arrows around the plots give calculated local orientation of subhorizontal principal tension. Principal stress orientations $\sigma1 \geq \sigma2 \geq \sigma3$ calculated with the software package of Sperner et al. (1993). s0, bedding; s1, foliation; str, stretching lineation; SZ, shear zone; sb, shear band; tg, tension gash; tf, tension fracture; b, fold axis.

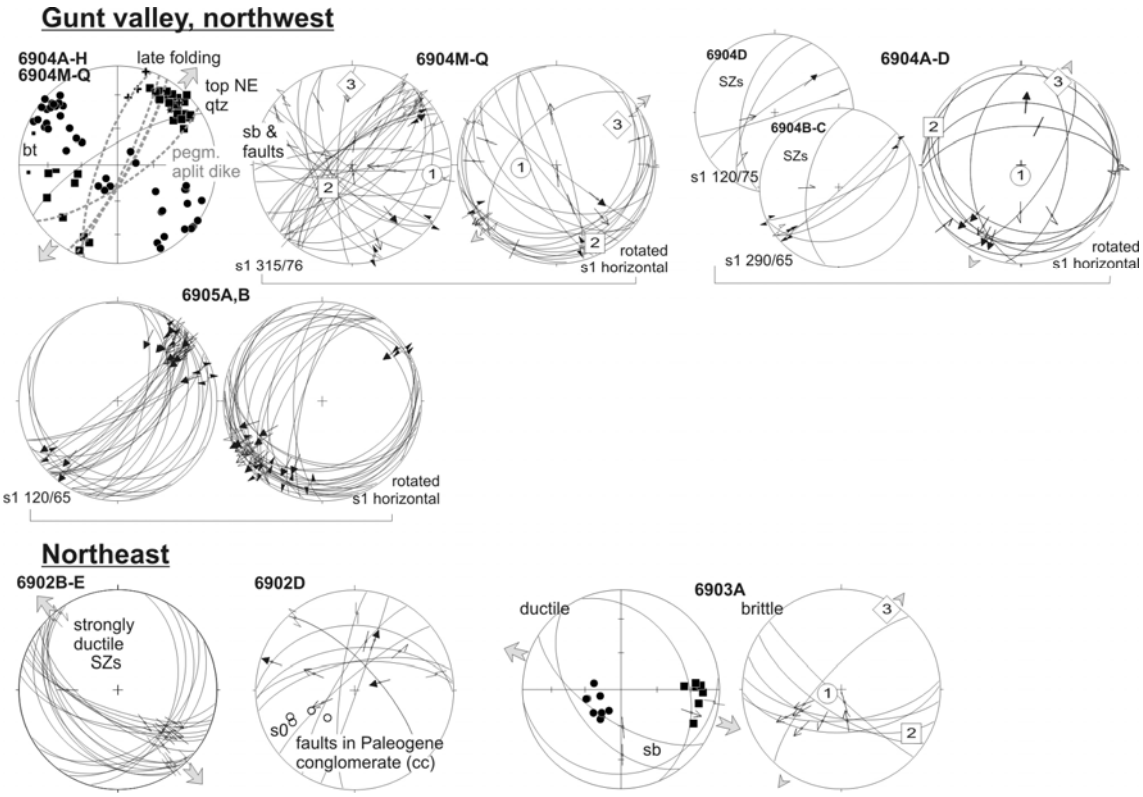

Figure 4. (continued)

Faulting is minor and occurs more often in the eastern and northern part of the dome (stations 6822D; 6901A; 6903A; 6904A-H). A major normal fault is observed in the southwest crosscutting shallow S dipping, top-S mylonites and juxtaposing them against Late Triassic metapelites (station 6822V). Late stage tilting of foliation to the NNE in the east and northeast (6831B, 6901A, 6903A) may originate from normal faulting.

We interpret the observed structures as a major normal fault zone accommodating exhumation of the Shaxdara gneiss dome. This fault zone is evidenced by our structural data (6822V) and the pronounced change in metamorphic grade between the dome gneisses and the Late Triassic metapelites of the southwestern dome at this station. The South Pamir Fault follows the southern Pjansch valley (Afghan-Tajik border, Fig. 2) but likely also affects rocks along the northern Wakhan corridor.

4. Thermochronology

4.1. Analytical Procedures

In the course of fieldwork, 20 samples of various lithologies were collected from the Shaxdara gneiss dome and 3 granitoid samples from north of the dome (Table 1). The samples were crushed, ground, and sieved; apatites in the 80-250 μm grain-size fraction were concentrated using standard magnetic and heavy-liquid techniques. From each apatite separate, 1-2 aliquots

were prepared for fission-track age determination by the external detector method (Hurford and Green, 1982). The fossil tracks were etched for 15 sec in 23% HNO_3 at 25°C and the induced tracks in the co-irradiated muscovite external detectors 50 min in 48%HF at 25°C. The apatite mounts were irradiated in two batches at the FRM-II research reactor of the Technische Universität München (Garching); the nominal thermal neutron fluences were: ϕ_{FG16}= 1.0 10^{15} cm^{-2} and ϕ_{FG17}= 2.5 10^{15} cm^{-2}; epithermal and fast fission of thorium and uranium isotopes is negligible at the irradiation position. The exact sample fluences and fluence gradient were calculated from the 1173 and 1332 keV γ-activities of co-irradiated metal activation monitors (IRMM-528R Al-1.0%Co; 3 Co-foils were included in each irradiation). The Co-concentration of the monitors is certified by the European Union Institute for Reference Materials and Measurements. The γ-activities were measured at the Institut für Angewandte Physik of the Technische Universität Bergakademie Freiberg (Prof. Dr. S. Unterricker). Consistent thermal neutron fluences were obtained with measurements calibrated against a Co standard and with (γ,γ)- and (β,γ)-coincidence measurements.

Tracks were counted in transmitted light at a magnification of 500 with a Zeiss Axioplan-2 microscope equipped with an Autoscan motorized stage, stage controller, and Trakscan fission-track software. To avoid cumbersome reference points and mirror image conversion during the track counts, the etched external detectors were repositioned track-side down on the apatite mounts (Jonckheere et al., 2003). Four samples were not countable due to the high densities of dislocations and/or inclusions. Six age standards (Durango apatite: 31.4±0.5 Ma; Hurford, 1991a,b) were included in each irradiation; the track counts for these standards and others included in earlier irradiations were used for calculating Z- and ζ- factors (Hurford and Green 1983). The Z- and ζ-ages of all the dated samples are in good agreement (Table 2). The closure temperature (T_c; Dodson 1973; 1979) is taken to be ~120°C (Ketcham et al., 1999) in view of the high cooling rate (25°C/Ma) suggested by the age-elevation profiles (see below) and an assumed average apatite composition.

Of the samples with sufficient apatite, a separate identical mount was prepared for confined track-length measurements, with the aim of modeling their cooling histories. These mounts were covered with 60 μm Al degraders and irradiated at 15° from normal incidence with 2.5 10^6 cm^{-2} 11.1 MeV/amu Xe-ions from the linear accelerator of the Gesellschaft für Schwerionenforschung (GSI, Darmstadt; Dr. C. Trautmann). The samples were etched for 20s in 5.5M at 21°C (Carlson et al., 1999) to be compatible with the annealing model of Ketcham et al. (1999; 2007). The ion irradiation has the effect of increasing the number of measureable confined tracks multiple times (Jonckheere et al., 2007; Min et al., 2007). Nevertheless, an

insufficient number of track lengths could be measured for modeling owing to the young ages and low uranium content of the samples.

Euhedral and, wherever possible, unbroken grains were selected for (U-Th)/He dating. The grains were examined for fluid and mineral inclusions in polarized transmitted light with a high-power Olympus SZX-16 stereo-zoom microscope. Inclusion-free grains were packed in Pt-tubes and their He, U, Th, and Sm measured at the Geoscience Centre, Universität Göttingen (Dr. I. Dunkl). For He, the Pt-tubes were heated in an Inconel furnace to 920°C for 60 minutes; degassing was checked by sequential reheating and He re-measurement; no analyzed crystal exhibited >1% residual gas after the first extraction. For Th and U, the samples were spiked with calibrated ^{230}Th and ^{233}U solutions following degassing and dissolved in 2% HNO_3–0.05% HF acid mixture in Teflon vials. The spiked solutions were analyzed by isotope dilution on a Perkin Elmer Elan DRC II ICP-MS with an APEX micro-flow nebulizer. Sm, Pt and Ca were determined by external calibration. The oxide formation rate and the PtAr–U interference were at all times monitored; their effect on the concentration of actinides was found to be negligible. Alpha ejection was corrected for using the method of Farley (2000) and the (U-Th)/He age was calculated using the Taylor expansion of the age equation (Des Patterson, CSIRO, Sydney). The Sm content was not considered for the age calculation, since its alpha decay constitutes a minor contribution to the He content. (U-Th)/He ages were determined for three single-grain aliquots from a selection of 15 samples (Table 3). The results show much scatter; often two ages are identical within error and a third one is much older. Further measurements are needed to determine reproducible ages. Ages older than the corresponding apatite fission-track age were discarded; those used are marked bold in Table 3.

4.2. Results

Samples for thermochronology are subdivided into a main group that comprises two elevation profiles, and eight regionally distributed samples; the latter are from the southern, central, and northern part of the dome. The northeastern dome margin and the Yazgulom gneiss complex of the Central Pamirs are discussed separately.

Central dome

All samples from the main group indicate late Miocene cooling through the fission-track closure temperature; 6824E1 from the western elevation profile and one aliquot of 6826D1 are identified as outliers. Apatite fission-track ages (AFT) from the western age-elevation profile together with sample 6823C1 south of the profile (Fig. 2) indicate rapid cooling during exhumation at a rate of ~1-2 mm/yr (Fig. 5a); the eastern profile is consistent with this, but less well constrained (Fig. 5b).

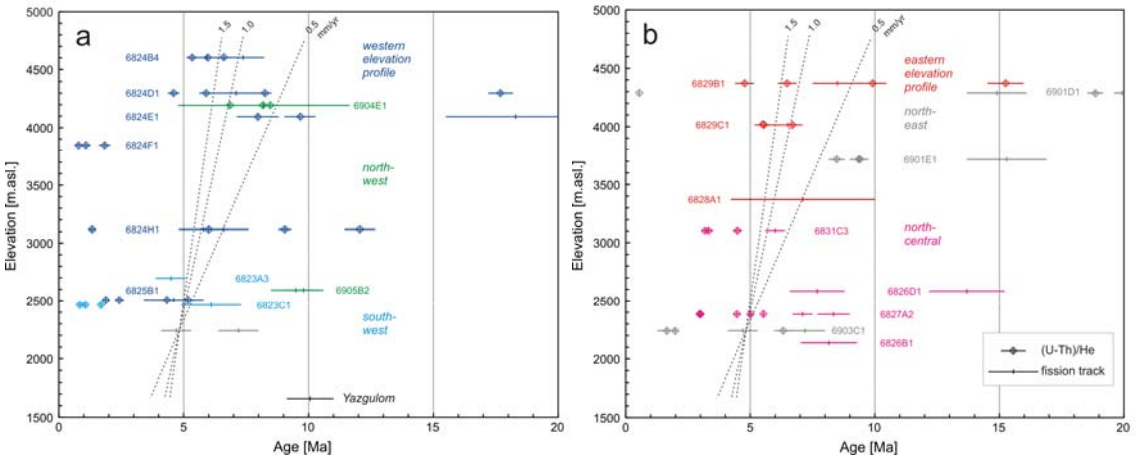

Figure 5. Fission-track and (U-Th)/He-ages (2σ-errors) vs. elevation; (a) western elevation profile, samples from the southwest (Pjansch), from the northwest (Gunt), and from the Yazgulom gneiss; (b) eastern elevation profile, samples from the Shaxdara valley (north and central dome), and from the northeast. Dotted grey lines indicate slopes of exhumation rates 0.5, 1.0, and 1.5 mm/yr. The elevation profiles are consistent with rapid exhumation ~1-2 mm/yr.

Our structural analysis suggests that cooling to ambient temperatures is attained by N-S to NW-SE extension along mostly south-dipping faults and shear zones. Figure 6a shows correlation between AFT age and distance to the southern section of the Pjansch river, which is interpreted to trace the southern dome-bounding fault. The age difference of ~5 myr between the northwestern and the southern dome points to structurally controlled exhumation of the footwall of the South Pamir Fault starting at or prior to 10 Ma.

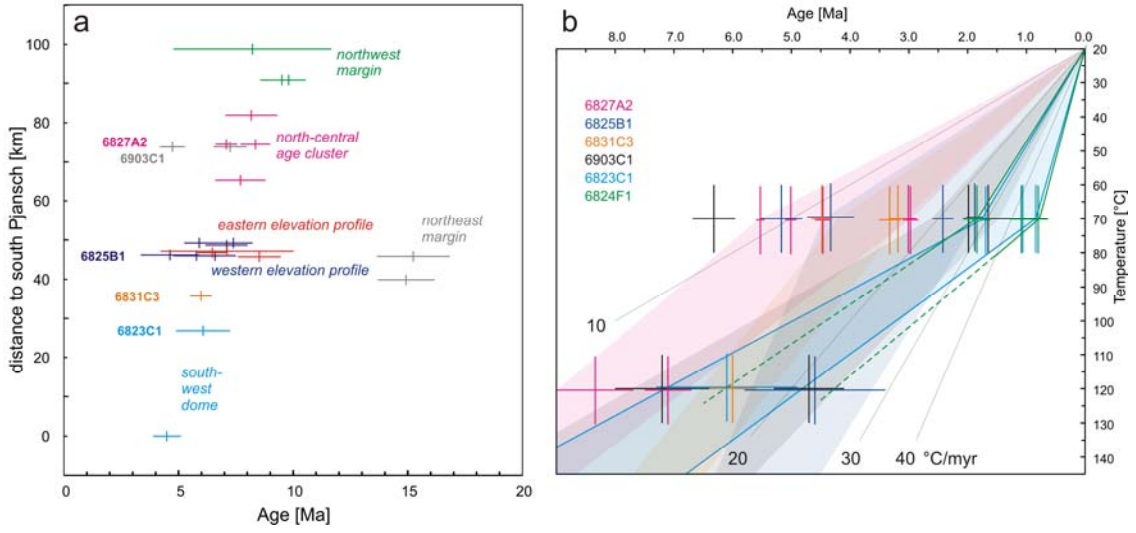

Figure 6. (a) AFT age vs. distance to southern Pjansch river. Note the clear trend towards older fission-track ages with increasing distance from the South Pamir Fault; samples from northeast constitute an exception. (b) Temperature history for low-elevation samples. Colored swaths indicate average cooling rates; black lines indicate cooling rates between 10 and 40°C/myr. Note that the samples with best constrained AHe ages (6823C1; 6824F1) suggest increased Pleistocene cooling (blue and green lines; AFT age for 6824F1 extrapolated from elevation profile).

Figure 6b outlines average cooling paths from combined AFT and (U-Th)/He (AHe) ages for five samples from low elevations (<3500 m.asl.) together with well constrained AHe ages for sample 6824F1 (3850 m.asl.). Cooling rates to ambient temperatures are in the order of ~15-20°C/myr and seem to increase below ~70°C; note that AFT and AHe are very well constrained for samples 6823C1 and 6824F1 (Fig. 6b, blue and green outlined cooling paths). Fewer and less well constrained data exist for high-elevation samples (Fig. 5); AHe ages are generally indistinguishable from AFT. Samples from high elevations and thus likely unaffected by the Pjansch-river gorge formation cooled below ~70°C during the late Miocene tectonic exhumation event.

Northeastern dome

Three samples from probably Cretaceous intrusions are located at the northeastern margin of the Shaxdara gneiss dome. Ages from low elevation sample 6903C1 are in agreement with data from the western dome (Fig. 4, 5b). However, two AFT ages (6901D1, 6901E1) are ~5 myr older than the oldest AFT ages along the northern dome margin, and ~8 myr older than expected based on their distance to the South Pamir Fault.

Yazgulom complex

One sample from a gneiss complex north of the dome (6818E1, AFT 10 Ma) is similar to AFT ages from samples along the Rushan-Pshart suture farther east (Schwab, 2004; see below). The complex constitutes an antiformal dome and is bounded by normal fault zones along its northern and southern margins. Preliminary U/Pb zircon dating gives ~45 and 21-18 Ma crystallization ages (B.R. Hacker, pers. comm.) for granitoids. These ages are similar to those found in the Sarez and Muzkol domes of the central and eastern Central Pamir (Fig. 1, 2). It appears that the southern Pamir and the central Pamir domes do not share a common history but that the central Pamir domes formed earlier.

5. Discussion

5.1. Cretaceous arc and early-middle Miocene exhumation

Migmatitic gneisses from the Shaxdara dome have previously been mapped as Archean and Proterozoic (Vlasov et al., 1991); major intrusions in the northern and eastern dome have been assigned Cretaceous ages. Unpublished zircon U/Pb LA-ICPMS ages from samples along the Gunt valley in the northern dome are mostly Mid-Cretaceous (B.R. Hacker, pers. comm.), the youngest ages are 21-29 Ma. Only two samples revealed Early Paleozoic (487 and 482 Ma) age components; both are interpreted as Mid-Cretaceous intrusions with inherited Paleozoic zircons. We interpret the Shaxdara gneisses to be high-grade (upper amphibolite facies; Hubbard et al., 1999) metamorphic equivalents of the Paleozoic clastic and Early Mesozoic carbonate

sequences that outcrop in the southeastern Pamir and the Wakhan range (Fig. 2). Wide-spread mid-Cretaceous magmatism is in line with the interpretation of flat-slab north-directed subduction of the Shyok back-arc basin (Schwab et al., 2004).

Field observations corroborated by latest Oligocene zircon U/Pb ages from a pegmatite (29-21 Ma) and a migmatitic orthogneiss (24 Ma; B.R. Hacker, pers. comm.) suggest that migmatization is contemporaneous with granitoid emplacement. Upper amphibolite facies conditions likely persisted through the Paleogene. Structural observations suggest continuous deformation from migmatitic to low-grade conditions under top-to-S extensional shear (see above). $^{40}Ar/^{39}Ar$ plateau-ages for hornblende (22.2±1.3 and 20.5±1.2 Ma), phlogopite (17.4±0.2 and 16.8±0.3 Ma) and biotite (18.3±0.3, 10.2±0.3 and 8.7±0.3 Ma; Hubbard et al., 1999) from the western Pjansch (Fig. 2) impose temporal constraints on tectonic exhumation to lower greenschist-facies conditions.

Early to middle Miocene hornblende and biotite $^{40}Ar/^{39}Ar$ ages (23.3-14.9 Ma; Schwab 2004) have also been reported from intrusive rocks of the Muzkol gneiss dome of the Central Pamirs (Fig. 1), suggesting common early Miocene onset of exhumation of all Pamir gneiss domes despite locations north and south of the Rushan-Pshart suture, respectively. AFT ages from the Muzkol dome are 15.7 and 15.4 Ma, one AFT age of the Sarez dome is 19.9 Ma (Schwab 2004). Thus rapid exhumation in the Central Pamir domes is confined to the early to middle Miocene; compared to the Shaxdara dome it was faster (older biotite $^{40}Ar/^{39}Ar$ ages), and ceased in the late Miocene, whereas in the Shaxdara dome high exhumation rates persisted until ~5 Ma.

5.2. Late Miocene tectonic denudation

Our apatite fission-track ages reveal rapid late Miocene cooling to below 120°C at exhumation rates of ~1-2 mm/yr, starting along the northern Shaxdara dome at least at 10 Ma and progressively exhuming the footwall of a major south-dipping shear zone; its southern margin is outlined by the southern Pjansch River. A rolling-hinge model of exhumation along a detachment fault (South Pamir Fault; Wernicke and Axen, 1988) is envisaged to account for late Miocene cooling (Fig. 7a).

Tectonic denudation ceased during the Pliocene. Quaternary incision of the Pjansch River, as suggested by the steep topography, may account for enhanced cooling, reflected by young AHe ages in the western elevation profile (Fig. 5a). Although not well documented yet by detailed AHe age-elevation profiles, the Pliocene Helium partial retention zone is inferred to be located at intermediate to high elevations (~4000 m.asl.) in the southwestern dome, as constrained by sample 6824F1 (Fig. 7b). River incision consequently exhumed samples now

located at lower elevations and amounts to ≤ 4 km since the ?late Pliocene-Pleistocene (assuming a recent location of the AHePRZ 2 km below the valley bottom). AHe ages from the Shaxdara valley (6831C3, 6827A2; Fig. 5b) are slightly older; if this difference in age is confirmed by further AHe ages along both rivers one might speculate that the Shaxdara valley is older than the N-S section of the Pjansch gorge, giving rise to local downwarping of isotherms and partial Helium retention in samples along the Shaxdara river. Depositional ages of river terraces and additional AHe cooling ages are necessary to quantify post-Miocene exhumation, verify river incision as its cause and test to what extent the individual valleys were affected.

Early–middle Miocene cooling rates estimated from $^{40}Ar/^{39}Ar$ ages (Hubbard et al., 1999) are ~30°C/myr; this is in the same order of magnitude as derived from our AFT age elevation profiles for late Miocene cooling assuming an elevated geothermal gradient of 30°C/km. The data are consistent with uniform tectonic denudation from the earliest to the latest Miocene (~20 to 5 Ma). If cooling of the high-grade gneisses is accommodated by a rolling-hinge mechanism, $^{40}Ar/^{39}Ar$ ages are expected to show the same correlation with distance to the dome-bounding fault as observed from AFT ages. Alternatively, a different style of denudation, likely encompassing mostly erosion, might have controlled early exhumation from amphibolite- to greenschist-facies conditions, followed by middle to late Miocene development of a rolling-hinge dome and cooling to ambient temperatures. Additional $^{40}Ar/^{39}Ar$ data are needed to assess whether cooling rates varied between early and late Miocene, and resolve possible N-S differences in timing or rate of exhumation from high-grade conditions.

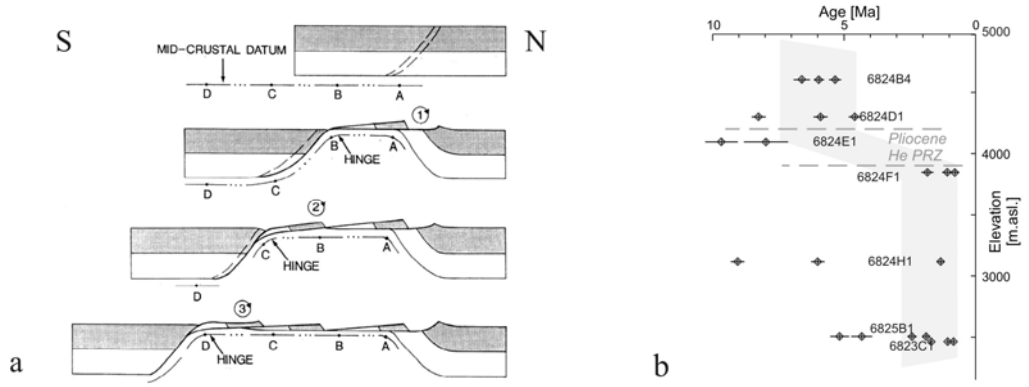

Figure 7. (a) Rolling-hinge model after Wernicke and Axen (1988; sketch from Wernicke et al., 1995) illustrating a N-S profile across the Shaxdara dome. Consecutive exhumation of footwall locations A-D is reflected in correlation of cooling ages with distance to dome-bounding fault at the active hinge. Note the low-angle detachment fault separating the exhumed footwall from north tilted blocks of low-grade metamorphic rocks. (b) Exhumed fossil AHe partial retention zone at ~4000 m.asl. constrained by AHe ages from the eastern elevation profile; high-elevation samples cooled during Miocene tectonic denudation, low-elevation samples due to river incision ~2 Ma.

Two ~15 Ma AFT ages from the northeastern dome seem to disagree with this general model. The data is still insufficient to assess the implications of the old ages. The two samples might belong to a fault block overlying the low-angle detachment fault (Fig. 7a), rather than the footwall gneisses. The AHe ages imply a cooling rate ~8°C/myr significantly lower than observed in the footwall rocks; this is consistent with slow exhumation by drag of hangingwall slices along the dome-bounding fault (Fig. 7a).

As mentioned above tectonic exhumation in the Muzkol and Sarez domes ceased ~10 myr earlier, during the middle Miocene. AFT ages from directly south of the eastern Rushan-Pshart suture (10.1 and 10.7 Ma; Schwab 2004; Fig. 2) are similar to AFT ages from the northern Shaxdara dome south (6905B1) and north (6904E1) of the Rushan-Pshart suture; they are within error the same as 6818E2 from the Yazgulom complex ~80 km north of the suture. We conclude that late Miocene tectonic denudation initiated along the Rushan-Pshart suture in the southeastern and southwestern Pamirs. Exhumation was asymmetric: in the southwest it continued for ~5 myr exposing basement over a N-S distance of 100 km width. To the east exhumation is confined to a narrow belt along the suture.

We tentatively propose that the low-angle detachment fault (Fig. 7a) dips eastward beneath low-grade sedimentary rocks of the southeastern Pamirs; this shear zone has previously been interpreted as low-angle fault beneath a nappe rooting in the Rushan-Pshart suture zone (Burtman and Molnar, 1993; Schwab et al., 2004). The model predicts that the low-grade cover consists of fault-bound blocks tilted up to 90° to the north. While normal faulting has been observed in the field (Ratschbacher, pers. comm.), tilting is difficult to assess due to intense folding of the Paleozoic-Mesozoic strata. A general northward tilting is, however, proposed based on the 1:200,000 geological maps (geol. map USSR). East of ~72°30'E it is unclear whether the South Pamir Fault continues along the Pamir valley north of the Afghan Pamirs or the Wakhan valley south of it; a low-angle detachment can be traced from east of the Afghan Pamirs to the northwest, where it connects with the Rushan-Pshart suture at ~72°30'E (Fig. 2). The detachment may continue eastward along the Rushan-Pshart suture as suggested by the ~10 Ma AFT ages at ~73°30'E, but has not yet been traced farther east.

The Muztagh-Ata and Kongur Shan of the Chinese Pamirs (Fig. 1) have been proposed to represent the eastward continuation of the Central Pamir domes (Robinson et al., 2007). There are, however, a number of significant differences in the development of the domes. In contrast to the South and Central Pamir domes crustal thickening, prograde metamorphism and partial melting persist until the late Miocene in the Muztagh-Ata (Robinson et al., 2004; Robinson et al., 2007). This has been ascribed to a ramp anticline growing over active intra-continental subduction of the Tarim along the Main Pamir Thrust (Fig. 1; Brunel et al., 1994). Onset of

rapid exhumation in the late Miocene is accommodated by the west-dipping Kongur Shan normal fault and continued at approximately constant rates until the present (Brunel et al., 1994; Robinson et al., 2004). For the southern Muztagh-Ata dome Robinson et al. (2007) report top-to-S kinematic indicators, which they relate to mid-crustal conditions; the authors infer middle Miocene exhumation accommodated by the south-dipping Shen-ti fault attested by $^{40}Ar/^{39}Ar$ muscovite and biotite cooling ages of ~10-8 Ma. Like the Kongur Shan exhumation to the surface was subsequently accommodated by E-W extension initiated during the latest Miocene.

The different cooling histories challenge correlation of the Muztagh-Ata–Kongur Shan with the Pamiran gneiss domes. Early-middle Miocene exhumation in the South and Central Pamir opposes crustal thickening in the Muztagh-Ata–Kongur Shan. Post-Miocene exhumation in the Muztagh-Ata–Kongur Shan is accommodated by E-W extension, but attributed to river incision, possibly climate-controlled, in the Shaxdara dome; no late or post-Miocene cooling has been documented in the Central Pamir domes. Only the mid-Miocene, top-to-S deformation and attendant cooling reported for the southern Muztagh-Ata shows some similarity with deformation in the Shaxdara dome. It is conceivable that the South Pamir detachment fault continues beyond 73°30'E and links with the Shen-ti fault; in this case late Miocene exhumation in the South Pamirs is kinematically related with deformation in the Muztagh-Ata at depth, the latter probably being overprinted by coeval ~NE-SW directed crustal thickening. This is, however, a hypothesis at best, which needs to be tested, e.g. by tracing the South Pamir detachment further east.

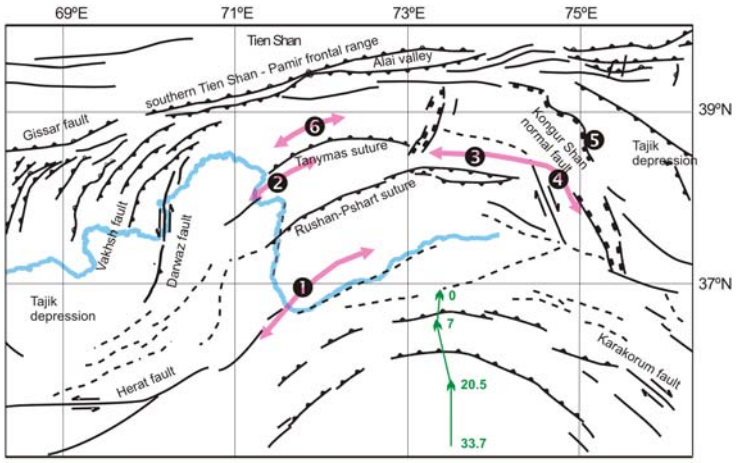

Figure 8. Active faults in the Pamir region from remote sensing data and from Burtman and Molnar (1993). 1: Shaxdara gneiss dome; 2: Yazgulom; 3: Muzkol; 4: Sarez dome; 5: Muztagh-Ata; 6: Pik Communism antiform. Green arrows indicate motion of India (western syntax) relative to Asia since Oligocene (from Le Pichon et al., 1992).

5.3. Driving mechanism for Miocene extension

Miocene N-S extension in the Pamirs causing formation of the South and Central Pamir gneiss domes has a major impact on the present day geometry of the Pamir Mountains. Extension is coeval with ongoing N-S directed convergence between India and Asia at a rate of 4.8 cm/yr (Le Pichon et al., 1992; Fig. 8). Convergence is compensated by development of a fold-thrust belt in the Tajik basin (Hamburger et al., 1992; Bourgeois et al., 1997), shortening along the frontal ranges (Hamburger et al., 1992; Sobel et al., 1997; Coutand et al., 2002), and imbrication of Tarim-basin strata along the Main Pamir Thrust (Brunel et al., 1994; Fig. 8) starting in the late Oligocene to Miocene. Transpressional strike-slip deformation along the Darvaz (sinistral) and Karakorum fault zones (dextral; Fig. 8) takes up an as yet unidentified amount of India-Asia convergence (e.g., Dunlap et al., 1998; Lacassin et al., 2004) since the Oligocene.

Crustal thickening within the Pamirs, possibly with concomitant reactivation of Paleozoic-Mesozoic sutures, is documented by late Oligocene zircon U/Pb ages of migmatites and pegmatites (see above). The *en echelon* arrangement of gneiss domes in the western Pamirs (Shaxdara, Yazgulom, Pik Communism; Fig. 8) suggests a common origin as antiforms resulting from sinistral transpression along the western margin of the Pamirs. Transpression resulted from indentation of the the western syntax of India into Asia and an overall anticlockwise rotation of India during its northward path (e.g., Le Pichon et al., 1992). Transpression is also evident from the Darvaz and Herat strike-slip faults and trend of fold-thrust belts in the Tajik basin (Fig. 8).

In the Shaxdara dome field structural evidence for transpression and N-S shortening is obscured by extensional top-to-S flow. This flow might be related to early Miocene onset of extension; alternatively, early Miocene hornblende cooling ages (Hubbard et al., 1999) may reflect the postulated early development of contractional antiforms; in this case extension started somewhat later. Extension was active at ~10 Ma at the latest, as documented by the interpreted development of the Shaxdara rolling-hinge dome in the footwall of the South Pamir Fault. The preferred interpretation of doming and extension is, however, overall transpressional thickening of the entire crust by frontal intra-continental subduction and long-wavelength–low amplitude buckling within the western Pamirs and concurrent to consecutive upper crustal extension compensating for excess thickening. Upper crustal extension may have been facilitated by thermal weakening due to Tertiary intrusions (see above) that are mostly confined to the domes. Low-wavelength buckling has been proposed for the distributed shortening and long-wavelength topographic changes in adjacent Tibet (Burg et al., 1994).

A relation between onset of syn-orogenic extension in the western Pamirs and a change in convergence direction from 000° to 347° at 20.5 Ma (Le Pichon et al., 1992) is speculative. Slowdown of India-Asia convergence from 4.8 to 4.5 cm/yr at 7 Ma (Le Pichon et al., 1992) likely put an end to extensional doming in the western Pamirs. At the same time convergence direction rotated clockwise by 20° (Le Pichon et al., 1992). This reorientation of the regional stress field coincides and may account for the onset of NE-SW extension across the Kongur Shan normal fault and exhumation of the Kongur Shan–Muztagh-Ata gneiss domes in the Chinese Pamirs (Brunel et al., 1994; Robinson et al., 2004; 2007).

6. Conclusions

The Shaxdara gneiss dome of southwestern Tajikistan is interpreted as a Paleozoic to Early Mesozoic marine sediment sequence, which experienced high-grade metamorphism and migmatization in the Cretaceous, when flat-slab subduction of the Shyok back-arc basin caused crustal thickening along the southern Asian continental margin and the development of a ~200 km broad magmatic arc. Low-grade equivalents of the Shaxdara gneiss source rocks are found in the southeastern Pamirs and in the Wakhan corridor of easternmost Afghanistan.

Continued convergence subsequent to the India–Asia-collision caused transpression along the western Pamirs resulting in crustal thickening within the Pamirs and formation of *en echelon* antiforms (Shaxdara, Yazgulom and Pik Communism gneiss complexes; Fig. 8). We suggest an either Oligocene or early Miocene age for antiform development. In the Shaxdara gneiss there is likely a continuous transition from hot, thickened magmatic arc crust to Cenozoic, post-collisional convergence and crustal shortening.

In the Shaxdara dome folding is concurrent with and passed into extension with the development of a major S-dipping normal fault along the southern dome margin (South Pamir Fault). Isostatic rebound beneath a rolling hinge (Fig. 7a; Wernicke and Axen, 1988) exhumed the gneiss dome under N-S extension. The onset of extension is at least ~10 Ma old but may be as old as early Miocene. We tentatively re-interpret the thrust sheet comprising most of southeastern Pamirs as tilted blocks overlying the low-angle detachment fault.

Synorogenic extension has been documented earlier in the Himalaya (South Tibetan Detachment fault; e.g., Burchfiel et al., 1992) and proposed to account for the Kongur Shan normal fault (Brunel et al., 1994). Identificantion of an extensional gneiss dome of comparable size is however unparalleled in the Himalaya-Tibet system.

Apatite (U-Th)/He data indicate post-Miocene incision of the deep gorge of the Pjansch river. River patters point to major reorganization of the drainage system likely related to this ?Pliocene or Pleistocene cooling event. Future research aims to unravel the neotectonic

evolution of the Southwest Pamirs and reveal possible links to deep seismicity located beneath the South Pamirs and Hindu Kush.

Acknowledgement

(U-Th)/He measurements were carried out by Dr. I. Dunkl at Univ. Göttingen. S. Unterricker and E. Curvo provided neutron fluence measurements for fission-track analysis. This research was funded by a fellowship from the Studienstiftung des Deutschen Volkes and a travel grant from DAAD to KS and by DFG grants RA 442-27 and RA 442-28.

References

Bourgeois, O., Cobbold, P.R., Rouby, D., and Thomas, J.-C. (1997) Least squares restoration of Tertiary thrust sheets in map view, Tajik depression, central Asia. J. Geophys. Res. 102, 27,553-27,573.

Brunel, M., Arnaud, N., Tapponnier, P., Pan, Y., and Wang, Y. (1994) Kongur Shan normal fault: Type example of mountain building assisted by extension (Karakoram fault, eastern Pamir). Geology 22, 707-710.

Buchroithner, M.F. and Scharbert, S.M. (1979) Geochronological data from the Great Afghan Pamir and the Eastern Hindu Kush. N. Jb. Geol. Paläont. Mh. 29, 449-456.

Buchroithner, M.F. (1980) An outline of the geology of the Afghan Pamirs. Tectonophysics 62, 13-35.

Burchfiel, B.C., Chen, Z.L., Hodges, K.V., Liu, Y.P., Royden, L.H., Deng, C.R., and Xu, J.N. (1992) The South Tibetan detachment system, Himalayan orogen: Extension contemporaneous with and parallel to shortening in a collisional mountain belt. Geol. Soc. Am. Spec. Publ. 269, 48 pp.

Burg, J.-P., Davy, Ph., and Martinod, J. (1994) Shortening of analogue models of the continental lithosphere: New hypothesis for the formation of the Tibetan plateau. Tectonics 13, 475-483.

Burtman, V.S. and Molnar, P. (1993) Geological and geophysical evidence for deep subduction of continental crust beneath the Pamir. Geol. Soc. Am. Spec. Pupl. 281, 76 pp.

Carlson, W.D., Donelick, R.A., and Ketcham, R.A. (1999) Variability of apatite fission-track annealing kinetics: I. Experimental results. Am. Mineral. 84, 1213-1223.

Coutant, I., Strecker, M., Arrowsmith, J.R., Hilley, G., Thiede, R.C., Korjenkov, A., and Omuraliev, M. (2002) Late Cenozoic tectonic development of the intramontane Alai Valley, (Pamir-Tien Shan region, central Asia): An example of intracontinental deformation due to the Indo-Eurasia collision. Tectonics 21, doi:10.1029/2002TC001358

Crawford, M.B. and Searle, M.P. (1992) Field relationships and geochemistry of pre-collisional (India-Asia) granitoid magmatism in the central Karakoram, northern Pakistan. Tectonophysics 206, 171-192.

Dodson, M.H. (1973) Closure temperature in cooling geochronological and petrological systems. Contrib. Mineral. Petrol. 40, 259-274.

Dodson, M.H. (1979) Theory of cooling ages. In : Lectures on isotope geology (E. Jäger and J.C. Hunziker, Editors), Springer Verlag, Berlin, 194-202.

Dunlap, J.W., Weinberg, R.F., and Searle, M.P. (1998) Karakoram fault zone rocks cool in two phases. J. Geol. Soc. London 155, 903-912.

Farley, K. (2002) (U-Th)/He Dating: Techniques, calibrations, and applications, in: Noble Gases in Geochemistry and Cosmochemistry, Rev. Mineral. Geochem. 47, 819-844.

Fraser, J.E., Searle, M.P., Parrish, R.R., and Noble, S. (2001) Chronology of deformation, metamorphism, and magmatism in the southern Karakoram Mountains. Geol. Soc. Am. Bull. 113, 1443-1455.

Hamburger, M.W., Sarewitz, D.R., Pavlis, T.L., and Popandopulo, G.A. (1992) Structural and seismic evidence for the intracontinental subduction in the Peter the First Range, Central Asia. Geol. Soc. Am. Bull. 104, 397-408.

Hildebrand, P.R., Noble, S., Searle, M.P., Waters, D.J., and Parrish, R.R. (2001) Old origin for an active mountain range: Geology and geochronology of the eastern Hindu Kush, Pakistan. Geol. Soc. Am. Bull. 113, 625-639.

Hubbard, M.S., Grew, E.S., Hodges, K.V., Yates, M.G., and Pertsev, N.N. (1999) Neogene cooling and exhumation of upper-amphibolite-facies 'whiteschists' in the southwest Pamir Mountains, Tajikistan. Tectonophysics 305, 325-337.

Hurford, A.J. (1990a) Standardization of fission-track dating calibration: Recommendation by the Fission-track Working Group of the I.U.G.S. Subcomission on Geochronology. Chem. Geol. 80, 171-178.

Hurford, A.J. (1990b) International-union-of-geological-sciences subcommission on geochronology recommendation for the standardization of fission-track dating calibration and data reporting. Nucl. Tracks Rad. Meas. 17, 233-236.

Hurford A.J. and Green P.F. (1982) A users' guide to fission-track dating calibration. Earth Planet. Sci. Lett. 59, 343-354.

Hurford A.J. and Green P.F. (1983) The zeta age calibration of fission-track dating. Isotope Geoscience 1, 285-317.

Jonckheere, R., Ratschbacher, L., and Wagner, G.A. (2003) A repositioning technique for counting induced fission tracks in muscovite external detectors in single-grain dating of minerals with low and inhomogeneous uranium concentrations. Rad. Meas. 37, 217-219.

Jonckheere, R., Enkelmann, E., Min, M., Trautmann, C., and Ratschbacher, L. (2007) Confined fission tracks in ion-irradiated and step-etched prismatic sections of Durango apatite. Chem. Geol. 242, 202-217.

Ketcham, R.A., Donelick, R.A., and Carlson, W.D. (1999) Variability of apatite fission-track annealing kinetics: III. Extrapolation to geological time scales. Am. Mineral. 84, 1235-1255.

Ketcham, R.A., Carter, A., Donelick, R., Barbarand, J., and Hurford, A.J. (2007) Improved modeling of fission-track annealing in apatite. Am. Mineral. 92, 799-810.

Lacassin, R., Valli, F., Arnaud, N., Leloup, P.H., Paquette, J.L., Li, H.B., Tapponnier, P., Chevalier, M.-L., Guillot, S. Maheo, G., and Xu, Z.Q. (2004) Large-scale geometry, offset and kinematic evolution of the Karakorum fault, Tibet. Earth Planet. Sci. Lett. 219, 255-269.

Le Pichon, X., Fournier, M., and Jolivet, L. (1992) Kinematics, topography, shortening, and extrusion in the India-Eurasia collision. Tectonics 11, 1085-1098.

Leven E.J. (1995) Permian and Triassic of the Rushan-Pshart zone (Pamir). Riv. Ital. Paleontol Stratigr. 101, 3-16.

Geological map of the USSR, sheets J-42-XXIV, J-42-XXX, J-43-XIII–XV, J-43-XIX–XXI, J-43-XXV.

Min, M., Enkelmann, E., Jonckheere, R., Trautmann, C., and Ratschbacher, L. (2007) Measurements of fossil confined fission tracks in ion-irradiated apatite samples with low track densities. Nucl. Instr. Meth. 259, 943-950.

Robinson, A.C., Yin, A., Manning, C.E., Harrison, T.M., Zhang, S.H., and Wang, X.F. (2004) Tectonic evolution of the northeastern Pamir: Constraints from the northern portion of the Cenozoic Kongur Shan extensional system, western China. Geol. Soc. Am. Bull. 116, 953-973.

Robinson, A.C., Yin, A., Manning, C.E., Harrison, T.M., Zhang, S.H., and Wang, X.F. (2007) Cenozoic evolution of the eastern Pamir: Implications for strain-accommodation mechanisms at the western end of the Himalayan-Tibetan orogen. Geol. Soc. Am. Bull. 119, 882-896.

Rolland, Y., Pêcher, A., and Picard, C. (2000) Middle Cretaceous back-arc formation and arc evolution along the Asian margin: the Shyok Suture Zone in northern Ladakh (NW Himalaya). Tectonophysics 325, 145-173.

Schwab, M. (2004) The amlgamation of the Pamirs and their subsequent evolution in the far field of the India-Asia collision. PhD thesis, TU Freiberg.

Schwab, M., Ratschbacher, L., Siebel, W., McWilliams, M., Minaev, V., Lutkov, V., Chen, F., Stanek, K., Nelson, B., Frisch, W., and Wooden, J. (2004) Assembly of the Pamirs: Age and origin of magmatic belts from the southern Tien Shan to the southern Pamirs and their relation to Tibet. Tectonics 23, doi:10.1029/2003TC001583.

Sobel, E.R. and Dumitru, T.A. (1997) Exhumation of the margins of the western Tarim basin during the Himalayan orogeny. J. Geophys. Res. 102, 5043–5064.

Sperner, B., Ratschbacher, L., and Ott, R. (1993) Fault-striae analysis: A Turbo Pascal program package for graphical presentation and reduced stress tensor calculation. Computers Geosciences 19, 1361–1388.

Vlasov, N.G., Dyakov, Yu.A. and Cherev, E.S. (Eds.) (1991) Geological map of the Tajik SSR and adjacent territories, 1:500,000. Vsesojuznoi Geol. Inst. Leningrad, Saint Petersburg.

Wernicke, B. and Axen, G.J. (1988) On the role of isostacy in the evolution of normal fault systems. Geology 16, 848-851.

Wernicke, B. (1995) Low-angle normal faults and seismicity: A review. J. Geophys. Res. 100, 20,159-20,174.

Yin, A. and Harrison, T.M. (2000) Geologic evolution of the Himalayan-Tibetan orogen. Annu. Rev. Earth Planet. Sci. 28, 211-280.

Zanchi, A., Gaetani, M., Angiolini, L., De Amicis, M., and Sironi, S. (2004) Geological map of Central–Western Karakoram, Pakistan. Univ. Milano.

Table 1. Sample descriptions and locations (WGS84)

Sample	Lithology	N latitude (°)	W longitude (°)	Elevation (m)
6818E2	leucogranite	38.11288	71.33740	1660
6819D2	granodiorite	37.83827	71.58802	2025
6823A3	leucogranitic gneiss	36.74068	71.90720	2696
6823C1	layered mafic rock	36.85353	71.53960	2464
6824B4	mylonitic, migmatitic metapelite	37.08388	71.53543	4603
6824D1	gneiss	37.07823	71.53568	4299
6824E1	gneiss	37.07657	71.53780	4096
6824F1	gneiss	37.07303	71.53915	3847
6824H1	orthogneiss	37.05322	71.54065	3118
6825B1	gneiss	37.02900	71.48365	2507
6826B1	kfs-granite	37.40495	71.49640	2137
6826D1	coarsegrained granite	37.33303	71.71740	2585
6827A2	granite	37.39782	71.64978	2383
6828A1	finegraine biotite-granite	37.18155	71.79857	3373
6929B1	biotite-hornblende-gneiss	37.14388	71.74752	4372
6829C1	gneiss	37.16062	71.75977	4014
6831C3	turmaline-bearing aplite	37.24173	72.18938	3104
6901D1	biotite-granite	37.47277	72.60627	4288
6901E1	biotite-granite	37.55715	72.65838	3716
6903C1	kfs-granite	37.73187	72.40135	2241
6904E1	granite	37.71355	71.78952	4194
6905B2	orthogneiss	37.61375	71.75363	2592

Table 2. Apatite fission-track data

sample (aliquot)		ϕ (10^{15} cm^{-2})	Grains	N_s	N_i	ρ_d (10^6 cm^{-2})	ζ-age (Ma) (pooled)	Z-age (Ma) (pooled)
6818E2		1.864	71	812	3943	0.359	10.4 (0.5)	10.1 (0.5)
6819D2	(a)	1.881				0.358		
	(b)	1.877				0.358		
6823A3		1.859	44	281	3068	0.359	4.6 (0.3)	4.5 (0.3)
6823C1		0.913	31	141	604	0.184	6.1 (0.6)	6.1 (0.6)
6824B4	(a)	0.915	39	536	2361	0.184	5.9 (0.3)	5.9 (0.3)
	(b)	1.855	54	441	2936	0.360	7.6 (0.4)	7.4 (0.4)
6824D1		0.917	32	359	1315	0.184	7.1 (0.5)	7.1 (0.5)
6824E1		0.920	68	341	484	0.184	18.3 (1.4)	18.3 (1.4)
6824F1		0.922				0.184		
6824H1	(a)	0.925	39	304	1199	0.184	6.6 (0.5)	6.6 (0.5)
	(b)	0.927	41	181	814	0.184	5.8 (0.5)	5.8 (0.5)
6825B1		0.929	27	65	365	0.184	4.6 (0.6)	4.6 (0.6)
6826B1		1.851	71	280	1691	0.360	8.4 (0.6)	8.2 (0.6)
6826D1	(a)	1.846	34	260	1670	0.361	7.9 (0.5)	7.7 (0.5)
	(b)	1.842	58	534	1929	0.361	14.0 (0.7)	13.7 (0.8)
6827A2	(a)	0.932	105	3173	11639	0.184	7.1 (0.2)	7.1 (0.2)
	(b)	1.837	70	1352	8045	0.361	8.5 (0.3)	8.3 (0.3)
6828A1		1.833	9	28	196	0.362	7.3 (1.5)	7.1 (1.4)
6929B1		0.804	57	578	1763	0.184	8.5 (0.5)	8.5 (0.5)
6829C1		0.794	53	705	2831	0.184	6.5 (0.3)	6.5 (0.3)
6831C3		0.784	67	1401	6089	0.184	6.0 (0.2)	6.0 (0.2)
6901D1		0.774	26	1521	2650	0.184	14.9 (0.6)	14.9 (0.6)
6901E1	(a)	0.764				0.184		
	(b)	0.754	125	782	1335	0.184	15.2 (0.8)	15.2 (0.8)
6903C1	(a)	0.744	72	451	2475	0.184	4.7 (0.3)	4.7 (0.3)
	(b)	0.734	101	712	2553	0.184	7.2 (0.4)	7.2 (0.4)
6904E1		1.829	4	27	164	0.362	8.4 (1.7)	8.2 (1.7)
6905B2	(a)	0.724	106	1796	4765	0.184	9.8 (0.4)	9.8 (0.4)
	(b)	0.714	34	766	2095	0.184	9.5 (0.5)	9.5 (0.5)

Table 3. (U-Th)/He analytical data

Sample	He conc.[1] [10^{-11} mol/g]	U conc.[1] [ppm]	Th conc.[1] [ppm]	Sm conc.[1] [ppb]	Apatite [µg]	Ft	Corr. Age[1] [Ma]
6823C1	20.7 (1.2)	49.2 (1.3)	41.4 (1.0)	64 (1)	3.21	0.77	**0.8 (0.0)**
	23.2 (1.2)	44.8 (1.4)	33.5 (0.9)	59 (2)	2.79	0.76	**1.1 (0.0)**
	42.2 (1.4)	51.3 (1.2)	35.4 (0.9)	96 (3)	3.65	0.77	**1.7 (0.0)**
6824B4	114.4 (3.5)	48.9 (1.9)	23.0 (0.6)	196 (6)	1.73	0.73	**5.3 (0.1)**
	129.2 (2.9)	45.6 (1.5)	29.4 (0.8)	176 (4)	2.73	0.76	**6.0 (0.1)**[2]
6824D1	136.4 (3.0)	34.9 (1.2)	26.3 (0.7)	129 (3)	2.66	0.74	**8.2 (0.1)**[2]
	275.1 (5.7)	28.4 (2.2)	58.0 (1.5)	103 (3)	1.35	0.68	17.7 (0.2)
	38.9 (1.3)	17.5 (0.7)	9.9 (0.3)	57 (2)	5.35	0.79	**4.6 (0.1)**
6824E1	292.9 (4.1)	3.7 (0.8)	2.5 (0.3)	99 (1)	5.13	0.80	155.8 (1.8)
	52.9 (2.3)	6.5 (1.9)	30.1 (0.8)	83 (2)	2.07	0.74	**9.7 (0.3)**
	12.4 (0.9)	3.4 (1.6)	1.4 (3.6)	68 (2)	2.86	0.76	**8.0 (0.4)**
6824F1	285.8 (4.2)	2.5 (1.8)	10.7 (0.3)	55 (2)	3.02	0.75	138.9 (1.6)
	4.8 (0.4)	4.4 (1.0)	8.1 (0.2)	107 (4)	3.66	0.77	**1.8 (0.1)**
	3.1 (0.4)	4.8 (1.8)	10.7 (0.3)	114 (3)	2.12	0.72	
6824H1	224.5 (4.5)	57.6 (1.5)	26.7 (0.7)	510 (6)	3.32	0.71	9.1 (0.1)
	62.3 (1.7)	20.6 (0.9)	15.1 (0.4)	649 (12)	3.83	0.79	**6.0 (0.1)**[2]
	121.4 (4.5)	23.3 (3.9)	14.0 (1.3)	518 (11)	0.98	0.70	12.1 (0.3)
6825B1	27.7 (1.3)	32.7 (1.1)	14.3 (0.4)	54 (2)	2.98	0.75	**1.9 (0.1)**
	43.4 (2.0)	12.4 (1.7)	32.7 (0.9)	43 (1)	2.23	0.77	**5.2 (0.2)**[2]
	17.3 (0.9)	12.0 (1.2)	25.0 (0.7)	46 (1)	3.07	0.74	**2.4 (0.1)**
6827A2	64.8 (1.9)	50.5 (1.3)	11.8 (0.3)	223 (5)	2.94	0.75	**2.6 (0.1)**
	231.9 (1.8)	91.3 (1.7)	5.4 (0.1)	235 (5)	13.98	0.84	**5.5 (0.0)**
	62.5 (1.9)	48.5 (1.2)	11.8 (0.3)	211 (7)	3.12	0.76	**3.0 (0.1)**
6829B1	30.9 (1.8)	16.3 (1.5)	2.5 (2.1)	51 (1)	2.66	0.71	**4.8 (0.2)**
	55.7 (2.1)	13.1 (1.6)	2.5 (2.8)	55 (1)	2.22	0.76	**9.9 (0.3)**[2]
	98.8 (3.3)	12.4 (2.1)	18.6 (0.5)	14 (1)	1.56	0.71	15.3 (0.4)
6829C1	227.7 (3.4)	73.1 (1.5)	26.3 (0.7)	94 (2)	4.23	1.00	**5.3 (0.1)**
	60.3 (2.0)	24.8 (1.1)	11.0 (0.3)	82 (2)	2.84	0.73	**5.5 (0.1)**
	38.5 (1.8)	15.2 (1.3)	12.4 (0.3)	96 (2)	2.28	0.71	**5.5 (0.2)**
6831C3	92.2 (2.4)	46.5 (1.4)	11.4 (0.3)	136 (3)	2.93	0.68	**5.1 (0.1)**
	112.9 (4.0)	77.5 (2.8)	63.1 (1.6)	139 (3)	1.45	0.71	**3.2 (0.1)**
6901D1	35.7 (2.3)	144.7 (3.3)	31.5 (0.9)	357 (5)	1.78	0.80	0.5 (0.0)
	800.6 (9.6)	106.1 (2.7)	21.5 (0.6)	275 (6)	1.60	0.70	18.9 (0.2)
	722.6 (13.2)	101.7 (5.2)	15.8 (2.7)	262 (7)	0.71	0.63	20.1 (0.2)
6901E1	274.7 (2.7)	42.2 (1.5)	134.3 (3.3)	431 (10)	2.21	0.73	**9.8 (0.1)**
	200.9 (5.6)	33.8 (3.2)	125.1 (3.1)	308 (8)	1.20	0.69	**8.5 (0.2)**
	116.4 (3.3)	20.3 (1.8)	50.2 (1.3)	276 (6)	1.80	0.71	**9.4 (0.2)**
6903C1	7.2 (1.2)	3.7 (69.7)	33.1 (2.8)	317 (7)	0.43	1.00	**1.2 (0.2)**[3]
	76.2 (2.6)	38.5 (1.7)	265.3 (6.4)	784 (18)	1.81	0.70	**2.0 (0.0)**
	31.4 (1.2)	8.9 (0.8)	13.4 (0.4)	329 (8)	3.75	0.76	**6.3 (0.2)**[2]
6904E1	565.8 (15.7)	101.8 (9.7)	604.9 (14.8)	805 (21)	0.38	0.50	**8.5 (0.1)**[2]
	343.6 (5.8)	53.5 (2.1)	244.7 (5.9)	704 (15)	1.51	0.70	**8.2 (0.1)**[2]
	296.4 (6.1)	56.5 (2.1)	277.7 (6.7)	731 (14)	1.49	0.65	79.9 (1.1)

[1] errors are 1s

[2] (U-Th)/He ages older than fission-track age but within error

[3] note the large error on U

bold letters indicate ages interpreted as reliable